Tribology International 175 (2022) 107795

Contents lists available at ScienceDirect

Tribology International

journal homepage: www.elsevier.com/locate/triboint

Tribological properties of vanadium oxides investigated with reactive molecular dynamics

Miljan Dašić [a,b,*], Ilia Ponomarev [a,**], Tomas Polcar [a], Paolo Nicolini [a]

[a] Department of Control Engineering, Faculty of Electrical Engineering, Czech Technical University in Prague, Technicka 2, Prague 6, 16627, Czech Republic
[b] Scientific Computing Laboratory, Center for the Study of Complex Systems, Institute of Physics Belgrade, University of Belgrade, Pregrevica 118, Belgrade, 11080, Serbia

ARTICLE INFO

Keywords:
Lubrication
Hard coatings
Vanadium oxides
Molecular dynamics
ReaxFF

ABSTRACT

We present a reactive molecular dynamics study on tribological properties of five vanadium oxides ($V_2O_3, V_3O_5, V_8O_{15}, V_9O_{17}, VO_2$) under elevated temperatures and pressures. All considered stoichiometries provide lubrication with a comparatively low coefficient of friction ($COF \sim 0.2$ at 600 K, $COF < 0.2$ at 800 and 1000 K) which is a valuable information relevant for the design of coatings containing vanadium as a lubricious agent. An overall tendency of the decrease of friction coefficient with the increase of temperature represents a tribological effect useful for self-adjusting lubrication. We observed the increasing trend of adhesion-related offset of the friction force with the decrease of oxygen content in vanadium oxides.

1. Introduction

Friction and wear represent a serious obstacle to the efficient operation of engineering systems in all areas of industry. There is an estimate that friction and wear cause a loss of approximately one-quarter of the global energy production [1]. In every system where a contact between surfaces in relative motion is present, the phenomenon of friction occurs and causes energy losses. Considering this fact, the usage of materials, referred to as *lubricants*, which can enable low friction and prevent wear, is necessary [2].

The most common choices include *liquid lubricants* like water-based ones [3–6], petroleum-based oils [7–9], or ionic liquids [10–14]. When it comes to more specific operating conditions, including high temperature or vacuum, *solid lubricants* need to be used instead of liquid ones. The two major families include *carbon-based* solid lubricants (such as graphite [15–17] or diamond-like carbon coatings [18,19]) and *transition metal dichalcogenides* (TMDs) [20–24]. However, both of them show a tendency to degrade at elevated temperatures in oxidative environment [25,26].

Taking into account that providing effective lubrication at high temperatures/pressures and under oxidation is relevant for various industrial applications, such as turbomachinery and cutting tools [27,28], there is a need for designing suitable coatings. Those are hard and oxidation-resistant coatings consisting of binary or ternary films (e.g., Cr–N, Ti–N, Cr–Al–N, Ti–Al–N), doped with an additional element (usually a metal) [27–33]. Such coatings operate in a way that the dopant diffuses to the surface of the coating, reacts with oxygen, and forms an oxide layer that serves as a lubricant. Out of several possibilities for the choice of the metal, *vanadium* and *silver* gained popularity. There is either oxide (V–O) or metallic (Ag) lubrication. Vanadium oxides and metallic silver reduce friction and melt at relatively low temperatures (below 700 °C in case of V_2O_5; melting point of metallic Ag is 961.8 °C, both at atmospheric pressure), hence providing liquid lubrication [28,32,34–39].

We have previously studied the tribological properties of vanadium pentoxide V_2O_5 [40]. We found out that even a single layer of it present on the surface of a vanadium doped solid lubricant provides efficient lubrication with the coefficient of friction $COF < 0.2$, which is an established value when considering lubrication based on solid-lubricating materials [26].

The dopant of solid coatings investigated in the present study is *vanadium* (as in the Ref. [40]), which reacts with oxygen and forms oxides with different stoichiometries, depending on the working conditions [41]. Accordingly, the amount of oxygen present in the oxidative environment, can be taken as a study parameter, leading to the consideration of different vanadium-oxide stoichiometries.

This study aims to explore the tribological performance of underoxidized vanadium lubricants. The key questions which we are targeting are related to the usability (i.e., providing lubrication regardless

---

* Corresponding author at: Scientific Computing Laboratory, Center for the Study of Complex Systems, Institute of Physics Belgrade, University of Belgrade, Pregrevica 118, Belgrade, 11080, Serbia.
** Corresponding author.
E-mail addresses: dasicmil@fel.cvut.cz, mdasic@ipb.ac.rs (M. Dašić), ponomili@fel.cvut.cz (I. Ponomarev).

https://doi.org/10.1016/j.triboint.2022.107795
Received 7 April 2022; Received in revised form 11 July 2022; Accepted 17 July 2022

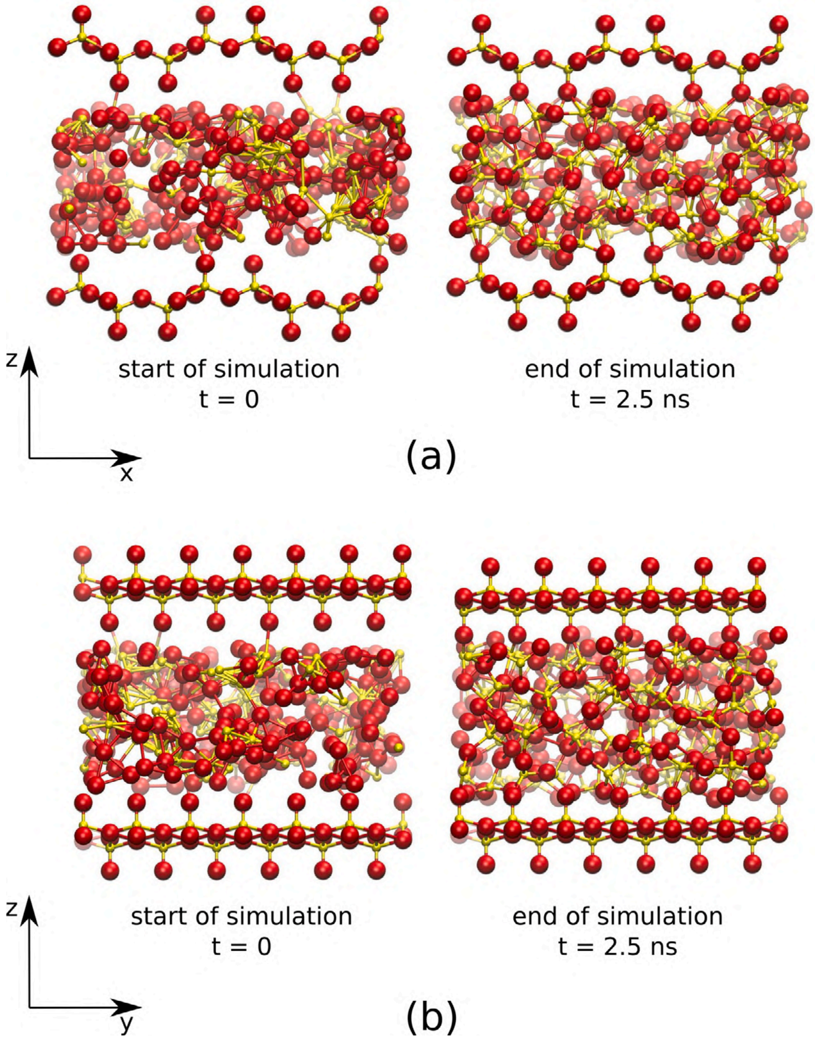

Fig. 1. Snapshots ((a) *xz* and (b) *yz* cross-sections) of the simulated tribological system taken at the start (t = 0) and at the end (t = 2.5 ns) of a simulation. Vanadium and oxygen atoms are represented as smaller yellow and bigger red spheres, respectively. The top and bottom V_2O_5 layer represent rigid counter-bodies, while V and O atoms confined between them constitute a vanadium oxide lubricant of a certain stoichiometry, in general labelled as V_xO_y.

of the stoichiometry) and efficiency (i.e., enabling low friction coefficient) of such lubricants. We have conducted a reactive molecular dynamics study on the tribological properties of five vanadium oxide stoichiometries. Our study includes $V_2O_3, V_3O_5, V_8O_{15}, V_9O_{17}, VO_2$, which are observed in experimental investigations of coatings with vanadium oxide-based lubrication [37,41,42].

2. Methods

We have employed an atomistic model within the *ReaxFF* (reactive force field) potential [43] to describe the interactions of vanadium and oxygen atoms. *ReaxFF* is an empirical potential based on the bond order concept. The total potential energy of the system is calculated as a sum of energies of different components: bonds, atoms, lone-pairs, valence and torsion angles, hydrogen bonds, van der Waals and Coulombic interactions. *ReaxFF* uses bond orders which change dynamically during the simulation, depending on the interatomic distances.

In this study, we used the *Chenoweth et al.* force field parameterization [44], which was originally developed for oxidative dehydrogenation on vanadium oxide catalysts. Besides that purpose, the aforementioned force field has been used to study the chemical stability and surface stoichiometry of solid vanadium oxide phases [45]. Also, the *Chenoweth et al.* force field has been used in a study on the tribological properties of crystalline and amorphous V_2O_5 lubricants [40]. All reactive molecular dynamics simulations presented in this work have been conducted using the *reax/c* package [46] of the *LAMMPS* code [47,48].

Since the main target of our study is the exploration of the effects of stoichiometry on the tribological properties of vanadium oxides, our present simulation setup is designed analogously to the one utilized in a previous study on the mechanism of tribological action of V_2O_5 [40]. Such approach allows comparisons of the tribological performance of under-oxidized vanadium and vanadium pentoxide lubricants. Our tribological system consists of two V_2O_5 layers, which are used as rigid counter-bodies, and an initially random arrangement of $N_V = 144$ vanadium atoms and an appropriate number of oxygen atoms N_O, which are used as a lubricant confined between the two V_2O_5 layers. The above-mentioned term *appropriate* means that the number of oxygen atoms is determined in correspondence with the chosen stoichiometry of vanadium oxides, which is in general labelled as V_xO_y, hence $N_O = \frac{y}{x} N_V$. The mass density of considered V_xO_y phases was selected in a way that it is equal to the mass density of the corresponding crystalline vanadium oxide, minus 10% to account for a lower density of the amorphous phase. Regarding the periodic boundary conditions applied, our system was periodic in all three directions (i.e., x, y and z), however in the z direction we effectively had rigid layers acting like walls.

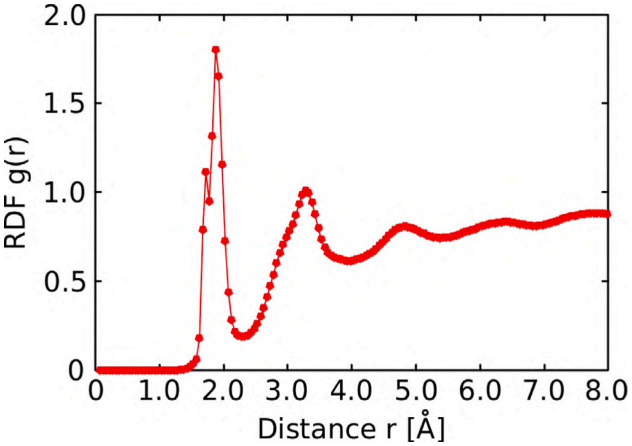

Fig. 2. Representative total radial distribution function (*RDF*), labelled as $g(r)$, for the set of parameters (V_3O_5, 4 GPa, 1000 K). For all sets of parameters the *RDFs* have a similar dependence on the distance, taking into account the presence of short-range and the lack of long-range ordering (check Figs. 3, 4 in Supplementary Information).

The first step of our simulations was a *structural relaxation* of the initially randomly arranged V_xO_y phase, where we applied the conjugate gradient method within *LAMMPS* [47,48], with the stopping tolerance of 10^{-12} for energy and 10^{-12} kcal/molÅ for force; both maximum number of iterations of minimizer and maximum number of force/energy evaluations were set at 10^5. After the relaxation, we proceeded to a *melt-quench* step at a target normal load of 0, 1, 2, 3 or 4 GPa, imposed on the top rigid V_2O_5 layer. We heated the V_xO_y phase up to 5000 K and then quenched it at a rate of −10 K/ps to the target temperature of 600 K, 800 K or 1000 K. After these steps, we proceeded with the system *equilibration* at the target temperature for 100 ps, and then we started the *sliding* of the top V_2O_5 layer in the x-direction at a velocity of $V_x = 1.133$ m/s. We chose the sliding velocity so that 1 ns of sliding corresponds to a run through the primitive cell of V_2O_5, which is consistent with our previous study [40]. The sliding part of our simulations lasted for 2 ns and during this production stage we recorded the atomic positions and forces, so that they can be used in a subsequent analysis. In all simulations, we used a timestep of 0.5 fs. For any simulation conditions (comprising selected stoichiometry, applied normal load and temperature), 5 independent runs were carried out. Different independent runs correspond to the usage of different seeds of the random number generator applied to obtain the starting configurations of the confined V and O atoms in the V_xO_y phase. Such a procedure enabled us to determine the averages and the standard deviations of the computed quantities. An illustration of our simulation setup at the start and at the end of a simulation is shown in Fig. 1.

3. Results and discussion

3.1. Tribological behaviour of amorphous vanadium oxides

Let us label the set of parameters defining a distinguishable simulation as $\left(V_xO_y, F_z, T, i\right)$, which correspond to the stoichiometry, normal load, temperature and index of the independent run, respectively. The friction force was defined as the force acting on the top rigid V_2O_5 layer in the direction opposite to the sliding direction; hence, we label it as F_x. For each set of parameters $\left(V_xO_y, F_z, T\right)$ we determine the friction force by computing the average value over five independent runs. The associated error was computed as the unbiased standard deviation over the independent runs.

In Fig. 2 we show the total radial distribution function related to the sliding segment of our simulations for the representative set of parameters (V_3O_5, 4 GPa, 1000 K). The results are analogous for all sets of parameters. We notice a short-range ordering, arising from distinct (though not fixed) bonding distances, but any long-range ordering is lacking, identifying our V_xO_y phase as *amorphous* or *liquid*. The boundary between an *amorphous solid* and a *liquid* state is not clearly and straightforwardly distinguishable, especially considering the working conditions of our study (i.e., relatively high temperatures and normal loads, together with sliding). Taking all relevant circumstances into account, we consider those two states as equivalent within the framework of our study.

In Fig. 3 we present the evolution of the sliding force with respect to time for the set of parameters (V_3O_5, 4 GPa, 1000 K). It is a representative case for the sliding force vs. time relationship; the profiles for other sets of parameters look qualitatively similar to the reported one. We can notice in Fig. 3(a) the absence of upward/downward trends, which implies that the system undergoes a steady sliding process. This kind of tribological behaviour is expected for amorphous/liquid lubricants, differently from, for example, crystalline V_2O_5 lubricant [40]. In Fig. 3(b) we show the temporal trends (computed as the moving average over 1000 values) of all five independent runs. Qualitatively, in all 5 cases the sliding force vs. time curves are analogous.

By following the standard approach in tribology, we applied a linear fitting on the dependence of the sliding force F_x on the normal load F_z:

$$F_x = COF \cdot F_z + F_x^0, \tag{1}$$

where the slope corresponds to the coefficient of friction (COF), while the offset F_x^0 corresponds to the sliding force when the normal load on

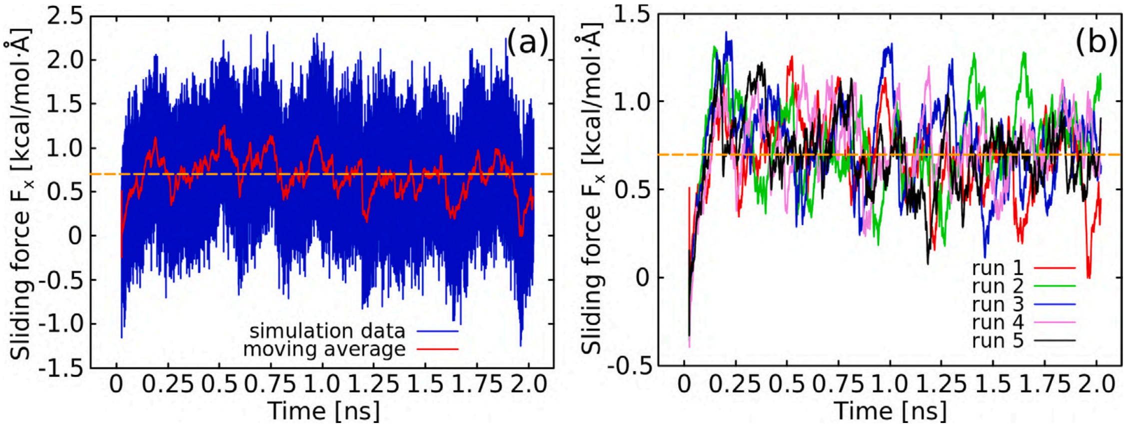

Fig. 3. Time profiles of the sliding force F_x in the case of V_3O_5 lubricant under the applied pressure of 4 GPa and at the temperature of 1000 K. Panel (a) reports the results of the independent run 1. In the panel (a), the solid blue line represents raw simulation data, the solid red line represents the moving average, while the horizontal dashed orange line is the global average. Panel (b) shows the moving averages of the sliding force corresponding to the 5 independent runs, represented by solid lines with different colours. It also includes the global average calculated over all 5 independent runs (for the same set of parameters (V_3O_5, 4 GPa, 1000 K)), marked with a horizontal dashed orange line.

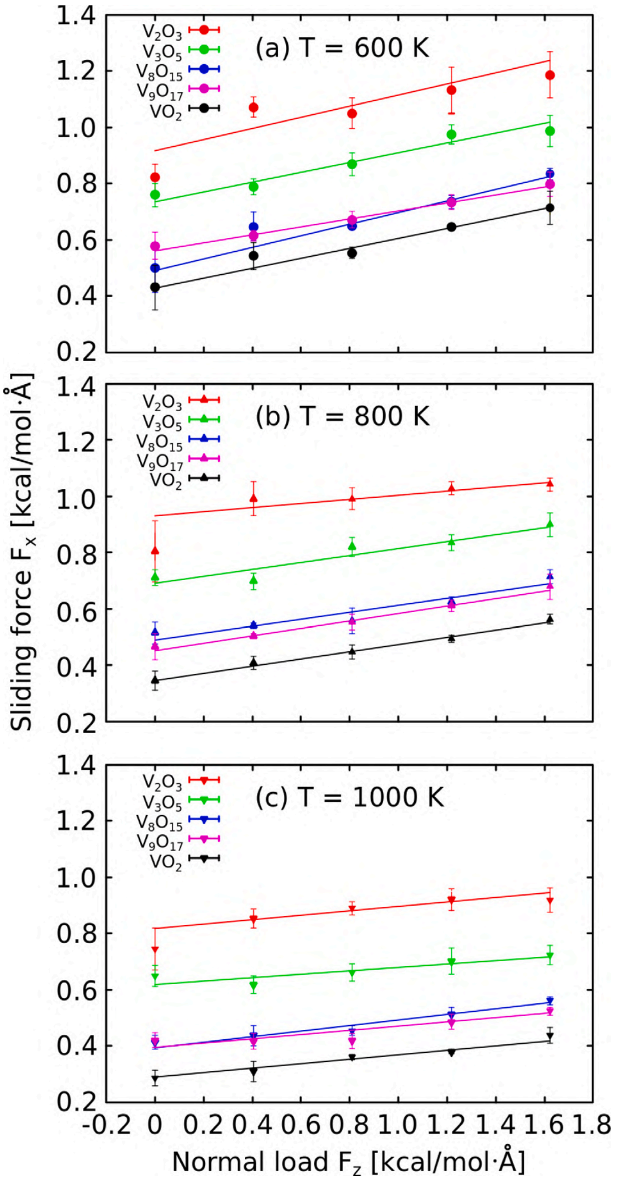

Fig. 4. Dependence of the sliding force F_x on the normal load F_z at the temperatures of (a) $T = 600$ K, (b) $T = 800$ K and (c) $T = 1000$ K. The error bars represent the standard deviation of the average values obtained from the sliding simulations. The solid lines were obtained by linear fitting via Eq. (1). Corresponding parameters of the applied linear fitting are listed in Table I of the Supplementary Information.

the top V_2O_5 layer is not applied (i.e., $F_z = 0$). In Fig. 4 we present the sliding force F_x vs. normal load F_z dependence for all considered stoichiometries and temperatures. We can notice the effects of stoichiometry and temperature on the frictional behaviour of amorphous vanadium oxide lubricants: there is a separation and ordering of the results (i.e., the offset of the linear fits) depending on the stoichiometry; temperature affects both the slope and the offset of the linear fits.

To gain a more detailed insight into the dependence of the slope and offset of applied linear fits (from Eq. (1)) on the stoichiometry and temperature, we prepared the COF and F_x^0 vs. stoichiometry plots at all studied temperatures, shown in Fig. 5(a) and Fig. 5(b), respectively. At a fixed temperature, we do not notice any statistically significant changes of the COF as a function of stoichiometry. The values which we obtained for the COF ($\sim$ 0.2 at 600 K, $\sim$ 0.15 at 800 K and $\sim$ 0.1 at 1000 K) are also in good agreement with the previously determined results for amorphous V_2O_5 lubricant at the same temperatures (e.g., see Fig. 8 and Table 6 in the Ref. [40]), which means that even under-oxidized vanadium is going to be an effective lubricant. There is also an overall tendency of the decrease of COF with the increase of temperature for all considered vanadium oxides, however, in some cases the values of COF at different temperatures are indistinguishable within the margin of error. The decrease of friction coefficient with the increase of temperature is an expected tribological effect in the case of the hydrodynamic lubrication regime of the Stribeck curve [49]. A higher temperature of an amorphous/liquid lubricant leads to its lower viscosity [50,51] and, consequently, to a lower friction coefficient. Another consequence of such behaviour is a somewhat self-adjusting character of the lubrication, which enables lowering of the friction coefficient. Sliding at a lower temperature with a higher COF would generate energy, dissipated in the form of heat, that would, in turn, increase the temperature of the coating and hence decrease the COF, allowing easier sliding. We added a dashed horizontal line in Fig. 5(a) at $COF = 0.2$ to denote an established boundary for the low value of the friction coefficient of high-temperature self-lubricating coatings. Such a boundary low value can be used for defining the quality of novel solid-lubricating materials (e.g., see Fig. 5 in the Ref. [26]). All the obtained values of COF at the temperatures of 800 and 1000 K are well-below this threshold of 0.2, while at 600 K the values belong to its vicinity. We should mention that there is a good agreement of our results regarding COF with the values of experimentally measured COF of vanadium-containing nitride coatings [29,37,52].

The offset F_x^0 of the linear fits from Eq. (1) is related to the adhesion component of the friction force [53–55]. In Fig. 5(b) we present the F_x^0 vs. stoichiometry dependence for the three studied temperatures. We notice an overall decreasing trend of the F_x^0 with the increase of the oxidation level of vanadium. As F_x^0 accounts for the adhesion between the top rigid V_2O_5 layer and the V_xO_y lubricant, a higher oxidation level of vanadium in V_xO_y enables formation of less bonds between the V_2O_5 layer and the lubricant, which leads to a lower adhesion. This represents mainly a qualitative explanation of the adhesion-stoichiometry relation. However, we provide a quantitative explanation based on counting the bonds between the V_xO_y lubricant and the top V_2O_5 layer in the following subsection titled *Structural analysis*.

As already stated in the *Methods* section, our simulation setup was built with the V_2O_5 layers as counter-bodies of the tribo-contact to make the results comparable with the previous study [40] dealing with the amorphous V_2O_5 lubricant. However, such a simulation setup can also be somewhat relevant for practical applications. In the operation of a real coating, utilized for example, as a cutting tool, we would expect the tribolayer of vanadium oxides to be sandwiched between the products of oxidation of the coating (primarily oxides like SiO_2 and TiO_2) and the surface of the stainless steel, which is also an oxidized surface. Even though our molecular dynamics model is far from perfect to simulate such interactions, it might show some relevant trends. In the applications like coatings for cutting tools, adhesion can be a very important phenomenon since the cutting tool should not be stuck on the surface.

3.2. Structural analysis

We have defined a V–O bond as V and O atoms being closer than the cutoff distance of 2.5 Å, which is the length of the longest V–O bond in crystalline oxides (2.2 Å, in ReaxFF-optimized V_2O_5), plus extra 15% to account for generally longer bonds in amorphous phase [56]. We looked at a number of V–O bonds, expressed as the average coordination numbers of vanadium, CN_V, and oxygen, CN_O. We paid special attention to the bonding between the rigid V_2O_5 layers and the amorphous V_xO_y oxide phase. These bonds are almost exclusively formed between the V atoms of the amorphous V_xO_y phase and the O atoms of the rigid V_2O_5 layers. Consideration of the aforementioned bonds provides us a good measure of the adhesion interactions between a rigid oxide body and an amorphous oxide. We quantify this type of

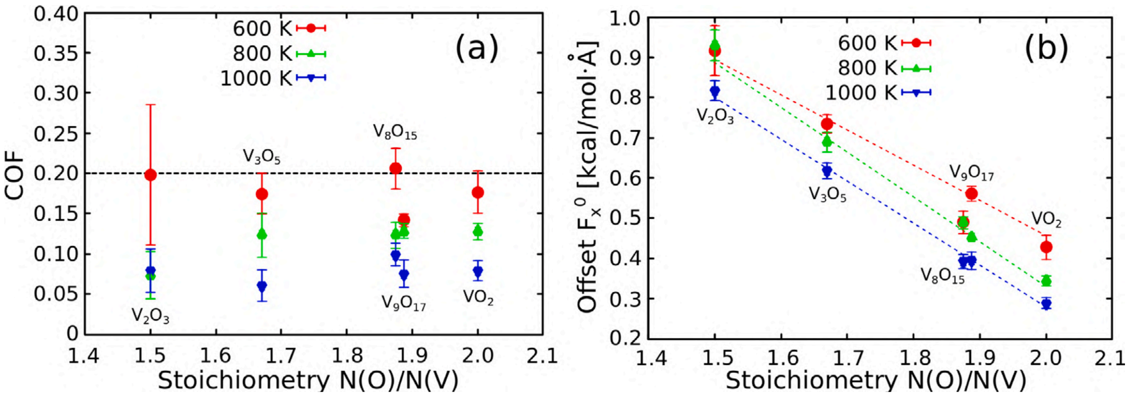

Fig. 5. (a) Dependence of the friction coefficient COF on the stoichiometry at the temperatures of $T = \{600, 800, 1000\}$ K. (b) Dependence of the offset of the sliding force F_x^0 on the stoichiometry at the temperatures of $T = \{600, 800, 1000\}$ K. The points presented in the panels (a) and (b) were obtained as slopes and offsets of the linear fits from Eq. (1), respectively, while the errorbars represent the associated error computed via the fitting procedure. Dashed lines in the panel (b) represent linear fits, that serve as guides to the eye.

bonding as the number of such bonds per a V atom, and denote it as CN_V^*.

We have seen from Fig. 5(a) that the stoichiometry of amorphous vanadium oxide lubricants weakly affects the friction coefficient. However, it clearly impacts the offset of the sliding force F_x^0, as we can observe from Fig. 5(b). This effect can also be noticed in the separation and ordering, with respect to stoichiometry, of the sliding force vs. normal load curves in Fig. 4. In order to quantitatively describe such a behaviour, we analysed the structural features of V_xO_y phases, looking primarily into V–O bonds.

The effect of stoichiometry on the network connectivity and the occurrence of such V_xO_y-to-V_2O_5 bonds at the temperature of 1000 K (results for the other two studied temperatures are analogous) is presented in Fig. 6. We observe the almost constant coordination numbers of vanadium ($CN_V \sim 4$ under the normal load of 0 GPa) throughout the stoichiometries. On the other side, the coordination number of oxygen CN_O decreases with the increase of the overall oxygen content in the V_xO_y phase, in order to provide enough bonding to vanadium. Also, as we move to more oxygen-poor stoichiometries, we observe a higher tendency of the vanadium atoms from V_xO_y to bond with the oxygen atoms from V_2O_5 rigid layers, i.e., CN_V^* increases. Since those bonds are to be considered the main cause of the adhesion between the V_xO_y lubricant and the rigid V_2O_5 layers, this tendency offers an explanation for the increase of the offset of the sliding force F_x^0 with the decrease of the oxygen content in V_xO_y, as shown in Fig. 5(b). Also, we obtained that, at a fixed stoichiometry, all coordination numbers (i.e., CN_V, CN_V^* and CN_O) increase with the increase of the normal load. This outcome can be easily explained taking into account that the increased normal load causes a closer contact of atoms in the V_xO_y lubricant (i.e., a lower volume per atom; see Fig. 1 in the Supplementary Information). Consequently, there are more atoms positioned within the bonding cutoff distance of 2.5 Å. As the oxygen content decreases, the overall increase of the average coordination number of oxygen causes the increase of the average V–O bond lengths, as we show it in Fig. 7. The elongation of the bonding distances lowers the bond energy, which makes bond switching in the course of sliding, and hence the changes in the network connectivity of the V_xO_y lubricant, easier. This might be a reason for the almost constant COF throughout the stoichiometries: there are more bonds per atom as the amount of oxygen in V_xO_y decreases (both by just increasing the fraction of atoms with a higher CN and by increasing the CN of oxygen atoms). However, those bonds are longer and, consequently, weaker. Hence, the opposite changes of the number of bonds and their length with respect to stoichiometry are the effects cancelling each other, which results in a weak dependence of the friction coefficient on stoichiometry (see Fig. 5(a)).

Similarly to a previous study (see Fig. 9 in Ref. [40]), we present the effect of the network connectivity of amorphous V_xO_y lubricant (expressed as the average coordination number of vanadium CN_V) on the sliding force F_x in Fig. 8. As in the case of V_2O_5, we observe a linear relation between the quantities in question, which is reasonable as a behaviour consistent with the fluid lubrication regime of the Stribeck curve [49]: higher network connectivity means higher viscosity [57, 58], which results in a higher friction force.

4. Conclusions

We have performed reactive molecular dynamics simulations to study the tribological properties of practically relevant vanadium oxide phases at elevated temperatures and pressures. Stoichiometries of vanadium oxides were selected in accordance with available experimental studies. Sliding simulations explored the tribocontact of two rigid V_2O_5 layers used as counter-bodies and a thermalized V_xO_y lubricant confined between them. Under the imposed working conditions, all vanadium oxides were amorphous.

In general, the available amount of oxygen in an oxidative environment in which a vanadium doped hard coating is used, might be insufficient to form V_2O_5. The main goal of our study was to explore the effectiveness of vanadium-based lubricants at lower oxidation states; in other words: can they provide low friction in oxygen-poor environment. We found no noticeable differences in friction coefficients between various amorphous vanadium oxide phases. All of the studied vanadium oxides provide lubrication with a considerably low friction coefficient ($COF \sim 0.2$ at the temperature of 600 K, $COF < 0.2$ at the temperatures of 800 and 1000 K). We figured out that the friction coefficient decreases with the increase of the temperature, which can be favourable for self-adjusting lubrication in the tribological conditions, when the energy dissipation leads to the temperature increase.

We observed the increasing trend of the adhesion-related offset of the friction force with the decrease of the oxygen content and explained it by the more-pronounced tendency of vanadium atoms to bond with the oxygen atoms of the counter-bodies in oxygen-poorer environment. For all vanadium oxides we observed a linear relation between the friction force and the network connectivity, consistent with previous findings regarding V_2O_5. We obtained an overall tendency of the increase in bond length and network connectivity with the increase of normal load, for all stoichiometries and at all studied temperatures.

As a concluding remark, our study on vanadium oxide lubricants provides a reliable reference relevant for the development of oxidation-resistant hard coatings containing vanadium as a lubricious element.

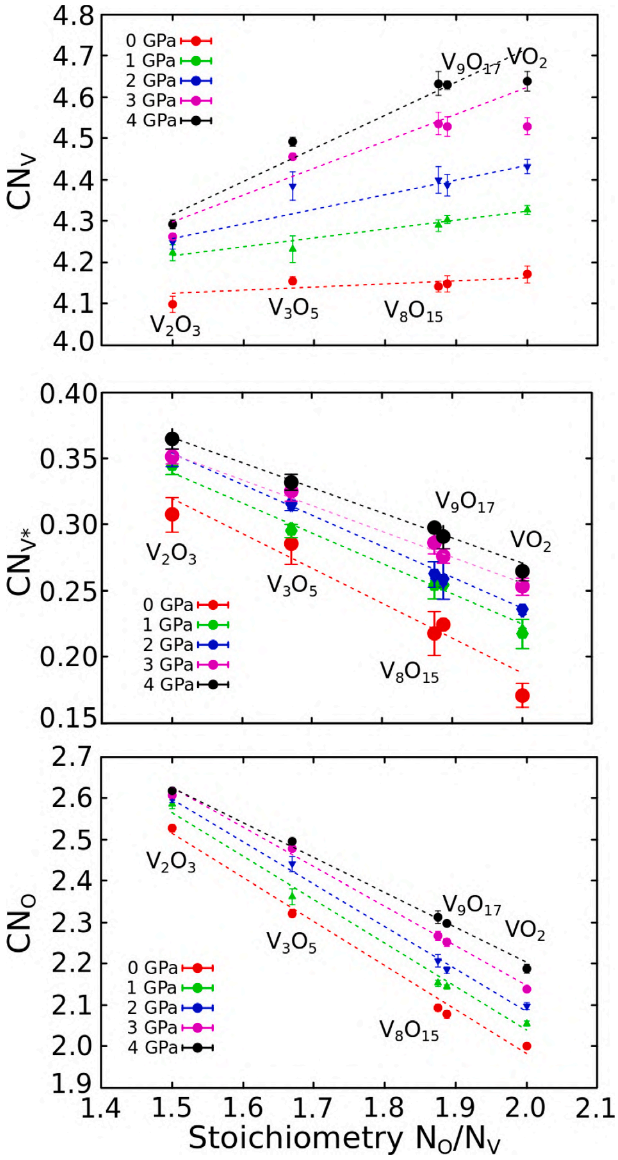

Fig. 6. Dependence of the average coordination numbers of vanadium (CN_V in the top and CN_{V^*} in the middle panel) and oxygen (CN_O in the bottom panel) on the stoichiometry at the temperature of 1000 K and under all applied normal loads. The results at 600 and 800 K are quantitatively similar (i.e., impact of the temperature within the studied range is negligible). The error bars represent the standard deviation of the average values obtained from the sliding simulations. Dashed lines were obtained by linear fitting and they serve as guides to the eye.

CRediT authorship contribution statement

Miljan Dašić: Methodology, Validation, Formal analysis, Investigation, Data curation, Writing – original draft, Writing – review & editing, Visualization. **Ilia Ponomarev:** Conceptualization, Methodology, Validation, Formal analysis, Investigation, Data curation, Writing – original draft, Writing – review & editing. **Tomas Polcar:** Resources, Writing – review & editing, Supervision, Funding acquisition. **Paolo Nicolini:** Conceptualization, Methodology, Resources, Writing – review & editing, Supervision, Project administration, Funding acquisition.

Declaration of competing interest

The authors declare that they have no known competing financial interests or personal relationships that could have appeared to influence the work reported in this paper.

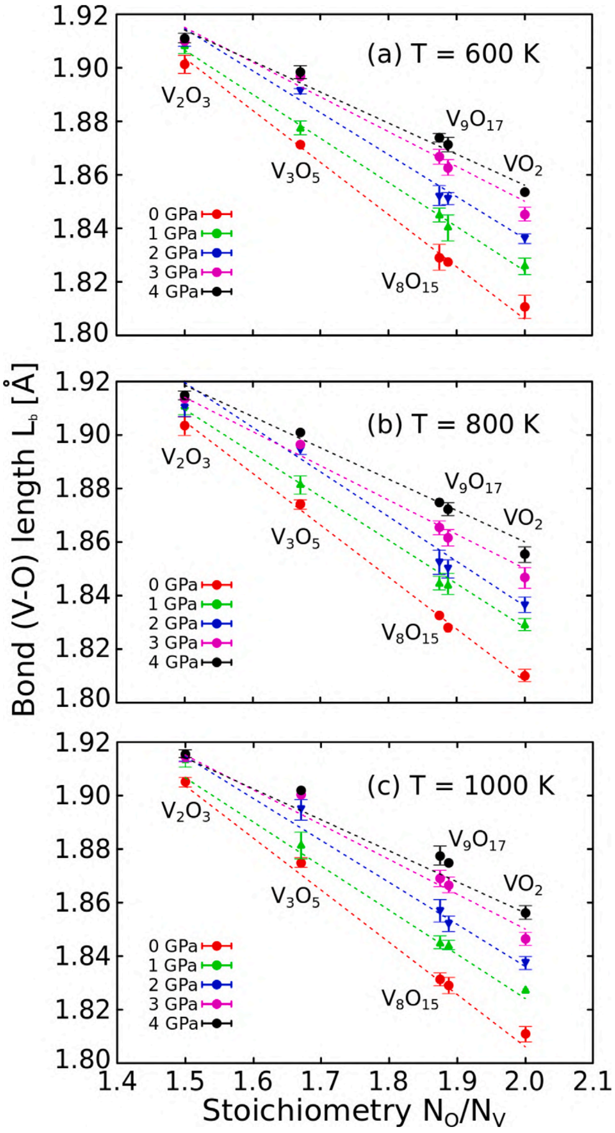

Fig. 7. Dependence of the average bond (V–O) length on the stoichiometry at the temperatures of (a) $T = 600$ K, (b) $T = 800$ K and (c) $T = 1000$ K and under all applied normal loads. The error bars represent the standard deviation of the average values obtained from the sliding simulations. Dashed lines were obtained by linear fitting and they serve as guides to the eye.

Acknowledgements

The authors highly acknowledge the financial support of the Austrian Science Fund (FWF) under the project I 4059-N36 and the Czech Science Foundation under the project 19–29679 L. I.P. thanks the ESI Fund, Czech Republic and the OPR DE International Mobility of Researchers MSCA-IF III, Czech Republic at CTU in Prague (no. CZ.02.2.69/0.0/0.0/20_079/0017983) for their support. This work was supported by the Ministry of Education, Youth and Sports of the Czech Republic through the e-INFRA CZ (ID:90140). We acknowledge that the results of this research have been achieved using the DECI resource Kay based in Ireland at the Irish Centre for High-End Computing (ICHEC) with support from the PRACE AISBL. The use of VMD [59] software for the visualization of our tribological system (available at http://www.ks.uiuc.edu/Research/vmd/) is also acknowledged.

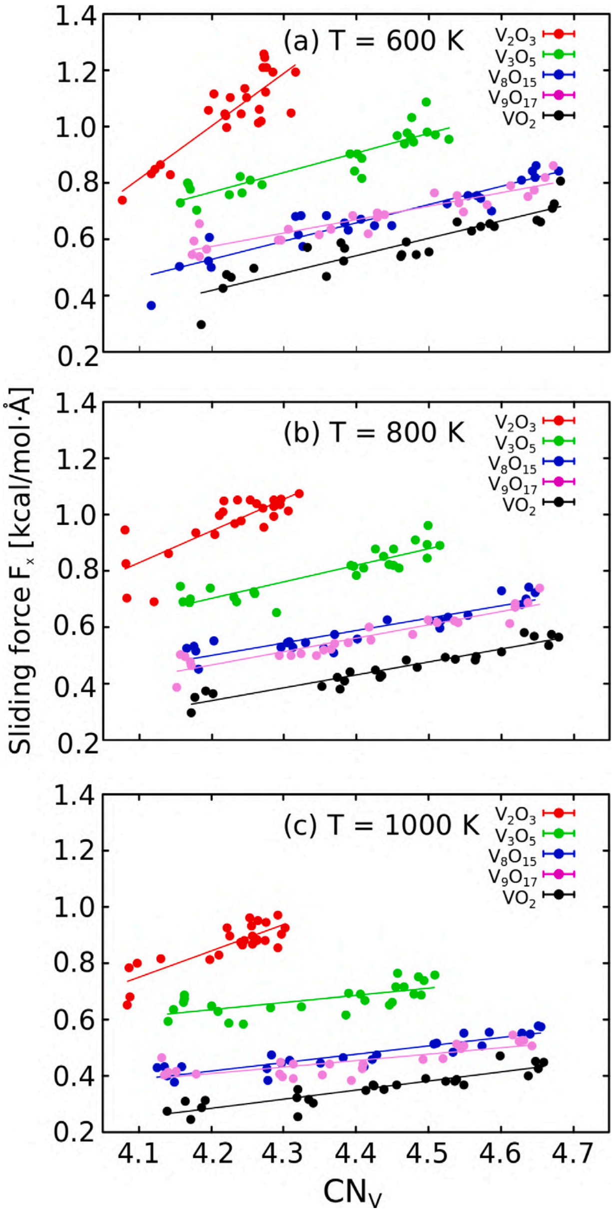

Fig. 8. Relation between the sliding force F_x and the average coordination number of vanadium CN_V at the temperatures of (a) $T = 600$ K, (b) $T = 800$ K and (c) $T = 1000$ K and for all considered vanadium oxide stoichiometries. Solid lines were obtained by linear fitting and they serve as guides to the eye, pointing out to a linear relation between F_x and CN_V.

Appendix A. Supplementary information

Supplementary material related to this article can be found online at https://doi.org/10.1016/j.triboint.2022.107795.

References

[1] Holmberg K, Erdemir A. Influence of tribology on global energy consumption, costs and emissions. Friction 2017;5(3):263–84.

[2] Mang T, Dresel W. Lubricants and lubrication. John Wiley & Sons; 2007.

[3] Tomala A, Karpinska A, Werner W, Olver A, Störi H. Tribological properties of additives for water-based lubricants. Wear 2010;269(11–12):804–10.

[4] Sagraloff N, Dobler A, Tobie T, Stahl K, Ostrowski J. Development of an oil free water-based lubricant for gear applications. Lubricants 2019;7(4):33.

[5] Chen W, Amann T, Kailer A, Rühe J. Macroscopic friction studies of Alkylglucopyranosides as additives for water-based lubricants. Lubricants 2020;8(1):11.

[6] Rahman MH, Warneke H, Webbert H, Rodriguez J, Austin E, Tokunaga K, et al. Water-based lubricants: Development, properties, and performances. Lubricants 2021;9(8):73.

[7] Girotti G, Raimondi A, Blengini GA, Fino D. The contribution of lube additives to the life cycle impacts of fully formulated petroleum-based lubricants. Am J Appl Sci 2011;8(11):1232.

[8] Raimondi A, Girotti G, Blengini GA, Fino D. Lca of petroleum-based lubricants: state of art and inclusion of additives. Int J Life Cycle Assess 2012;17(8):987–96.

[9] Madanhire I, Mbohwa C. Mitigating environmental impact of petroleum lubricants. Springer; 2016.

[10] Xiao H. Ionic liquid lubricants: basics and applications. Tribol Trans 2017;60(1):20–30.

[11] Gkagkas K, Ponnuchamy V, Dašić M, Stanković I. Molecular dynamics investigation of a model ionic liquid lubricant for automotive applications. Tribol Int 2017;113:83–91.

[12] Dašić M, Stanković I, Gkagkas K. Influence of confinement on flow and lubrication properties of a salt model ionic liquid investigated with molecular dynamics. Eur Phys J E 2018;41(11):1–12.

[13] Dašić M, Stanković I, Gkagkas K. Molecular dynamics investigation of the influence of the shape of the cation on the structure and lubrication properties of ionic liquids. Phys Chem Chem Phys 2019;21(8):4375–86.

[14] Cai M, Yu Q, Liu W, Zhou F. Ionic liquid lubricants: When chemistry meets tribology. Chem Soc Rev 2020.

[15] Field S, Jarratt M, Teer D. Tribological properties of graphite-like and diamond-like carbon coatings. Tribol Int 2004;37(11–12):949–56.

[16] Chen B, Bi Q, Yang J, Xia Y, Hao J. Tribological properties of solid lubricants (graphite, h-BN) for Cu-based P/M friction composites. Tribol Int 2008;41(12):1145–52.

[17] Egea AS, Martynenko V, Abate G, Deferrari N, Krahmer DM, de Lacalle LL. Friction capabilities of graphite-based lubricants at room and over 1400 K temperatures. Int J Adv Manuf Technol 2019;102(5):1623–33.

[18] Hauert R. An overview on the tribological behavior of diamond-like carbon in technical and medical applications. Tribol Int 2004;37(11–12):991–1003.

[19] Erdemir A. Genesis of superlow friction and wear in diamondlike carbon films. Tribol Int 2004;37(11–12):1005–12.

[20] Polcar T, Cavaleiro A. Review on self-lubricant transition metal dichalcogenide nanocomposite coatings alloyed with carbon. Surf Coat Technol 2011;206(4):686–95.

[21] Yang J-F, Parakash B, Hardell J, Fang Q-F. Tribological properties of transition metal di-chalcogenide based lubricant coatings. Front Mater Sci 2012;6(2):116–27.

[22] Nicolini P, Capozza R, Restuccia P, Polcar T. Structural ordering of molybdenum disulfide studied via reactive molecular dynamics simulations. ACS Appl Mater Interfaces 2018;10(10):8937–46.

[23] Serpini E, Rota A, Valeri S, Ukraintsev E, Rezek B, Polcar T, Nicolini P. Nanoscale frictional properties of ordered and disordered MoS2. Tribol Int 2019;136:67–74.

[24] Rapuc A, Simonovic K, Huminiuc T, Cavaleiro A, Polcar T. Nanotribological investigation of sliding properties of transition metal dichalcogenide thin film coatings. ACS Appl Mater Interfaces 2020;12(48):54191–202.

[25] Zhang S, Bui XL, Li X. Thermal stability and oxidation properties of magnetron sputtered diamond-like carbon and its nanocomposite coatings. Diam Relat Mater 2006;15(4–8):972–6.

[26] Zhu S, Cheng J, Qiao Z, Yang J. High temperature solid-lubricating materials: A review. Tribol Int 2019;133:206–23.

[27] Papi PA, Mulligan C, Gall D. CrN–Ag nanocomposite coatings: control of lubricant transport by diffusion barriers. Thin Solid Films 2012;524:211–7.

[28] Voevodin AA, Muratore C, Aouadi SM. Hard coatings with high temperature adaptive lubrication and contact thermal management. Surf Coat Technol 2014;257:247–65.

[29] Fateh N, Fontalvo G, Gassner G, Mitterer C. Influence of high-temperature oxide formation on the tribological behaviour of TiN and VN coatings. Wear 2007;262(9–10):1152–8.

[30] Aouadi SM, Luster B, Kohli P, Muratore C, Voevodin AA. Progress in the development of adaptive nitride-based coatings for high temperature tribological applications. Surf Coat Technol 2009;204(6–7):962–8.

[31] Aouadi SM, Gao H, Martini A, Scharf TW, Muratore C. Lubricious oxide coatings for extreme temperature applications: A review. Surf Coat Technol 2014;257:266–77.

[32] Xu YX, Hu C, Chen L, Pei F, Du Y. Effect of V-addition on the thermal stability and oxidation resistance of CrAlN coatings. Ceram Int 2018;44(6):7013–9.

[33] Wang C, Xu B, Wang Z, Li H, Wang L, Chen R, et al. Tribological mechanism of (Cr, V) N coating in the temperature range of 500–900° C. Tribol Int 2021;159:106952.

[34] Lugscheider E, Knotek O, Bärwulf S, Bobzin K. Characteristic curves of voltage and current, phase generation and properties of tungsten-and vanadium-oxides deposited by reactive dc-MSIP-PVD-process for self-lubricating applications. Surf Coat Technol 2001;142:137–42.

[35] Mitterer C, Fateh N, Munnik F. Microstructure–property relations of reactively magnetron sputtered VCxNy films. Surf Coat Technol 2011;205(13–14):3805–9.

[36] Perfilyev V, Moshkovich A, Lapsker I, Laikhtman A, Rapoport L. The effect of vanadium content and temperature on stick–slip phenomena under friction of CrV (x) N coatings. Wear 2013;307(1–2):44–51.

[37] Franz R, Mitterer C. Vanadium containing self-adaptive low-friction hard coatings for high-temperature applications: A review. Surf Coat Technol 2013;228:1–13.

[38] Bondarev AV, Kvashnin DG, Shchetinin IV, Shtansky DV. Temperature-dependent structural transformation and friction behavior of nanocomposite VCN-(Ag) coatings. Mater Des 2018;160:964–73.

[39] Tillmann W, Hagen L, Kokalj D, Paulus M, Tolan M. Temperature-induced formation of lubricous oxides in vanadium containing iron-based arc sprayed coatings. Coatings 2019;9(1):18.

[40] Ponomarev I, Polcar T, Nicolini P. Tribological properties of V2o5 studied via reactive molecular dynamics simulations. Tribol Int 2021;154:106750.

[41] Fernandes F, Morgiel J, Polcar T, Cavaleiro A. Oxidation and diffusion processes during annealing of TiSi (V) N films. Surf Coat Technol 2015;275:120–6.

[42] Fernandes F, Loureiro A, Polcar T, Cavaleiro A. The effect of increasing V content on the structure, mechanical properties and oxidation resistance of Ti–Si–V–N films deposited by DC reactive magnetron sputtering. Appl Surf Sci 2014;289:114–23.

[43] Van Duin AC, Dasgupta S, Lorant F, Goddard WA. Reaxff: a reactive force field for hydrocarbons. J Phys Chem A 2001;105(41):9396–409.

[44] Chenoweth K, Van Duin AC, Persson P, Cheng M-J, Oxgaard J, Goddard Iii WA. Development and application of a ReaxFF reactive force field for oxidative dehydrogenation on vanadium oxide catalysts. J Phys Chem C 2008;112(37):14645–54.

[45] Jeon B, Ko C, Van Duin AC, Ramanathan S. Chemical stability and surface stoichiometry of vanadium oxide phases studied by reactive molecular dynamics simulations. Surf Sci 2012;606(3–4):516–22.

[46] Aktulga HM, Fogarty JC, Pandit SA, Grama AY. Parallel reactive molecular dynamics: Numerical methods and algorithmic techniques. Parallel Comput 2012;38(4–5):245–59.

[47] Plimpton S. Fast parallel algorithms for short-range molecular dynamics. J Comput Phys 1995;117(1):1–19.

[48] Thompson AP, Aktulga HM, Berger R, Bolintineanu DS, Brown WM, Crozier PS, et al. LAMMPS-a flexible simulation tool for particle-based materials modeling at the atomic, meso, and continuum scales. Comput Phys Comm 2021;108171.

[49] Lu X, Khonsari MM, Gelinck ERM. The stribeck curve: Experimental results and theoretical prediction. J Tribol 2006;128(4):789–94.

[50] Seeton CJ. Viscosity-temperature correlation for liquids. In: International joint tribology conference, Vol. 42592, 2006. p. 131–42.

[51] Ojovan MI. Viscosity and glass transition in amorphous oxides. Adv Condens Matter Phys 2008;2008.

[52] Fateh N, Fontalvo G, Gassner G, Mitterer C. The beneficial effect of high-temperature oxidation on the tribological behaviour of V and VN coatings. Tribol Lett 2007;28(1):1–7.

[53] Ogletree D, Carpick RW, Salmeron M. Calibration of frictional forces in atomic force microscopy. Rev Sci Instrum 1996;67(9):3298–306.

[54] Carpick RW, Salmeron M. Scratching the surface: fundamental investigations of tribology with atomic force microscopy. Chem Rev 1997;97(4):1163–94.

[55] Gao J, Luedtke W, Gourdon D, Ruths M, Israelachvili J, Landman U. Frictional forces and Amontons' law: from the molecular to the macroscopic scale. J Phys Chem B 2004;108(11):3410–25.

[56] Fan C, Liaw P, Liu C. Atomistic model of amorphous materials. Intermetallics 2009;17(1–2):86–7.

[57] Wang Y, Sakamaki T, Skinner LB, Jing Z, Yu T, Kono Y, et al. Atomistic insight into viscosity and density of silicate melts under pressure. Nature Commun 2014;5(1):1–10.

[58] Bauchy M, Micoulaut M. Atomic scale foundation of temperature-dependent bonding constraints in network glasses and liquids. J Non-Crystall Solids 2011;357(14):2530–7.

[59] Humphrey W, Dalke A, Schulten K. VMD: visual molecular dynamics. J Mol Graph 1996;14(1):33–8.

Supplementary Information: Tribological Properties of Vanadium Oxides Investigated with Reactive Molecular Dynamics

Miljan Dašić*
Department of Control Engineering, Faculty of Electrical Engineering,
Czech Technical University in Prague, Technicka 2, 16627 Prague 6, Czech Republic and
Scientific Computing Laboratory, Center for the Study of Complex Systems,
Institute of Physics Belgrade, University of Belgrade, Pregrevica 118, 11080 Belgrade, Serbia

Ilia Ponomarev,† Tomas Polcar, and Paolo Nicolini
Department of Control Engineering, Faculty of Electrical Engineering,
Czech Technical University in Prague, Technicka 2, 16627 Prague 6, Czech Republic

We have applied a linear fitting on the dependence of the sliding force F_x on the normal load F_z:

$$F_x = COF \cdot F_z + F_x^0, \tag{1}$$

where the slope corresponds to the coefficient of friction COF, while the offset F_x^0 corresponds to the sliding force when the normal load is not applied. The fitting coefficients are listed in Table I.

We show the dependence of the estimated volume per atom (labeled as V^*) of amorphous V_xO_y lubricants on the applied normal load F_z for all stoichiometries and temperatures, in Fig. 1. In this case we have applied an exponential fitting of the data according to:

$$V^* = I \cdot e^{-J \cdot F_z} + K. \tag{2}$$

The above-mentioned dependence V^* vs. F_z can be well-approximated using an exponential decay fit. Such a result is in a good agreement with the high-pressure behaviour of compressible liquids/amorphous melted solids [1–3].

In Fig. 2(a),(b),(c) we show the dependence of the exponential fitting coefficients I, J, K (check Eq. 2) respectively, on the stoichiometry, at all studied temperatures. The fitting coefficient J can be taken as a measure of compressibility. We can notice in Fig. 2(b) that the coefficient J overlaps, within the error bars, for all stoichiometries and temperatures. Hence, compressibility of amorphous vanadium oxides is weakly affected by their stoichiometry and temperature. Speaking about the impact of the temperature, we expectedly got that V^* slightly increases with the increase of the temperature T, for the studied range of temperatures. In Table II we present the fitting parameters of the applied exponential fitting procedure defined in the Eq. 2, for all oxides and temperatures.

V_xO_y	T [K]	slope COF	offset F_x^0 [kcal/molÅ]
V_2O_3	600	0.19 ± 0.09	0.92 ± 0.06
V_2O_3	800	0.07 ± 0.03	0.93 ± 0.04
V_2O_3	1000	0.08 ± 0.03	0.82 ± 0.02
V_3O_5	600	0.17 ± 0.02	0.73 ± 0.02
V_3O_5	800	0.12 ± 0.03	0.69 ± 0.02
V_3O_5	1000	0.06 ± 0.02	0.62 ± 0.02
V_8O_{15}	600	0.21 ± 0.02	0.49 ± 0.03
V_8O_{15}	800	0.12 ± 0.02	0.49 ± 0.01
V_8O_{15}	1000	0.09 ± 0.01	0.39 ± 0.02
V_9O_{17}	600	0.14 ± 0.01	0.561 ± 0.006
V_9O_{17}	800	0.132 ± 0.006	0.451 ± 0.004
V_9O_{17}	1000	0.07 ± 0.02	0.39 ± 0.02
VO_2	600	0.18 ± 0.03	0.43 ± 0.03
VO_2	800	0.13 ± 0.01	0.34 ± 0.01
VO_2	1000	0.08 ± 0.01	0.29 ± 0.01

TABLE I: Parameters of the linear fits of the sliding force F_x vs. normal load F_z dependence for all stoichiometries V_xO_y and temperatures T.

Typeset by REVTEX

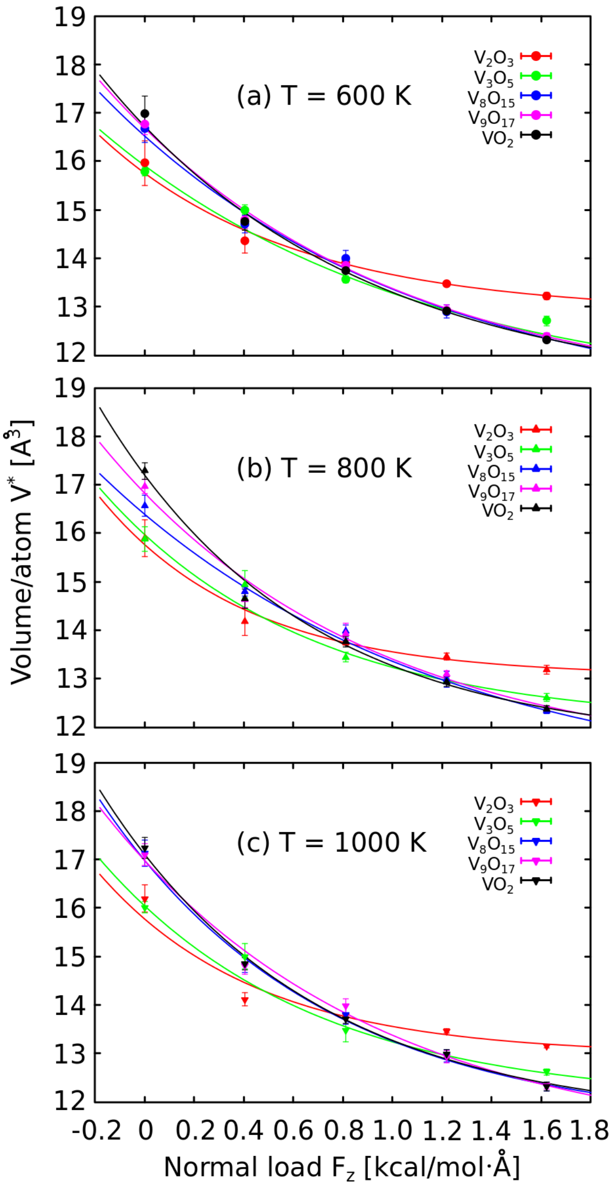

FIG. 1: Dependence of the volume per atom V^* on the normal load F_z at the temperatures (a) $T = 600$ K, (b) $T = 800$ K and (c) $T = 1000$ K. The error bars represent the standard deviation of the average values obtained from the sliding simulations. The curves showing the compression trends were obtained by exponential fitting (check Eq. 2) and the corresponding parameters are listed in Table II.

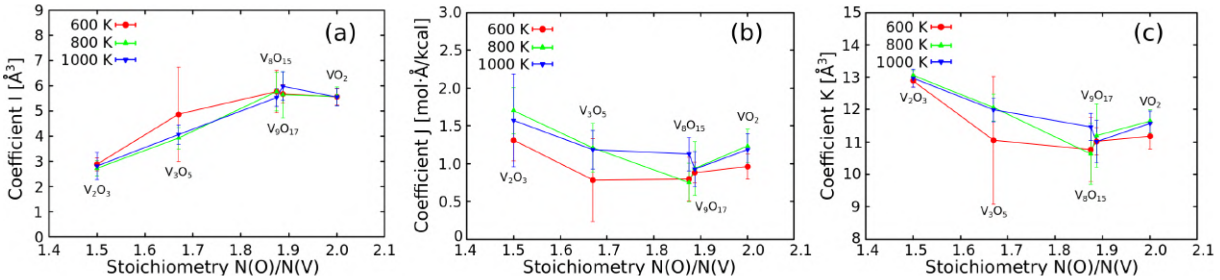

FIG. 2: Dependence of the coefficients (a) I, (b) J and (c) K of the exponential fitting on the stoichiometry at the temperatures $T = \{600, 800, 1000\}$ K. Points were obtained as the coefficients of the exponential fits from Eq. 2, while errorbars represent the associated error computed with the fitting procedure.

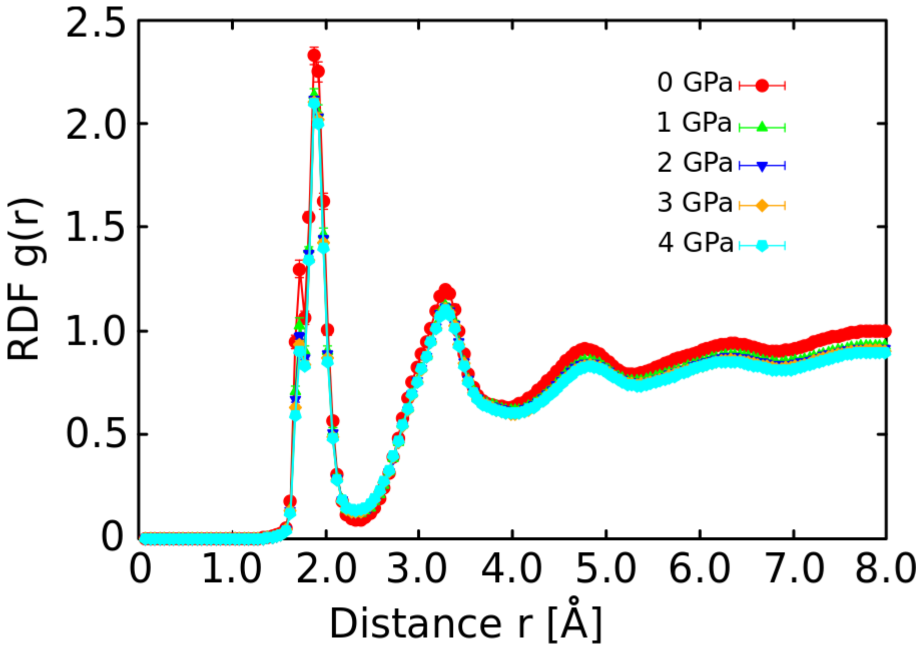

FIG. 3: Total radial distribution functions $g(r)$ of the V_3O_5 lubricant at the temperature of $T = 1000$ K under the normal loads of $F_z = \{0, 1, 2, 3, 4\}$ GPa. We can notice the effect of the normal load: increase of F_z lowers the RDF curves.

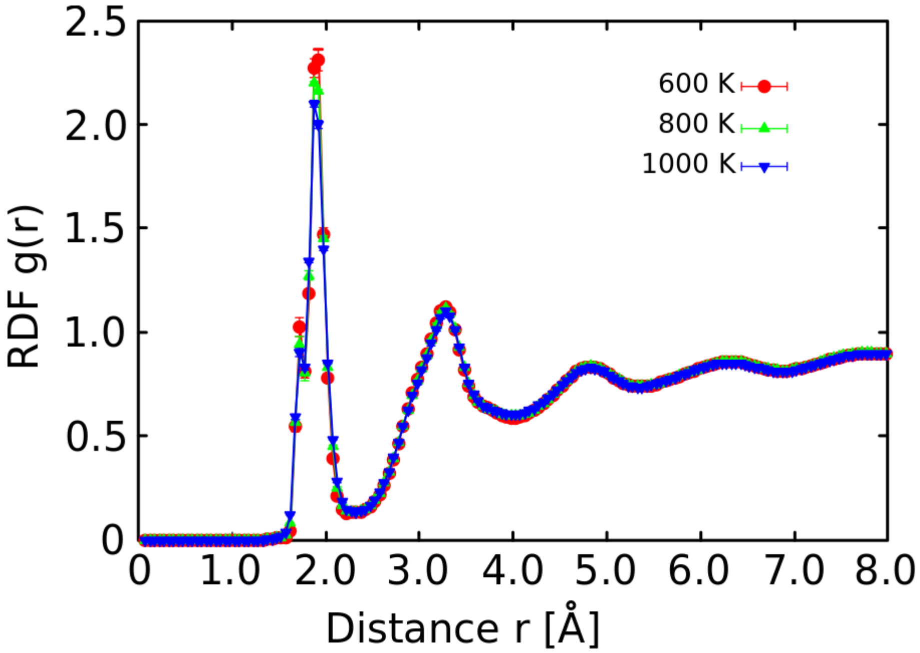

FIG. 4: Total radial distribution functions $g(r)$ of the V_3O_5 lubricant under the normal load of $F_z = 4$ GPa at the temperatures of $T = \{600, 800, 1000\}$ K. We can notice the effect of the temperature: increase of T lowers the RDF curves.

Within the scope of the performed structural analysis, we computed the radial distribution functions (RDF-s), labeled as $g(r)$. In Fig. 4 we present the $g(r)$ of the V_3O_5 lubricant at a fixed temperature of $T = 1000$ K, under all applied normal loads F_z. In Fig. 3 we present the $g(r)$ of the V_3O_5 lubricant under the fixed normal load of $F_z = 4$ GPa, at all applied temperatures T.

V_xO_y	T [K]	coefficient I [Å^3]	coefficient J [mol·Å/kcal]	coefficient K [Å^3]
V_2O_3	600	2.9 ± 0.2	1.3 ± 0.3	12.9 ± 0.2
V_2O_3	800	2.7 ± 0.3	1.7 ± 0.3	13.1 ± 0.1
V_2O_3	1000	2.8 ± 0.5	1.6 ± 0.6	12.9 ± 0.3
V_3O_5	600	4.9 ± 1.9	0.8 ± 0.5	11.0 ± 2.0
V_3O_5	800	3.9 ± 0.4	1.2 ± 0.3	12.1 ± 0.4
V_3O_5	1000	4.1 ± 0.4	1.2 ± 0.2	12.0 ± 0.4
V_8O_{15}	600	5.8 ± 0.8	0.8 ± 0.3	10.8 ± 1.0
V_8O_{15}	800	5.8 ± 0.8	0.8 ± 0.3	10.6 ± 1.0
V_8O_{15}	1000	5.5 ± 0.3	1.1 ± 0.2	11.5 ± 0.4
V_9O_{17}	600	5.7 ± 0.4	0.9 ± 0.1	11.0 ± 0.4
V_9O_{17}	800	5.6 ± 0.9	0.9 ± 0.4	11.2 ± 1.0
V_9O_{17}	1000	6.0 ± 0.6	0.9 ± 0.2	11.0 ± 0.7
VO_2	600	5.6 ± 0.3	1.0 ± 0.2	11.2 ± 0.4
VO_2	800	5.6 ± 0.4	1.2 ± 0.2	11.6 ± 0.4
VO_2	1000	5.5 ± 0.4	1.2 ± 0.2	11.6 ± 0.4

TABLE II: Parameters of the exponential fits (check Eq. 2) of the volume per atom V^* vs. normal load F_z dependence for all stoichiometries V_xO_y and temperatures T.

References

---

[*] Electronic address: `dasicmil@fel.cvut.cz;mdasic@ipb.ac.rs`

[†] Electronic address: `ponomili@fel.cvut.cz`

[1] J. R. MACDONALD, Rev. Mod. Phys. **38**, 669 (1966).
[2] A. Hayward, British Journal of Applied Physics **18**, 965 (2002).
[3] W. Habchi and S. Bair, Journal of Tribology **135** (2012).

Small Structures

www.small-structures.com

RESEARCH ARTICLE OPEN ACCESS

Linking Density and Nanoscale Crystallinity to Hydration in Nafion PEMFC Membranes: Insights From Experiment and Molecular Dynamics Simulations

Mateja Jovanović[1,2,3] | Nicolas Bernhard[1] | Matthias Baldofski[1] | Marcin Rybicki[1,4] | Miljan Dašić[3] | Igor Stanković[3,5]

[1]Freudenberg Technology Innovation SE&Co., Weinheim, Germany | [2]Institute of Technical Sciences of the Serbian Academy of Sciences and Arts (SASA), Belgrade, Serbia | [3]Institute of Physics, University of Belgrade, Zemun, Serbia | [4]Freudenberg e-Power Systems GmbH, München, Germany | [5]Departamento de Ingenería Mecánica, Universidad Técnica Federico Santa María, Valparaíso, Chile

Correspondence: Mateja Jovanović (Mateja.Jovanovic@ipb.ac.rs) | Matthias Baldofski (Matthias.Baldofski@freudenberg.com) | Igor Stanković (Igor.E.Stankovic@gmail.com)

Received: 26 August 2025 | **Revised:** 15 November 2025 | **Accepted:** 16 November 2025

Keywords: crystallinity | fuel cell | molecular dynamics | proton exchange membrane | water content

ABSTRACT

Proton exchange membrane fuel cells (PEMFCs) powered by hydrogen are promising for a wide range of energy-conversion applications, with Nafion remaining the most widely used membrane material. Here, by comparing experimental data and molecular dynamics (MD) simulation results, we examine how a measurable property, the density, relates to the structure of Nafion at different water contents (λ). Voronoi tessellation and free-volume analysis of MD results confirm that crystallinity and effective density are strongly correlated, highlighting the role of structural ordering. Further analysis of water clustering reveals isolated molecules at low hydration, while percolating networks form at higher λ, particularly within crystalline systems. Simultaneously, the density of confined water exhibits variations reaching values up to $\approx 1.2\ \mathrm{g/cm^3}$. We propose a model that bridges experimental and molecular observations by quantitatively linking water uptake to density variations, offering a predictive framework for optimising hydration and transport in membranes. Understanding how membranes with varying levels of crystallinity respond to changes in water content helps translate nanoscale mechanisms into practical designs for industrial PEMFCs.

1 | Introduction

Hydrogen energy is regarded as a solution to mitigate carbon emissions and reduce our dependence on fossil fuels. Among the various technologies for converting hydrogen's chemical energy into electricity, proton exchange membrane fuel cells (PEMFCs) stand out thanks to their high power density and efficiency [1–3]. Nafion, a perfluorinated sulphonic acid (PFSA) ionomer, is an industrial standard and benchmark material in electrochemical technology and specifically for PEMFC membranes due to its outstanding chemical and mechanical stability and excellent proton conductivity [4–8]. It comprises a semicrystalline polytetrafluoroethylene (PTFE) backbone [6, 9, 10] and randomly attached side chains with pendant sulphonic acid groups. PFSA membranes exhibit high resistance to free water loss due to their semicrystalline structure, concentrated ionic domains, and strong electrostatic interactions. For example, pressures of up to 25 MPa are required to achieve a 50% reduction in hydration level (λ) [11, 12]. At full hydration, the membrane structure consists of channel hydrophilic domains interspersed with crystalline regions, while the morphology at lower levels of hydration is less clearly understood [13–15]. Crystalline bundles in Nafion form during processing [9, 13, 16, 17] and their presence can be quantified experimentally [9, 10], for instance, using wide-angle X-ray scattering (WAXS) or transmission electron microscopy (TEM), where WAXS provides overall crystallinity despite broad scattering features, while TEM reveals the distribution of crystalline regions.

Crystalline and semicrystalline regions of the polymer behave as physical cross-links that restrict excessive swelling and maintain the membrane's mechanical integrity [5, 10, 18]. Based on small-angle X-ray (SAXS) and neutron scattering experiments, Rubatat et al. [4] proposed a structural model of hydrated Nafion. Their results revealed cylindrical or ribbon-like polymer aggregates [4, 7, 19] surrounded by sulphonic acid groups and water molecules, forming an interconnected network of hydrophilic and hydrophobic regions. At moderate hydration, water molecules form local hydration shells around ionic groups, inducing nanoscale swelling confined to ionic clusters [20, 21]. When hydration increases into the "free-water" regime, absorbed water expands the hydrophilic domains, alters the phase-separated morphology, and enhances the stabilising role of the semicrystalline backbone in preventing over-swelling [4, 18]. Furthermore, multiaxis nuclear magnetic resonance (NMR) and synchrotron SAXS experiments revealed a linear coupling between water channel alignment and anisotropic transport [22]. Proton conductivity in Nafion is highly sensitive to hydration, as water uptake simultaneously promotes proton transport and reshapes the nanoscale morphology. Understanding the interplay between hydration, crystallinity, and nanoscale morphology in PFSA membranes remains essential for optimising PEMFCs [13, 23]. Water–polymer interfacial area, channel alignment, and free volume critically govern effective density and conductivity [22–24]. These findings bridge nanoscale morphology with macroscopic transport properties, yet a quantitative molecular-level connexion between local density, crystalline ordering, and hydration state has remained elusive.

Density-hydration relationships in Nafion have been probed experimentally and computationally for decades. In seminal measurements on Nafion 117, Morris and Sun [25] quantified density and dimensional changes as a function of water content (λ), reporting swelling onset near $\lambda \approx 1.9$ and anisotropic expansion. A closer look shows their densities are within 5% of an ideal-mixture prediction. Subsequent simulations diverged: numerous studies [26–30] reported a density dependence on water content that departs markedly from the ideal mixing law, especially at lower hydration levels. Further, other MD studies [31–33] reported a density trend closer to the theoretical prediction at comparable λ. More recently, Cui et al. [34] reproduced ideal mixing trends with excellent fidelity.

To reconcile these discrepancies, we examine how structural ordering governs the local density of hydrated Nafion membranes, thereby rationalising both our own and literature experimental observations [25, 35] as well as previous molecular models [26–34]. From our perspective, molecular simulations should be regarded as nanoscale samples of a membrane rather than as complete representations of the entire material, whose structure results from the combined effects of synthesis, processing conditions, and operating history. Density fluctuations in polymers have long been theoretically predicted [36] and experimentally measured [37]. For instance, X-ray scattering with a spatial resolution of about 10^8 nm^3 reveals density variations of roughly 2% (at half-maximum intensity) around the average bulk density [37]. At the molecular level, such fluctuations are expected to be an order of magnitude larger [38]. Guided by this understanding, we employ free-volume analysis, polydisperse Voronoi tessellation, and DBSCAN clustering to establish a quantitative link between nanoscale packing, crystallinity, and hydration-dependent effective density. Accordingly, this study elucidates the microscopic origins of the structure–property relationships observed experimentally in hydrated ionomers.

2 | Results and Discussion

2.1 | Simulated Nafion Configurations

Molecular dynamics (MD) simulations were performed on Nafion systems with distinct hydration levels (i.e., λ = 3, 6, 9, 12, 15, 20), where λ represents the number of water molecules per sulphonic group. These values were selected based on Nafion's maximum water uptake corresponding to $\lambda = 20$ and the typical hydration level at room temperature corresponding to $\lambda = 9$. The initial molecular structures of a Nafion polymer chain and hydronium ions were constructed using the MAPS platform of Scienomics (Materials and Processes Simulations Platform, Version 4.2, Scienomics SARL, Paris, France). Due to nonuniform water distribution during operation, Nafion membranes exhibit heterogeneous structures throughout their thickness, leading to variations in their morphological and physical properties. To capture this behaviour, separate simulation cells with varying water content and Nafion morphology are constructed as representative volume elements (RVEs) using the procedure described in Ref. [39]. Initial configurations were a larger simulation cell, containing 25 replicated polymer chains and up to 25 water molecules per sulphonate group. To maintain charge neutrality, one hydronium ion (H_3O^+) was added per sulphonate group. Energy minimisation using the conjugate gradient (CG) algorithm [40] was performed for each cell, followed by compression to a density of 1.7 g/cm^3 [41], which brings the system closer to its equilibrated density. An initial energy minimisation is further followed by an annealing cycle with increasing temperature from 300 to 600 K. Annealing step was a 1 ns (ns) NPT simulation using the barostat at 1 bar at 300 K, cf. the white stripes in Figure 1a. In this way, dominantly amorphous Nafion configurations are created. Depending on λ, annealing was followed by the relaxation of the system, also with NPT barostat at 300 K and 1 bar until potential energy and density relaxed, cf. grey stripes and dotted (blue) curve for density in Figure 1a. After relaxation, the final configurations were analysed. This iterative process of annealing and relaxation, represented by alternating grey and white stripes in Figure 1a, was repeated to create a series of realisations of similar systems with the same hydration level, similar densities, and local Nafion configurations. The crystalline configurations were created by shearing the system with increasing temperature from 300 to 600 K, i.e., two lengths of the system during a 0.5 ns annealing and followed by steady shear [42–44] for 0.5 ns with shear rate $\dot{\gamma} = 1\, ns^{-1}$, indicated in Figure 1b as the vertical white and grey stripes, respectively. The total shear deformation distance during 1 ns was $\gamma L_y = 2L_y$, i.e, two system linear dimensions along the y-direction. The annealing and shearing steps were followed by system relaxation under an NPT barostat at 300 K and 1 bar, which was continued until both the potential energy and the density equilibrated (cf. the grey stripes in Figure 1b). The semicrystalline configurations are obtained by annealing without shear, starting from the crystalline configurations obtained in the previous step. We should note that crystalline bundles in Nafion form during processing due to thermal annealing, solvent evaporation, mechanical stretching, or

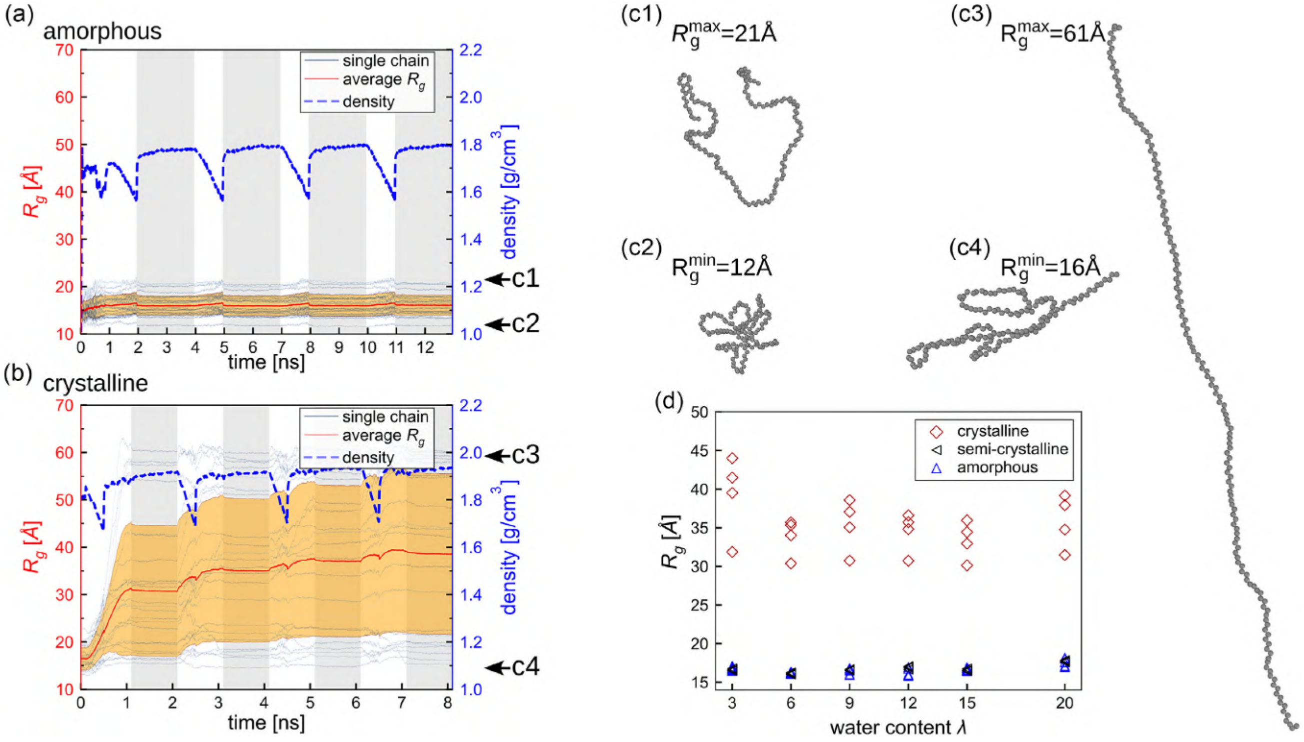

FIGURE 1 | Time evolution and statistical analysis of the radius of gyration (R_g) and density of Nafion in case of (a) amorphous and (b) crystalline systems for $\lambda = 9$. Representative Nafion polymer conformations with their values for R_g are given as an inset (c1)-(c4). (d) The dependence of R_g on water content (λ).

shear flow [10, 13, 16, 17]. In this work, a moderate flow field was applied solely to accelerate molecular ordering and reduce equilibration time, without affecting the intrinsic morphology or chemistry of the Nafion backbone.

2.2 | Geometry of Nafion Chains

Large molecules, such as Nafion, will not dissolve in water but may only swell. This system may contain both elongated and compact polymer chains, which interpenetrate. The density of a single polymer coil is often described in terms of how tightly its monomer units are packed within the space it occupies. One key parameter used to characterise the spatial extent of a polymer chain is the radius of gyration (R_g). This enables us to investigate how the bundling and the unfolding of polymers evolve with annealing due to the expansion of the system, followed by the contraction, see Figure 1a,b.

Figure 1 illustrates the variation of the radius of gyration in various Nafion systems. Panels (a) and (b) display the time evolution of R_g of individual polymer chains in amorphous and crystalline configurations, respectively, at water content $\lambda = 9$, during their respective annealing. An average trend line is shown in red, and a shaded region indicates the standard deviation of the R_g distribution. Time evolution of R_g for each configuration considered in this paper is shown in the Supporting Information, cf. Figures S1-S2, Supporting Information.

By analysing the time evolution of R_g, one can assess polymer relaxation dynamics and structural transitions. When a crystalline system in Figure 1b is compared to an amorphous system in Figure 1a, the most notable difference is not only the increase in average value, but also a wider spread of end-to-end chain distances. Somewhat surprisingly, despite the substantial expansion of the system followed by its contraction, there is no significant change in the spatial distribution of individual chains: the bundled chains remain bundled during the expansion, and the unfolded chains remain unfolded during the compactification. Still, we can see that, overall, the commonly used annealing procedure cannot unfold the bundled Nafion chains in amorphous systems. On the contrary, we see that annealing an already unbounded system tends to extend further its polymer chains. The snapshots in Figure 1(c1–c4) provide a visual representation of a polymer backbone conformation of the individual Nafion polymers with the highest and lowest gyration radii in amorphous and crystalline systems. For clarity, we represented only carbon atoms in a Nafion backbone, showing the geometry of chains with maximal and minimal R_g at the end of the annealing procedures shown in Figure 1a,b.

At this point, we should note that the unfolded Nafion backbone can align and create a crystal phase. There exist chains almost completely stretched out in a crystalline configuration, e.g., Figure 1(c3). Also, the Nafion backbone in Figure 1(c4) is folded in a way that distant segments of the backbone are parallel to itself. In the amorphous case, we do not observe self-alignment, cf. Figure 1(c1) and (c2). Crystalline polymers adopt more elongated and/or ordered structures than their amorphous counterparts. To quantify crystallinity, Nafion polymer backbones are analysed by separating them into three carbon-atom-long segments. The analysis determines the alignment of segments by measuring distances r between central atoms and the angles between polymer segments within a cutoff ($r < r_c$, $r_c = 8$ Å), i.e., first-neighbour segments. Angles are calculated between vectors connecting the end atoms in a segment. Segments are considered aligned if the angle between them is less than 5°. Figure 1d shows the variation of the mean radius of gyration (R_g) for each considered polymer configuration, as a function of hydration level. The crystalline samples (red diamonds) exhibit significantly larger R_g values, typically between 30 Å and 45 Å, with noticeable scatter but no clear dependence on water content. In contrast, the semicrystalline (grey triangles) and amorphous (blue triangles) configurations exhibit much smaller, nearly constant R_g values of 16–18 Å across all hydration levels. The result also suggests that hydration primarily influences interfacial morphology, due to a lower dispersive force between the PFSA polymer and water molecules [45, 46], rather than the intrinsic chain dimensions within the bulk polymer matrix. The similar R_g values in amorphous and semicrystalline regions indicate that chain conformations in both regions remain compact and largely unaffected by water uptake. Therefore, we can conclude that R_g is indicative of polymer backbone compactness, but not an indicator of overall local order. Figure 2a further explores the dependence of R_g on crystalline fraction (χ-crystallinity). The associated error bars represent the standard deviation of R_g in single configurations and reveal variability in polymer conformations, emphasising the structural differences between crystalline, amorphous, and semicrystalline backbone phases. The large standard deviation observed in R_g for the crystalline samples can be attributed to the entropic tendency of polymer chains to minimise conformational extension, leading to significant structural variations between fully extended and bundled chains. Consistently, our results show that annealing reduces R_g substantially, bringing it closer to values characteristic of amorphous systems, reflecting relaxation toward more entropically favourable chain conformations. The reduction of R_g and its homogeneity over different backbones (i.e., comparatively low standard deviation) in annealed systems suggests that highly crystalline configurations, while useful as limiting cases, may not fully represent realistic systems, where thermal disorder dominates, cf. Ref. [9, 10].

Figure 2b shows the dependence of the crystallinity (χ) on the water content (λ). Similar to R_g, the crystalline samples (red diamonds) exhibit large fluctuations in crystallinity, ranging approximately from 0.35 to 0.7. The semicrystalline samples (black triangles) exhibit intermediate crystallinity values, typically 0.2–0.55, with a dominantly crystalline system and only low water content ($\lambda < 6$). The stability of the crystalline phase during annealing of the system can be attributed to the low mobility of bundled Nafion chains, which cannot move within the water

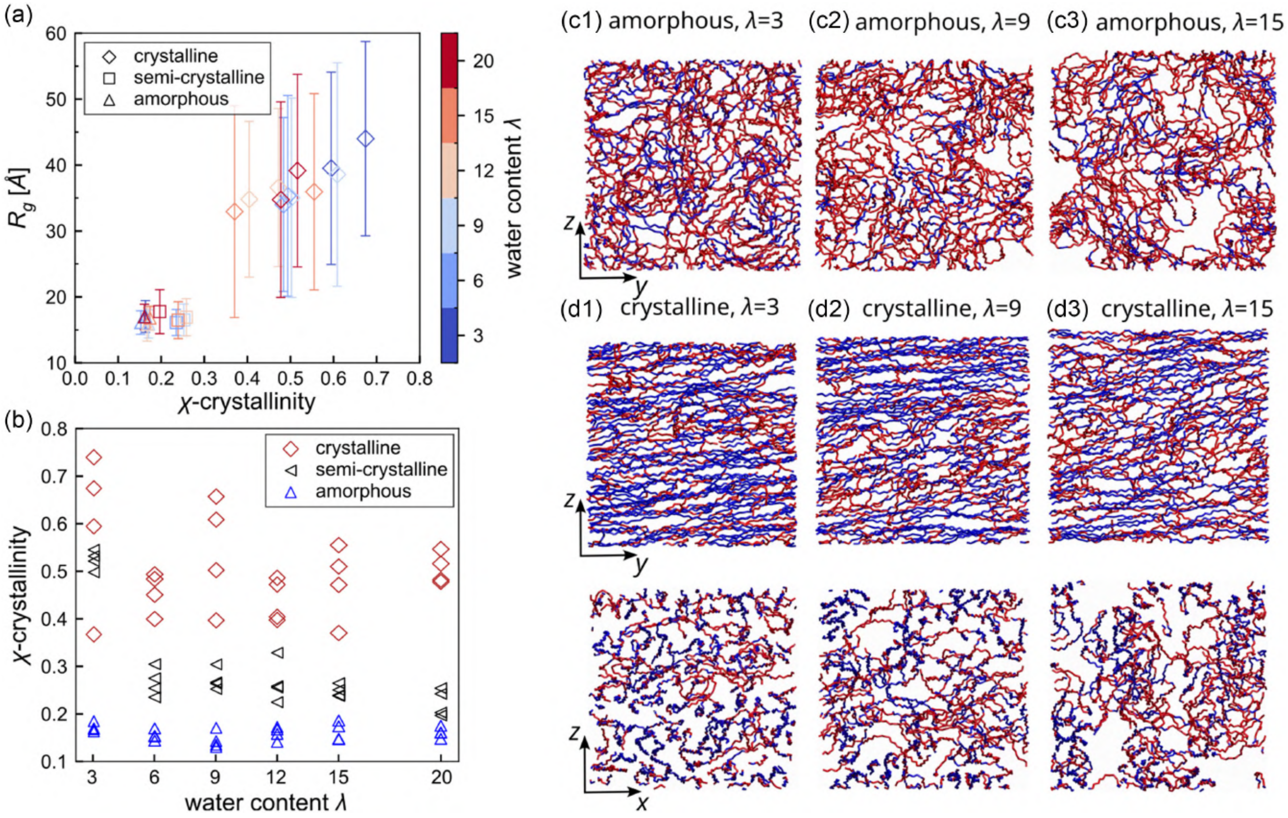

FIGURE 2 | (a) The dependence of gyration radius (R_g) on crystallinity (χ), with a colour map representing an additional parameter (i.e., water content λ), emphasising the structural differences between crystalline and amorphous polymer states. (b) The dependence of crystallinity (χ) on water content (λ). (c1–3, d1–3) Molecular simulations of polymer configurations under varying hydration conditions (λ) and different thermal histories. The segments with aligned pairs are coloured blue and assigned to the crystalline phase, while the others are red and assigned to the amorphous phase. Nafion polymer backbones are analysed into three-carbon-atom segments. Alignment angles are calculated between vectors connecting end atoms in a segment inside a cutoff radius for their central atoms ($r < r_c$, $r_c = 8$ Å). Segments are aligned if the angle between them is less than 5°. The top row (panels c1–c3) shows amorphous structures, while the middle and bottom rows (panels d1–d3) display crystalline structures. The increasing hydration levels ($\lambda = 3, 9, 15$) illustrate the influence of water content on polymer morphology, with the crystalline structures retaining a higher degree of order than their amorphous counterparts.

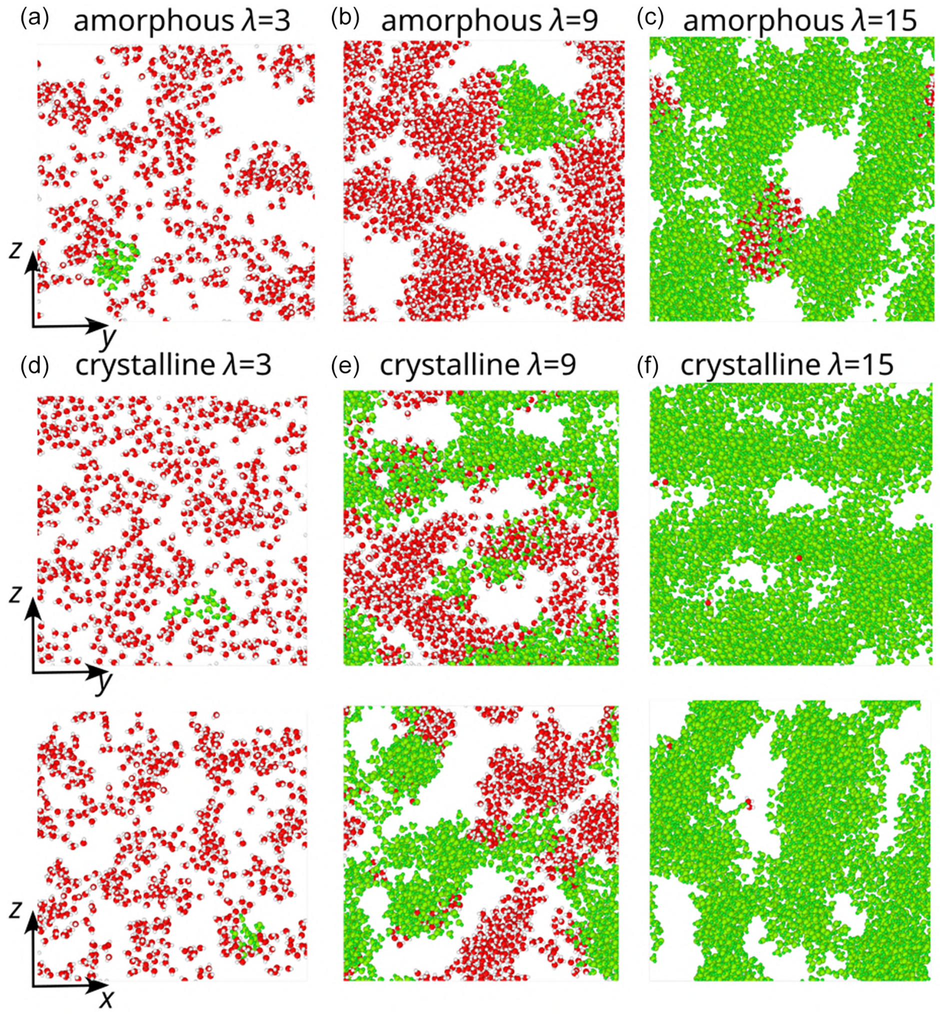

FIGURE 3 | Spatial distribution of water molecules in the Nafion-water system at different hydration levels (λ) and structural configurations. Red spheres represent individual water molecules, while green clusters highlight the largest connected water aggregates, as defined by the corresponding criteria. (a–c) The top row corresponds to an amorphous configuration, and (d–f) the middle and bottom rows show two projections for the Nafion-water crystalline configuration, with hydration levels increasing from left to right ($\lambda = 3, 9, 15$). The configurations correspond to the Nafion phase snapshots shown in Figure 2. This figure illustrates the transition from isolated water molecules at low hydration to percolating water networks at high hydration, particularly in crystalline configurations. Water clusters are determined by the DBSCAN (Density Based Spatial Clustering of Applications with Noise) [47] algorithm.

phase and thus cannot relax the structure. With increasing water content ($\lambda \geq 6$), a sharp drop in crystallinity is visible. The amorphous samples (blue triangles) maintain consistently low crystallinity levels around 0.1–0.2, independent of hydration. These results indicate that water uptake does not affect the crystalline order. Still, differences in crystallinity persisted across configurations (e.g., semicrystalline and amorphous) at different hydration levels, suggesting that the morphological distinction between phases is robust and is not significantly altered by water.

In the previous analysis, the crystallinity χ was treated as a global, averaged parameter. However, in reality, crystallinity is inherently local, arising from aligned backbones. To illustrate the relation between crystallinity and pore structure, Figures 2c,d show snapshots of molecular simulations of Nafion under different hydration conditions (parameter λ). Only backbones are shown. The aligned segment pairs are referred to as crystalline and coloured blue in Figure 2, while others are red. The top row Figure 2(c1–c3) shows annealed amorphous structures with increasing hydration levels ($\lambda = 3, 9, 15$), while the middle and lower rows in Figure 2(d1–d3) depict crystalline configurations in the direction of and perpendicular to the shear under the same hydration conditions as the amorphous configurations. The amorphous structures exhibit more disordered and entangled arrangements, whereas the crystalline structures maintain a more ordered, layered configuration. In the crystalline configurations in Figure 2(d1–d3), Nafion backbones are aligned and oriented parallel to the y-axis. The bottom row in Figure 2 provides an additional perspective on the structural arrangements by cutting perpendicular to the aligned backbones of Nafion polymers. This confirms their alignment, since in such a projection fewer Nafion polymers (i.e., their backbones) are visible than in the upper panels, which are oblique to the polymer backbones, or in the amorphous cases.

2.3 | Water Phase Morphology

Figure 3 shows the snapshots of the distribution and clustering of water molecules in the Nafion-water system under different hydration conditions ($\lambda = 3, 9, 15$). Only water molecules are shown, with red spheres representing individual water molecules and green clusters indicating the largest water cluster within the system. The top row, i.e., Figure 3a–c, corresponds to amorphous configurations at increasing hydration levels (λ), while the lower two rows, Figure 3d–f, represent crystalline configurations at the same hydration states. The corresponding Nafion backbone configurations are given in Figure 2(c1–c3) and (d1–d3), respectively. Water clusters are determined using the DBSCAN (Density-Based Spatial Clustering of Applications with Noise) [47] algorithm, which groups molecules that are densely packed together while marking sparse regions as noise. Operation of the DBSCAN algorithm is governed by the two main parameters: density threshold defined as the minimum number of points within a radius ε from another point of the cluster, and radius ε. By iteratively expanding clusters from chosen core points, in our case, oxygen atoms in water molecules, that satisfy a minimum density threshold, DBSCAN effectively identifies arbitrarily shaped clusters, while mitigating the influence of outliers. In this study, the density threshold is chosen to be three and the radius $\varepsilon = 3.5$Å, cf. Ref. [48].

Visualisation in Figure 3 highlights the fundamental differences in water distribution between amorphous and crystalline structures. At low hydration ($\lambda = 3$), water remains in small, isolated clusters, with only minor connectivity between molecules. As hydration increases ($\lambda = 9$), larger water clusters emerge, exhibiting more prominent percolation in crystalline structures. A nearly continuous water network is formed at high hydration ($\lambda = 15$), particularly in the crystalline case, where the largest cluster spans almost the entire system. Surprisingly, one can see that the percolating cluster in this case does not span solely in the direction of crystalline Nafion molecular backbones (i.e., along the y-axis, cf. Figure 2(d1–d3)) but also orthogonally, in the xz plane. This suggests that crystallinity promotes the formation of extended water clusters, potentially influencing the transport properties and hydration dynamics.

The radial pair distribution functions are shown in Figure 4a,b at all studied hydration levels (i.e., $\lambda = 3$, 6, 9, 12, 15, 20) for two configurations under consideration: (a) crystalline and (b) amorphous. For the semicrystalline configuration, the corresponding radial pair distribution function is shown in Figure S4, Supporting Information. In the context of the Radial Distribution Function (RDF), $g_{\mathrm{O-O}}(r) = 1$ indicates that, at distance r, the probability of finding another particle equals the mean density, meaning that there is no structural correlation at that range. In liquids such as water, this behaviour is observed over larger distances, where the molecular distribution becomes homogeneous. At shorter distances, $g_{\mathrm{O-O}}(r)$ exhibits characteristic peaks and troughs due to intermolecular interactions such as hydrogen bonding. The first maximum of $g_{\mathrm{O-O}}(r)$, typically found around 2.8 Å for oxygen–oxygen pairs in water, corresponds to the most probable nearest-neighbour distance and reflects the local structuring. Across all systems, the first peaks are located in the range 2.8–3.1 Å. The second peaks are located in the range 5.1–5.4 Å and they correspond to the second solvation shell. For the hydration level $\lambda = 3$, the peak is absent at those values because water distribution is sparse and the water connectivity network is not well defined, as in higher hydration levels. Heights of the peaks generally decrease as the hydration level increases. Furthermore, peak heights decrease as crystallinity increases, indicating more separated, disjoined water clusters.

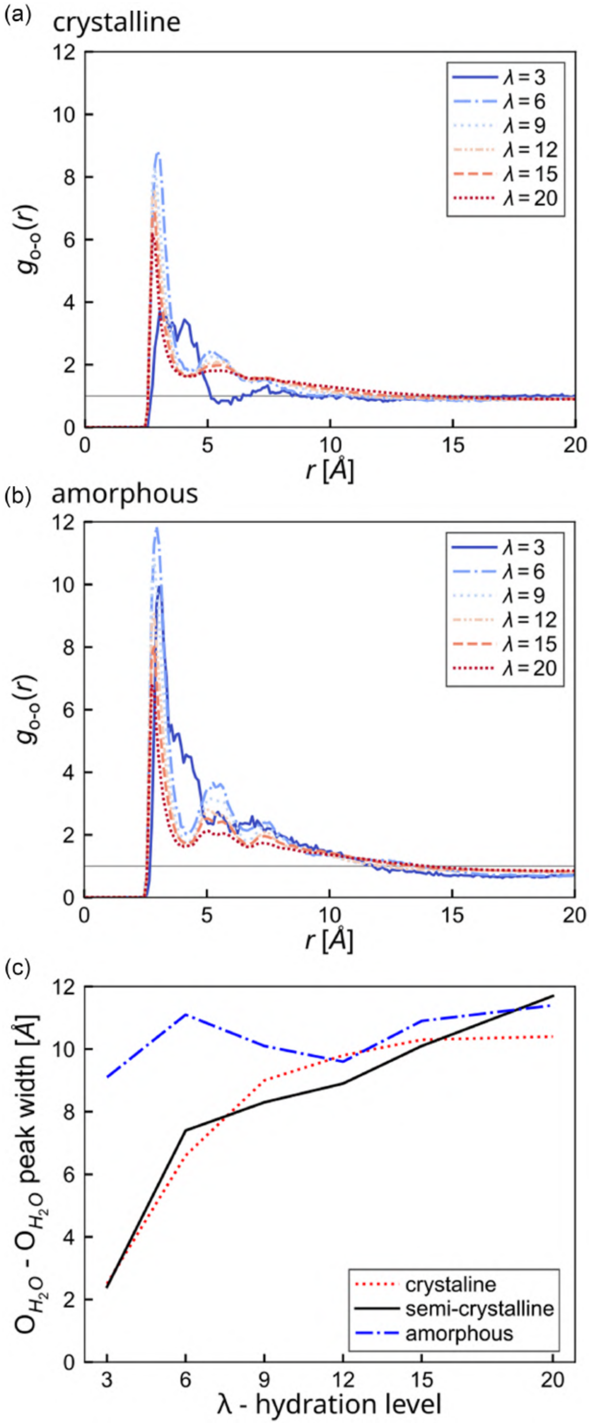

FIGURE 4 | Structural ordering of water molecules in Nafion membranes at different hydration levels (λ) for crystalline and amorphous morphologies. (a) Oxygen–oxygen radial distribution function $g_{\mathrm{O-O}}(r)$ for water in the crystalline phase shows a sharp first peak and distinct oscillations at low λ, indicating a higher degree of local ordering. (b) Corresponding $g_{\mathrm{O-O}}(r)$ for the amorphous phase reveals broader and less pronounced features, consistent with disordered environments. (c) Peak width of the first O–O correlation plotted as a function of λ for crystalline, semicrystalline, and amorphous phases.

Another indicator of cluster separation is the behaviour of the tail of RDFs. At distances $r > 10$ Å, values of distribution functions are visibly lower than $g_{\mathrm{O-O}} = 1$ in the case of the amorphous configuration compared to the other two configurations. This demonstrates the phase separation of water and Nafion in the crystalline configuration, as shown in Figure 3.

Based on the shape of RDFs, we can estimate the radius of the water pores in our systems. When analysing confined systems, such as water clusters within Nafion membranes, the RDF differs from that in bulk water, cf. Ref. [49, 50] for other relevant systems. In confined water systems, the observed RDF is effectively a convolution of the intrinsic water–water correlations with the geometry of the confining environment, in this case, the volume occupied by Nafion, which excludes water. As a result, the size of a water cluster can be estimated by identifying the distance at which $g_{\mathrm{O-O}}(r) < 1$ beyond the well-defined coordination shell peaks, where the influence of the confining wall begins to suppress water density. The results are shown in Figure 4c. We observe an increase in pore radius with increasing water content for both crystalline and semicrystalline configurations, ranging from ≈2 Å to 10 Å or 12 Å. In contrast, the amorphous configuration exhibits a nearly-constant pore radius of around 10 Å across all hydration levels. Such a behaviour suggests that in crystalline systems, predominantly linear water-filled pores expand radially as more water is introduced. Meanwhile, in the less phase-separated amorphous system, initially spherical pores composed of a few water molecules tend to coalesce and elongate, leading to pore growth primarily in length rather than in radius.

2.4 | Separating Phase Densities

The densities of confined water and Nafion can be directly extracted from the simulation configurations by using atomic positions to determine the volume occupied by each phase. This is done via polydisperse Voronoi tessellation [51]. Summing the volumes of Voronoi cells for atoms belonging to water or Nafion allows for a direct calculation of phase-specific densities [52]. Figure 5 presents the effective densities of Nafion and water, which were obtained via the Voronoi-based analysis, across different structural configurations—crystalline, semicrystalline, and amorphous—at varying hydration levels λ. The points at the top of Figure 5a represent the effective density of Nafion, while the results at the bottom are water density. The results highlight a clear trend in which crystalline structures exhibit higher densities (i.e., $\rho_{\mathrm{eff,vor}} \approx 2.1\ \mathrm{g/cm^3}$) than their amorphous counterparts (i.e., $\rho_{\mathrm{eff,vor}} < 2\ \mathrm{g/cm^3}$), emphasising the role of molecular ordering in determining the spatial packing

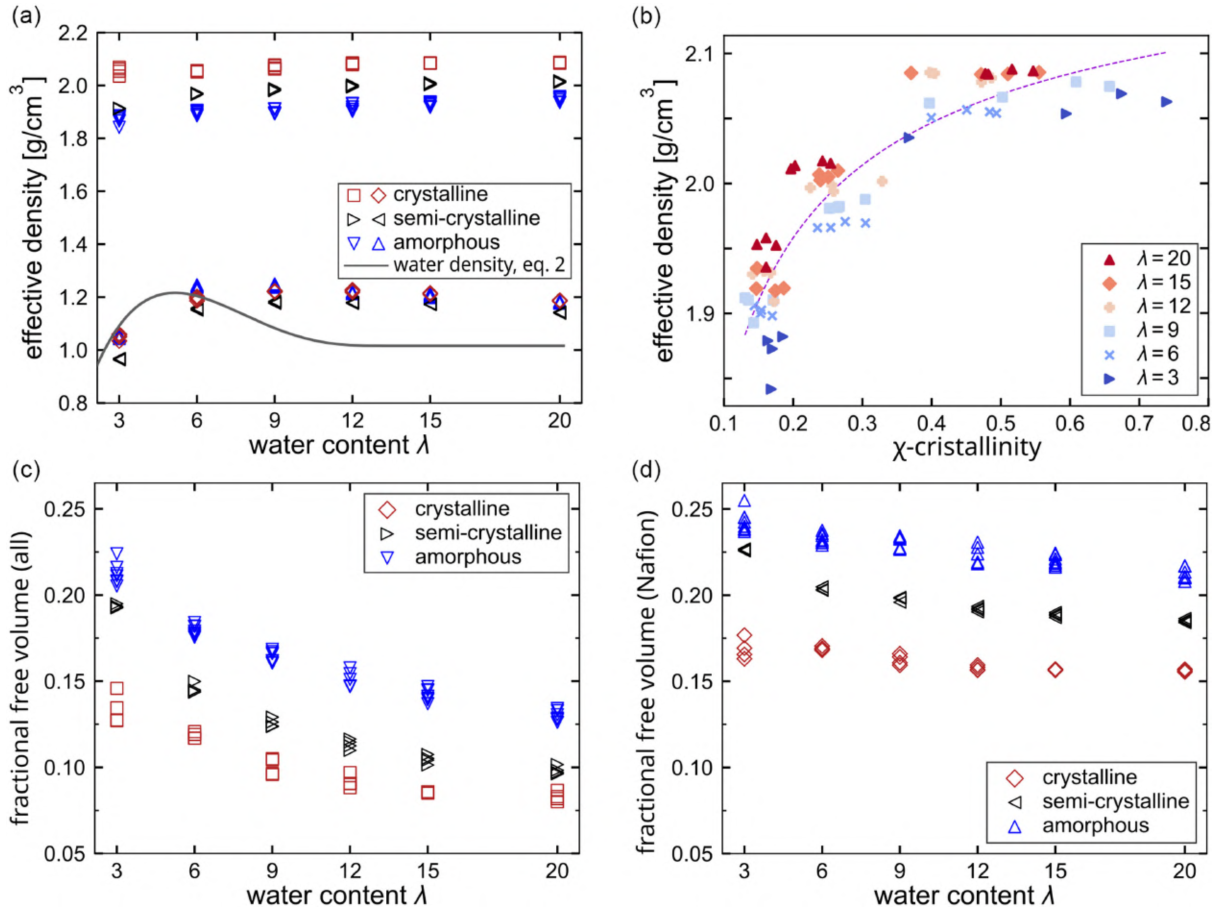

FIGURE 5 | (a) Effective densities of Nafion (top symbols) and confined water (bottom symbols) computed from polydisperse Voronoi tessellation of the simulation snapshots at various water contents (λ) for crystalline, semicrystalline, and amorphous morphologies. Empirical model for dependence of effective water density on water content $\rho_{\mathrm{w}}(\lambda)$, cf. Equation (2), is given for comparison (line). (b) Correlation between the effective Nafion density and structural crystallinity (χ) for all simulated configurations at different hydration levels. The dashed line represents a fit to the empirical relation: $\rho_{\mathrm{eff}} = \rho_0 - \Delta\rho(1-\chi)^2$. (c) Evolution of the FFV with λ for the whole system, i.e., including both Nafion and water. (d) Variation of FFV in Nafion phase with λ for crystalline, semicrystalline, and amorphous morphologies.

efficiency. Moreover, we also observe a higher water density ($\rho_{\mathrm{w}}^{\mathrm{confined}} = 1.2\,\mathrm{g/cm^3}$) compared to the density of bulk water ($\rho_{\mathrm{w}}^{\mathrm{bulk}} = 0.997\,\mathrm{g/cm^3}$). This elevated water density reflects the well-known characteristic of water in nanoconfined environments, where molecular interactions with the surrounding polymer matrix result in structural rearrangements, increased hydrogen bonding, and altered water packing. Confinement effects often result in a denser water phase than in bulk, as observed in various nanoporous and polar systems [53, 54].

The correlation between the Nafion effective density and crystallinity for all configurations is presented in Figure 5b, where different colours represent different hydration levels. The data show that the trend of increasing crystallinity leads to an increase in the Nafion effective density, which reaches a plateau at higher crystallinity levels. If we denote the crystallinity as χ, we can describe the dependence of the effective Nafion density on the crystallinity by the formula: $\rho_{\mathrm{eff}} = \rho_0 - \Delta\rho(1-\chi)^2$, with $\rho_0 = 2.107\,\mathrm{g/cm^3}$ denoting the density of the dry Nafion and $\Delta\rho = 0.238\,\mathrm{g/cm^3}$ being the fitted parameter. Shown as the dashed curve in Figure 5b, the formula mentioned above captures an asymptotic density–crystallinity dependence, whereby enhanced packing with increasing crystallinity elevates the effective density toward a limiting value (i.e., in fully crystalline system $\chi = 1$, $\rho_{\mathrm{eff}} = \rho_0$). Since higher crystallinity enhances the Nafion backbone ordering, allowing them to pack closer together, resulting configurations have a densely packed hydrophobic phase, while at the same time allowing hydrophilic sulphonic groups of the side chain to be in contact with water.

Fractional free volume (FFV) provides a measure of available void in membrane space for molecules and functional groups. The free volume primarily stems from interchain voids and hydration channels in hydrated membranes, and its availability enhances the mobility of molecules and chains, yielding higher transport coefficients and elasticity [24, 55]. Just as with overall density, FFV can be measured experimentally using positron annihilation lifetime spectroscopy (PALS) [37, 56]. Sodaye et al. estimated local free-volume with radii of $R \approx 3.5$ Å across various cationic forms of Nafion 117 [56]. Still, frequently, the experimental studies provide information on the size of free-volume cavities but do not report the density of voids or the overall fractional free volume. Nevertheless, the estimated void sizes are of the same order as a single structural unit of Nafion, suggesting that these cavities correspond to the free space associated with individual polymer segments.

Figure 5c,d compare FFV among crystalline, semicrystalline, and amorphous Nafion morphologies. In all morphologies, the FFV decreases monotonically with λ. The magnitude of FFV strongly depends on structural ordering: amorphous regions exhibit the largest FFV (≈0.13–0.22), while crystalline domains show a comparable increase in packing density with water content (≈0.08–0.15). The semicrystalline phase shows intermediate behaviour, confirming that amorphous cross-links between nanocrystalline lamellae are causing free-volume retention. In Figure 5d, we evaluated FFV only for polydisperse Voronoi tessellation volume belonging to Nafion, denoted as $V_{\mathrm{free}}/V_{\mathrm{Nafion}}$, and compared among crystalline, semicrystalline, and amorphous Nafion morphologies. One can note that, due to the size of Nafion molecules and the rigidity of its polymer backbone, this phase contains a higher proportion of void space than the system as a whole. Also, for these morphologies, the FFV decreases monotonically with λ, reflecting the stretching of the polymer chains, which leads to better alignment and more compact configurations, and the magnitude of FFV strongly depends on structural ordering.

Furthermore, the amorphous configurations exhibit the largest FFV (≈0.22–0.25), while crystalline domains show a limited increase in packing density with water content (≈0.15–0.17). Therefore, in contrast to the global FFV, the change in free volume in Nafion phase is smaller in the range of investigated λ. Comparing Figure 5c,d, we can conclude that at the simulation box level, with swelling, the absorbed water progressively occupies available spaces. Over the range of investigated $\lambda = 3-20$, the main contribution to the free-volume change stems from the water-Nafion interface.

An inverse relationship between FFV and effective density is observed when comparing Figure 5a,c,d. Analogous trends are reported [24] for sulphonated poly(phenylene) ionomers ($\mathrm{sPP^M}$), where higher density led to reduced FFV. The present MD results thus bridge microscopic cavity statistics with macroscopic density: as crystallinity increases, void spaces collapse and the fractional free volume decreases, supporting the mechanism of crystallinity-controlled density. This correspondence reinforces the physical interpretation that mechanical processing or annealing, which enhances crystallinity, can be exploited experimentally to tune the free volume and, consequently, the transport properties of PFSA membranes. Increasing crystallinity improves mechanical stiffness and dimensional stability. Conversely, lowering crystallinity or inducing backbone disordering enlarges the free-volume fraction, facilitating faster water transport. Thus, by controlling processing parameters, we can rationally balance water uptake and mechanical integrity of the membranes.

2.5 | Measured Density Dependence on Water Content

Figure 6 presents the relationship between the bulk density of hydrated Nafion 117 and the water content λ, defined as the number of water molecules per sulphonic acid group.

As the water content λ increases, the membrane density ρ decreases, reflecting the swelling of the polymer matrix due to water uptake. A basic approach to describing the change in water volume can be derived under the assumption of volume additivity between dry Nafion and absorbed water. Using mass of water m_{w} and Nafion m_0, we can define the corresponding fraction of absorbed water, $f_{\mathrm{w}} = m_{\mathrm{w}}/m_0$, in case of Nafion 117, $f_{\mathrm{w}} \approx 0.0155\lambda$ when molecular masses of water and Nafion are accounted. We denote by ρ_0 the density of dry Nafion and by ρ_{w} the density of water. Then, using the definition of the density, $\rho = m/V$, we obtain the ideal mixing law for the Nafion-water system

$$\rho(\lambda) = \frac{(1+f_{\mathrm{m}})\rho_0\rho_{\mathrm{w}}}{\rho_{\mathrm{w}} + f_{\mathrm{m}}\rho_0} \tag{1}$$

The dashed line in Figure 6 corresponds to this ideal behaviour using $\rho_{\mathrm{w}} = \rho_{\mathrm{w,b}} = 0.997\,\mathrm{g/cm^3}$ and $\rho_0 = 2.107\,\mathrm{g/cm^3}$, assuming no residual water after drying at 200°C. The dotted red curve uses a slightly lower reference density of dry Nafion $\rho_0 = 2.05\,\mathrm{g/cm^3}$

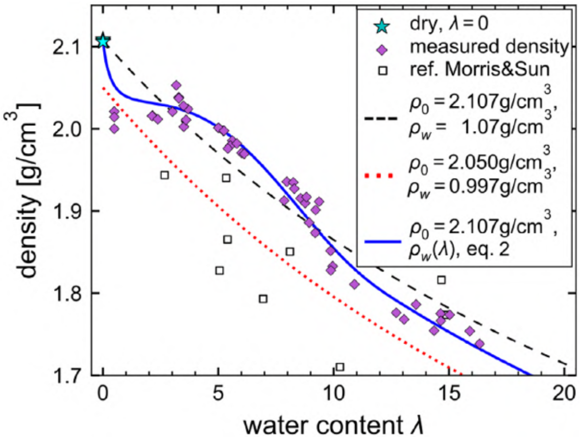

FIGURE 6 | Comparison between experimental data and the model describing the evolution of effective water density $\rho_w(\lambda)$ in hydrated Nafion (bold blue line). The measured density of Nafion 117 as a function of water content λ. Purple diamonds represent experimental data obtained through hydrostatic weighing using Archimedes' principle, while the blue star represents the four measured density points of the dry membrane. For comparison the experimental data from Ref. [25] (squares) are given. The dashed black and dotted red lines correspond to a model assuming a dry membrane density [25] of $\rho_0 = 2.107\,\text{g/cm}^3$ and here estimated $\rho_0 = 2.05\,\text{g/cm}^3$, respectively. All measurements were performed following the drying and conditioning procedures described in the experimental section of this paper.

[25], illustrating the sensitivity of the predicted density to the dry-state baseline.

Equation (1) assumes no excess volume arising from polymer–water interactions, implying that the total volume equals the sum of component volumes. However, this idealisation neglects molecular interactions and structural rearrangements within hydrated Nafion, such as those illustrated in Figure 5a. A more realistic description requires accounting for the initial organisation of ionic clusters and the formation of water domains.

To capture these effects, we introduce a phenomenological Hoover-Hess functional [57], representing the coupling of effective water density with hydration

$$\rho_w(\lambda) = \begin{cases} \rho_{w,b} + \delta_w \dfrac{4(\lambda_c - \lambda_{max})(\lambda_c - \lambda)^3 - 3(\lambda_c - \lambda)^4}{(\lambda_c - \lambda_{max})^4}, & \lambda < \lambda_c, \\ \rho_{w,b}, & \lambda \geq \lambda_c. \end{cases} \tag{2}$$

Physically, in this model, $\lambda_{max} = 5$ defines the water content at which density reaches its maximum $\rho_{w,b} + \delta_w = 1.217\,\text{g/cm}^3$, and $\lambda_c = 12.91$ defines the extent of the variation. The parameters were obtained by the nonlinear least-squares method from experimental data in Figure 6. Here, we note that the model parameters δ_w, λ_{max}, and λ_c are material parameters of the Nafion 117 that describe its measured behaviour. The model qualitatively captures the rapid initial increase followed by a gradual decrease in water density, consistent with molecular-simulation trends, cf. Figure 5a.

The ideal mixing density model in Equaton (1) combined with hydration-dependent water density (Equation (2)) reproduces the characteristic evolution of hydrated Nafion's density, consistent with experimental observations in Figure 6. Initially, membrane density decreases with increasing λ due to swelling of the hydrophilic domains, cf. also Ref. [58, 59]. At low hydration ($\lambda < 3$), the model accounts for tightly bound water to sulphonate groups, residing primarily in tightly bound solvation shells around sulphonic groups, resulting in reduced density [29, 32, 60]. As hydration increases, ρ_w rises to a maximum near $\lambda \approx 5$–6, corresponding to the completion of the first hydration shell (water creates tight clusters around bound anions such as the sulphonate group, cf. Ref. [61]). As a result, we observe a weaker dependence of density on water content for $\lambda < 6$ in Figure 6. The proposed model captures the transition from bound to free water, observed in Figure 6 for $6 \leq \lambda < 10$ and also experimentally reported in Refs. [55, 58, 62]. The model smoothly decays to $\rho_{w,b} = 1.017\,\text{g/cm}^3$ at $\lambda \geq \lambda_c$, ensuring a continuous transition from dispersed water molecules within the Nafion matrix to water in the channels. As a result, at high water content, the ideal mixing law with water and Nafion densities independent of the water content is recovered.

2.6 | Densities from Simulations Versus Experiment

Figure 7 compares the relationship between the overall density of the Nafion-water system and the water content(λ) from our simulations and experiments. The densities for three different configurations obtained via MD simulations are plotted on top of the experimental results: amorphous configurations obtained by annealing (blue shaded bottom area), semicrystalline configurations obtained by annealing of crystalline configurations (green shaded area in the middle), and crystalline configurations obtained by shearing the system during annealing (orange shaded area on the top). The shaded regions highlight the variations in density behaviour under different conditions. Those results indicate a general decrease in Nafion-water density with increasing water content, with notable differences between

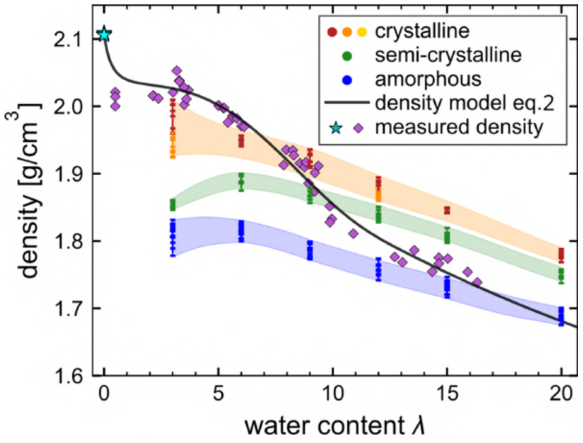

FIGURE 7 | Comparison between experimental data, the analytic model (bold line) $\rho_w(\lambda)$ and densities obtained in simulations in hydrated Nafion. The various structural configurations obtained via MD simulations within the scope of this study: amorphous (blue shaded region), semicrystalline (green shaded region), and crystalline (orange shaded region). Those results indicate a decreasing trend in density with increasing water content, with crystallinity influencing the configuration-dependent behaviour.

configurations obtained by different procedures and within configurations obtained by the same procedure.

Therefore, one can observe from Figure 7 that the combined effect of water content and membrane structure determines the density of the hydrated Nafion membrane. At all levels of hydration, crystalline configurations have higher densities than their amorphous counterparts. That is because the spatial ordering allows hydrophobic Nafion backbones to pack closely together, with water channels following the backbone direction. On the other hand, the globular nature of the water channels in amorphous configurations hinders backbone packing, resulting in lower density. One can also see from Figure 7 that the crystalline configurations more closely match experimental values at lower water content, whereas for a fully hydrated membrane ($\lambda = 15$), the amorphous configuration aligns more closely with both. As the water level increases, Nafion polymers rearrange themselves from a crystalline to an amorphous configuration.

3 | Conclusions

This work integrates experimental and simulation approaches to elucidate the relationship between structure and density in hydrated Nafion systems. By combining molecular simulations, Voronoi-based effective density calculations, and an analytical model, we have uncovered key relationships among polymer morphology, crystallinity, and the effective densities of polymer and water phases. The results consistently demonstrate that crystallinity plays an important role in determining both structural organisation and hydration behaviour, leading to significant differences in density and water distribution. One key finding is the impact of hydration (λ) on the polymer structure, with increased water content leading to distinct morphological changes. As the hydration level increases, Nafion chains undergo a rearrangement from a more crystalline structure into a disordered, amorphous configuration. Voronoi-based density calculations further validate these trends, showing that the crystalline structures maintain a higher effective density than the annealed configurations. This difference arises due to the efficient packing of polymer chains, which reduces the available free volume and limits the extent of water penetration. Additionally, a strong correlation between effective density and crystallinity (χ), as captured by the relationship: $2.107 - 0.238(1-\chi)^2\,\mathrm{g/cm^3}$, suggests a saturation effect, where increased ordering increases the density up to a limit. Crystalline configurations exhibit more extended chain conformations, resulting in higher radii of gyration, whereas annealed structures show more compact molecular arrangements. This behaviour highlights that increasing structural order restricts chain mobility and promotes the formation of a stiffer, more rigid network.

Analysis of the experimental density data reveals that water within the Nafion matrix exhibits a complex, nonlinear dependence on hydration. The proposed model successfully reproduces these experimental trends, capturing both the rise and decay of the effective water density with increasing λ, and the transition from bound to channel-confined water seen in simulation. The fitted curve qualitatively agrees with molecular dynamics simulations and literature results, where the density of confined water increases in the range $3 \leq \lambda \leq 6$ as the first hydration shell becomes filled, followed by a gradual relaxation toward bulk-like values once continuous water networks form for $\lambda > 9$. At very low hydration levels ($\lambda < 3$), the experimentally observed low effective water density is consistent with literature interpretations that attribute it to water molecules localised near sulphonic groups, starting dissociation of their hydrogen to form hydronium and sulphonate ions. The model reproduces the key experimental features of the water content dependent density profile: an initial rapid decrease in membrane density as water first penetrates the polymer, a local plateau corresponding to the formation of denser confined water ($\approx 1.2\,\mathrm{g/cm^3}$) in the intermediate hydration range ($4 < \lambda < 8$), and a secondary gradual decrease at higher λ as water domains coalesce. The model parameters describe the evolution of the water state within the ionomer structure and represent its material properties, specifically here those of Nafion 117. This description provides a coherent interpretation linking the macroscopic density evolution to the microscopic organisation of water within the Nafion matrix.

Overall, the presented results provide a deeper understanding of how structural ordering influences the density, hydration, and mechanical properties of polymer systems. Our approach provides a microscopic interpretation of long-observed experimental trends, such as deviations in measured density from the ideal-mixture law. It also reveals how confined water reorganises within Nafion domains. Beyond reproducing structural motifs, our analysis helps explain how crystallinity, which is controlled by processes such as annealing, stretching, or extrusion, affects structural elements that determine mechanical integrity and transport pathways in PFSA membranes. These insights support the informed selection of processing conditions and material modifications to optimise the performance of next-generation proton-conductive materials.

4 | Methods

4.1 | Density Measurement

Nafion 117 membranes (MIL-PRF-131K) were used for the water sorption experiments and were obtained from Merck via Sigma–Aldrich. As a pretreatment, the membrane samples were soaked in liquid deionised water at room temperature for 2.5 h. This step served both to activate the membrane and to remove residual oligomers or low-molecular-weight compounds that may have remained from the manufacturing process. After pretreatment, the samples were subjected to a controlled drying protocol before each conditioning and measurement cycle.

The drying process consisted of three steps. First, the membrane samples were placed in a laboratory oven and dried at 110°C for 24 h. This temperature was selected to ensure the effective removal of loosely bound water while minimising the thermal degradation of the polymer. Second, the dried samples were allowed to cool to room temperature for 30 min in a desiccator containing dry silica gel. Finally, the initial dry weight of each sample was measured using an analytical balance. Time-resolved mass measurements showed that the membrane mass stabilised after ≈3.5 h of drying, with no significant further mass loss up to 24 h. Consequently, 24 h was adopted as the standard drying duration to ensure consistent reference conditions. To further assess the presence of tightly bound water that may not be fully removed at 110°C, additional drying steps at up to 200°C were performed on a subset of samples. We refer to these measurements as dry, i.e., $\lambda = 0$ and use them to evaluate residual moisture and recalibrate hydration levels.

Conditioning was conducted to explore water uptake under different environmental conditions and at different hydration levels. The membrane samples during conditioning were exposed to three environments at 80°C: dry air in an oven, humid air in a climate chamber, and immersion in liquid deionised water to achieve different hydration levels. In all three environments, fully desalinated water was used. During oven exposure, samples were held in metal mesh cages to prevent movement due to air convection. After conditioning, the samples were quickly sealed in glass vessels and stored in a desiccator to minimise postconditioning changes in water content.

The mass and density of the samples following the conditioning were determined using a Sartorius analytical balance with a precision of 0.1 miligram (mg) and a density measurement kit, following the Archimedes' principle: the conditioned sample is first weighed directly on the scale to obtain m_{air}, and afterwards fully submerged in water and weighed again to obtain m_{water}. The density of the conditioned sample ρ is

$$\rho = \frac{m_{\mathrm{air}}}{m_{\mathrm{air}} - m_{\mathrm{water}}} \rho_w \tag{3}$$

where $\rho_w = 0.997\ \mathrm{g/cm^3}$ is the density of bulk water.

Determining the weight of the sample by buoyancy m_{water} is performed in water which contains <0.1% of a surfactant to ensure proper surface wetting, according to the DIN EN ISO 1183-1 standardised method. To avoid the artefacts arising from the additional water absorption during measurement, the weighing process in water was performed rapidly, within 1 min. Control measurements confirmed that the change in sample density due to water uptake, during immersion, remained below 0.8% over 5 min, indicating minimal error from the additional sorption.

4.2 | Model and Simulation

Model Nafion has a polymerisation degree of 10, cf. Figure 8, resulting in an equivalent weight (EW) of 1100, representing the molecular weight per sulphonate group—a standard Nafion research value. Following Wang et al. [63], the present study adopts a membrane model in which the protons dissociate entirely from the sulphonate groups. Although a recent work by Donnelly, Yang et al. [64] has demonstrated the persistence of protonated sites even at elevated hydration levels, the intrinsic limitations of classical molecular dynamics prohibit an accurate treatment of such effects. Accordingly, we confine our simulations to Nafion polymer membranes, where the water content (λ), defined as the number of water molecules per sulphonate group, is at least 3 [63]. The DREIDING force field, modified by Mabuchi et al. [32], was employed to model molecular interactions in Nafion. In contrast, the classical hydronium model [65] and TIP4P-2005 [66] model were used for hydrated protons and water molecules, respectively. The interactions between Nafion and water were calculated using the common Lorentz-Berthelot mixing rules [67–69]. All simulations were carried out using the LAMMPS MD software package [70, 71] with fully periodic boundary conditions. To maintain the desired temperature, the Nosé–Hoover thermostat [72–74] was utilised, while the velocity-Verlet algorithm was applied to solve the equations of motion [75]. The timestep was 1 fs. Constant-pressure simulations (at the normal pressure of 1 bar) were performed using the Parrinello-Rahman barostat [76] coupled to the overall box volume. The external pressure was specified as a scalar (isobaric ensemble). The damping parameters for the thermostat and barostat were 10 fs and 1 ps, respectively. Our comprehensive simulation setup enables the detailed analysis of the Nafion membrane behaviour under varying hydration conditions.

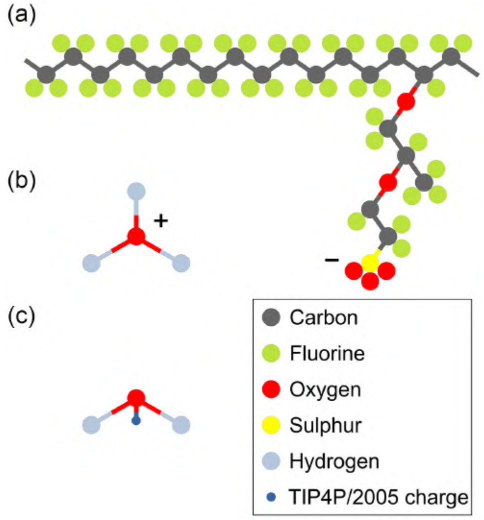

FIGURE 8 | Representation of molecular components used in the simulations. (a) One monomer unit of Nafion 117 polymer showing hydrophobic ($-\mathrm{CF_2}-$) and hydrophilic ($-\mathrm{SO_3}^-$) regions; the sulphonic acid group of the side chain is deprotonated, making the side chain negatively charged. In our simulation, one Nafion polymer consists of 10 of these monomeric units. (b) Hydronium ion ($\mathrm{H_3O^+}$). (c) TIP4P/2005 water model, with a virtual negative charge site indicated. Atom colours: carbon (grey), fluorine (green), oxygen (red), sulphur (yellow), hydrogen (light blue), TIP4P/2005 negative charge site (blue).

4.3 | Radius of Gyration, Polydisperse Voronoi, and FFV Analysis

The radius of gyration represents the root mean square distance of the monomer units from the centre of mass of the polymer coil, and is given by the formula

$$R_g = \sqrt{\frac{1}{M}\sum_i m_i (r_i - R)^2} \tag{4}$$

where M and R are the mass and position of the centre of mass of the whole Nafion polymer, and m_i and r_i are the mass and position of individual atoms of that polymer. Therefore, R_g quantifies the spatial distribution of monomers around the polymer's centre of mass. The radius of gyration provides insight into the overall shape and conformation of chains, distinguishing between unfolded and bundled polymers.

Voronoi analysis was used to partition the simulation domain into regions corresponding to the water and Nafion phases and quantify their respective local volumes. In the method, space is partitioned into polyhedra, each containing all points closer to a given atom than to any other [51, 77, 78]. The extension of this method, the polydisperse Voronoi tessellation, accounts for each atom's Van der Waals radius as a weight to partition space between atoms. The volume of each Voronoi cell, therefore, represents the local environment available to that atom, providing a direct measure of local density. The fractional mass density (compactness) of the Nafion and water phases is obtained from their calculated Voronoi volumes. The Voronoi analysis can capture the distribution of local densities arising from irregular chain packing and entanglements, revealing spatial fluctuations that are often greater than macroscopic variations.

Still, Voronoi analysis also has a limitation. While this method can accurately delineate Nafion from water clusters, it does not capture the free volume, unoccupied by the van der Waals volumes of individual atoms. Consequently, it provides little insight into the void spaces that enable molecular mobility, which governs both water's transport properties and the mechanical stiffness of the polymer matrix. To assess these aspects, an explicit evaluation of the FFV is required as a complementary property. The FFV provides a molecular-level estimate of the occupied volume, while the remainder corresponds to free volume available for chain motion and penetrant diffusion.

The FFV in the Nafion membrane was estimated using a relation

$$\mathrm{FFV} = 1 - \left(\frac{V_{\mathrm{o}}}{V}\right) = 1 - \left[1.3 \sum_{k=1}^{K} \left(\frac{V_{\mathrm{w},k}}{M_{\mathrm{ru}}}\right)\right] \rho \qquad (5)$$

where V_{o} is the van der Waals occupied volume, V the specific volume of the polymer or water molecule, $V_{\mathrm{w},k}$ the van der Waals volume contribution of the k-th structural group, M_{ru} the molecular weight of the repeat unit, and ρ the simulated density. The relation is derived from group-contribution theory (GCT) by Bondi [79] and includes an empirical factor of 1.3 accounting for tight packing in the condensed phase. The total van der Waals volume of the repeat unit is calculated by summing the contributions of all K structural fragments according to their stoichiometric occurrence. The relevant volumes for water and CF_2, CF_3, O, and SO_3H moieties were taken from group-contribution parameters [24, 79, 80].

Acknowledgments

This research project has received funding from the European Union's Horizon Europe research and innovation programme under the Marie Sklodowska-Curie Doctoral Network grant agreement no 101072578—Bridging Models at Different Scales To Design New Generation Fuel Cells for Electrified Mobility. I.S. and M.D. acknowledge funding provided by the Institute of Physics Belgrade through the Grant by the Ministry of Science, Technological Development and Innovations of the Republic of Serbia. Molecular dynamics simulations were run on the PARADOX supercomputing facility at the Scientific Computing Laboratory, Centre for the Study of Complex Systems, Institute of Physics Belgrade. M.J., M.D., and I.S. acknowledge the training and support received by the COST (European Cooperation in Science and Technology) Action Cosy CA21101.

Funding

This study was supported by HORIZON EUROPE Framework Programme (101072578), and Ministarstvo Prosvete, Nauke i Tehnološkog Razvoja Republike Srbije.

Conflicts of Interest

The authors declare no conflicts of interest.

Data Availability Statement

The data that support the findings of this study are available from the corresponding author upon reasonable request.

References

1. B. C. H. Steele and A. Heinzel, "Materials for Fuel-Cell Technologies," *Nature* 414 (2001): 345–352.

2. R. Borup, J. Meyers, B. Pivovar, et al., "Scientific Aspects of Polymer Electrolyte Fuel Cell Durability and Degradation," *Chemical Reviews* 107 (2007): 3904–3951.

3. S. Lee, S. Oh, S. Kim, et al., "Patterned Ion-Pair Membrane for High-Temperature Proton-Exchange Membrane Fuel Cells," *Small Structures* 6, no. 4 (2025): 2400430.

4. L. Rubatat, A. L. Rollet, G. Gebel, and O. Diat, "Evidence of Elongated Polymeric Aggregates in Nafion," *Macromolecules* 35 (2002): 4050–4055.

5. O. Teschke, P. S. Casagrande, D. M. Soares, and W. E. Gomes, "Nanosized Water Channels Associated with Hydrophobic and Hydrophilic Fibrillar Arrangements Formed on Nafion Surfaces in Confined Regions," *ACS Omega* 9, no. 22 (2024): 23567–23572.

6. G. A. Giffin, G. M. Haugen, S. J. Hamrock, and V. Di Noto, "Interplay between Structure and Relaxations in Perfluorosulfonic Acid Proton Conducting Membranes," *Journal of the American Chemical Society* 135 (2013): 822–834.

7. C. Laberty-Robert, K. Valle, F. Pereira, and C. Sanchez, "Design and Properties of Functional Hybrid Organic–Inorganic Membranes for Fuel Cells," *Chemical Society Reviews* 40 (2011): 961–1005.

8. Y. Chen, C. Liu, J. Xu, et al., "Key Components and Design Strategy for a Proton Exchange Membrane Water Electrolyzer," *Small Structures* 4, no. 6 (2023): 2200130.

9. C. Welch, A. Labouriau, R. Hjelm, B. Orler, C. Johnston, and Y. S. Kim, "Nafion in Dilute Solvent Systems: Dispersion or Solution? *ACS Macro Letters* 1, no. 12 (2012): 1403–1407.

10. Y. S. Kim, C. F. Welch, R. P. Hjelm, N. H. Mack, A. Labouriau, and E. B. Orler, "Origin of Toughness in Dispersion-Cast Nafion Membranes," *Macromolecules* 48, no. 7 (2015): 2161–2172.

11. M. K. Budinski and A. Cook, "Osmotic Pressure of Water in Nafion," *Tsinghua Science & Technology* 15, no. 4 (2010): 385–390.

12. C. Arthurs and A. Kusoglu, "Mechanical Characterization of Electrolyzer Membranes and Components Under Compression," *Journal of the Electrochemical Society* 171, no. 9 (2024): 094510.

13. K. Schmidt-Rohr and Q. Chen, "Parallel Cylindrical Water Nanochannels in Nafion Fuel-Cell Membranes," *Nature Materials* 7, no. 1 (2008): 75–83.

14. O. Kwon, S. J. Wu, and D. M. Zhu, "Configuration Changes of Conducting Channel Network in Nafion Membranes Due to Thermal Annealing," *The Journal of Physical Chemistry B* 114 (2010): 14989.

15. S. Rongpipi, J. M. Chan, A. Bird, G. Freychet, A. Kusoglu, and G. M. Su, “Revealing Mesoscale Ionomer Membrane Structure by Tender Resonant X-ray Scattering,” *ACS Applied Polymer Materials* 6, no. 23 (2024): 14115–14123.

16. T. Mabuchi, S.-F. Huang, and T. Tokumasu, “Dispersion of Nafion Ionomer Aggregates in 1-Propanol/Water Solutions: Effects of Ionomer Concentration, Alcohol Content, and Salt Addition,” *Macromolecules* 53, no. 9 (2020): 3273–3283.

17. A. Tarokh, K. Karan, and S. Ponnurangam, “Atomistic MD Study of Nafion Dispersions: Role of Solvent and Counterion in the Aggregate Structure, Ionic Clustering, and Acid Dissociation,” *Macromolecules* 53, no. 1 (2020): 288–301.

18. P. Guan, Y. Zou, M. Zhang, et al., “High-Temperature Low-Humidity Proton Exchange Membrane with “Stream-Reservoir” Ionic Channels for High-Power-Density Fuel Cells,” *Science Advances* 9, no. 17 (2023): eadh1386.

19. G. Gebel and O. Diat, “Neutron and X-ray Scattering: Suitable Tools for Studying Ionomer Membranes,” *Fuel Cells* 5, no. 2 (2005): 261–276.

20. A. Z. Weber and J. Newman, “Transport in Polymer-Electrolyte Membranes: I. Physical Model,” *Journal of the Electrochemical Society* 150, no. 7 (2003): A1008.

21. A. Kusoglu and A. Z. Weber, “New Insights into Perfluorinated Sulfonic-Acid Ionomers,” *Chemical Reviews* 117, no. 3 (2017): 987–1104.

22. J. Li, J. K. Park, R. B. Moore, and L. A. Madsen, “Linear Coupling of Alignment with Transport in a Polymer Electrolyte Membrane,” *Nature Materials* 10, no. 7 (2011): 507–511.

23. X. Kong and K. Schmidt-Rohr, “Water–Polymer Interfacial Area in Nafion: Comparison with Structural Models,” *Polymer* 52, no. 9 (2011): 1971–1974.

24. T. Largier, F. Huang, W. Kahn, and C. J. Cornelius, “Poly(phenylene) Synthesized using Diels-Alder Chemistry and Its Sulfonation: Sulfonate Group Complexation with Metal Counter-Ions, Physical Properties, and Gas Transport,” *Journal of Membrane Science* 572 (2019): 320–331.

25. D. R. Morris and X. Sun, “Water-Sorption and Transport Properties of Nafion 117 H,” *Journal of Applied Polymer Science* 50, no. 8 (1993): 1445–1452.

26. M. Ozmaian and R. Naghdabadi, “Molecular Dynamics Simulation Study of Glass Transition in Hydrated Nafion,” *Journal of Polymer Science Part B: Polymer Physics* 52, no. 13 (2014): 905–915.

27. M. Ozmaian and R. Naghdabadi, “Modeling and Simulation of the Water Gradient within a Nafion Membrane,” *Physical Chemistry Chemical Physics : Pccp* 16 (2014): 3173–3186.

28. A. Venkatnathan, R. Devanathan, and M. Dupuis, “Atomistic Simulations of Hydrated Nafion and Temperature Effects on Hydronium Ion Mobility,” *The Journal of Physical Chemistry B* 111, no. 25 (2007): 7234–7244.

29. R. Devanathan, A. Venkatnathan, and M. Dupuis, “Atomistic Simulation of Nafion Membrane: I. Effect of Hydration on Membrane Nanostructure,” *The Journal of Physical Chemistry B* 111, no. 28 (2007): 8069–8079.

30. S. Ban, C. Huang, X.-Z. Yuan, and H. Wang, “Molecular Simulation of Gas Adsorption, Diffusion, and Permeation in Hydrated Nafion Membranes,” *The Journal of Physical Chemistry B* 115, no. 39 (2011): 11352–11358.

31. J. Liu, N. Suraweera, D. J. Keffer, S. Cui, and S. J. Paddison, “On the Relationship between Polymer Electrolyte Structure and Hydrated Morphology of Perfluorosulfonic Acid Membranes,” *The Journal of Physical Chemistry C* 114, no. 25 (2010): 11279–11292.

32. T. Mabuchi and T. Tokumasu, “Effect of Bound State of Water on Hydronium Ion Mobility in Hydrated Nafion using Molecular Dynamics Simulations,” *The Journal of Chemical Physics* 141, no. 10 (2014): 104904.

33. A.-T. Kuo, W. Shinoda, and S. Okazaki, “Molecular Dynamics Study of the Morphology of Hydrated Perfluorosulfonic Acid Polymer Membranes,” *The Journal of Physical Chemistry C* 120, no. 45 (2016): 25832–25842.

34. R. Cui, S. Li, C. Yu, and Y. Zhou, “The Evolution of Hydrogen Bond Network in Nafion via Molecular Dynamics Simulation,” *Macromolecules* 56, no. 4 (2023): 1688–1697.

35. L. A. Zook and J. Leddy, “Density and Solubility of Nafion: Recast, Annealed, and Commercial Films,” *Analytical Chemistry* 68, no. 21 (1996): 3793–3796.

36. F. Bueche, “Mobility of Molecules in Liquids near the Glass Temperature,” *The Journal of Chemical Physics* 30, no. 3 (1959): 748–752.

37. G. Floudas, T. Pakula, M. Stamm, and E. W. Fischer, “Density Fluctuations in Bisphenol A Polycarbonate and Tetramethyl Bisphenol A Polycarbonate as Studied by X-Ray Diffraction,” *Macromolecules* 26, no. 7 (1993): 1671–1675.

38. Z. Stachurski, “Strength and Deformation of Rigid Polymers: Structure and Topology in Amorphous Polymers,” *Polymer* 44, no. 19 (2003):6056–6066.

39. R. Hill, “Elastic Properties of Reinforced Solids: Some Theoretical Principles,” *Journal of the Mechanics and Physics of Solids* 11, no. 5 (1963): 357–372.

40. M. R. Hestenes and E. Stiefel, “Methods of Conjugate Gradients for Solving Linear Systems,” *Journal of Research of the National Bureau of Standards* 49, no. 6 (1952, 409–436.

41. The Initial Density of 1.7 $\mathrm{g m^{-3}}$ Was Selected to Match the Equilibrium Density of Hydrated Nafion at the Highest Water Content Studied ($\lambda = 20$). Tests with Different Initial Densities Showed that Increasing the Density Produced No Significant Change in Morphology, while Decreasing It Only Prolonged the NPT Equilibration. This Reflects that the Annealing Procedure Adopted from Ref. [29] and the Applied Flow Field, in Both Crystalline and Semi-Crystalline Configurations, Had a much Stronger Influence on the Final Structure than the Precise Stopping Point of the Initial Compression, Cf. SI.,

42. Y. Qi and Y.-H. Lai, “Mesoscale Modeling of the Influence of Morphology on the Mechanical Properties of Proton Exchange Membranes,” *Polymer* 52, no. 1 (2011): 201–210.

43. Y. R. Sliozberg, I.-C. Yeh, M. Kröger, K. A. Masser, J. L. Lenhart, and J. W. Andzelm, “Ordering and Crystallization of Entangled Polyethylene Melts under Uniaxial Tension: A Molecular Dynamics Study,” *Macromolecules* 51 (2018): 9635–9648.

44. J. Wen, J. Yang, M. Kröger, et al., “Molecular Details of the “Catalytic Effect” of Long Chains on Short Chains in Stretch-Induced Polymer Crystallization,” *Macromolecules* 57, no. 4 (2024): 1612–1624.

45. A. P. Sunda and A. Venkatnathan, “Atomistic Simulations of Structure and Dynamics of Hydrated Aciplex Polymer Electrolyte Membrane,” *Soft Matter* 8, no. 42 (2012): 10827–10836.

46. S. Akbari, M. H. Mosavian, F. Moosavi, and A. Ahmadpour, “Molecular Dynamics Simulation of Keggin HPA Doped Nafion 117 as a Polymer Electrolyte Membrane,” *Rsc Advances* 7, no. 70 (2017): 44537–44546.

47. M. Ester, H.-P. Kriegel, J. Sander, and X. Xu, in *Proceedings of the Second International Conference on Knowledge Discovery and Data Mining, KDD’96* (AAAI Press, 1996), 226–231.

48. A. Luzar and D. Chandler, “Hydrogen-Bond Kinetics in Liquid Water,” *Nature* 379 (1996): 6560–6555.

49. I. Stanković, M. Dašić, M. Jovanović, and A. Martini, “Effects of Water Content on the Transport and Thermodynamic Properties of Phosphonium Ionic Liquids,” *Langmuir* 40, no. 17 (2024): 9049–9058.

50. M. K. Borg, D. A. Lockerby, K. Ritos, and J. M. Reese, “Multiscale Simulation of Water Flow through Laboratory-Scale Nanotube Membranes,” *Journal of Membrane Science* 567 (2018): 115–126.

51. M. d. Berg, O. Cheong, M. v. Kreveld, and M. Overmars, *Computational Geometry: Algorithms and Applications*, 3rd ed. (Springer-Verlag TELOS, 2008).

52. A. Stukowski, “Visualization and analysis of atomistic simulation data with OVITO–the Open Visualization Tool,” *Modelling and Simulation in Materials Science and Engineering* 18, no. 1 (2010): 015012.

53. M. H. Köhler and L. B. da Silva, “Size Effects and The Role of Density on The Viscosity of Water Confined in Carbon Nanotubes, *Chemical Physics Letters* 645 (2016): 38–41.

54. O. Ramon, E. Kesselman, R. Berkovici, Y. Cohen, and Y. Paz, “Attenuated Total Reflectance/Fourier Transform Infrared Studies on the Phase-Separation Process of Aqueous Solutions of Poly(n-isopropylacrylamide),” *Journal of Polymer Science Part B: Polymer Physics* 39, no. 14 (2001): 1665–1667.

55. Q. Zhao, P. Majsztrik, and J. Benziger, “Diffusion and Interfacial Transport of Water in Nafion,” *The Journal of Physical Chemistry B* 115, no. 12 (2011): 2717–2727.

56. H. S. Sodaye, P. K. Pujari, A. Goswami, and S. B. Manohar, “Probing the Microstructure of Nafion-117 using Positron Annihilation Spectroscopy,” *Journal of Polymer Science Part B: Polymer Physics* 35, no. 5 (1997): 771–776.

57. W. Hoover and S. Hess, “Anisotropic Plasticity with Embedded-Atom Potentials,” *Physica A: Statistical Mechanics and Its Applications* 267, no. 1 (1999): 98–110.

58. Y. Bai, M. S. Schaberg, S. J. Hamrock, et al., “Density Measurements and Partial Molar Volume Analysis of Different Membranes for Polymer Electrolyte Membrane Fuel Cells,” *Electrochimica Acta* 242 (2017): 307–314.

59. P. Choi, N. H. Jalani, and R. Datta, “Thermodynamics and Proton Transport in Nafion: Role of Water Content and Temperature,” *Journal of the Electrochemical Society* 152, no. 3 (2005): E123–E130.

60. S. Yamamoto and S. Hyodo, “A Computer Simulation Study of the Mesoscopic Structure of the Polyelectrolyte Membrane Nafion,” *Polymer Journal* 35, no. 6 (2003): 519–527.

61. M. A. Aslam, I. Stankovic, G. Murastov, et al., “Water Induced Ferroelectric Switching: The Crucial Role of Collective Dynamics,” *Nature Communications* (in press), https://doi.org/10.1038/s41467-025-65922-6.

62. M. Rahbar, Q. Alahmad, J. Bai, L. Zhang, and X. Wang, “Exceptional Thermal Conductivity Increase of Nafion by Hydrogen-Bonded Water Molecules,” *Applied Physics Letters* 124, no. 26 (2024): 262202.

63. C. Wang, J. K. Clark, M. Kumar, and S. J. Paddison, “An Ab Initio Study of the Primary Hydration and Proton Transfer of CF_3SO_3H and $CF_3O(CF_2)_2SO_3H$: Effects of the Hybrid Functional and Inclusion of Diffuse Functions,” *Solid State Ionics* 6 (2011): 199–200.

64. D. J. Donnelly, M. Y. Yang, N. Dimakis, S. S. Jang, W. A. Goddard, and E. S. Smotkin, “Atomistic Characterization of Hydration-Dependent Fuel Cell Ionomer Nanostructure: Validation by Vibrational Spectroscopy,” *Journal of Materials Chemistry A* 13 (2025): 24495.

65. S. S. Jang, V. Molinero, T. Çağın, and W. A. Goddard, “Nanophase-Segregation and Transport in Nafion 117 from Molecular Dynamics Simulations: Effect of Monomeric Sequence,” *The Journal of Physical Chemistry B* 108, no. 10 (2004): 3149–3159.

66. J. L. F. Abascal and C. Vega, “A General Purpose Model for the Condensed Phases of Water: TIP4P/2005,” *The Journal of Chemical Physics* 123, no. 23 (2005): 234505.

67. H. A. Lorentz, “Ueber die Anwendung des Satzes vom Virial in der kinetischen Theorie der Gase,” *Annalen der Physik* 248, no. 1 (1881): 127–146.

68. D. Berthelot, “Sur le melange des gaz,” *Comptes Rendus* 126 (1898): 315–316.

69. M. P. Allen and D. J. Tildesley, *Computer Simulation of Liquids* (Oxford University Press, 2017).

70. S. Plimpton, “Fast Parallel Algorithms for Short-Range Molecular Dynamics,” *Journal of Computational Physics* 117, no. 1 (1995): 1–19.

71. A. P. Thompson, H. M. Aktulga, R. Berger, et al., “LAMMPS - A Flexible Simulation Tool for Particle-based Materials Modeling at the Atomic, Meso, and Continuum Scales,” *Computer Physics Communications* 271 (2022): 108171.

72. S. Nosé, “A Unified Formulation of the Constant Temperature Molecular Dynamics Methods,” *The Journal of Chemical Physics* 81, no. 1 (1984): 511–519.

73. W. G. Hoover, “Canonical Dynamics: Equilibrium Phase-Space Distributions,” *Physical Review. A, Atomic, Molecular, and Optical Physics* 31 (1985): 1695–1697.

74. D. J. Evans and B. L. Holian, “The Nose–Hoover thermostat,” *Journal of Computational Physics* 83 (1985): 4069–4074.

75. Q. Spreiter and M. Walter, “Classical Molecular Dynamics Simulation with the Velocity Verlet Algorithm at Strong External Magnetic Fields,” *Journal of Computational Physics* 152 (1999): 102–119.

76. M. Parrinello and A. Rahman, “Polymorphic Transitions in Single Crystals: A New Molecular Dynamics Method,” *Journal of Applied Physics* 52, no. 12 (1981): 7182–7190.

77. G. Voronoi, “Nouvelles Applications des paramètres continus à la théorie des formes quadratiques. Deuxième mémoire. Recherches sur les parallélloèdres primitifs,” *Journal für Die Reine Und Angewandte Mathematik (Crelles Journal)* 134 (1908): 198–287.

78. I. Stanković, M. Kröger, and S. Hess, “Recognition and Analysis of Local Structure in Polycrystalline Configurations,” *Computer Physics Communications* 145, no. 3 (2002): 371–384.

79. A. Bondi, “Van der Waals Volumes and Radii,” *The Journal of Physical Chemistry* 68, no. 3 (1964): 441–451.

80. D. van Krevelen and K. te Nijenhuis, *Properties of Polymers: Their Correlation with Chemical Structure; Their Numerical Estimation and Prediction from Additive Group Contributions* (Elsevier Science, 2009).

Supporting Information

Additional supporting information can be found online in the Supporting Information section. **Supporting Fig. S1:** Time evolution of density (a–c, g–i) and radius of gyration R_g (d–f, j–l) of crystalline Nafion configurations at different hydration levels λ. Blue curves show density fluctuations; grey lines correspond to R_g of individual chains, red lines the ensemble average R_g, and orange shaded regions the statistical spread. Each panel shows simulated annealing and relaxation. The first two rows correspond to $\lambda = 3, 6, 9$, while the bottom two rows correspond to $\lambda = 12, 15, 20$. In both cases, the hydration is increasing from left to right. **Supporting Fig. S2:** Time evolution of density (a–c, g–i) and radius of gyration R_g (d–f, j–l) of semi-crystalline Nafion configurations (i.e., starting from crystalline configuration and then annealed without shear deformation) at different hydration levels λ. Blue curves show density fluctuations; grey lines correspond to R_g of individual chains, red lines the ensemble average R_g, and orange shaded regions the statistical spread. Each panel shows simulated annealing and relaxation. The first two rows correspond to $\lambda = 3, 6, 9$, while the bottom two rows correspond to $\lambda = 12, 15, 20$. In both cases, the hydration is increasing from left to right. **Supporting Fig. S3:** Time evolution of density (a–c, g–i) and radius of gyration R_g (d–f, j–l) of amorphous Nafion configurations at different hydration levels λ. Blue curves show density fluctuations; grey lines correspond to R_g of individual chains, red lines the ensemble average R_g, and orange shaded regions the statistical spread. Each panel shows simulated annealing and relaxation. The first two rows correspond to $\lambda = 3, 6, 9$, while the bottom two rows correspond to $\lambda = 12, 15, 20$. In both cases, the hydration is increasing from left to right. **Supporting Fig. S4:** Oxygen-oxygen radial distribution function gO-O(r) of water molecules at varying hydration levels (λ) in semicrystalline configuration.

Biographies

Mateja Jovanović is a computational physicist whose work focuses on transport phenomena, hydration mechanisms, and nanoscale ageing in polymer electrolyte membranes for fuel cells. He is currently a Marie Skłodowska—Curie doctoral fellow in the European Union-funded BLESSED project, actively collaborating with academic and industrial partners across Europe in materials science, energy technologies, and multiscale modeling.

Nicolas Bernhard is a molecular scientist specializing in membrane materials for energy applications, including fuel cells, electrolyzers, and Li-ion batteries. He completed his Ph.D. on membrane-based CO_2 separation and gained experience in industrial R&D on non-wovens and functional polymer systems. He now works as a project manager in industrial research and European Union-funded collaborations, the BLESSED and BeBoP projects.

Matthias Baldofski is a computational chemist with more than 10 years of academic and industrial experience in atomistic simulations of solid and liquid phases, heterogeneous catalysis, and materials informatics. He has extensive expertise in developing advanced simulation methodologies. After his academic career, he moved to the industry, where he supports R&D through multiscale simulation approaches, focusing on lubricants, polymer materials, fuel-cell and electrolyzer components, and elastomers for sealing applications.

Marcin Rybicki is a computational chemist and physicist with more than 14 years of academic experience in atomistic simulations of liquid phases, heterogeneous catalysis, and the magnetic properties of ultrathin metallic layers. He has extensive expertise in developing advanced simulation methodologies. After his academic career, he transitioned to industry, where he supports research and development through multiscale simulation approaches, focusing on electrocatalysts and polymer materials for fuel-cell and electrolyzer applications, as well as elastomers for sealing solutions.

Miljan Dašić is a computational physicist specializing in molecular modeling and multiscale simulations of complex systems across diverse fields, including nanotribology, computer-aided drug design, and computational biophysics. He has contributed to international collaborations in materials science with partners in Belgium, France, the Czech Republic, and Israel. He is actively involved in joint academic—industrial research initiatives to develop predictive computational workflows for next-generation materials.

Igor Stanković has worked in academia for 16 years, after a brief period in the industry. His research focuses on the behavior of confined water in polar and nanoconfined systems, computational tribology of 2D materials, and multiphysics modeling of functional materials. He contributed to international collaborations and interdisciplinary projects in materials science and nanotechnology, mainly as the principal investigator for Serbian partners in European Union-funded consortia, including BLESSED and ULTIMATE-I, and as a member of the Managing Committee of COST Action MecaNano.

Supplementary information: Linking density and nanoscale crystallinity to hydration in Nafion PEMFC membranes: insights from experiment and molecular dynamics simulations

Mateja Jovanović Nicolas Bernhard Matthias Baldofski Marcin Rybicki Miljan Dašić Igor Stanković

Mateja Jovanović
Freudenberg Technology Innovation SE&Co. KG, Hoehnerweg 2-4, 69469 Weinheim, Germany
Institute of Technical Sciences of the Serbian Academy of Sciences and Arts (SASA), K. Mihailova 35/IV, Belgrade, Serbia
Institute of Physics Belgrade, University of Belgrade, Pregrevica 118, 11080 Zemun, Serbia
Email Address: Mateja.Jovanovic@ipb.ac.rs

Dr. Nicolas Bernhard, Matthias Baldofski, Dr. Marcin Rybicki
Freudenberg Technology Innovation SE&Co. KG, Hoehnerweg 2-4, 69469 Weinheim, Germany
Email Address:Matthias.Baldofski@freudenberg.com

Dr. Miljan Dašić, Dr. Igor Stanković
Institute of Physics Belgrade, University of Belgrade, Pregrevica 118, 11080 Zemun, Serbia
Email Address: Igor.Stankovic@ipb.ac.rs

Keywords: *fuel cell, proton exchange membrane, crystallinity, water content, molecular dynamics*

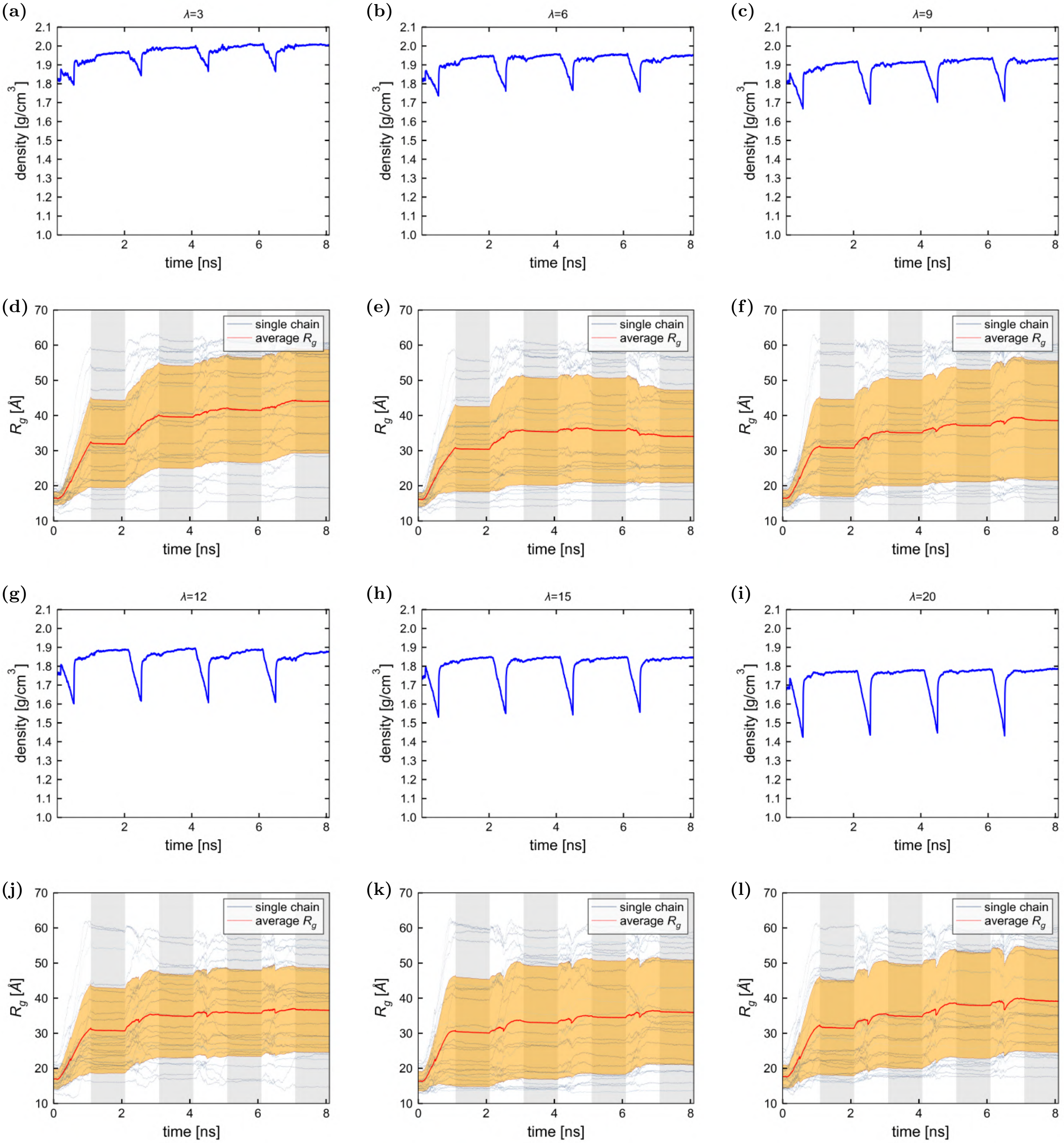

Figure S1: Time evolution of density (a–c, g–i) and radius of gyration R_g (d–f, j–l) of crystalline Nafion configurations at different hydration levels λ. Blue curves show density fluctuations; grey lines correspond to R_g of individual chains, red lines the ensemble average R_g, and orange shaded regions the statistical spread. Each panel shows simulated annealing and relaxation. The first two rows correspond to $\lambda = 3, 6, 9$, while the bottom two rows correspond to $\lambda = 12, 15, 20$. In both cases, the hydration is increasing from left to right.

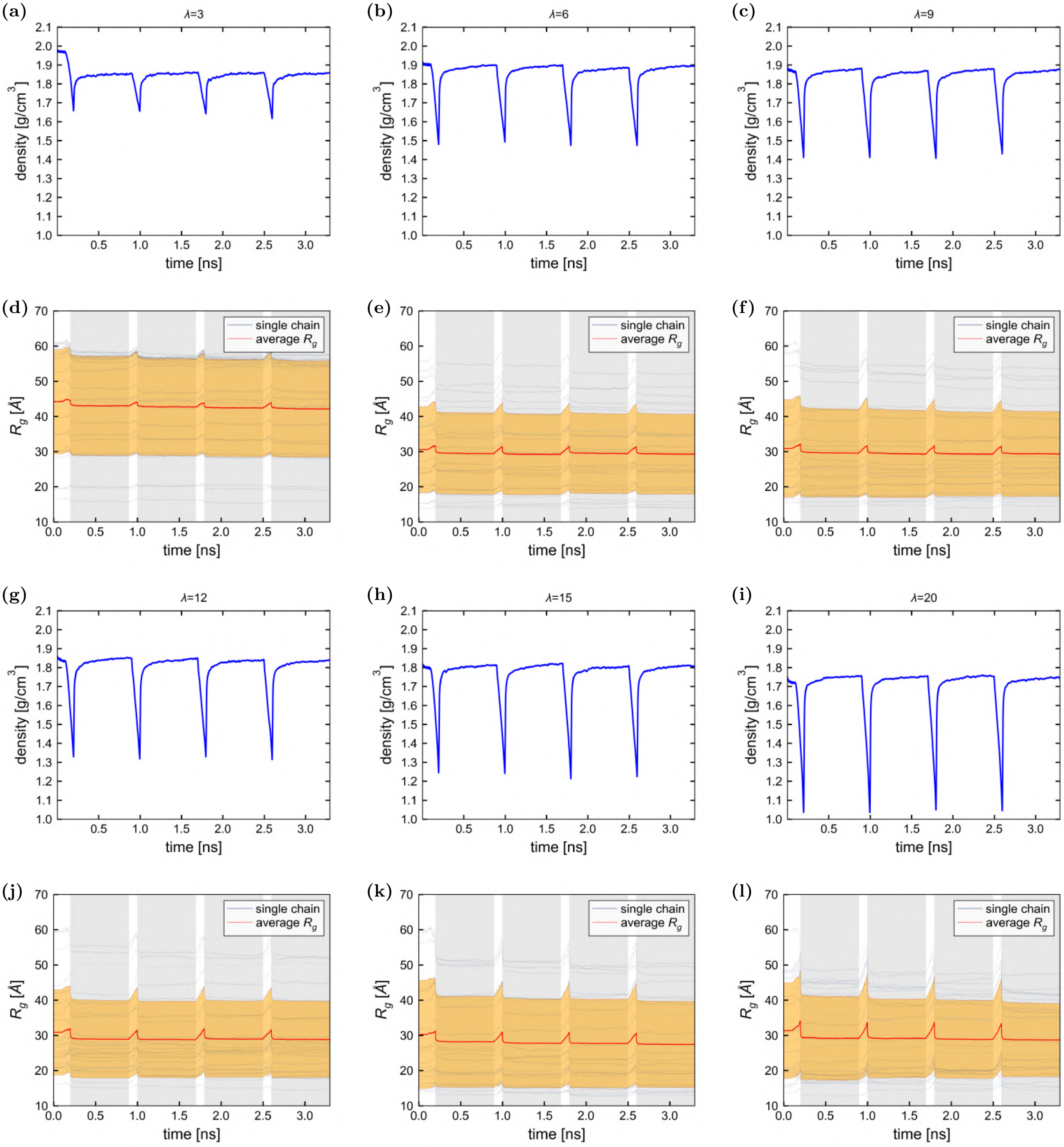

Figure S2: Time evolution of density (a–c, g–i) and radius of gyration R_g (d–f, j–l) of semi-crystalline Nafion configurations (i.e., starting from crystalline configuration and then annealed without shear deformation) at different hydration levels λ. Blue curves show density fluctuations; grey lines correspond to R_g of individual chains, red lines the ensemble average R_g, and orange shaded regions the statistical spread. Each panel shows simulated annealing and relaxation. The first two rows correspond to $\lambda = 3, 6, 9$, while the bottom two rows correspond to $\lambda = 12, 15, 20$. In both cases, the hydration is increasing from left to right.

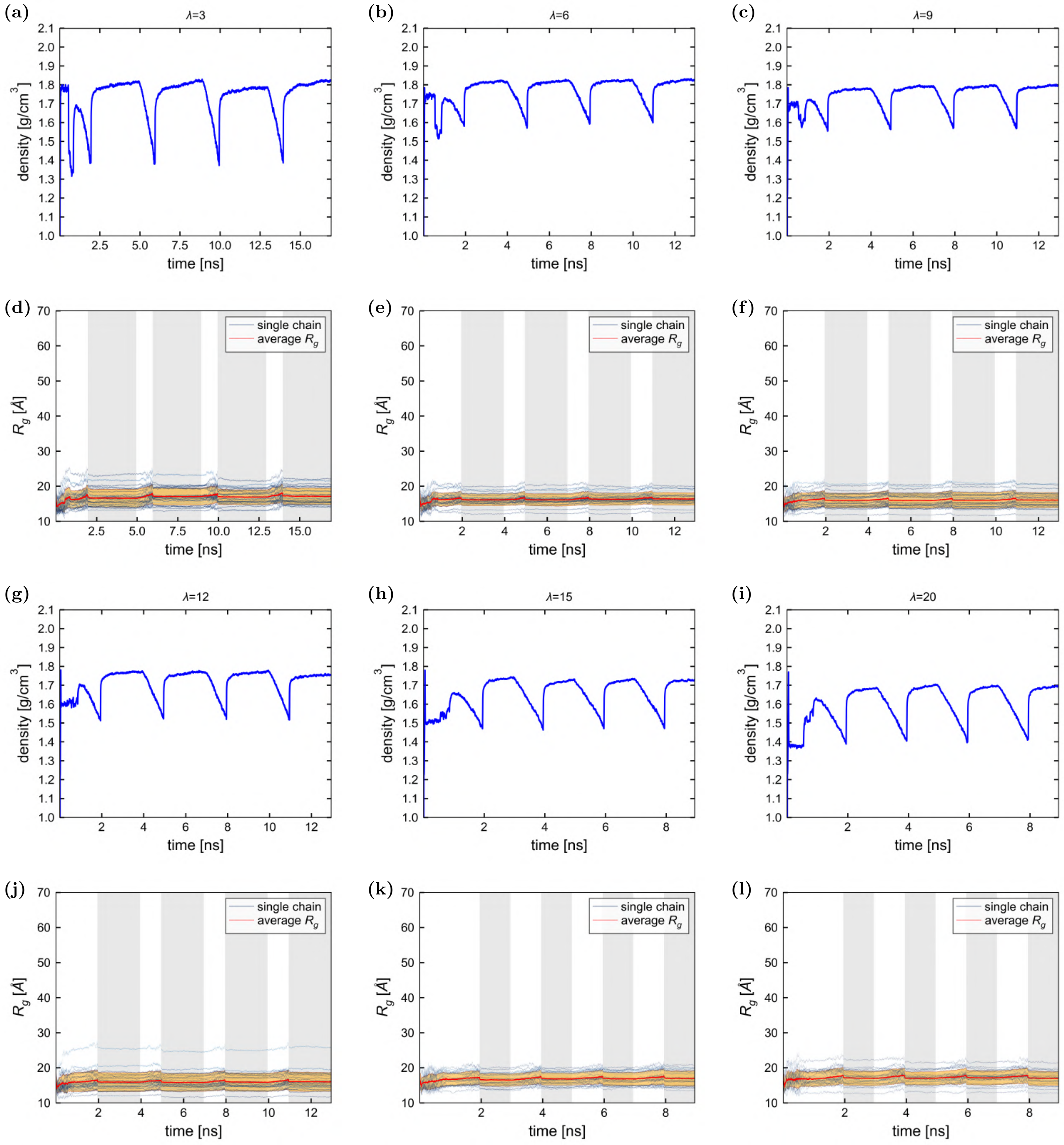

Figure S3: Time evolution of density (a–c, g–i) and radius of gyration R_g (d–f, j–l) of amorphous Nafion configurations at different hydration levels λ. Blue curves show density fluctuations; grey lines correspond to R_g of individual chains, red lines the ensemble average R_g, and orange shaded regions the statistical spread. Each panel shows simulated annealing and relaxation. The first two rows correspond to $\lambda = 3, 6, 9$, while the bottom two rows correspond to $\lambda = 12, 15, 20$. In both cases, the hydration is increasing from left to right.

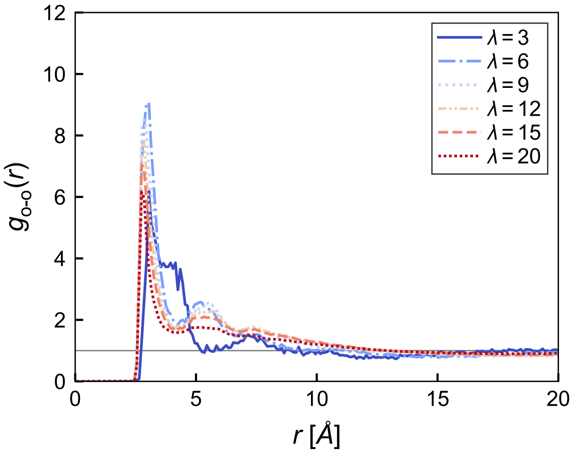

Figure S4: Oxygen-oxygen radial distribution function $g_{\text{O-O}}(r)$ of water molecules at varying hydration levels (λ) in semi-crystalline configuration

ACS APPLIED MATERIALS & INTERFACES

www.acsami.org Research Article

Role of Trapped Molecules at Sliding Contacts in Lattice-Resolved Friction

Miljan Dašić,* Roy Almog, Liron Agmon, Stav Yehezkel, Tal Halfin, Jürgen Jopp, Assaf Ya'akobovitz, Ronen Berkovich,* and Igor Stanković*

Cite This: *ACS Appl. Mater. Interfaces* 2024, 16, 44249−44260 Read Online

ABSTRACT: Understanding atomic friction within a liquid environment is crucial for engineering friction mechanisms and characterizing surfaces. It has been suggested that the lattice resolution of friction force microscope in liquid environments stems from a dry contact state, with all liquid molecules expelled from the area of closest approach between the tip and substrate. Here, we revisit this assertion by performing in-depth friction force microscopy experiments and molecular dynamics simulations of the influence of surrounding water molecules on the dynamic behavior of the nanotribological contact between an amorphous SiO_2 probe and a monolayer MoS_2 substrate. An analysis of simulation and experimental stick−slip patterns demonstrates the entrapment of water molecules at the contact interface. These trapped water molecules behave as an integral component of the probe and participate in its interaction with the substrate, affecting the dynamics of the probe and preventing long slips. Significantly, surrounding water from the capillary or layer exhibits a replenishing effect, acting as a water reservoir during sliding. This phenomenon facilitates the preservation of lattice-scale resolution across a range of applied normal loads.

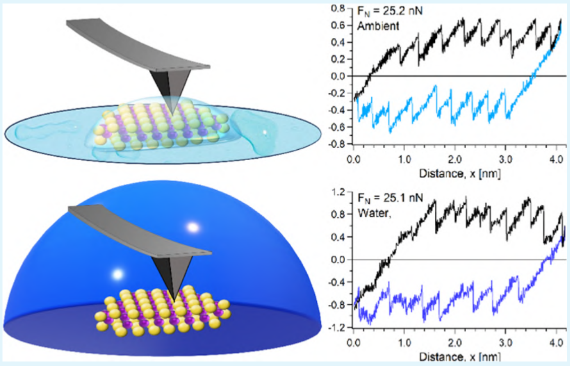

KEYWORDS: *molybdenum disulfide, water, friction, stick−slip, friction force microscopy, molecular dynamics*

■ INTRODUCTION

Water can effectively perform as a lubricant under certain conditions, yet it is not a suitable lubricant in many technological applications, since it is easily expelled from the contacts.[1,2] Such scenarios can be encountered during the synthesis of ionic liquid lubricants, where water migrates toward surfaces,[3−6] also in case of solid lubricants,[7] or in case of humidity condensation.[8,9] Although the accepted notion states that a direct solid−solid contact stays dry under an applied load, the presence of single molecules trapped between sliding surfaces has been suggested.[10−13]

Atomic force microscopy (AFM) can measure frictional dynamics at the nanoscale in different environments, such as in air,[14] liquids,[15] and ultrahigh vacuum (UHV).[16] In a typical friction force microscopy (FFM) experiment, a sharp AFM tip is elastically driven across a solid surface, while capturing its interaction with single asperities across atomical corrugation in the nanometer range.[17] Throughout this process, dissipation mechanisms at lattice resolution can be accessed by recording friction forces at the interface over time, while creating lateral friction loops and maps. Measuring at the lattice resolution, the friction signal manifests binding and unbinding across atoms at the contacting surfaces, with a stick−slip pattern.[18,19]

Experimentally achieving high subnanometer resolution under UHV is highly demanding, while measuring in ambient conditions can involve the possible presence of contaminants and the formation of water bridges (i.e., capillary condensation) between the tip and the surface.[2,19−21] The latter was shown to be eliminated in case the measurement is performed in liquid surroundings[17,22,23] when the probe tip and the sample are completely immersed in liquid.

FFM measurements and molecular dynamics (MD) simulations of a silicon AFM probe scanning across a graphene surface revealed that a high-resolution signal obtained in the liquid environment is comparable to the signal obtained in UHV, albeit with noisier results due to the thermal collisions of water molecules with the AFM tip.[17] The MD simulations showed that this equivalency resulted from the removal of all water molecules from the tip−sample gap, as the tip engaged in full contact (while breaking hydration layers) with the sample,

Received: May 19, 2024
Revised: July 22, 2024
Accepted: July 24, 2024
Published: August 6, 2024

https://doi.org/10.1021/acsami.4c08226

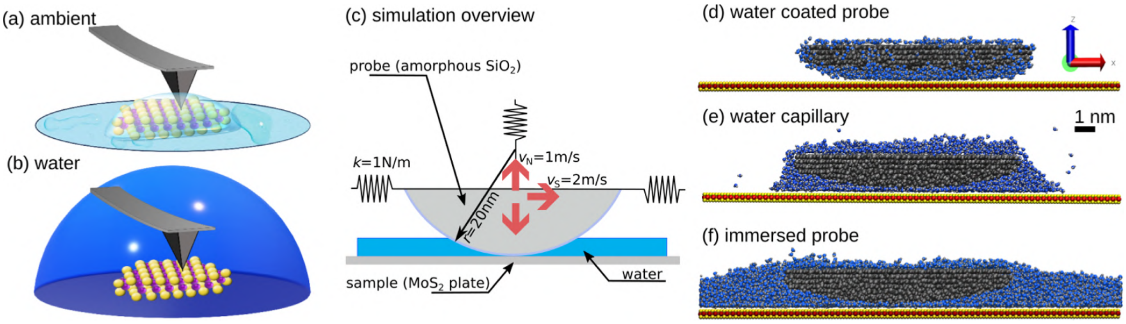

Figure 1. Schematic illustration of the experimental FFM setup in (a) ambient conditions (air, room temperature). At RH ≈ 35−40%, a thin (molecular) layer of water condenses on the surface. (b) Water (double distilled) layer completely immersing the sample and the cantilever. (c) Schematic representation of the implemented simulation setup, which is designed following the experimental FFM setup shown in panels (a, b) of this figure. The values of the parameters defining the simulation setup are velocities v_N = 1 m/s and v_S = 2 m/s that are related to the force−distance and sliding simulations, respectively; spring stiffness coefficient k = 1 N/m is the same for the elastic springs attached to the probe in all three Cartesian directions (i.e., in x−, y−, and z− directions); radius r = 20 nm defines the curvature of the probe. Illustration of different water setups: (d) configuration snapshot in case of a water coated probe, (e) probe surrounded by a water capillary, and (f) probe immersed in a continuous layer of water.

thus forming a completely dry contact. Nevertheless, recent FFM studies on NaCl crystal in ethanol surroundings suggested that under the assumption that no solvent molecules interfere at the contact, the liquid environment creates different thermodynamic conditions from those in UHV.[24] In the liquid environment, the solvent serves as a heat reservoir, maintaining isothermal conditions. Consequently, there was an increase in lateral stiffness,[23,24] which remained hardly unchanged in UHV,[25] but exhibited longer slip-length dynamics[26] that were not observed in the liquid surrounding.[24] It was also shown that the presence of adsorbed molecules could contribute to enhanced energy dissipation mechanisms during kinetic friction.[13]

In order to deepen our understanding of these differences, we explore here the influence of water-moderated friction on the sliding contact between molybdenum disulfide (MoS$_2$) monolayer and silicon/silica (Si/SiO$_2$) tip in two cases: in ambient conditions, i.e., in air with ≈35−40% relative humidity (RH), and with the tip being fully immersed in double distilled water. The FFM measurements were complemented by MD simulations that provided additional information and deepened our understanding of the underlying mechanisms, cf. Figure 1.

MoS$_2$ belongs to a chemical family of transition metal dichalcogenides (TMDs).[27] It is known for its remarkable mechanical properties (such as the high stiffness and extremely low friction coefficients), and it is widely explored in nanotribological studies.[23,27−30] Additionally, the quality of MoS$_2$ as a solid lubricant strongly depends on the level of air humidity from a purely tribological perspective, where a humid environment leads to an increased friction coefficient.[28] To elucidate the influence of water on the nanoscale tribological properties of monolayer MoS$_2$, we performed a synergistic investigation that combines FFM experiments with MD simulations. Such a comprehensive approach, encompassing both water capillary environments and full immersion scenarios of the AFM probe, yielded invaluable insights into the interplay between water and nanotribological behavior of MoS$_2$. First and foremost, we investigate whether a setup with a thin water layer formed due to condensation or a probe fully immersed in water influences the lateral interaction between the Si/SiO$_2$ probe and the monolayer MoS$_2$. We investigate the presence of water molecules and their impact on the lateral interaction between the Si/SiO$_2$ probe and the monolayer MoS$_2$. A scenario is outlined in which the trapped water molecules become an integral parameter in the overall tribological interaction. Different friction coefficients and local stiffness, as well as different slip-length dynamics, manifest such an impact. Overall, the combined experimental and simulation approaches offer a comprehensive understanding of the intricate dynamics governing the slip events, thus providing valuable insights into the tribo-system's behavior under varying operating conditions.

METHODS

Experimental Methods. The FFM measurements were performed in ambient conditions (i.e., air; room temperature; RH ≈ 35−40%), and in water (double distilled), where the cantilever and surface were fully immersed, as illustrated in Figure 1(a,b), respectively. In the presence of vapor (in this study, the water moisture), local pressure and temperature can induce condensation.[31] The experiments were performed with an Asylum Research Cypher-ES AFM (Oxford Instruments) in the contact mode using silicon probes (SNL-D, Bruker), with a normal spring constant of $k_N \approx 0.065$ N/m and a lateral sensitivity of α = 96.7 nN/V. The lateral sensitivity was measured with the wedge calibration method.[32,33] Fresh new cantilevers were used for the measurements. After being mounted and sealed within the AFM measuring chamber, extensive scans over tens of micrometers were conducted to identify the desired measurement regions within the MoS$_2$ flakes precisely. During this process, the surfaces of the tips were gently cleaned mechanically. Although the tip is made of silicon, when exposed to ambient air, it gets oxidized and covered with a thin (1−2 nm) layer of amorphous SiO$_2$. Accordingly, we refer to the tip as Si/SiO$_2$, and in the MD simulations, the tip's surface is modeled as amorphous SiO$_2$. For further details regarding the synthesis and characterization of the MoS$_2$ monolayers (on a silicon wafer), cf. ref 23. Figure 2 presents two micrographs of MoS$_2$ flakes. Before every experiment, the MoS$_2$ monolayer was rinsed with acetone and ethanol.

The measurements were performed by scanning back and forth across the distance of 5 nm at 90° scan angle (perpendicular to the axis of the cantilever), collecting friction loops at a constant scanning rate of 2 Hz. To account for the effect of crystallographic orientation on the MoS$_2$-tip interaction,[30,34,35] the FFM measurements were conducted across a statistically significant sampling of MoS$_2$ flakes and orientations, thereby averaging out inherent local variations in frictional behavior.[23] During the measurements, external normal loads of F_N = {4.2, 8.4, 12.6, 16.8, 21.0, 25.2, 29.5} nN were applied (with the corresponding number of slip events at each load of n = {501, 996, 518, 269, 456, 1640, 529}) in the ambient conditions (air);

Figure 2. Optical images of MoS_2 flakes.

while normal loads of $F_N = \{3.1, 6.3, 9.4, 12.6, 15.7, 22.0, 25.2\}$ nN were applied (with the corresponding number of slip events at each load of $n = \{423, 225, 239, 820, 498, 731, 843\}$) in water surroundings. Some of the friction traces exhibit strengthening of the friction signal with the sliding distance (sometimes referred to as "tilted loops"),[36] which is associated with puckering,[37] and other underlying interfacial mechanisms.[38−40] Accordingly, the friction forces were analyzed using the same approach reported in the literature, where tilted friction loops were observed, where the friction signal was taken as half of the difference between the slip forces in the forward and the backward scans.[39,41−44] Local stiffnesses were obtained by taking the slopes in the stick phase in the friction traces, and slip lengths were calculated using Hooke's law.[24,26,45] All these parameters were assembled into distributions, from which their median and interquartile ranges were calculated to provide their characteristic values. IGOR Pro 6.3.7.2 (WaveMetrics) and MATLAB (R2021b) software were used to process and analyze the force spectroscopy data.

Interaction Model. A classical molecular dynamics method enabled the consistency with experimental investigation and the capture of relevant interatomic interactions. As a result, we could properly model the system's length and time scales. We employed an atomistic model to describe the interactions of all atoms in the system. Intramolecular interactions between the water molecule are modeled with the SPC potential,[46,47] with LJ parameters $\sigma_O = 3.166$ Å, $\epsilon_O = 0.155$ kcal/mol, $r_{OH} = 1$ Å, H−O−H angle 109.47°, oxygen charge −0.8476e and hydrogen charge 0.4238e. Interactions between the water and the solids are modeled as nonbonded and described via the Lennard-Jones (LJ) and Coulombic potentials. In the case of the molybdenum atom in MoS_2, LJ parameters were taken at $\sigma = 4.43$ Å, $\epsilon = 0.116$ kcal/mol, and charge 0.5*e*, while for sulfur, $\sigma = 3.34$ Å, $\epsilon = 0.4983$ kcal/mol, and charge −0.25*e*.[48] In the case of the oxygen atom in SiO_2, LJ parameters were taken at $\sigma = 3.826$ Å, $\epsilon = 0.15$ kcal/mol, and charge −0.45e, while for silicon, $\sigma = 3.112$ Å, $\epsilon = 0.3$ kcal/mol, and charge 0.9e.[49] We distinguish the oxygen atoms in the SiO_2 probe from the ones in the water molecules since they have slightly different LJ parameters (ϵ, σ). Within the implemented description of the system, each of the atomic types is defined by its LJ parameters and its charge. The LJ parameters defining the pair interaction of two atoms belonging to the same type (labeled as α) are ($\epsilon_{\alpha\alpha}$, $\sigma_{\alpha\alpha}$), while all the atoms belonging to the same type have the same charge q_α. Cross-interaction parameters between different atomic types are calculated using the Lorentz−Berthelot mixing rules,[50,51] i.e., $\epsilon_{\alpha\beta} = \sqrt{\epsilon_{\alpha\alpha}\epsilon_{\beta\beta}}$, $\sigma_{\alpha\beta} = \frac{\sigma_{\alpha\alpha} + \sigma_{\beta\beta}}{2}$.

Water is in the liquid state, meaning that the H_2O molecules are not ordered in any regular structure. The studied temperature of $T = 350$ K in sliding simulations belongs to the temperature range corresponding with the liquid state of water. The relative positions of atoms in the substrate and the probe are fixed. The curvature of the probe is defined by its radius of 20 nm, the in-plane size of the substrate is 24 × 24 nm^2, and the periodic boundary conditions (PBC) are applied in the substrate plane (i.e., in the *xy* plane of the Cartesian coordinate system).

All MD simulations have been performed using the LAMMPS software package,[52] with time steps of 2 fs and a Nose-Hoover thermostat set to the chosen temperature. We used the particle−particle particle-mesh (PPPM) solver[53] for handling the long-range electrostatic interactions with the accuracy (i.e., the desired relative error in forces) of 10^{-5}, and LJ interactions had a cutoff distance of 12 Å.

Simulation Setup. A schematic representation of the developed MD simulation setup is shown in Figure 1(c). An amorphous SiO_2 probe with a curvature radius of $r = 20$ nm is placed above the sample (within the framework of this study, that is a monolayer crystalline MoS_2 plane). The amorphous SiO_2 probe was obtained via a melt-quench technique: by heating the α-quartz at $T = 1000$ K, and then quenching it at $T = 300$ K. The probe was spherically shaped by cutting it correspondingly. We designed a water coating by placing $N = 1200$ water molecules under the probe on the planar substrate, see Figure 1(d), thus obtaining a water coated probe. When the number of water molecules is higher ($N = 6415$), the probe is surrounded by a water capillary, see Figure 1(e). The layer of water in which the probe

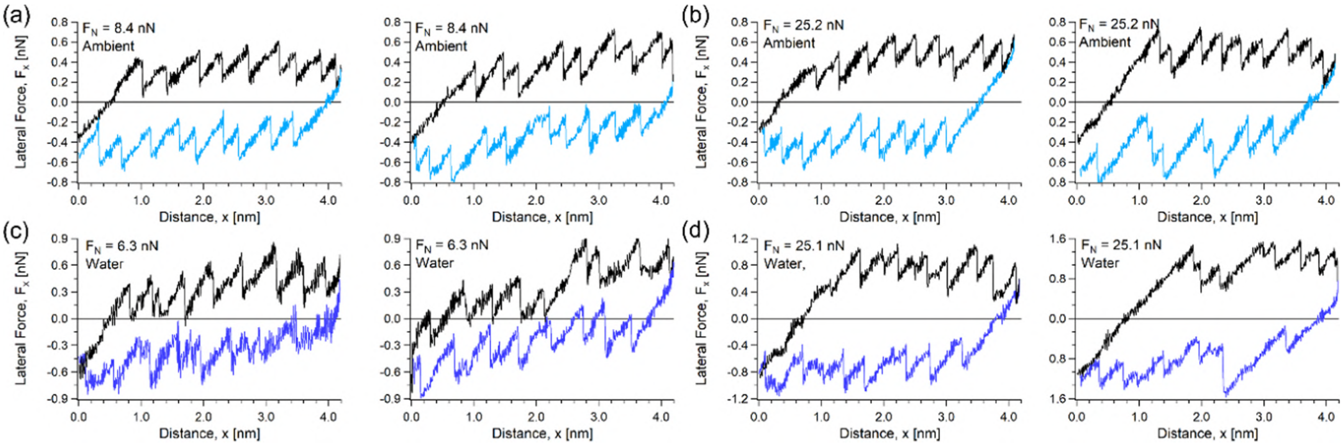

Figure 3. Representative Si/SiO_2−MoS_2 experimental friction loops displaying the stick−slip pattern measured in air (black-light blue) under a load of 8.4 nN (a), and 25.2 nN (b), and in water (black-blue) under a load of 6.3 nN (c), and 25.1 nN (d).

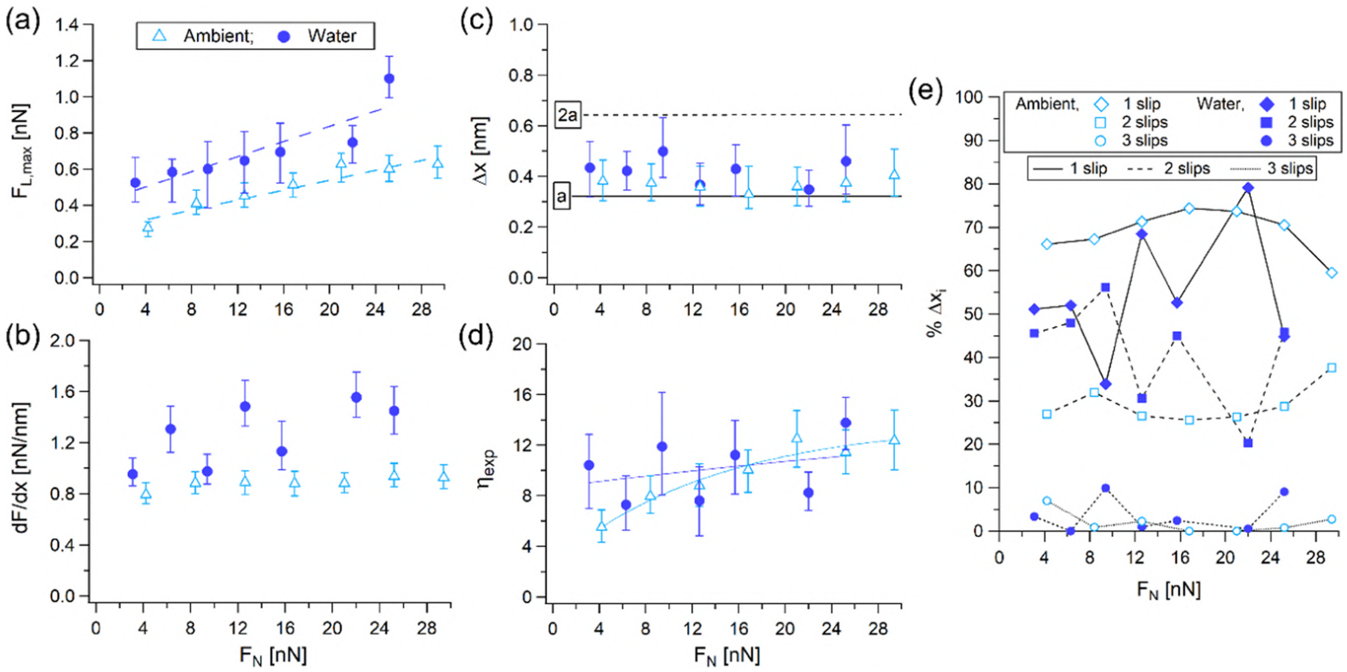

Figure 4. Frictional behavior of Si/SiO_2−MoS_2 with the normal load measured in ambient conditions (empty light blue triangles) and in water (blue circles). (a) Lateral slip forces with linear fits (dashed lines). (b) Local shear stiffness. (c) Slip lengths. The continuous and the dashed lines correspond to the values of the single and double lattice constants. (d) PT parameter η_{exp}, with lines drawn to guide the eye. (e) Percentage of the slip length populations denoted by continuous (single slip events), dashed (double slip events), and dotted (triple slip events) lines.

is fully immersed, see Figure 1(f), consists of N = 24,000 water molecules. The fully immersed probe and capillary scenarios help us understand the effects of significant water presence, while the third scenario examines the impact of a minimal amount of water. These setups allow us to investigate the role of water quantity and distribution on the structure−property relationships in the studied nanotribological system. The probe is connected to the support via harmonic elastic springs in all three orthogonal directions (i.e., in x-, y-, and z- directions), to measure the lateral and normal forces similar to the FFM experiment. The support is pulled at a constant velocity in a direction parallel (x) or orthogonal (z) to the substrate (the xy plane). The probe has a spring stiffness of k = 1 N/m in all three orthogonal directions.

We performed MD sliding simulations at the temperature of T = 350 K since experimental measurements are usually performed at much lower velocities than those achievable in MD simulations. In part, we tried to compensate for high velocity in MD simulations by increasing the mobility of water molecules. The elevated temperatures result in the water molecules having a higher probability of leaving the moving contact, compared to the room temperature of T = 300 K. We moved the probe: (i) orthogonal to the MoS_2 sample with a velocity of v_N = 1 m/s (i.e., along the z- direction), and (ii) parallel to the MoS_2 sample with a lateral sliding velocity of v_S = 2 m/s; the directions and values of the two imposed velocities are indicated in Figure 1(c).

■ RESULTS

Effect of the Normal Load on the Stick−Slip Friction in FFM Experiments. Figure 3 shows several FFM friction loops measured at low and high loads under ambient conditions (black and light-blue, Figure 3(a,b)), and when fully immersed in water (black and blue, Figure 3(c,d)). Friction loops show the stick−slip friction pattern, in which more than single slip events can be observed. We characterized the frictional behavior of the two systems in terms of the medians and interquartile ranges (IQR) of the slip forces, $F_{L,max}$, and local stiffness, given by their slopes, dF_x/dx, under each applied normal load. Figure 4(a) plots $F_{L,max}$ with the change of normal load F_N, fitted with a linear form of Amontons' law: $F_{L,max} = F_{L,0} + \mu F_N$, where $F_{L,0}$ defines the frictional force at zero normal force (which is associated with adhesion), and μ represents the friction coefficient. From the fitting of the experimental data, see the dashed lines in Figure 4(a), the following values were obtained: $F_{L,0}^{ambient} = 0.26 \pm 0.04$ nN, and $\mu_{ambient} = 0.014 \pm 0.002$ for the lateral interaction in ambient conditions, and $F_{L,0}^{water} = 0.42 \pm 0.08$ nN, and $\mu_{water} = 0.021 \pm 0.005$ in water. When we compare the measurements in ambient conditions and in water, it is interesting to observe that both the friction force at zero normal force ($F_{L,0}$), and friction coefficient (μ) differ. Based on this behavior, the friction interaction in water appears to be somewhat stronger, yet the last force point at 25.2 nN numerically affects the fitted values. Excluding this point results with $F_{L,0}^{water} = 0.50 \pm 0.01$ nN, and $\mu_{water} = 0.012 \pm 0.001$, which is very close in value to the fitted friction coefficient at ambient conditions. This indicates that the local lubrication conditions at the contact may not be so different in both cases, where several water molecules may be trapped in the sliding contact.

Figure 4(b) illustrates that the local shear stiffness under ambient conditions is narrowly distributed around approximately 0.9 nN/nm, with no clear trend. However, in water it increases with the normal load, from 0.95 to 1.45 nN/nm, exhibiting significant fluctuations. It is interesting to compare the observed behavior in water to a similar system measured in ethanol surroundings. Similar FFM experiments on monolayer MoS_2 with the same brand of the cantilever in ethanol surroundings reported values close to those measured in water (i.e., $F_{L,0}^{ethanol}$ = 0.503 nN, $\mu_{ethanol}$ = 0.019).[23] The consistent behavior observed in analogous sliding contacts under different environments indicates not only the explicit influence of water molecules trapped at the contact but also the role of the external environment surrounding the contact area.[24]

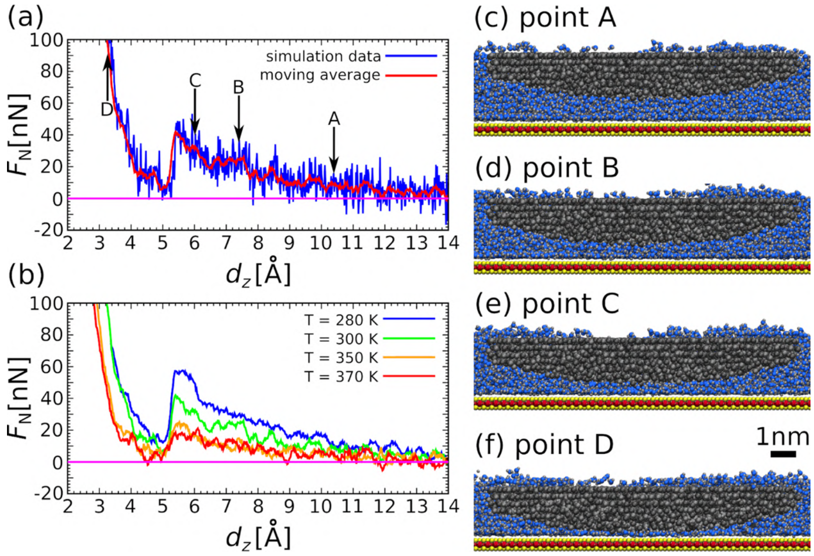

Figure 5. Force−distance $F_N(d_z)$ characteristic simulated at the temperature of $T = 300$ K. (a) The blue line corresponds to the raw MD simulation data, while the red line represents the moving average (0.1 Å window). (b) The force−distance characteristic at $T = 280$, 300, 350, and 370 K. The cross sections through the middle of the probe at the characteristic points (c−f) correspond to the respective points in panel (a).

To extract more information on the effect of the different environments, we calculated the slip length, labeled as Δx, which is defined as the distance between slip events. The median slip lengths at each applied load, for both air and water, are shown in Figure 4(c). It can be observed that the measured slip lengths are slightly larger than a single lattice constant ($a_{\mathrm{MoS_2}} = 3.212$ Å[54]), but smaller than two lattice constants. The IQRs that characterize the shape of the slip length distributions in Figure 4(c) indicate that several slip length populations are involved. These deviations from the exact value of the lattice constant emerge from the way in which the slip length is calculated, i.e., by dividing the force drop at the slip event by the local stiffness.[24,26,45] Hence, experimental errors in the evaluations of these parameters (related to instrumental effects and anisotropy-associated averaging) lead to these small differences between the calculated and the actual slip lengths.

Multiple slip length dynamics can be described with the Prandtl-Tomlinson (PT) parameter and the dissipative state of the system.[24,26,45,55,56] The PT parameter[57,58] is a dimensionless number, defined within the PT model.[59] It describes the tip−sample sliding interaction through the ratio between the amplitude of the tip−sample interaction and the elastic energies, $\eta = (2\pi/a) \times 2U_0/K_{\mathrm{eff}}$, where a is the lattice periodicity (constant), U_0 is the corrugation interaction amplitude, and K_{eff} is the effective spring constant that represents the elastic interaction at the sliding contact. Since U_0 and K_{eff} are unknown, the PT can be redefined in terms of the experimental measurables,[25] i.e., in terms of $F_{\mathrm{L,max}}$ and $\mathrm{d}F_x/\mathrm{d}x$, as $\eta_{\mathrm{exp}} = (2\pi/a)(\mathrm{d}x/\mathrm{d}F_x)F_{\mathrm{L,max}} - 1$. The calculated η_{exp} at the different loads (Figure 4(d)), shows an increase from ≈4 to ≈12 in air, and large fluctuations between ≈7 and ≈13 with a slight increase trend, for water. Such large values mean that the corrugation interaction energy is larger than the elastic energy at the contacts, which is associated with the multiple slip dynamics.[24,26,45,55,56]

We distinguish between the slip lengths that distribute into single, double, and triple slip events, i.e., occurring over one, two, or three lattice constants, and the extent to which these jumps take place. Figure 4(e) plots the percentage of these slip events at every applied normal load. During low-load sliding, a higher occurrence of single-slip events is observed in ambient conditions than in the aqueous environment. This disparity diminishes for the applied loads exceeding 8 nN, due to the emergence of pronounced fluctuations within the measured slip lengths for water. While the dynamic in water is more erratic, in ambient conditions we can notice a larger number of single-slip events compared to the double-slip events, which are more frequent than the three-slips, cf. Figure 4(e). With an increase of the load, the fraction of the single-slip events increases from ≈67 to ≈74% and then reduces to ≈59%. Oppositely, the fraction of the double-slip events increases from ≈26 to ≈38%. The three-slip population demonstrates an intriguing behavior: it peaks at the lowest load, constituting the largest proportion of ≈7%, then it quickly decays to zero, and afterward, it slightly grows at high loads to ≈3%. The increase of the two- and three-slip events with the normal load is expected, due to the changes in the η parameter with the damping state of the system.[24,26,45,56] The relatively high percentage of the three-slip events at the applied normal load of 4 nN (at $\eta_{\mathrm{exp}} = 5.5$) in ambient conditions, can indicate the possible presence of trapped condensate water molecules in the contact, which are pushed out with the increase of the local pressure at higher loads.

MD Simulations: Force−Distance Characteristics. Typically, the inefficiency of water as a lubricant is attributed to its limited resistance to being squeezed out. Therefore, gaining insights into the normal forces that the water layer can sustain before becoming dislodged from the contact is crucial. Using MD simulations: the temperature, the probe-substrate distance and the resulting normal load are followed, together with the structure of the confined water layer. Figure 5(a) shows the force−distance evolution $F_N(d_z)$ at $T = 300$ K including the raw simulation data (solid blue line) and the moving average (solid red line). The values of F_N remain under 10 nN at high probe-sample distances, i.e., $d_z > 10$ Å. As the gap decreases, the normal force steadily increases at lower probe-sample distances, i.e., $d_z < 10$ Å. Point A in panel (a) of Figure 5 corresponds to the roughly three layers of water molecules (i.e., hydration layers) confined in the probe-sample gap. We measure the number of confined water layers based on the gap width versus the diameter of the water molecule. The distinctive steps are visible, cf. points B and C in Figure 5(a). At these steps, the final hydration layers exert resistance before being expelled from the gap by the probe. As a result, the normal force increases at these points as the number of layers decreases from three layers to two and further, from two layers to a single layer. This behavior is reminiscent of previously seen behavior in the studies on ionic liquids and alkanes.[60−63] The hydration layers are broken at somewhat low normal loads, which agrees with previous results obtained with frequency-modulation AFM.[64] Distance points in Figure 5(a) labeled as A, B, C, and D, correspond to the configuration snapshots provided in the panels (c−f) of Figure 5, respectively. We observe that the water molecules remain trapped in the space between the probe and the substrate after a single full layer gets squeezed out, cf. panel (f) of Figure 5. For $d_z < 5.0$ Å, the normal force F_N further increases with the reduction of the probe-substrate gap distance d_z. After the point of local minimum of the normal force F_N, i.e., at the distance $d_z \approx 5.0$ Å, cf. Figure 5(a), the normal force F_N steadily increases again, as the remaining trapped water molecules get squeezed out. The probe-substrate (i.e., SiO_2−MoS_2) direct contact is detectable from the final and steep increase of the normal force F_N, cf. point D in Figure 5(a).

In their MD simulation study, Vilhena et al.[17] reported that the normal force required to break the first hydration layer was 2 nN for $S_{contact} = 0.8$ nm^2 diamond tip on graphene at $T = 300$ K, i.e., $F_N/S_{contact} = 2.5$ GPa. In our current MD simulations, the estimated contact surface is larger (20 nm^2), and the maximal load is 40 nN. The resulting load-bearing capacity of the first hydration layer is $F_N/S_{contact} = 2$ GPa, which is in proximity to the result of Vilhena et al.[17]

The effect of temperature on the force−distance characteristic of the studied nanotribological system is shown in Figure 5(b). Force−distance curves were obtained at temperatures below the water's boiling point, i.e., $T = \{280, 300, 350, 370\}$ K. As the temperature increases, there is an apparent decrease in the normal force F_N. Also, we observe that the normal force minima becomes more profound, while simultaneously the point of the probe-sample minimal distance gets delayed with an increasing temperature, cf. Figure 5(b). We should note that according to our MD simulation setup, the probe and substrate atoms cannot change their relative positions. Simultaneously, the mobility of water molecules increases with the temperature. We observe that, at higher temperatures, fewer water molecules are trapped in the probe-sample contact area. Elevation of temperature results in kinetic energy increase of water molecules confined within the microscopic roughness of the amorphous SiO_2 surface, facilitating their escape from the roughness. The effect of temperature and the resulting mobility of water molecules is manifested in the cross-section of the system parallel to the MoS_2 plate at $d_z = 3.2$ Å in Figure 6. Configuration snapshots show an evident decrease in the number of water molecules (colored in blue) trapped inside the probe-sample gap, with the temperature increase. Simultaneously, with increasing temperature the diameter of the void space under the probe increases, and the density of trapped water molecules decreases. We observe in the temperature range $T = 280$ K to $T = 300$ K about 20 water molecules less in the gap, while in both ranges 300−350 and 350−370 K, there were roughly further 60 molecules less, for each increment of the temperature.

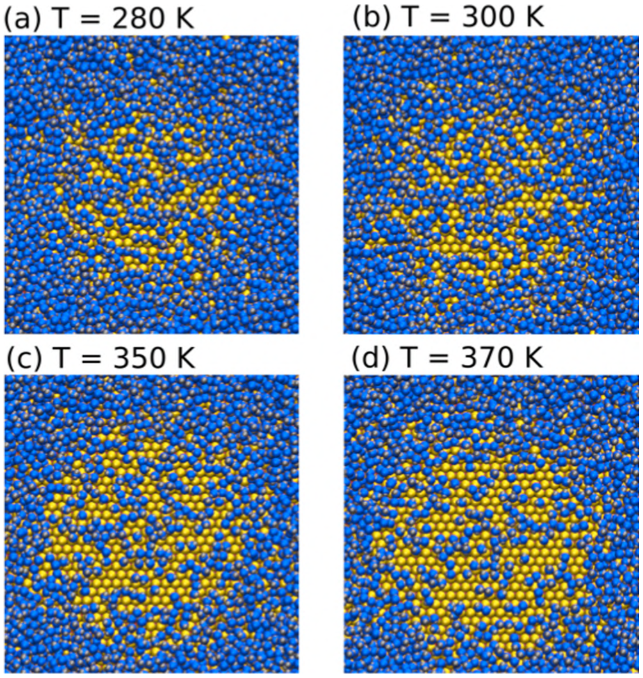

Figure 6. Cross sections of the probe-sample contact (a−d) show water molecules above MoS_2 plate at $T = 280$, 300, 350, and 370 K for $d_z = 3.2$ Å, respectively. The water molecules (blue oxygen) and substrate (yellow sulfur) are visible. The effect of temperature is visually noticeable as the area comprising MoS_2 surface atoms increases with temperature increase.

Simulated Dynamics of the AFM Probe. To examine the interactions between water, the amorphous probe, and the substrate, and to explore potential mechanisms leading to the lattice-resolved stick−slip friction, we conducted FFM MD simulations with explicit water. One could argue that the water molecules trapped under the AFM probe will leave once the sliding starts and that only the atoms of the two solids will remain in contact. We investigate this point in Figure 7(a) by following the evolution of the probe-substrate gap Δz_{gap} with the sliding distance Δx. The results are presented as the difference between the current and the initial positions. Accordingly, Figure 7 illustrates the extension of the spring in the sliding direction due to the lateral force, as well as the spring release in the direction of the substrate, during the sliding process. In our MD sliding simulations, the probe covered a distance of $\Delta x = 15$ nm, corresponding to roughly 46 MoS_2 hollow (i.e., Mo top) site distances. At the onset of sliding, the AFM probe rapidly descends toward the substrate, as water molecules get squeezed out, cf. $\Delta x < 3$ nm, cf. Figure 7(a). For the case of both the water coated and the capillary water systems, $x \approx 3$ nm corresponds to the length of the initial stick. After the initial descent, the probe's elevation does not change in immersed and capillary water systems. Further stepwise descends are visible for the water coated probe at $x \approx \{3, 6, 9\}$ nm. Such behavior could be attributed to the individual water molecules that are squeezed out or displaced within the probe-substrate gap during the shear. A contact point between the atoms of the probe and the substrate devoid of water molecules, i.e., in case of a "dry contact", would not exhibit a reduction of the probe-to-substrate distance during the sliding process since in all three systems probe is geometrically equivalent. Without water molecules trapped in the probe-substrate gap, all three systems would exhibit an

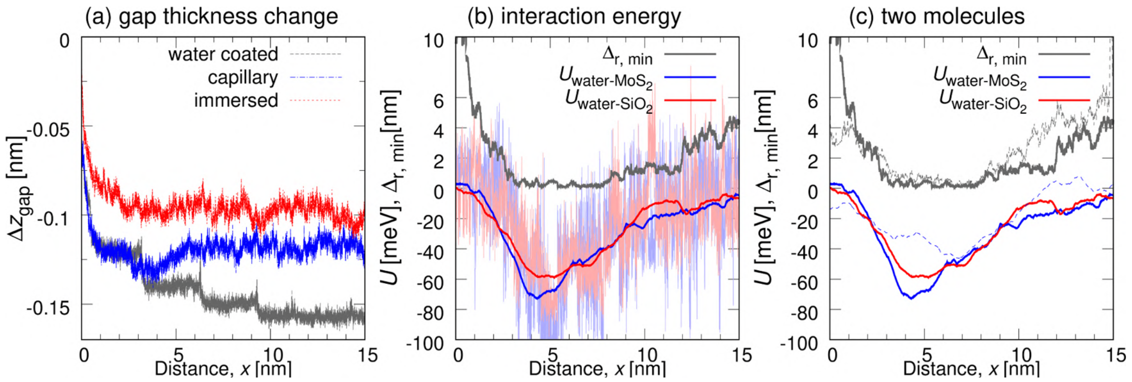

Figure 7. (a) Evolution of the Δz_{gap} gap thickness during a sliding simulation at an applied normal load of F_N = 17.3 nN in case of the three studied water setups along the x-axis. (b) The dependence of interaction energy (U) between a single water molecule and MoS_2 and SiO_2 surfaces and distance from energy minima $\Delta_{r,min}$ is given as the probe moves along the x-axis. The smoothed using moving average (bold lines) and raw numerical data (light lines) showing energy fluctuations are shown. (c) The evolution of dependence of interaction energy (U) is compared for two water molecules as the probe moves along the x-axis.

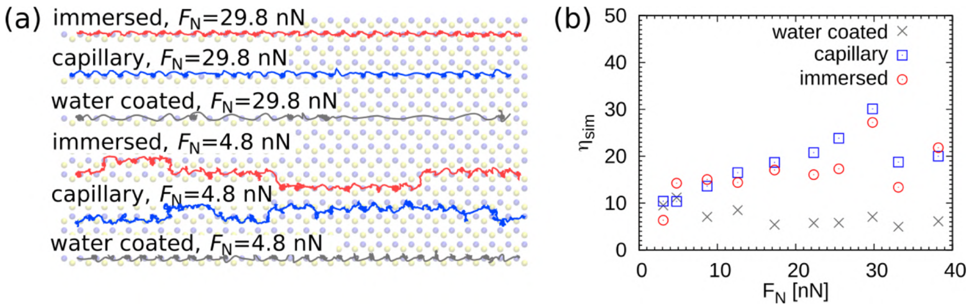

Figure 8. (a) Top views (xy- plane) of the trajectories of the center of mass of the water coated, surrounded by capillary water, and fully immersed probe's center of mass at applied loads of F_N = 4.8 nN and 29.8 nN. (b) PT model η_{sim} parameter determined in MD simulations.

identical probe-to-substrate distance. This indicates that the evolution of the center of mass $z-$ position in Figure 7(a) results from the water molecules' presence in the probe-substrate contact. In both scenarios, whether the probe is immersed in a layer of water or surrounded by capillary water, the probe-to-substrate distance stabilizes after an initial descent. The eventual penetration of water molecules inside the sliding contact and their removal are dynamically balanced out. Therefore, it can be deduced that, when aiming to obtain high-resolution images using a water-based atomic force microscopy technique, a specific minimal value of the normal pressure is crucial for breaking the first hydration layer. After that, water molecules are not completely removed, but they behave as an integral part of the probe. The normal pressure necessary to break the first hydration layer is temperature-dependent, decreasing from 2.5 GPa at T = 280 K down to 1 GPa at T = 370 K, cf. Figure 5(b). Still, Figure 7(a) shows that the lattice resolved stick−slip motion is obtained with the capillary water. In a scenario where the probe is coated with a few water molecules, the close approach to the substrate results in exceptionally long slips. Conversely, the continuous water layer in the case of the probe immersed in water, causes an excessive separation between the probe and the substrate, thereby introducing a dynamic interference of water molecules into the stick−slip motion of the probe. It is important to note that changes in probe elevation and the geometry of the contact with the substrate in the experiment could also arise from various processes, such as the mobility of surface defects on the amorphous SiO_2 surface or tribochemical reactions between SiO_2 and water.[65,66]

Figure 7(b,c) illustrates the evolution of interaction energies (U) between single water molecule and MoS_2 and SiO_2 surfaces with sliding distance. The interaction energy values were derived from MD simulation data in Figure 7(a). These energies represent the combined effects of Coulombic and van der Waals forces between a single water molecule and the substrate/probe. While van der Waals forces are typically quite small, around 0.05 eV, Coulomb attractive forces dominate the present system. In Figure 7(b,c), the distance from the minima of this energy is also given ($\Delta_{r,min}$), so we can follow how the water molecule enters into the gap and leaves it. These results reveal that the interaction energies between water−solid surfaces are higher than thermal energy (ca. 30 meV) or energy of surface defects on SiO_2.[65] The interaction energy with MoS_2 approaches 80 meV, consistent with results, cf. ref 67. The distance of minimum shows that molecules can reside for an extended (about 6 nm) sliding distance in the tribological contact at one point due to stronger interactions with SiO_2 without chemically reacting with the surface.[66] We can also see by comparing two molecules that can move within their position taking different configurations with different interaction energies.

At this point, we focus on the effect of the normal load on the probe-substrate interaction, in the presence of water molecules. To better understand this problem, the center of mass trajectory in the substrate plane (xy plane) projected onto the MoS_2 plate, is visualized in Figure 8(a). The stick locations are seen as clumps at the Mo top sites, connected by curved slip paths between the S atoms. We performed a fast Fourier transform (FFT) on the lateral force for the F_N = 4.8

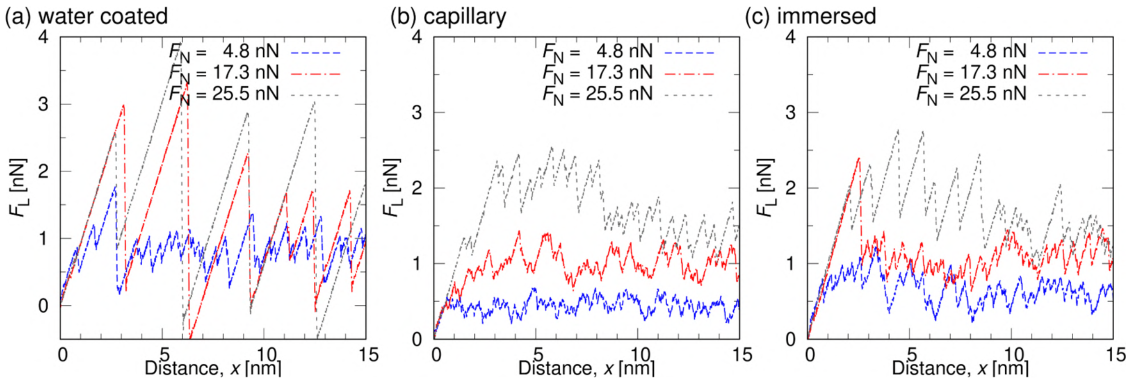

Figure 9. Representative lateral force traces, F_L acting on the probe which is sliding along the x-direction for (a) water coated probe, (b) surrounded by capillary water probe, and (c) fully immersed water probe. The lateral force traces are shown for the three normal forces F_N = 4.8, 17.3, and 25.5 nN. The sliding velocity was v_s = 2 m/s, while the spring stiffness was k = 1 N/m.

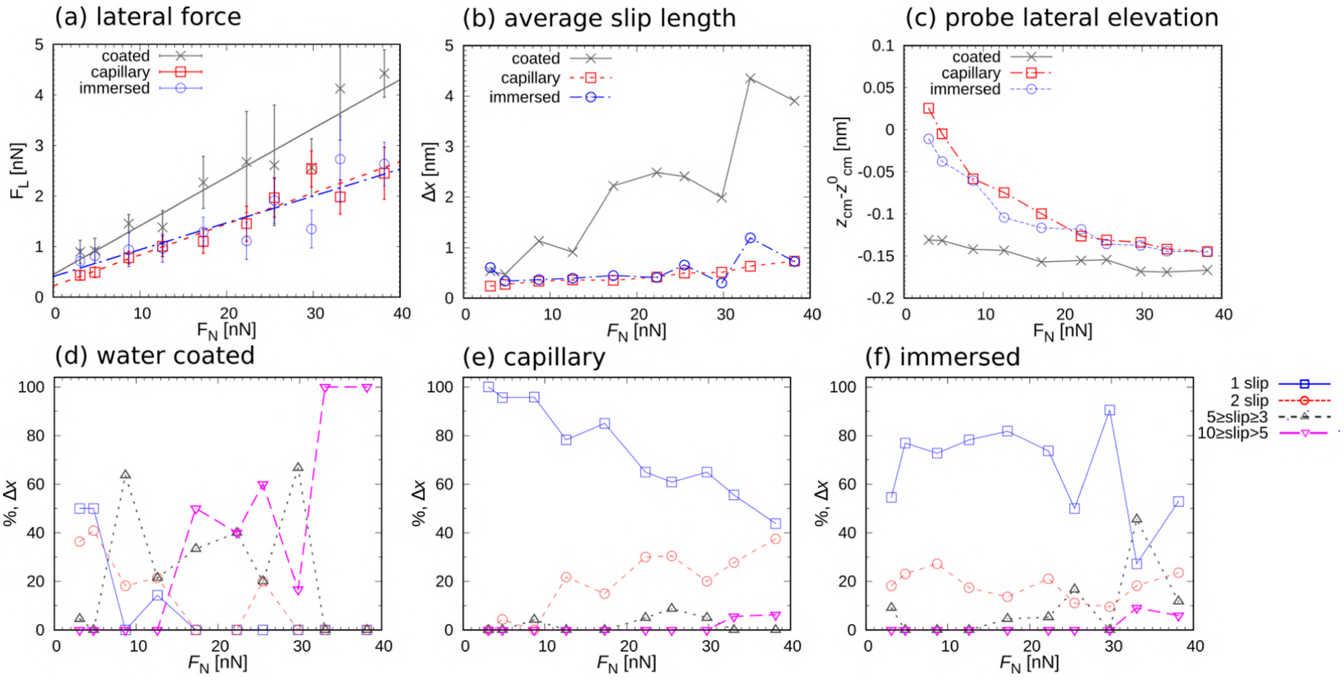

Figure 10. Simulated frictional behavior of SiO_2-MoS_2 tribosystem. Load dependence (F_N) in water coated (black), capillary (red), probe immersed in water (blue) of (a) average maximal lateral force (F_L), (b) average slip length Δx, and (c) probe's lateral elevation ($z_{cm} - z^0_{cm}$) after 15 nm of sliding. Percentage of the slip length populations of single slip events (denoted by blue continuous line), double slip events (red dashed), three to five lattice lengths (black dashed), and long jumps (cyan) are shown in panels (d) for water coated, (e) capillary, and (f) immersed probes, respectively.

nN normal load in all three systems, from which we resolved its underlying lattice periodicity which determines the single slip-length of ≈0.33 nm. Accordingly, the analysis of the dynamics and the distances between lateral force minima/maxima, indicates that the tip is immobilized at the hollow sites of MoS_2 monolayers (i.e., Mo top sites). Also from Figure 8(a), one can see that slip lengths correspond to the single or integer multiples of lattice from the in-plane position of the probe's center of mass projected onto the MoS_2 plate. The differences are striking when comparing normal loads of F_N = 4.8 and 29.8 nN, in both scenarios with abundant and scarce water. At low loads, the center of mass switches between different tracks, but at high loads the probe follows a single track when surrounded by a water capillary or immersed in water. This affects the lattice resolution and sometimes results in half-lattice-long constant slips. In the case of a water coated probe, we observe a single-track lattice resolved motion of the probe at a low load (F_N = 4.8 nN), while at a higher load (F_N = 29.8 nN), the slip paths are multiple lattice constants long.

Effect of the Normal Load on the Stick–Slip Friction in MD Simulations. Figure 9 presents the simulated lateral force traces of the system with (a) water coated probe, (b) probe surrounded by water capillary, and (c) probe immersed in a continuous layer of water. The traces are shown for the three normal forces of F_N = 4.8, 17.3, and 25.5 nN. We also calculated the PT parameter, like in the FFM experiment, to obtain insight into effective tip–sample sliding interaction, cf. Figure 8(b). The calculated η_{sim} at the different loads in Figure 8(b) shows an increase from ≈10 to ≈25 for capillary and layered water, and large fluctuations at F_N > 30 nN. Therefore, based on PT model observations, the corrugation interaction energy is greater than the elastic energy in these two systems.

The PT parameter η_{sim} also evolves with increasing load, which is observed for the experimental PT parameter η_{exp} in ambient conditions. In the case of a water coated probe, the PT parameter is $\eta_{sim} \approx 6$ and does not depend on the applied normal load. In the case of a water coated probe, a lattice-resolved stick−slip friction pattern is obtained only at $F_N < 5$ nN, cf. Figure 9(a). At higher normal loads, i.e., 17.3, and 25.5 nN, we observe the multiple slip events. For all three systems, the averages of the maximal lateral force during the stick phase, are plotted in Figure 10(a). We extracted the friction coefficient and the zero-force of the water coated probe: $\mu_{coated} = 0.1 \pm 0.01$ and $F_{L,0} = 0.45 \pm 0.2$ nN, respectively. In the cases of the probe surrounded by capillary water, and the water-immersed probe, the friction coefficient is smaller: $\mu_{water} = 0.06 \pm 0.001$. The corresponding zero-force is $F_{L,0} = 0.31 \pm 0.1$ nN for the probe moving through the water layer.

All slopes, during the stick phase when the lateral force increases linearly with the sample's displacement, are similar and they are independent of the normal load, cf. Figure 9. The lateral stiffness calculated from the slopes is roughly 1 nN/nm, and therefore it is determined by the spring's stiffness which keeps the probe in place in both water-probe configurations.

We focus now on two important factors for lattice resolved stick−slip: the role of water in the contact region, and the impact of interactions between the probe and the surrounding water molecules (either in the capillary or water layer). As we already saw, the modeled system exhibits a stick−slip friction behavior even at the smallest investigated normal loads $F_N < 5$ nN, cf. Figure 9. The evolution of the average slip length in different environments is compared for different normal loads in Figure 10(b). In all three investigated systems, we observe a steady increase in the slip length with increasing normal load F_N. At the normal forces $F_N > 30$ nN, we observe the average slip lengths larger than 0.66 nm for immersed and capillary systems, cf. Figure 10(b). Still, even at $F_N < 40$ nN, high-resolution (lattice resolved) images are achievable in the full water layer. The increase of the average slip length with load is much larger for the water coated probe, cf. Figure 10(b). In the case of the water coated probe, the average slip length is larger than 3 nm for the normal forces $F_N > 30$ nN. A few water molecules trapped between the probe and the substrate can induce a slip with a lattice resolution in the case of a water coated probe only at the lowest investigated loads ($F_N < 5$ nN). Even under the normal force of $F_N = 8.7$ nN, the average slip length is larger than 1 nm.

Notably, the tip is not in direct contact with the surface in either of the three modeled systems. From Figure 10(c), we see that keeping the probe and the substrate somewhat separated increases the resolution of the measurements. Therefore, lattice resolved measurements become less sensitive to normal loads if the probe is immersed in a water layer or surrounded with water from a capillary. As a result, the FFM experiments could be conducted with a wider range of normal loads. Also, experimental measurements at higher normal loads can be performed. Both experimental conditions, the wider range and the inclusion of higher values of the applied normal load, improve the signal-to-noise ratio, which is advantageous.

To obtain a detailed insight into the evolution of the slip length in different configurations, we categorize the slip lengths into: single, double, three to five, and longer than five slip events, thus representing occurrences over one, two, three to five, or six and more lattice constants, respectively, along with the extent of these jumps in Figure 10(d−f). The probability of double (≈ 0.66 nm) and multiple-slip events is increasing in frequency at higher loads $F_N > 4.8$ nN. Figure 10(d−f) summarizes the evolution of the percentage of these slip events at varying applied normal loads for the three investigated systems. For the probe surrounded by a water capillary, there is a notable prevalence of the single-slip over the double-slip events, with the longer slip events being the least frequent. As the normal load increases, the portion of the single-slip events decreases from 100 to 50%, while the number of the double slips increases consequently, cf. Figure 10(e). In the case of the probe immersed in the water layer, the double-slip events are also present at low loads, i.e., $F_N < 5$ nN. The occurrence of double-slip events is around 20%. The three-slip population exhibits an intriguing behavior, initially being nonexistent, it is peaking at the lowest load $F_N = 25.5$ nN, subsequently declining to zero, and resurging at higher loads with approximately 40%, cf. $F_N = 33.1$ nN in Figure 10(f).

DISCUSSION

Analysis of the experimental data reveals distinct distributions in the measured slip lengths. Slip lengths exhibit characteristic distributions, with a notable prevalence of single-slip events under low loads in ambient conditions, compared to the probe immersed in water. Also in simulation, under low loads for the probe surrounded by capillary water, single-slip events are significantly more prevalent when compared to those observed for the probe fully immersed in water. The capillary simulation results above 10 nN align well with the experimental findings for ambient conditions, showing a shift from predominantly single-slip to double-slip events. Furthermore, both systems exhibit only single-slip and double-slip events. Similarly to the experiments, the simulations show an early presence of double-slip events in the water-immersed probe simulation. In addition, an interplay between the single-slip and double-slip events is observed with the normal load increase, for the water-immersed probe. That interplay is characterized by an initial decrease and subsequent increase in single-slip events, accompanied by a reciprocal trend in double-slip events, both in simulations and experiments.

The simulations allow investigation of cases that were not treated experimentally. The steep increase of the slip length and a high friction coefficient determined for the probe coated with a few water molecules (i.e., not enough water molecules to form a capillary) are seen in simulations. While single-slip and double-slip events dominate the experimental results, the simulations of the probe coated with water reveal a longer average slip length, which involves three or more slips. Also, the friction coefficient of $\mu_{coated} = 0.1$ for the probe coated with water is higher than both the experimentally observed value of 0.02 and the simulated value when an abundant amount of water is present, with the value of 0.06. Importantly, the discrepancy in the friction coefficient results suggests that the experimentally measured system under ambient conditions involved a probe surrounded by capillary water.

The simulations indicate that the presence of water extends the range of normal forces within which lattice-resolved resolution is achievable. Our analysis suggests that water molecules introduce interactions with energy levels between those of the thermally activated motion of amorphous SiO_2 probe surface defects (approximately 5−25 meV,[65]) and the elastic energies in the solids (probe/substrate), thereby enhancing the measurement sensitivity.

The ratio between the tip−sample interaction and the cantilever elastic energy (i.e., the PT parameter η), increases by factor 3 in the ambient condition experiments, and by factor 2 in the simulations. The mean values of the corrugation interaction energy were larger than the elastic energy at the contacts in both experiments and simulations. At the same time, in the simulations of the water coated probe, the ratio η was independent of the normal load. Such a result further indicates that the trapped water molecules modify probe-substrate contact.

■ CONCLUSIONS

We have conducted extensive FFM experiments and MD simulations to investigate the structural, mechanical, and nanotribological properties of the studied nanoscale SiO_2/MoS_2 system in different aqueous environments. The simulation study focused on the interaction between an amorphous SiO_2 probe and a monolayer crystalline MoS_2 substrate, in the presence of three distinct configurations of water with respect to the probe: a water layer coating the probe and the probe-substrate gap, a sufficient amount of water surrounding the probe which enables the formation of a water capillary, and the probe fully immersed in a continuous layer of water. The experimental setup was 2-fold: an AFM probe immersed in a full layer of water and air with a relative humidity of 35−40%, where capillary condensation was a highly probable effect.

To understand the behavior of the water layer under the applied normal load and the breaking of the first hydration layer, we explored the vertical approach of the probe toward the substrate, and we obtained the force−distance characteristics at various temperatures. This molecular dynamics study revealed a significant influence of the temperature on the presence of water molecules within the probe-sample gap. Higher temperatures rendered the water molecules more mobile, resulting in fewer water molecules trapped in the probe-sample gap. However, both the heating of the system and the shear forces proved to be insufficient to expel the trapped water molecules.

Achieving lattice resolved images through water-based atomic force microscopy requires critical consideration of the minimal normal pressure needed to disrupt the initial hydration layer. Once this threshold is surpassed, the water molecules persist as integral components of the probe, rather than being entirely removed from the probe-sample gap.

The friction curves obtained via simulations and experiments exhibited well-defined lattice-resolved stick−slip patterns. Our MD simulations have explicitly revealed that the contact does not remain dry and that water molecules that get trapped become an integral factor in the overall nanotribological interaction. The simulations have shown that the slip length increases with the applied load to a prolonged stick−slip above 1 nm, when the amount of water surrounding the probe is low, as in the case of water coated probe. This result indicates that an abundance of water, either in the form of a capillary or water layer, allows the water molecules that get removed during sliding, to be replenished. In turn, the water trapped in the nanotribological probe-sample contact keeps the probe and sample separated further apart, compared to the dry case, or when the amount of water present is insufficient to form a capillary, hence resulting in the lattice resolution at the studied normal loads. By exploring the quantity and the spatial distribution of the water present in a nanoscopic contact of amorphous SiO_2 probe and monolayer MoS_2 sample, our combined simulation-experimental study contributes valuable insights into the intricate nature of the nanoscale tribological phenomena. Outlined phenomena involving trapped molecules may play an important role in nanotribological contact and have a strong impact on the quality and reliability of AFM measurements performed in liquid environments. However, open questions remain regarding the interaction of trapped water with surface SiO_2, particularly through hydroxylation and the interaction with surface defects. Additionally, given the anisotropic friction properties of MoS_2, further studies should investigate how does water influence this characteristic.

■ AUTHOR INFORMATION

Corresponding Authors

Miljan Dašić − *Scientific Computing Laboratory, Center for the Study of Complex Systems, Institute of Physics Belgrade, University of Belgrade, Belgrade 11080, Serbia;* orcid.org/0000-0002-1739-0784; Email: miljan.dasic@ipb.ac.rs

Ronen Berkovich − *Department of Chemical Engineering, Ben-Gurion University of the Negev, Beer Sheva 84105, Israel; The Ilse Katz Institute for Nanoscale Science and Technology, Ben-Gurion University of the Negev, Beer Sheva 84105, Israel;* orcid.org/0000-0002-0989-6136; Email: berkovir@bgu.ac.il

Igor Stanković − *Scientific Computing Laboratory, Center for the Study of Complex Systems, Institute of Physics Belgrade, University of Belgrade, Belgrade 11080, Serbia;* orcid.org/0000-0001-5756-7196; Email: igor.stankovic@ipb.ac.rs

Authors

Roy Almog − *Department of Chemical Engineering, Ben-Gurion University of the Negev, Beer Sheva 84105, Israel*

Liron Agmon − *Department of Chemical Engineering, Ben-Gurion University of the Negev, Beer Sheva 84105, Israel*

Stav Yehezkel − *Department of Chemical Engineering, Ben-Gurion University of the Negev, Beer Sheva 84105, Israel*

Tal Halfin − *Department of Chemical Engineering, Ben-Gurion University of the Negev, Beer Sheva 84105, Israel*

Jürgen Jopp − *The Ilse Katz Institute for Nanoscale Science and Technology, Ben-Gurion University of the Negev, Beer Sheva 84105, Israel*

Assaf Ya'akobovitz − *Department of Mechanical Engineering and The Ilse Katz Institute for Nanoscale Science and Technology, Ben-Gurion University of the Negev, Beer Sheva 84105, Israel;* orcid.org/0000-0002-5836-0549

Complete contact information is available at:
https://pubs.acs.org/10.1021/acsami.4c08226

Notes

The authors declare no competing financial interest.

■ ACKNOWLEDGMENTS

M.D. and I.S. acknowledge funding provided by the Institute of Physics Belgrade, through the grant of the Ministry of Science, Technological Development and Innovation of the Republic of Serbia. R.B., L.A., R.A., and S.Y. acknowledge the support of the Pazy Foundation grant ID 133-2020, and Deutsche Forschungsgemeinschaft No. DFG GN 92/16-1. All computer simulations were performed on the PARADOX supercomputing facility at the Scientific Computing Laboratory of the Institute of Physics Belgrade, University of Belgrade, Serbia. The use of VMD[68] software for the visualization of our

nanotribological system (available at http://www.ks.uiuc.edu/Research/vmd/) is also acknowledged.

REFERENCES

(1) de Beer, S.; Kutnyanszky, E.; Schön, P. M.; Vancso, G. J.; Müser, M. H. Solvent-induced immiscibility of polymer brushes eliminates dissipation channels. *Nat. Commun.* **2014**, *5*, No. 3781.

(2) Noël, O.; Mazeran, P.-E.; Stanković, I. Nature of Dynamic Friction in a Humid Hydrophobic Nanocontact. *ACS Nano* **2022**, *16*, 10768−10774.

(3) Wallace, A. G.; Symes, M. D. Water-splitting electrocatalysts synthesized using ionic liquids. *Trends Chem.* **2019**, *1*, 247−258.

(4) Feng, G.; Jiang, X.; Qiao, R.; Kornyshev, A. A. Water in Ionic Liquids at Electrified Interfaces: The Anatomy of Electrosorption. *ACS Nano* **2014**, *8*, 11685−11694.

(5) Fajardo, O. Y.; Bresme, F.; Kornyshev, A. A.; Urbakh, M. Water in Ionic Liquid Lubricants: Friend and Foe. *ACS Nano* **2017**, *11*, 6825−6831.

(6) Stanković, I.; Dašić, M.; Jovanović, M.; Martini, A. Effects of Water Content on the Transport and Thermodynamic Properties of Phosphonium Ionic Liquids. *Langmuir* **2024**, *40*, 9049−9058.

(7) Stella, M.; Lorenz, C. D.; Righi, M. C. Effects of intercalated water on the lubricity of sliding layers under load: a theoretical investigation on MoS2. *2D Mater.* **2021**, *8*, No. 035052.

(8) Arif, T.; Colas, G.; Filleter, T. Effect of humidity and water intercalation on the tribological behavior of graphene and graphene oxide. *ACS Appl. Mater. Interfaces* **2018**, *10*, 22537−22544.

(9) Zhao, X.; Zhang, G.; Wang, L.; Xue, Q. The tribological mechanism of MoS 2 film under different humidity. *Tribol. Lett.* **2017**, *65*, No. 64.

(10) He, G.; Müser, M. H.; Robbins, M. O. Adsorbed Layers and the Origin of Static Friction. *Science* **1999**, *284*, 1650−1652.

(11) Müser, M. H.; Robbins, M. O. Conditions for static friction between flat crystalline surfaces. *Phys. Rev. B* **2000**, *61*, 2335−2342.

(12) Müser, M. H.; Wenning, L.; Robbins, M. O. Simple Microscopic Theory of Amontons's Laws for Static Friction. *Phys. Rev. Lett.* **2001**, *86*, 1295−1298.

(13) Ouyang, W.; de Wijn, A. S.; Urbakh, M. Atomic-scale sliding friction on a contaminated surface. *Nanoscale* **2018**, *10*, 6375−6381.

(14) Bistac, S.; Schmitt, M.; Ghorbal, A.; Gnecco, E.; Meyer, E. Nano-scale friction of polystyrene in air and in vacuum. *Polymer* **2008**, *49*, 3780−3784.

(15) Yu, Y.; Cirelli, M.; Kieviet, B. D.; Kooij, E. S.; Vancso, G. J.; de Beer, S. Tunable friction by employment of co-non-solvency of PNIPAM brushes. *Polymer* **2016**, *102*, 372−378.

(16) Van den Oetelaar, R.; Flipse, C. Atomic-scale friction on diamond (111) studied by ultra-high vacuum atomic force microscopy. *Surf. Sci.* **1997**, *384*, L828−L835.

(17) Vilhena, J. G.; Pimentel, C.; Pedraz, P.; Luo, F.; Serena, P. A.; Pina, C. M.; Gnecco, E.; Pérez, R. Atomic-Scale Sliding Friction on Graphene in Water. *ACS Nano* **2016**, *10*, 4288−4293.

(18) Filleter, T.; Bennewitz, R. Structural and frictional properties of graphene films on SiC(0001) studied by atomic force microscopy. *Phys. Rev. B* **2010**, *81*, No. 155412.

(19) Goryl, M.; Budzioch, J.; Krok, F.; Wojtaszek, M.; Kolmer, M.; Walczak, L.; Konior, J.; Gnecco, E.; Szymonski, M. Probing atomic-scale friction on reconstructed surfaces of single-crystal semiconductors. *Phys. Rev. B* **2012**, *85*, No. 085308.

(20) Steiner, P.; Gnecco, E.; Krok, F.; Budzioch, J.; Walczak, L.; Konior, J.; Szymonski, M.; Meyer, E. Atomic-Scale Friction on Stepped Surfaces of Ionic Crystals. *Phys. Rev. Lett.* **2011**, *106*, No. 186104.

(21) Riedo, E.; Lévy, F.; Brune, H. Kinetics of Capillary Condensation in Nanoscopic Sliding Friction. *Phys. Rev. Lett.* **2002**, *88*, No. 185505.

(22) Pina, C. M.; Miranda, R.; Gnecco, E. Anisotropic surface coupling while sliding on dolomite and calcite crystals. *Phys. Rev. B* **2012**, *85*, No. 073402.

(23) Agmon, L.; Almog, R.; Gaspar, D.; Voscoboynik, G.; Choudhary, M.; Jopp, J.; Klausner, Z.; Ya'akobovitz, A.; Berkovich, R. Nanoscale contact mechanics of the interactions at monolayer MoS2 interfaces with Au and Si. *Tribiol. Int.* **2022**, *174*, No. 107734.

(24) Skuratovsky, S.; Agmon, L.; Gnecco, E.; Berkovich, R. Surroundings affect slip length dynamics in nanoscale friction through contact stiffness and damping. *Friction* **2023**, *11*, 216−227.

(25) Socoliuc, A.; Bennewitz, R.; Gnecco, E.; Meyer, E. Transition from stick-slip to continuous sliding in atomic friction: entering a new regime of ultralow friction. *Phys. Rev. Lett.* **2004**, *92*, No. 134301.

(26) Roth, R.; Glatzel, T.; Steiner, P.; Gnecco, E.; Baratoff, A.; Meyer, E. Multiple slips in atomic-scale friction: an indicator for the lateral contact damping. *Tribol. Lett.* **2010**, *39*, 63−69.

(27) Curry, J. F.; Argibay, N.; Babuska, T.; Nation, B.; Martini, A.; Strandwitz, N. C.; Dugger, M. T.; Krick, B. A. Highly Oriented MoS2 Coatings: Tribology and Environmental Stability. *Tribol. Lett.* **2016**, *64*, No. 11.

(28) Khare, H. S.; Burris, D. L. The Effects of Environmental Water and Oxygen on the Temperature-Dependent Friction of Sputtered Molybdenum Disulfide. *Tribol. Lett.* **2013**, *52*, 485−493.

(29) Winer, W. O. Molybdenum disulfide as a lubricant: a review of the fundamental knowledge. *Wear* **1967**, *10*, 422−452.

(30) Vazirisereshk, M. R.; Hasz, K.; Carpick, R. W.; Martini, A. Friction Anisotropy of MoS2: Effect of Tip−Sample Contact Quality. *J. Phys. Chem. Lett.* **2020**, *11*, 6900−6906.

(31) Xiao, X.; Qian, L. Investigation of humidity-dependent capillary force. *Langmuir* **2000**, *16*, 8153−8158.

(32) Ogletree, D. F.; Carpick, R. W.; Salmeron, M. Calibration of frictional forces in atomic force microscopy. *Rev. Sci. Instrum.* **1996**, *67*, 3298−3306.

(33) Varenberg, M.; Etsion, I.; Halperin, G. An improved wedge calibration method for lateral force in atomic force microscopy. *Rev. Sci. Instrum.* **2003**, *74*, 3362−3367.

(34) Irving, B. J.; Nicolini, P.; Polcar, T. On the lubricity of transition metal dichalcogenides: an ab initio study. *Nanoscale* **2017**, *9*, 5597−5607.

(35) Cao, X.; Gan, X.; Lang, H.; Yu, K.; Ding, S.; Peng, Y.; Yi, W. Anisotropic nanofriction on MoS2 with different thicknesses. *Tribiol. Int.* **2019**, *134*, 308−316.

(36) Almeida, C. M.; Prioli, R.; Fragneaud, B.; Cançado, L. G.; Paupitz, R.; Galvão, D. S.; De Cicco, M.; Menezes, M. G.; Achete, C. A.; Capaz, R. B. Giant and Tunable Anisotropy of Nanoscale Friction in Graphene. *Sci. Rep.* **2016**, *6*, No. 31569.

(37) Lee, C.; Li, Q.; Kalb, W.; Liu, X.-Z.; Berger, H.; Carpick, R. W.; Hone, J. Frictional Characteristics of Atomically Thin Sheets. *Science* **2010**, *328*, 76−80.

(38) Li, S.; Li, Q.; Carpick, R. W.; Gumbsch, P.; Liu, X. Z.; Ding, X.; Sun, J.; Li, J. The evolving quality of frictional contact with graphene. *Nature* **2016**, *539*, 541−545.

(39) Zeng, X.; Peng, Y.; Liu, L.; Lang, H.; Cao, X. Dependence of the friction strengthening of graphene on velocity. *Nanoscale* **2018**, *10*, 1855−1864.

(40) Xu, C.; Zhang, S.; Du, H.; Xue, T.; Kang, Y.; Zhang, Y.; Zhao, P.; Li, Q. Revisiting frictional characteristics of graphene: Effect of in-plane straining. *ACS Appl. Mater. Interfaces* **2022**, *14*, 41571−41576.

(41) Cho, D.-H.; Wang, L.; Kim, J.-S.; Lee, G.-H.; Kim, E. S.; Lee, S.; Lee, S. Y.; Hone, J.; Lee, C. Effect of surface morphology on friction of graphene on various substrates. *Nanoscale* **2013**, *5*, 3063−3069.

(42) Vazirisereshk, M. R.; Hasz, K.; Zhao, M.-Q.; Johnson, A. C.; Carpick, R. W.; Martini, A. Nanoscale friction behavior of transition-metal dichalcogenides: Role of the chalcogenide. *ACS Nano* **2020**, *14*, 16013−16021.

(43) Zhang, D.; Huang, M.; Klausen, L. H.; Li, Q.; Li, S.; Dong, M. Liquid-Phase Friction of Two-Dimensional Molybdenum Disulfide at the Atomic Scale. *ACS Appl. Mater. Interfaces* **2023**, *15*, 21595−21601.

(44) Zhang, S.; Hou, Y.; Li, S.; Liu, L.; Zhang, Z.; Feng, X.-Q.; Li, Q. Tuning friction to a superlubric state via in-plane straining. *Proc. Natl. Acad. Sci. U.S.A.* **2019**, *116*, 24452−24456.

(45) Gnecco, E.; Roth, R.; Baratoff, A. Analytical expressions for the kinetic friction in the Prandtl-Tomlinson model. *Phys. Rev. B* **2012**, *86*, No. 035443.

(46) Vega, C.; de Miguel, E. Surface tension of the most popular models of water by using the test-area simulation method. *J. Chem. Phys.* **2007**, *126*, No. 154707.

(47) Chatterjee, S.; Debenedetti, P. G.; Stillinger, F. H.; Lynden-Bell, R. M. A computational investigation of thermodynamics, structure, dynamics and solvation behavior in modified water models. *J. Chem. Phys.* **2008**, *128*, No. 124511.

(48) Sresht, V.; Rajan, A. G.; Bordes, E.; Strano, M. S.; Pádua, A. A.; Blankschtein, D. Quantitative Modeling of MoS2−Solvent Interfaces: Predicting Contact Angles and Exfoliation Performance using Molecular Dynamics. *J. Phys. Chem. C* **2017**, *121*, 9022−9031.

(49) Cruz-Chu, E. R.; Aksimentiev, A.; Schulten, K. Water-Silica Force Field for Simulating Nanodevices. *J. Phys. Chem. B* **2006**, *110*, 21497−21508.

(50) Allen, M. P.; Tildesley, D. J. *Computer Simulation of Liquids*; Oxford University Press, 2017.

(51) van Gunsteren, W. F. *Computer Simulation of Biomolecular Systems*; ESCOM Science Publishers BV, 1989.

(52) Plimpton, S. Fast parallel algorithms for short-range molecular dynamics. *J. Comput. Phys.* **1995**, *117*, 1−19.

(53) Pollock, E.; Glosli, J. Comments on P3M, FMM, and the Ewald method for large periodic Coulombic systems. *Comput. Phys. Commun.* **1996**, *95*, 93−110.

(54) Dumcenco, D.; Ovchinnikov, D.; Marinov, K.; Lazic, P.; Gibertini, M.; Marzari, N.; Sanchez, O. L.; Kung, Y.-C.; Krasnozhon, D.; Chen, M.-W.; et al. Large-area epitaxial monolayer MoS2. *ACS Nano* **2015**, *9*, 4611−4620.

(55) Medyanik, S. N.; Liu, W. K.; Sung, I.-H.; Carpick, R. W. Predictions and observations of multiple slip modes in atomic-scale friction. *Phys. Rev. Lett.* **2006**, *97*, No. 136106.

(56) Gnecco, E.; Agmon, L.; Berkovich, R. Friction and chaos: Influence of the damping coefficient on atomic-scale stick-slip on hexagonal crystal lattices. *Phys. Rev. B* **2022**, *105*, No. 235427.

(57) Helman, J. S.; Baltensperger, W.; Hol, J.; et al. Simple model for dry friction. *Phys. Rev. B* **1994**, *49*, No. 3831.

(58) Gnecco, E.; Bennewitz, R.; Gyalog, T.; Meyer, E. Friction experiments on the nanometre scale. *J. Phys.: Condens. Matter* **2001**, *13*, No. R619.

(59) Popov, V. L.; Gray, J. *Prandtl-Tomlinson Model: History and Applications in Friction, Plasticity, and Nanotechnologies*; Wiley Online Library, 2012; Vol. *92*, pp 683−708.

(60) Heyes, D. M.; Smith, E. R.; Dini, D.; Spikes, H. A.; Zaki, T. A. Pressure dependence of confined liquid behavior subjected to boundary-driven shear. *J. Chem. Phys.* **2012**, *136*, No. 134705.

(61) Perkin, S. Ionic liquids in confined geometries. *Phys. Chem. Chem. Phys.* **2012**, *14*, 5052−5062.

(62) Dašić, M.; Stanković, I.; Gkagkas, K. Molecular dynamics investigation of the influence of the shape of the cation on the structure and lubrication properties of ionic liquids. *Phys. Chem. Chem. Phys.* **2019**, *21*, 4375−4386.

(63) Gao, J.; Luedtke, W. D.; Landman, U. Layering Transitions and Dynamics of Confined Liquid Films. *Phys. Rev. Lett.* **1997**, *79*, 705−708.

(64) Suzuki, K.; Oyabu, N.; Kobayashi, K.; Matsushige, K.; Yamada, H. Atomic-Resolution Imaging of Graphite−Water Interface by Frequency Modulation Atomic Force Microscopy. *Appl. Phys. Express* **2011**, *4*, No. 125102.

(65) Xu, R.-G.; Zhang, G.; Xiang, Y.; Leng, Y. On the Friction Behavior of SiO2 Tip Sliding on the Au(111) Surface: How Does an Amorphous SiO2 Tip Produce Regular Stick−Slip Friction and Friction Duality? *Langmuir* **2023**, *39*, 6425−6432.

(66) Yeon, J.; van Duin, A. C. T.; Kim, S. H. Effects of Water on Tribochemical Wear of Silicon Oxide Interface: Molecular Dynamics (MD) Study with Reactive Force Field (ReaxFF). *Langmuir* **2016**, *32*, 1018−1026.

(67) Heiranian, M.; Wu, Y.; Aluru, N. R. Molybdenum disulfide and water interaction parameters. *J. Chem. Phys.* **2017**, *147*, No. 104706.

(68) Humphrey, W.; Dalke, A.; Schulten, K. VMD: visual molecular dynamics. *J. Mol. Graphics* **1996**, *14*, 33−38.

NOTE ADDED AFTER ASAP PUBLICATION

This paper originally published ASAP on August 6, 2024. As author Assaf Ya'akobovitz's name was incorrectly spelled in this version, this was corrected and a new version reposted on August 12, 2024.

The Journal of
Chemical Physics

RESEARCH ARTICLE | AUGUST 26 2024

Integrating Newton's equations of motion in the reciprocal space

Antonio Cammarata ; Miljan Dašić ; Paolo Nicolini

J. Chem. Phys. 161, 084111 (2024)
https://doi.org/10.1063/5.0224108

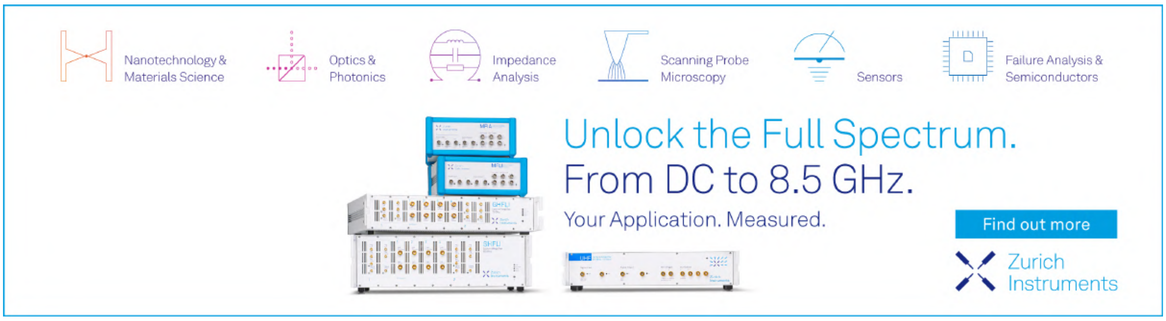

AIP Publishing

The Journal
of Chemical Physics

ARTICLE

pubs.aip.org/aip/jcp

Integrating Newton's equations of motion in the reciprocal space

Cite as: J. Chem. Phys. 161, 084111 (2024); doi: 10.1063/5.0224108
Submitted: 19 June 2024 • Accepted: 11 August 2024 •
Published Online: 26 August 2024

Antonio Cammarata,[1,a)] Miljan Dašić,[1,2] and Paolo Nicolini[1,3,a)]

AFFILIATIONS

[1] Department of Control Engineering, Faculty of Electrical Engineering, Czech Technical University in Prague, Technicka 2, 16627 Prague, Czech Republic
[2] Scientific Computing Laboratory, Center for the Study of Complex Systems, Institute of Physics Belgrade, University of Belgrade, Pregrevica 118, 11080 Belgrade, Serbia
[3] Institute of Physics (FZU), Czech Academy of Sciences, Na Slovance 2, 18200 Prague, Czech Republic

[a)] **Authors to whom correspondence should be addressed:** cammaant@fel.cvut.cz and nicolini@fzu.cz

ABSTRACT

We here present the normal dynamics technique, which recasts the Newton's equations of motion in terms of phonon normal modes by exploiting a proper sampling of the reciprocal space. After introducing the theoretical background, we discuss how the reciprocal space sampling enables us to (i) obtain a computational speedup by selecting which and how many wave vectors of the Brillouin zone will be considered and (ii) account for distortions realized across large atomic distances without the use of large simulation cells. We implemented the approach into an open-source code, which we used to present three case studies: in the first one, we elucidate the general strategy for the sampling of the reciprocal space; in the second one, we illustrate the potential of the approach by studying the stabilization effect of temperature in α-uranium; and in the last one, we investigate the characterization of Raman spectra at different temperatures in MoS_2/MX_2 transition metal dichalcogenide heterostructures. Finally, we discuss how the procedure is general and can be used to simulate periodic, semiperiodic, and finite systems such as crystals, slabs, nanoclusters, or molecules.

I. INTRODUCTION

Molecular Dynamics (MD) simulation is the technique of choice to study a vast variety of atomic systems, spanning biological matter and inorganic materials.[1] In an MD simulation, interactions among a given set of atoms are defined by a function, i.e., the potential energy, which depends on the position of the atoms in the space; such interactions are provided as analytical functions or numerical datasets, which define the *force field*.[1] The vast majority of force fields rely on a classical description of interactions; in the past decades, several of them have been developed for both organic and inorganic systems.[2–7] Despite such an abundance of parameterizations, shortcomings of classical force fields are still present, e.g., in terms of accuracy and availability of the description for the system under study.[8–12] Moreover, the parameterization procedure presents an unavoidable degree of arbitrariness (for example, in the choice of the analytical form of the force field, or in the reference data to be used, or even in the fitting scheme to be employed), as well as possibly being very time-demanding.[13,14] Another issue is represented by the difficulty of describing how the subtle details of the electronic density determine the force field, especially when the polarity of the bonds,[15] charge anisotropy,[16] and covalent character are decisive in the system dynamics.[17–19] On the other hand, one can perform *ab initio* molecular dynamics (AIMD)—such as in the Car–Parrinello scheme[20]—in order to overcome the above-mentioned limitations imposed by classical force fields. In this case, the classical Hamiltonian is substituted by a quantum mechanical one, which can be built for any atom topology and atomic type. The major drawback of such schemes is that they might become very computationally demanding. Another possibility is represented by the QM/MM scheme,[21] where the system is split into two regions, one treated at the quantum mechanical (QM) level and the other (MM) at the classical one. Such an approach has the advantage that, in general, the simulations scale roughly as $O(N^2)$, where N is the number of atoms in the system. However, the identification of the QM region requires *a priori* knowledge of the physical phenomena to be studied; moreover, the truncation of the bonds crossing the QM/MM interface is not trivial at all in, e.g., solid systems. Finally, in the QM/MM approach, a classical force field including all the chemical species of the system must be available.

In addition to this, large geometric models are often required in order to produce accurate data comparable with experiments,[22] resulting in resource-demanding MD simulations. The computational cost to produce a dynamical trajectory might become prohibitive if the simulations must be carried out at the quantum mechanical level. This issue is usually mitigated by limiting the size of the simulation box; however, it is known that this may affect the reliability of the results.[23] This is the case when it is necessary to include distortions realized across large interatomic distances, which account for ripples, and determine thermal transport, diffusion coefficients, and nucleation processes.[23–30]

Here, we propose an approach that can help circumvent these difficulties. The technique uses an approximation of the real potential energy surface by means of a Taylor expansion about a reference configuration, and it produces dynamical trajectories by solving Newton's equations of motion in terms of phonon normal coordinates. This, in turn, corresponds to a suitable sampling of the reciprocal space; such sampling enables the user to tune the computational load to target a desired accuracy. Moreover, long-wave structural modulations are accounted for with a suitable choice of sampling set, without the need to consider large unit cells. The general formulation of our approach enables us to parameterize the interatomic forces at any level of quantum mechanical description; such forces can be calculated from either ground or excited electronic configurations, even in the presence of external electric or magnetic fields, and may include quantum-mechanical electron–nuclei interactions such as the hyper-fine Hamiltonian. Since the atomic interactions appearing in the equations of motion can be parameterized with quantum mechanical descriptions, the sampling strategy of the technique makes it possible to generate dynamical trajectories of large systems on ordinary desktop computers. As the scheme is aimed at obtaining dynamical trajectories by integrating Newton's equations expressed in terms of normal coordinates, we termed it *Normal Dynamics* (ND).

In this work, we present the theoretical derivation of the method, the implementation into a freely available FORTRAN code, and advantages and drawbacks of this approach by considering three case studies. In the first one, we illustrate the general idea about how to perform the sampling of the reciprocal space, for example, by considering a reduced set of wave vectors of the Brillouin zone in order to obtain a computational speedup or by enlarging such a set in order to obtain the desired accuracy of the results. In the second one, we show that the ND scheme can be employed in order to observe the stabilization effect of temperature, which has been already reported in the literature,[31] but at the cost of performing computationally demanding AIMD simulations. In the third one, we exploit the ND technique to study the thermal effect in the Raman spectra of transition metal dichalcogenide heterostructures and discuss possible mistakes that may occur in the attribution of the Raman peaks.

II. THEORETICAL BACKGROUND

Differently from most of the classical force fields,[2–6] the ND technique does not rely on the definition of a bonding topology. It is rather based on a description that is general with respect to the atomic type and the geometric arrangement forming the system. Such a description relies on the Taylor expansion of the potential energy V in terms of the atomic displacements $\boldsymbol{u}$ with respect to a specified reference configuration,[32]

$$V(u_{i_k}^{\alpha_k}) = V_0 + \sum_{p\geq 1} \frac{1}{p!} \sum_{\substack{\alpha_1\ldots\alpha_p \\ i_1\ldots i_p}} \Theta_{i_1\ldots i_p}^{\alpha_1\ldots\alpha_p} \prod_{k=1}^{p} u_{i_k}^{\alpha_k}, \tag{1}$$

where V_0 is the energy reference, p is the order of the terms in the sum, i_k and α_k identify the atom and the Cartesian component of the displacement from its reference position, respectively, and k enumerates the approximation orders. The Cartesian tensors $\boldsymbol{\Theta}_p = \Theta_{i_1\ldots i_p}^{\alpha_1\ldots\alpha_p}$ are formed by the pth order partial derivative of the potential energy with respect to the atomic positions calculated at the reference position. For $p = 1$, $\boldsymbol{\Theta}_1 = \Theta_{i_1}^{\alpha_1}$ is the net force active on the ith atom along the Cartesian direction α and is null when V is evaluated at equilibrium; for $p \geq 2$, $\boldsymbol{\Theta}_p$ contains the pth order interatomic force constants. If Eq. (1) is truncated at $p = 2$, the interatomic forces are of the harmonic kind; the anharmonic effects are instead included in the terms with $p \geq 3$. The $\boldsymbol{\Theta}_p$ tensors can be evaluated numerically at any order by means of a quantum mechanical Hamiltonian,[33–38] which avoids the limitations imposed by the availability of existing force fields or the need to parameterize a new one.[39] The use of a Taylor expansion to approximate the real potential energy surface is not new, and it is currently exploited in previous formulations[40] (also in different contexts[41]) and relative software packages, such as HIPHIVE,[34] A-TDEP,[31] and SSCHA.[42] The novelty of the ND method relies on the fact that we make use of the Fourier transform of such a Taylor expansion in order to explicitly perform dynamical simulations in the reciprocal space. To the best of our knowledge, this has never been proposed in the literature, and currently, there is no other software capable of performing such a task.

Equation (1) can be used to describe the atomic interactions of any system, irrespective of the atomic type, the stoichiometry, and the atom geometry. Moreover, the $\boldsymbol{\Theta}_p$ tensors represent harmonic ($p = 2$) and anharmonic ($p > 2$) contributions determined by the electronic density and the conditions at which the latter is calculated (e.g., ground or excited states, in the presence or not of external fields). However, it must be stressed that the technique relies on the Fourier transform of a Taylor expansion, which needs to be truncated for practical reasons, and therefore, it has a finite convergence radius. This results from the fact that the description of the interactions is somehow local, and it can become unreliable if the dynamics brings the system far away from the reference state, i.e., if large displacements take place during the dynamics. We address this point in Sec. III D, where we also present some strategies on how to (partially) amend this.

A. The equations of motion

Here, we present the equations employed by the ND scheme; the full derivation is reported in the supplementary material. We begin by exploiting the fact that, at each $\boldsymbol{q}$ wave vector of the Brillouin zone of a system with N atoms in the unit cell, the $3N$ normal coordinates $Q_{\boldsymbol{q},j}$ are a complete basis set for the $3N$ Cartesian components of the atomic displacements u_i^α. We shorten the notation as Q_λ, with $\lambda = (\boldsymbol{q}, j)$ and j labeling the normal mode (for more details on the notation, see Sec. I of the supplementary material). The kinetic energy T and the potential energy V in terms of the Q_λ coordinates are then read as[32,43]

$$T = \frac{1}{2}\sum_\lambda \dot{Q}_\lambda \dot{Q}_\lambda^*, \tag{2}$$

$$V = \frac{1}{2}\sum_\lambda \omega_\lambda^2 Q_\lambda Q_\lambda^* + \sum_{p\geq 3}\frac{1}{p!}\sum_{\lambda_1\ldots\lambda_p}\Phi_{\lambda_1\ldots\lambda_p}\prod_{k=1}^{p} Q_{\lambda_k}, \tag{3}$$

where ω_λ is the eigenfrequency of the dynamical matrix associated with the phonon mode λ, the symbol "$*$" indicates the complex conjugation, p is the order of approximation, and the tensors $\boldsymbol{\Phi}_p = \{\Phi_{\lambda_1\ldots\lambda_p}\}$ are the Fourier transforms of the tensors $\boldsymbol{\Theta}_p$ by means of the eigenvectors of the dynamical matrix.[32,43] We then write the Lagrangian of the system $\mathscr{L} = T - V$ by using Eqs. (2) and (3) and solving the Euler–Lagrange equations for the normal coordinates Q_λ,

$$\frac{d}{dt}\frac{\partial \mathscr{L}}{\partial \dot{Q}_\lambda} - \frac{\partial \mathscr{L}}{\partial Q_\lambda} = 0, \tag{4}$$

which are the Newton's equations of motion written in terms of the normal modes. The time integration of Eq. (4) represents the dynamic evolution of the normal modes of the system, and it is equivalent to the time integration of the Newton's equations of motion in Cartesian space. The explicit form of Eq. (4) is

$$\ddot{Q}_\lambda = -\omega_\lambda^2 Q_\lambda - \left(\sum_{p\geq 3}\frac{1}{(p-1)!}\sum_{\lambda_1\ldots\lambda_{p-1}}\Phi_{\lambda\lambda_1\ldots\lambda_{p-1}}\prod_{k=1}^{p-1} Q_{\lambda_k}\right)^*, \tag{5}$$

which shows that the atomic motion can be computed as a harmonic oscillation modulated by anharmonic contributions represented by the term in parenthesis, where p is the order of the anharmonic correction. If no anharmonic effects are present, that is, if all the $\boldsymbol{\Phi}_p$ tensors are null, we recover the equation for the harmonic oscillator. The derivation of Eq. (5) and the calculation of harmonic phonons and anharmonic $\boldsymbol{\Phi}_p$ tensors do not rely on the assumption that the reference unit cell represents a perfect crystal.

Indeed, the presence of defects can be taken into account by using a unit cell, which consists of a supercell containing the defect(s) and with a size that reproduces the desired defect concentration.

The choice of the $\boldsymbol{q}$-points entering Eqs. (2) and (3) is done according to the kind of system that the cell represents, that is, periodic (bulk), semiperiodic (slab), or finite (cluster or molecule).

With the choice of the potential energy as shown in Eq. (3), Eq. (5) enables us to sample the phase space in the microcanonical ensemble (NVE). In order to simulate the canonical (NVT) ensemble within the ND scheme, Eqs. (2) and (3) must include the energy terms representing the degrees of freedom of a thermostat coupled with the system. We, therefore, derived the equations, which include the Nosé–Hoover thermostat[44–46] (see Secs. II–IV of the supplementary material),

$$\ddot{Q}_\lambda = -\omega_\lambda^2 Q_\lambda - \left(\sum_{p\geq 3}\frac{1}{(p-1)!}\sum_{\lambda_1\ldots\lambda_{p-1}}\Phi_{\lambda\lambda_1\ldots\lambda_{p-1}}\prod_{k=1}^{p-1} Q_{\lambda_k}\right)^* - \dot{\xi}\dot{Q}_\lambda, \tag{6}$$

$$\ddot{\xi} = \frac{1}{Q_{th}}\left(\sum_\lambda \dot{Q}_\lambda \dot{Q}_\lambda{}^* - 3Nk_B T\right), \tag{7}$$

where ξ and Q_{th} are the dynamical variable and the "mass" associated with the thermostat, respectively, k_B is the Boltzmann's constant, and T is the set temperature. If ξ is constant during the whole simulation, Eq. (6) reduces to Eq. (5), and the simulated ensemble is the microcanonical one.

To the best of our knowledge, equations in the form of Eq. (5) or Eq. (6) have not been reported before, and we refer to them as *normal equations*.[47] In order to obtain the dynamical trajectory, the number of equations to be integrated is equal to the number of normal coordinates, that is, $3N \times N_{\boldsymbol{q}}$, where $N_{\boldsymbol{q}}$ is the number of $\boldsymbol{q}$ points chosen to sample the Brillouin zone. The form of the normal equations provides a direct way to decompose the atomic motions into harmonic and anharmonic contributions, thus facilitating the study of anharmonic effects; indeed, the latter reduces to the study of the tensors $\boldsymbol{\Phi}_p$ and how they determine the phonon scattering.[48–53]

We also developed FORTRAN software named *Phonon-Inspired Normal Dynamics Of Lattices* (PINDOL)[54] to simulate dynamical trajectories with the ND technique. At the moment, we implemented the harmonic and the first anharmonic term ($p = 3$); however, including higher orders is straightforward, and it will be done in future releases. We also plan to derive the normal equations to sample the phase space in the isobaric (NpT) ensemble in an upcoming work and implement them in a future version of the software. The equations that the PINDOL software solves are of the form

$$\ddot{Q}_\lambda = -\omega_\lambda^2 Q_\lambda - \left(\sum_{\lambda_1\lambda_2}\Phi_{\lambda\lambda_1\lambda_2}Q_{\lambda_1}Q_{\lambda_2}\right)^* \tag{8}$$

reproducing the microcanonical ensemble, or

$$\ddot{Q}_\lambda = -\omega_\lambda^2 Q_\lambda - \left(\sum_{\lambda_1\lambda_2}\Phi_{\lambda\lambda_1\lambda_2}Q_{\lambda_1}Q_{\lambda_2}\right)^* - \dot{\xi}\dot{Q}_\lambda \tag{9}$$

reproducing, together with Eq. (7), the canonical ensemble with the Nosé–Hoover thermostat.[44–46]

B. The $\boldsymbol{q}$-point set

As it is apparent from the equations above, the essence of the normal dynamics technique is to recast Newton's equations in the reciprocal space by selecting a suitable set of $\boldsymbol{q}$-points in the Brillouin zone. This results in several computational benefits.

One of the main advantages of the ND scheme can be appreciated by considering that, in order to describe distortions with long wavelengths in crystalline systems, one needs to simulate large unit cells, hence a large number of atoms. In fact, a standard molecular dynamics simulation can sample all and only the distortions that are commensurate with the simulation box; such distortions can be represented by the $3N$ phonon modes of the Γ point of the corresponding reciprocal lattice. In periodic systems, in order to capture the effect of long-range distortions, that is, to capture the effect of lattice distortions represented by waves with large wavelengths, we need to consider a suitable number, $N_r = N_a \times N_b \times N_c$, of replicas of the chosen unit cell; in this way, the number of equations of motion to be solved increases from $3N$ to $3N \times N_r$.

Let us consider a unit cell formed by N atoms and suppose that long-range structural modulations must be taken into account. We then create, for example, a $3 \times 3 \times 3$ supercell of the unit cell; the number of dynamical variables to be evolved in the Cartesian space is, therefore, $3N \times 3 \times 3 \times 3 = 81N$. In the case of the ND scheme (for more details, see Sec. V of the supplementary material), the number of dynamical variables in the *complete* set of *non-redundant* $\boldsymbol{q}$-points is $42N$, which amounts to $(1 + 13 \times 2) \times 3N = 81N$ real variables, as for the Cartesian case, since the $Q_{\boldsymbol{q},j}$ are all complex quantities except for $\boldsymbol{q} = (0, 0, 0)$. However, as we will show in the case studies, in principle, a similar result can be obtained by considering a *reduced* set of $\boldsymbol{q}$-points (for example, by exploiting the symmetries of the unit cell). This immediately leads to a reduction of the degrees of freedom with respect to the Cartesian case, likely opening up a computational advantage.

Let us now imagine that, after an MD simulation, we realize that we need to further expand the size of our original $3 \times 3 \times 3$ system by considering, for example, a $6 \times 6 \times 6$ supercell; in this case, the number of dynamical variables increases from $81N$ to $648N$. In the ND scheme, instead, one can think of expanding the $\{\boldsymbol{q}\}$ set by including suitable $\boldsymbol{q}$-points only. For example, adding $\boldsymbol{q} = (1/6, 1/6, 1/6)$ to the $\boldsymbol{q}_{333}$ set enables us to introduce atomic displacements that require a $6 \times 6 \times 6$ supercell to be represented in the real space; in this case, the number of variables increases from $81N$ to $81N + 6N = 87N$; that is, we reduced the number of dynamical variables by a factor of ~7. It is true that the vector $\boldsymbol{q} = (1/6, 1/6, 1/6)$ alone does not fully represent a $6 \times 6 \times 6$ supercell, as the corresponding complete set would be made of 112 non-redundant $\boldsymbol{q}$-points; however, we can incrementally include in our set more and more points of the kind $\boldsymbol{q}_{666}$ until we reach the desired accuracy.

The key point here is that ND simulations can be run *regardless of whether the* $\{\boldsymbol{q}_i\}$ *set is complete or not*; the optimal size of the set is decided by the user according to the required accuracy. The ND sampling scheme then provides fine control over the computational load and of the accuracy the results. The number of dynamical (normal) variables increases as $O(N_{\boldsymbol{q}})$, where $N_{\boldsymbol{q}}$ is the number of $\boldsymbol{q}$-points in the set; instead, in the standard Cartesian scheme, the number of variables increases as $O(L^3)$, where L is the number of replicas along one of the three directions. From this consideration and by keeping in mind that the scheme is essentially a coordinate transformation, it is clear that, in the case where one needs to consider the complete $\{\boldsymbol{q}_i\}$ set, no computational speedup can be expected by using the ND technique. On the other hand, as we will show in Sec. III, in our case studies we do not need to consider a complete $\{\boldsymbol{q}_i\}$ set to obtain a correct description of the relevant physical quantities, and we believe that this is likely to be the general case.

Another advantage of the ND scheme is that we can focus the computational load only on the relevant aspects of the dynamics. For example, let us imagine that only long waves traveling across a $12 \times 12 \times 12$ supercell are relevant for our study and that the contributions from waves commensurate with a subset of the supercell could be neglected. In the Cartesian scheme, $3N \times 12 \times 12 \times 12 = 5184N$ variables must be somehow integrated, with no possibility of reducing such a number by neglecting unnecessary phonon contributions. On the contrary, in the ND scheme, it might be enough to consider, for example, just two wave vectors, $\boldsymbol{q}_1 = (1/12, 1/12, 1/12)$ and $\boldsymbol{q}_2 = (1/6, 1/6, 1/6)$, while neglecting all the other commensurate ones; in this case, we would need to integrate only $3N \times 2 \times 2 = 12N$ real variables $(N_{\boldsymbol{q}} = 2)$ instead of $5184N$.

III. RESULTS AND DISCUSSIONS

The goal of our case studies is to show that the ND scheme (i) is able to produce dynamical trajectories of large systems by using a common desktop computer and (ii) is capable of taking into account the effect of temperature, as is the case with standard Cartesian simulations. We extract the effective interatomic force constants[31,40,55–60] from ND runs at finite temperatures with the help of the HIPHIVE software;[34] we use the PHONOPY[61] and PHONO3PY[62] software for the necessary pre- and post-processing of the data. The steps to prepare, run, and analyze the simulations are reported in Sec. VI of the supplementary material.

The HIPHIVE software relies on a Taylor expansion of the forces on the atoms of the kind

$$F_i^{\alpha} = -\Theta_{ij}^{\alpha\beta} u_j^{\beta} - \frac{1}{2}\Theta_{ijk}^{\alpha\beta\gamma} u_j^{\beta} u_k^{\gamma} - \cdots, \tag{10}$$

where F_i^{α} is the force on the ith atom along the Cartesian direction α evaluated as the negative gradient of the Taylor expansion of the potential energy V in Eq. (1).

The atomic displacements u and forces F are obtained from the normal coordinates Q and accelerations $\ddot{Q}$ calculated at each ND step and are supplied as an input to the HIPHIVE software; the latter performs a fitting of Eq. (10) and returns the effective interatomic force constants $\boldsymbol{\Theta}$ at a finite temperature.

The first two case studies have been chosen to show how the method works as they have already been reported in the literature. The last case study, instead, has not been reported yet; indeed, we exploit the capabilities of the ND scheme to study the influence of temperature on the Raman spectrum of MoS_2/MX_2 bilayers and suggest how to properly characterize the Raman peaks.

To perform the simulations, the PINDOL code has been compiled with the GNU Cross Compiler v. 9.4.0 included in the software packages of the Ubuntu operative system version 20.04.5, Long Term Stable release. The trajectories have been produced on a local workstation equipped with an Intel Core i7-4770 CPU at 3.40 GHz; although we implemented a basic OpenMP parallelization, we did not use it for the present simulations.

The main quantities affecting the accuracy of an ND simulation are the Cartesian $\boldsymbol{\Theta}_p$ tensors and the sampling of the reciprocal space: the first depends on the level of theory (i.e., classical or *ab initio*) and on the technical parameters used to evaluate the derivatives of the potential energy, while the latter is set by the user with the choice of the $\{\boldsymbol{q}_i\}$ set. For example, the third order derivatives of the potential energy are the fundamental quantities determining the anharmonic effects at the first order. Their importance in determining the accuracy of the model has already

TABLE I. Wall-clock time [hours and minutes] required by the ND simulations on crystalline silicon, α-uranium, and MoS_2/MX_2 systems at different samplings of the Brillouin zone ($N_{\boldsymbol{q}}$) and the number of unique non-null $\boldsymbol{\Phi}_3$ elements. The time shown is normalized to 4 × 10^6 dynamical steps and two atoms in the unit cell.

Case	Time	$N_{\boldsymbol{q}}$	$\#\boldsymbol{\Phi}_3$
Si $\boldsymbol{q}_{333}$	8 h 10′	14	12 789
Si $\boldsymbol{q}_{555}$	69 h 39′	63	279 568
Si $\boldsymbol{q}_{555}^{red}$	1 h 53′	10	3 277
Si $\boldsymbol{q}_{666}^{red}$	4 h 6′	16	5 389
U $\boldsymbol{q}_{423}$	11 h 40′	14	38 059
U $\boldsymbol{q}_{423}^{red}$	7 h 30′	12	19 933
MoS/MX $\boldsymbol{q}_{441}$	96 h 10′	10	101 255
MoS/MX $\boldsymbol{q}_{441}^{red}$	1 h 25′	4	11 453

been discussed in previous computational studies;[63,64] in these, the authors also show that the use of a truncated Taylor expansion representing the potential energy abstracts the cost of a full AIMD when computing thermal conductivity. As for any computational model, the optimal simulation setup is the result of a compromise between the computational requirements and the accuracy of the produced data. The procedure to obtain an accurate evaluation of $\boldsymbol{\Theta}_p$ is not the subject of the present discussion, as it does not depend on the ND framework; the reader can find information on the subject in any computational work that makes use of the $\boldsymbol{\Theta}_p$ tensor (see Ref. 62 as an example). Instead, the choice of the $\{\boldsymbol{q}_i\}$ set is crucial to obtain reliable results from ND simulations.

In the present implementation of the ND technique within the PINDOL code, the computational load mainly depends on the number of elements in the $\boldsymbol{\Phi}_3$ tensor; such a number, in turn, depends on the number of $\boldsymbol{q}$-points considered, on the number of phonon modes per $\boldsymbol{q}$-point (i.e., $3N$), and on the components of the vectors forming the $\{\boldsymbol{q}_i\}$ set. In fact, only the phonon triplets $(\boldsymbol{q}, \boldsymbol{q}_1, \boldsymbol{q}_2)$ that satisfy the selection rule $\Delta(\boldsymbol{q} + \boldsymbol{q}_1 + \boldsymbol{q}_2) = 1$ are considered in the generation of the $\boldsymbol{\Phi}_3$ elements, as all the other triplets produce null elements.[32,43] In Table I, we report the simulation time for all the case studies that we consider; with $\boldsymbol{q}_{mnp}$, we indicate a complete $\{\boldsymbol{q}_i\}$ set formed by corresponding $N_{\boldsymbol{q}}$ $\boldsymbol{q}$-points, representing an $m \times n \times p$ supercell. The superscript "*red*" indicates that the set is formed by reducing the full sampling to only the irreducible $\boldsymbol{q}$-points; this has been obtained with the help of the SPGLIB library,[65] which is capable of exploiting the symmetries of the unit cell. We anticipate that, by inspecting Table I, in some cases, the use of a reduced set can drastically cut the computation time when compared with the full set case. For example, the time required to run the Si $\boldsymbol{q}_{555}$ case is reduced by 97% when the reduced $\boldsymbol{q}_{555}^{red}$ set is used, while in the case of the U and MoS_2/MX_2 systems, the time is reduced by 36% and 98%, respectively.

A. Convergence of the phonon dispersion with respect to the number of *q*-points

As mentioned already, one of the main quantities governing the accuracy of the ND simulation is the sampling of the reciprocal space. In order to show this, we consider the Si crystal structure with the symmetries of the space group $Fd\bar{3}m$ (group number 227). The starting geometry is the primitive unit cell with an optimized lattice parameter $a_p = 3.852$ Å, corresponding to the lattice parameter $a_c = 5.448$ Å of the conventional face centered cubic unit cell. The primitive cell contains only two Si atoms with reduced positions $(3/4, 3/4, 3/4)$ and $(1/2, 1/2, 1/2)$, respectively.

The interatomic forces are calculated within the density functional theory framework as implemented in the ABINIT software.[66–68] The Si atomic type is represented by a norm-conserving pseudopotential generated following the Troullier–Martins scheme[69] in the Kleinman–Bylander form,[70] considering four electrons in the valence shell and a cutoff radius of 2.1 Böhr, leading to a cutoff energy equal to 380 eV. Concerning the Self Consistent Field (SCF) parameters, we select the LDA Teter parameterization[71] as an energy functional, a 13 × 13 × 13 Monkhorst–Pack mesh[72] to sample the Brillouin zone, and a plane wave cutoff equal to 500 eV; convergence is considered to be achieved when the difference in the total energy after three subsequent SCF cycles is below 3×10^{-10} eV. The starting atomic positions and lattice parameters are fully relaxed within a tolerance of 10^{-6} eV/Å; after relaxation, the structure preserves the initial cubic symmetry with a primitive (conventional) lattice parameter equal to 3.853 Å (5.445 Å), in good agreement with the experimental values.

In order to show how Brillouin zone sampling determines the accuracy of the ND simulations, we consider the harmonic phonon dispersion obtained from the finite displacements method[61] as our reference and compare it with the one calculated from the effective force constants extracted from the normal dynamics trajectory. To achieve this aim, the ND simulations are performed at different $\boldsymbol{q}$-samplings in the NVT ensemble with temperatures as low as 10 K in order to avoid anharmonic effects. Irrespective of the sampling, the maximum harmonic frequency is found to be $\nu_{\max} \sim 11$ THz; according to the Nyquist–Shannon theorem, the time step can be $\Delta t = 1/(2\nu_{\max}) \sim 23$ fs, but we reduce it to 1 fs as a safe value. The simulation window is 4 ns for a total of 4×10^6 dynamics steps. The time needed for each ND simulation is reported in Table I.

For the first ND simulation, we select a 3 × 3 × 3 Monkhorst–Pack sampling, corresponding to the complete set $\boldsymbol{q}_{333}$ ($N_{\boldsymbol{q}_{333}} = 14$) representing a 3 × 3 × 3 supercell. We observe that the phonon dispersion obtained from the effective force constants does not correctly reproduce the reference one (Fig. 1). We then increase the sampling of the reciprocal space by repeating the simulation with a 5 × 5 × 5 mesh, corresponding to the complete set $\boldsymbol{q}_{555}$ ($N_{\boldsymbol{q}_{555}} = 63$); in this case, we obtain an improvement of the phonon dispersion. As a further test, we then perform the same simulation by using the set $\boldsymbol{q}_{555}^{red}$ ($N_{\boldsymbol{q}_{555}^{red}} = 10$), obtained by reducing the full 5 × 5 × 5 mesh sampling to only the irreducible (and non-redundant) $\boldsymbol{q}$-points. In addition, in this case, we obtain a close agreement with the reference; this shows that similar accuracy can be reached via reciprocal space mesh sampling with reduced size. In this case, we used $2 \times 3 \times N_{\boldsymbol{q}_{555}^{red}} = 60$ dynamical variables, that is 5/7 and ~1/6 of the full 3 × 3 × 3 and 5 × 5 × 5 sampling, respectively ($2 \times 3 \times N_{\boldsymbol{q}_{333}} = 84$, $2 \times 3 \times N_{\boldsymbol{q}_{555}} = 378$). A further improvement has been obtained by considering the set $\boldsymbol{q}_{666}^{red}$ ($N_{\boldsymbol{q}_{666}^{red}} = 16$).

It is worth pointing out that, as described above, we could have proceeded in an alternative way. For example, we could have started from the set containing only the Γ and $(1/5, 1/5, 1/5)$ $\boldsymbol{q}$-points and

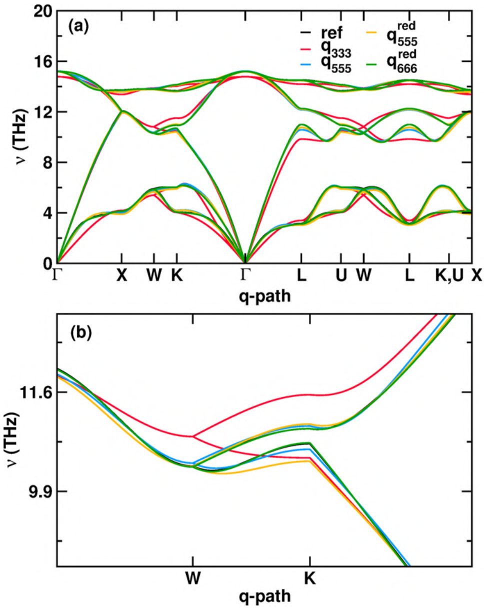

FIG. 1. (a) Phonon dispersion of crystalline silicon as obtained from the frozen phonon approach (ref) and extracted from the effective force constants at 10 K at different sampling sets. (b) Details of the phonon dispersion in (a). The best agreement is obtained for the $\boldsymbol{q}_{666}^{red}$ sampling; for this reason, the black line representing the reference dispersion is barely visible.

incrementally added further points until we reached agreement with the reference phonon dispersion. However, the irreducible $\boldsymbol{q}$-point set contains high symmetry points, which are likely[73] to have a large role in the determination of the system dynamics. For this reason, and considering the little computation time, we decided to skip the incremental test and selected the mentioned $\{\boldsymbol{q}\}$ sets as case examples. Such an approach also has the advantage that it does not require manual effort from the user thanks to the availability of libraries (e.g., SPGLIB[65]) that can automatically provide the list of the reduced set of $\boldsymbol{q}$-points. Finally, it must be noted here that the accuracy of the phonon dispersion cannot be further improved when the sampling corresponds to supercells, including interatomic distances larger than the cutoff range used to calculate the force constants.

B. Stabilization of the optical Γ-Y branch in α-U

Let us now consider the case of α-uranium, where the effect of temperature is explicitly investigated. By lowering the temperature, uranium is known to undergo a phase transition at 50 K due to the softening of the longitudinal optical phonon mode in the [100] direction, involving the doubling of the unit cell.[74–77] In Ref. 31, this phenomenon has been studied by means of AIMD simulations performed by using hundreds to thousands of processors; here, we propose the same study carried out by means of ND simulations, each executed on one processor, and by using a computational setup equivalent to that adopted in the same published AIMD work. This shows that the ND approach enables one to perform the same study with reduced computational resources.

More in detail, we carried out ND simulations in the NVT ensemble at 50, 300, and 900 K, with a simulation window equal to 6 ns; the Brillouin zone sampling is performed by using the irreducible points of the $4 \times 2 \times 3$ Monkhorst–Pack mesh ($\boldsymbol{q}_{423}^{red}$ set), while the time step is set at 1 fs, being the maximum harmonic frequency equal to ~3.65 THz. In this case, we chose not to perform the convergence study as in the previous case, as here our main goal is to make a direct comparison with the results reported in Ref. 31. The lattice parameters and atomic positions of the reference structures are taken from experimental data at each considered temperature,[78–81] as has been done in previous simulations.[82] The interatomic forces are calculated within the density functional theory framework as implemented in the VASP software.[83–87] The plane wave energy cutoff is set to 435 eV, the k-mesh sampling to $2 \times 4 \times 2$ divisions according to the Monkhorst–Pack scheme, and the tolerance on the SCF convergence to 10^{-8} eV. The phonon and the third-order force constants have been calculated by using $4 \times 2 \times 3$ supercells of the conventional unit cell.

In Fig. 2, we report the phonon dispersion of the longitudinal optic-like phonon mode calculated by using the standard finite displacement approach, which does not take into account the effect of the temperature; in the same figure, for comparison, we report the phonon dispersion extracted from the ND simulations at the selected temperatures by calculating the corresponding effective interatomic force constants. The reference phonon dispersions [calculated with the finite displacement approach in Figs. 2(a)–2(c) and with DFPT in Figs. 2(d) and 2(e)] are evaluated at the experimental lattice parameters and atomic positions obtained at each temperature, as shown in Ref. 31. By comparing the dispersions at different temperatures, we observe that the ND simulations capture the hardening of the soft mode as the temperature increases, unlike the finite displacement approach [black line in Fig. 2, panels (a)–(c)]; this is expected because the phonon interaction is not taken into account in the latter method. We notice that the position of each dispersion minimum extracted from the ND simulations is slightly shifted with respect to the reference; we believe that this occurs for the following reason: The ND simulations are run using a primitive unit cell in order to exploit the computational advantages of the ND formalism; such a cell is obtained by means of the SPGLIB library,[65] which follows the convention of the Bilbao Crystallographic Server.[88,89] Our reference band dispersion is instead calculated by using the conventional unit cell as we think it is used in Ref. 31; in fact, we could not find enough computational details in Ref. 31, such as, for example, the specific settings (standard or arbitrary) and orientation of the unit cell used in the AIMD simulations. For this reason, we cannot determine the relative orientation between the conventional cell used for the reference and the primitive cell used for the ND simulations. We here recall that the components of the lattice parameters of the direct unit cell uniquely determine the components of the lattice parameters of the reciprocal unit cell, hence the coordinates of all the points of any path in the reciprocal space. Therefore, different direct lattice parameters generate different components of the points along the Γ-Y path and, as a consequence, a different position of the reference and ND-obtained dispersion minima. However, such a difference is small, and the experimentally observed hardening of the soft mode is reproduced by both ND and AIMD simulations. In addition, the quasi-harmonic approximation is not able to account for the frequency shift, while explicit temperature effects must be

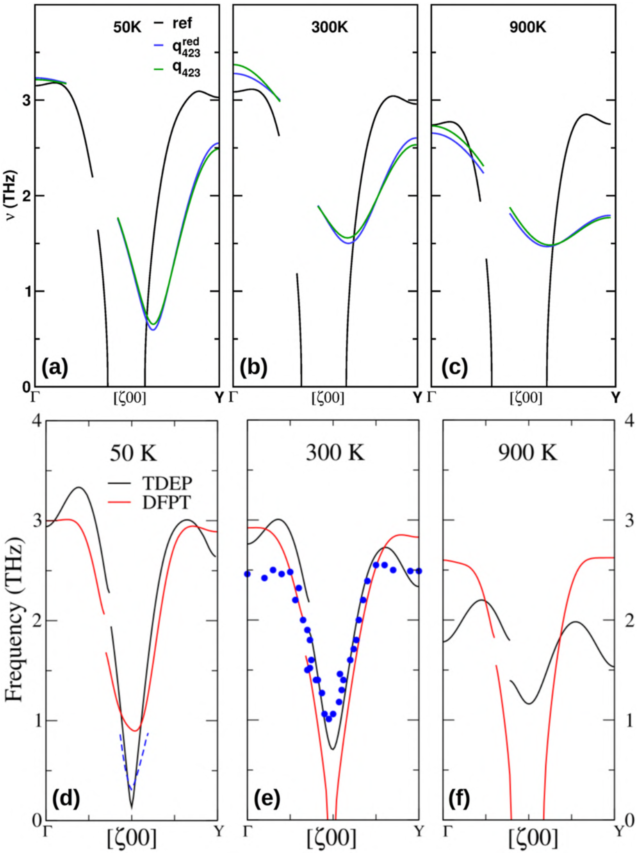

FIG. 2. Optic-like longitudinal branch of α-U at (a) 50 K, (b) 300 K, and (c) 900 K. The black, blue, and green lines represent the phonon dispersion obtained by the finite displacement approach and extracted from the ND simulations at the reduced ($\boldsymbol{q}^{red}_{423}$) and full ($\boldsymbol{q}_{423}$) sampling sets, respectively. Panels (d)–(f) are an adapted reproduction of Fig. 9 reported in Ref. 31 here reported for comparison; in such panels, black and red lines represent the results obtained by considering finite temperature effects explicitly and density functional perturbation theory, respectively. Experimental neutron-scattering data at 30 K[76] are denoted by a dashed line in panel (d) and at room temperature[75] by blue circles in panel (e), both here shown in the same way as in Ref. 31.

considered, as has been shown in the AIMD study, which we consider here for comparison.[31] The time needed to produce each ND trajectory is about 7 h 30′ (Table I) on a standard desktop computer (Sec. III). Finally, in order to show the computational benefits of working with a reduced set of $\boldsymbol{q}$-points, we also performed the calculations using the complete set. One can notice that there is no appreciable difference in accuracy between the two calculations, while the computational speedup is about 36% (see Table I).

C. Raman shift in MoS_2/MX_2 bilayers

Heterostructures based on layered transition metal dichalcogenides (TMDs) find application in many fields, including photovoltaic devices, lithium-ion batteries, hydrogen evolution catalysis, desulfurization of fossil fuels, transistors, photodetectors, DNA detection, nanoelectromechanical systems, memory devices, and tribology.[90–97] Research in these fields relies on local and noninvasive characterization methods capable of identifying the evolution of the physical properties with the number of layers and the temperature, assessing sample quality, and probing interlayer interactions; in this context, Raman spectroscopy is the technique of choice.[98] The positions of the Raman peaks depend on the Brillouin zone center phonons and their effective frequencies, as determined by phonon–phonon scattering processes; as a consequence, the positions depend on the temperature of the sample. Since the proper labeling of the Raman spectrum is central to the characterization of the material, the evolution of the peak position with temperature must be determined with adequate accuracy.

Transition metal dichalcogenides are layered structures with the general formula MX_2; each MX_2 layer is composed of a transition metal M atomic layer sandwiched between two chalcogen X atomic layers, while adjacent MX_2 layers are bound by weak van der Waals forces. In the present study, we consider bilayer heterostructures with M = Mo, W and X = S, Se. The space group symmetry of such systems is $P3m1$ (group number 156), with point group $3m$ (C_{3v} in Schöenflies notation[99]); accordingly, the active Raman modes own the character of the E and A representations.[100] The temperature effect on the E and A Raman peaks with the largest intensities has been studied experimentally mainly in MX_2 homostructures[101–105] and a few different heterostructures;[106–108] however, a full *ab initio* treatment is generally missing due to the highly demanding computational resources needed to run the supporting AIMD simulations. Here, we exploit the ND scheme to perform atom dynamics simulations with temperature values in the range [50, 500] K. Our references are the experimental 2H polymorph geometries of the MoS_2,[109] $MoSe_2$,[110] and WS_2[111] bulk systems. For each structure, we consider two subsequent MX_2 layers and set the length of the $\boldsymbol{c}$ crystallographic axes to 40 Å. We then substitute the Mo and S atoms in one layer with W and Se, respectively; in this way, we obtain the model geometries for the $MoS_2/MoSe_2$, MoS_2/WS_2, and MoS_2/WSe_2 bilayer heterostructures, which we name as MoS/MoSe, MoS/WS, and MoS/WSe, respectively (Fig. 3).

The optimized geometries and the interatomic forces are calculated within the density functional theory framework as implemented in the ABINIT software.[66–68] The plane wave energy cutoff is set to 500 eV and the Monkhorst–Pack k-mesh to 11 × 11 × 1 divisions, while the tolerance on the SCF and the geometry convergence are set to 10^{-8} eV and 2.6×10^{-7} eV Å^{-1}, respectively. Following the results of previous studies,[112] we select the vdw-DFT-D3(BJ) correction[113] to account for the van der Waals interactions. The phonon spectrum and the third-order force constants have been calculated

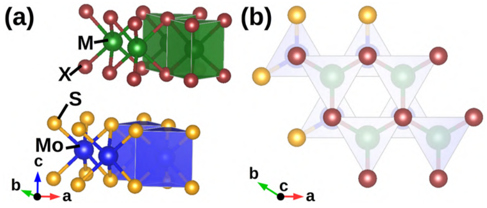

FIG. 3. (a) Lateral and (b) $\boldsymbol{c}$-axis views of the model geometry of the trigonal P3m1 MoS/MX systems (M = Mo, W; X = S, Se).

by using $3 \times 3 \times 1$ supercells of the conventional unit cell. The effective force constants have been obtained from ND simulations in the NVT ensemble at 50, 100, 150, 200, 250, 300, 350, 400, 450, and 500 K by using the irreducible points of the $4 \times 4 \times 1$ Monkhorst–Pack mesh ($\boldsymbol{q}_{441}^{red}$ set); the simulation window is 4 ns, and it has been sampled with a time step equal to 1 fs. The corresponding Raman spectra have been obtained by means of the PHONOPY-SPECTROSCOPY tool,[114] which implements the formalism described in Ref. 115. The intensity I of the Raman signal at a frequency ν and temperature T is calculated as

$$I(\nu, T) = \sum_{\lambda} \frac{I_0(\lambda)}{\pi} \frac{\frac{1}{2}\Gamma_\nu(\lambda, T)}{(\nu - \nu(\lambda))^2 + \left(\frac{1}{2}\Gamma_\nu(\lambda, T)\right)^2}, \tag{11}$$

where $I_0(\lambda)$ is the height of a delta function at the frequency $\nu = \nu(\lambda)$ of the Raman active mode λ obtained from the second order force constants, while the base intensity is spread over a range of frequencies due to the measurement uncertainty arising from the finite lifetime of the mode $\tau(\lambda, T) = \frac{1}{2\Gamma(\lambda, T)}$.

In turn, $\Gamma(\lambda, T)$ is calculated as

$$\begin{aligned} \Gamma(\lambda, \omega, T) = {} & \frac{18\pi}{\hbar^2} \sum_{\lambda'\lambda''} |\Phi_{-\lambda\lambda'\lambda''}|^2 \\ & \times \{[n(\lambda', T) + n(\lambda'', T) + 1]\delta[\omega - \omega(\lambda') - \omega(\lambda'')] \\ & + [n(\lambda', T) - n(\lambda'', T)][\delta[\omega + \omega(\lambda') - \omega(\lambda'')] \\ & - \delta[\omega - \omega(\lambda') + \omega(\lambda'')]]\}, \end{aligned} \tag{12}$$

where $\Phi_{\lambda\lambda'\lambda''}$ are the Fourier transforms of the third order force constants obtained at the temperature T, n is the occupation number of the mode λ at the temperature T calculated from the Bose–Einstein distribution, and $\omega = 2\pi\nu$.

The delta functions in Eq. (12) enforce the conservation of energy, and the mode linewidths $\Gamma(\lambda, T)$ are obtained by setting $\omega = \omega(\lambda)$.

The force constants that are fed into such formulations are extracted from each ND trajectory by means of the HIPHIVE software,[34] as described at the beginning of Sec. III.

The Raman active phonons are those belonging to the center of the Brillouin zone; therefore, only the phonons at $\boldsymbol{q} = \Gamma$ will be considered in our analysis. Irrespective of the system, all such phonons are Raman active; however, most Raman intensity concentrates in three intense peaks, two with the E character and one with the A character, which we label as E^1, E^2, and A, respectively. Each peak corresponds to a specific set of atom displacements, i.e., the phonon eigenvector, which identifies in a unique way the phonon responsible for a specific Raman transition (Fig. 4). It is, therefore, crucial to correctly characterize the eigendisplacements of the Raman active phonons in order to properly describe the layer interactions, track their evolution with any change in temperature, and compare their position across different chemical compositions.

We begin our analysis by taking the MoS/MoSe system as a reference. In order to find the corresponding E^1, E^2, and A peak positions in the MoS/WS and MoS/WSe systems, it is not enough to compare the eigenfrequency values and select the closest ones with the same character (i.e., E or A). In fact, at fixed character, the corresponding atom displacements might be different, despite the small difference between the two frequency values. Therefore, in order to make a one-to-one correspondence among Raman peaks obtained at different temperatures and chemical compositions, we must identify the phonons with eigenvectors generating the same set of atom displacements. To achieve this aim, we can compare the eigendisplacements by direct inspection with suitable visualization software;[116,117] however, this is a non-rigorous and time-consuming approach. We choose instead to consider the scalar product between the real part of the phonon eigenvectors as a quantitative measure of the similarity between two sets of atomic displacements: the two sets are identical if the angle between the eigenvectors is null, while the smaller the angle, the more similar the displacement sets. In this way, we can systematically scan the eigenvectors of the MoS/WS and MoS/WSe systems and make a quantitative comparison with those of the reference (i.e., MoS/MoSe) generating the E^1, E^2, and A Raman peaks. We report the formalism in Sec. VII of the supplementary material, and implement it in the `eigmap` code.[118] The formalism is analogous to the one used in Ref. 119 to calculate the atom character of phonon eigenvectors. Following this phonon map procedure, we label the Raman peak positions of the three systems as shown in Fig. 5. We notice that the displacement pattern generating the A peak in MoS/WS does not correspond to the one generating the A peak in MoS/MoSe. This proves that a mapping procedure is actually needed in order to perform the correct peak attribution.

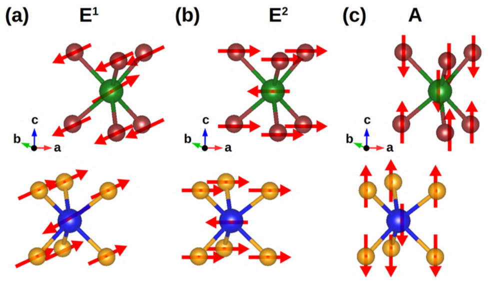

FIG. 4. Atom displacement patterns (red arrows) generating the most intense Raman peaks in the MoS/MX systems. The color code for the atoms is the same as in Fig. 3.

We now track the evolution of the modes with the temperature in each system. Let us recall here that the phonon modes are ordered

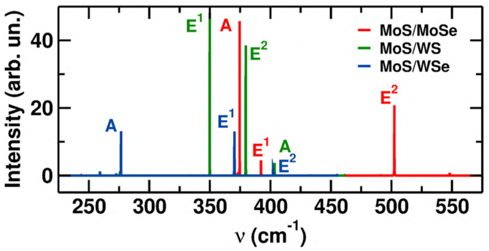

FIG. 5. Raman spectrum of the MoS/MX systems at 50 K. We focus the frequency range on the Raman signals with the largest intensity; the width of the peaks is not clearly visible due to the low temperature and the range of values chosen for the x-axis. The displacement pattern generating the A peak in MoS/WS does not correspond to the one generating the A peak in MoS/MoSe.

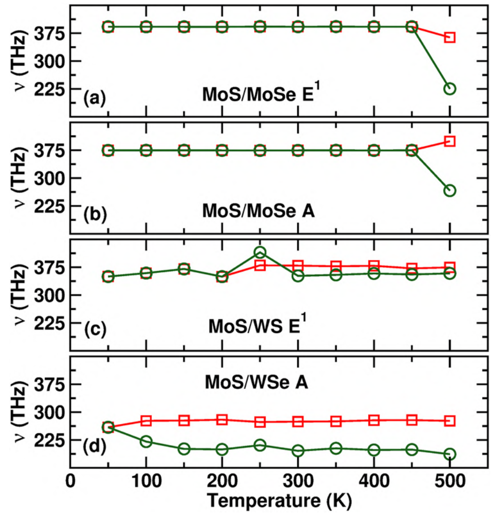

FIG. 6. Evolution of the Raman peaks of the systems with temperature. The right and wrong assignments are indicated by green and red symbols, respectively. Lines are a guide for the eye.

according to increasing eigenfrequencies and labeled with increasing integer numbers. Here, we would like to stress that, by increasing the temperature, the ordering of the modes can, in principle, change, and therefore, a mapping procedure is needed in order to perform a meaningful attribution. We first consider the MoS/MoSe system and focus on the peak E^1 at 392.35 cm^{-1} calculated at 450 K; this peak is labeled as $j = 12$. If we neglect the phonon mapping based on the atomic displacements and characterize the peaks only on the basis of the E symmetry and the difference between the frequencies, that peak would be considered shifted down to 363.54 cm $^{-1}$ at 500 K [Fig. 6(a)]. Such a Raman signal is generated by the phonon mode $j = 15$. However, the displacement pattern of the two phonons is different. Instead, by means of the phonon mapping procedure discussed above, we understand that at 500 K, the E^1 peak is shifted down to 225.29 cm^{-1}, the latter generated by the mode $j = 9$ having the same eigendisplacement pattern as the mode $j = 12$ calculated at 450 K. This again shows that it is not enough to focus on a specific label of a phonon mode and track how its frequency changes at varying temperatures; at the same time, phonon labeling cannot be used to track the frequency of a phonon mode across different temperatures, as the label changes as the frequency of the phonon changes. Concerning peak A at 500 K, if the phonon displacement is not taken into account, a frequency of 399.42 cm $^{-1}$ instead of 266.25 cm $^{-1}$ would be assigned [Fig. 6(b)]. The abrupt drop of the E^1 and A frequencies going from 450 to 500 K is due to a sensitive softening of the corresponding phonon modes, indicating the possible appearance of structural instabilities at higher temperatures. Finally, in the MoS/WS and MoS/WSe systems, the erroneous attribution may occur already at 200 K [Fig. 6(c)] and 50 K [Fig. 6(d)], respectively.

The results show that a careful analysis of the phonon eigenvectors is essential for the correct assignment of the character of Raman peaks. This study has been feasible thanks to the ND scheme; in fact, it has made it possible to run dynamics simulations with a limited amount of computational resources (Table I). As done for the previous case studies, we also performed the same calculations using the complete set of $\boldsymbol{q}$-points. We recall that considering the complete set corresponds to perform dynamical simulations in the Cartesian space (i.e., the number of dynamical variables to be integrated is the same). In addition, in this case, it turned out that using a reduced set of $\boldsymbol{q}$-points leads to a computational speedup, specifically of about 98% of the walltime. Finally, we would like to note that the scheme avoided the burden of parameterizing classical force fields, which are specific to the TMD chemical topology and composition considered in this case study.

D. Limitations of the ND approach

At the moment, being in their infancy, both the ND formulation and the PINDOL code show several limitations, which we plan to overcome as future developments of the present work.

The Cartesian tensors $\boldsymbol{\Theta}_p$, hence their Fourier transform $\boldsymbol{\Phi}_p$, representing the interatomic force constants, are evaluated by considering small atomic displacements from the reference position. However, during the dynamics, the atomic positions can change significantly, and, accordingly, the actual force constants might become very different from those provided as input to the simulation. This can be the case, for instance, of phase changes or diffusion of an adatom on a surface. In such scenarios, the computed normal forces may no longer be accurate. Moreover, the use of truncated polynomials as in Eq. (3) may produce unphysical saddle points in the potential energy landscape that lead to regions where the energy is not lower-bounded, with a possible divergence of the total energy during the dynamics.[120] In order to tackle this issue, perturbative approaches can be used.[121] Another possibility is the use of a multireference scheme. In fact, in cases where interrupting the dynamics and restarting it with a different reference configuration are not major issues, it is possible to foresee that a (possibly automatized) procedure of updating the $\boldsymbol{\Phi}_p$ tensors can be employed. For example, it is, in principle, possible to introduce a tolerance on the atomic displacements (set by the user at the beginning of the simulation), and if during the simulation the displacement of some atom becomes larger than the set tolerance, then the simulation is stopped. At this point, a new reference configuration can be created (such configuration may be built, e.g., by averaging the atom positions over a specified time window before the simulation stopped) and used as an input, together with the atomic positions and forces obtained in such a time window, for example, for the temperature dependent effective potential (TDEP) method[31] or the HIPHIVE code,[34] which will yield the updated force constants. Alternatively, the new reference configuration can be used to recalculate the phonons and the $\boldsymbol{\Phi}_p$ tensors with the same procedure used to prepare the input for the ND simulation. Both the tolerance on the atom displacements and the width of the time window can be chosen by the user. The former might be estimated from the variation of the total energy with respect to the starting configuration, while the latter should correspond to the last part of the trajectory where the interatomic distances are considered to be constant. At the moment, we have not implemented the tolerance check in PINDOL, but we plan to do it in future versions. At any rate, it must be stressed that even in cases where producing discontinuous dynamics is not an issue, if the potential energy surface of the system under study is very corrugated, that is, if it presents a large number of local minima separated by low barriers (which is the case for, e.g., proteins[122]), then the benefits deriving from the exploitation of the ND scheme can be easily nullified by the need to frequently update the description based on the reference configuration. Nevertheless, we are confident that the proposed technique can be exploited for the investigation of a still large set of systems.

Moreover, when the phonon lifetimes are shorter than the Ioffe–Regel limit in time, it is no longer possible to describe phonon scattering in terms of the phonon wave vector $\boldsymbol{q}$ and index j, and the anharmonic effects here accounted for by the $\boldsymbol{\Phi}_p$ tensors require a different formulation.[123] For this reason, the present ND formulation is valid whenever the $\boldsymbol{\Phi}_p$ tensors are a good approximation of the anharmonic effects, the latter being the case of the majority of the simulation studies on lattice anharmonicity reported in the literature.

Concerning the PINDOL code, the amount of memory to store the $\boldsymbol{\Phi}_3$ tensor is minimized by exploiting its properties; the full tensor is reconstructed on the fly when evaluating the sum in Eq. (5), and the number of operations depends on the kind of triplet (see Sec. VI of the supplementary material). The computation time can then be reduced by a suitable parallelization of this step, which will be realized in the next version of the PINDOL code. At the moment, a simple OpenMP parallelization has been implemented but not used for the case studies discussed here. The size of the $\boldsymbol{\Phi}_3$ tensor can be further reduced by taking into account the phonon–phonon scattering selection rules involving the mode eigenvectors;[49] however, this feature is not yet implemented in the present version of PINDOL.

IV. CONCLUSIONS AND OUTLOOK

In this paper, we present the normal dynamics technique, introducing the theoretical background and showing its applicability in three case studies thanks to the open-source implementation that we developed.[54] These are some examples of the many possible uses of the proposed technique. In fact, normal dynamics simulations can produce dynamical trajectories that can be analyzed to calculate temperature- and pressure-dependent quantities, which are usually calculated with existing molecular dynamics techniques. With respect to these latter, among the advantages of the ND scheme, it is worth recalling that (i) we do not need to parameterize interatomic potentials specific to the system's chemical composition and topology and (ii) we can produce long dynamical trajectories of large systems on an ordinary desktop computer. The normal dynamics scheme also provides a straightforward decomposition of the atomic motions in terms of normal coordinates, thus facilitating the analysis of several phenomena such as heat transfer,[124–126] hydrodynamic phonon transport,[127] carrier transport,[128] thermoelectric effect,[129] and energy dissipation in tribological conditions.[48] The normal equations of motion can be modified in order to include atomic constraints or the presence of external forces that may simulate, for example, an external field exciting specific phonon modes[130,131] or dragging forces producing atomic drifts;[132,133] indeed, we plan to develop the corresponding equations and add such features in future versions of the PINDOL software. This approach can also pave the way for a novel route to study the entangled electronic and dynamic features. In fact, by calculating the $\boldsymbol{\Phi}_p$ tensors for both the ground and the excited state(s), it would be possible to run multiple parallel normal dynamics simulations coupled in a replica exchange fashion,[134] thus making it possible to investigate how electronic excited states determine the atom dynamics at a finite temperature. We finally note that the PINDOL software and the calculation of the $\boldsymbol{\Phi}_p$ tensors can be interfaced with structure databases[135,136] and used in high-throughput calculations[137] for the discovery of new materials with target physical properties.

Standard molecular dynamics simulations require large unit cells in order to take into account long-range distortions. This results in a computational load that rapidly scales with the number of atoms; the situation is even worse if *ab initio* methods are to be used because of accuracy reasons and/or a lack of force fields. In these cases, the computational requirements might become unaffordable for the majority of researchers. The normal dynamics sampling scheme overcomes these difficulties. Since the equations of motion are integrated in the reciprocal space, a computational speedup can be obtained by a sensible selection of the considered $\{\boldsymbol{q}\}$-points. In fact, optimal sampling can be achieved via the exploitation of the symmetries of the unit cell, a systematic increase in the $\{\boldsymbol{q}\}$ set size, or any user-decided choice of the reciprocal points. The $\{\boldsymbol{q}\}$ set determines the size of the simulated direct unit cell; each $\boldsymbol{q}$-point of the kind $(1/m, 1/n, 1/p)$ represents an $m \times n \times p$ supercell by using only $6N$ instead of $3N \times m \times n \times p$ variables; this makes it possible to consider the effect of long-wave structural modulations at a limited computational load.

The sampling scheme of the normal dynamics technique implicitly includes periodic boundary conditions. The periodicity of the system is, in fact, accounted for by the use of the reciprocal space integration scheme, which is based on the concept of phonons. Nonetheless, the normal dynamics approach is also able to simulate semiperiodic or finite systems such as nanoclusters or molecules. Examples of semiperiodic systems are the MoS_2/MX_2 bilayers discussed in the last case study, for which we chose sets of the kind $\{(q_a, q_b, 0)\}$ in order to truncate the periodicity along the $\boldsymbol{c}$ axis. Finite (non-periodic) systems, instead, can be simulated by using only the Γ point, even though in this case the benefits coming from a custom selection of the reciprocal space are no longer in place.

Most of the computation time is spent for the evaluation of the sum in Eq. (8), appearing also in the NVT equations in Eq. (9), and depends on the number of $\Phi_{\lambda\lambda'\lambda''}$ elements; however, the latter is not directly proportional to the number of $\boldsymbol{q}$-points in the set. In fact, the scattering rule $\Delta(\boldsymbol{q} + \boldsymbol{q}_1 + \boldsymbol{q}_2) = 1$[32,43] excludes the $\{\lambda, \lambda_1, \lambda_2\}$ triplets that do not satisfy it and sets the corresponding $\Phi_{\lambda\lambda'\lambda''}$ elements to zero. This reduces the number of terms in the sum, but whether the rule is satisfied or not depends on the components of the points in the set. Another control of the computational load can then be obtained by selecting suitable $\boldsymbol{q}$-points that limit the number of $\Phi_{\lambda\lambda'\lambda''}$ elements but also provide accurate results.

The results that we presented show that, in order to run long dynamical simulations on large systems, it is not always necessary to expand our computational capabilities (e.g., from standard to quantum computers); instead, as an alternative, it is better to focus on reducing the related computational demand, thus minimizing energy consumption, power costs, and technological effort. In this respect, the normal dynamics sampling scheme represents a tool to perform all-atom dynamical simulations on an ordinary desktop computer, making the generation of dynamical trajectory calculations more and more accessible to a larger audience of researchers.

SUPPLEMENTARY MATERIAL

See the supplementary material for the detailed descriptions of the notation used (Sec. I), the derivation of the equations reported in the main text (Secs. II–IV), the partitioning of the $\boldsymbol{q}$-point set (Sec. V), how to prepare, run, and post-process ND simulations (Sec. VI), and the mapping procedure described in the third case study (Sec. VII).

ACKNOWLEDGMENTS

We thank Elliot Perviz for checking the English form of the output messages in the PINDOL software. This work was co-funded by the European Union under the project "Robotics and advanced industrial production" (Reg. No. CZ.02.01.01/00/22_008/0004590). The authors also acknowledge the financial support of the Austrian Science Fund (FWF), Project No. I 4059-N36, and the Czech Science Foundation, Project No. 19-29679L. A.C. acknowledges the financial support of the Czech Science Foundation, Project No. 24-12643L. This work was supported by the Ministry of Education, Youth, and Sports of the Czech Republic through e-INFRA CZ (ID:90254). Access to the computational infrastructure of the OP VVV funded Project No. CZ.02.1.01/0.0/0.0/16_019/0000765 "Research Center for Informatics" is also acknowledged.

AUTHOR DECLARATIONS

Conflict of Interest

The authors have no conflicts to disclose.

Author Contributions

Antonio Cammarata: Conceptualization (equal); Formal analysis (equal); Funding acquisition (equal); Investigation (equal); Methodology (equal); Software (equal); Writing – original draft (lead); Writing – review & editing (equal). **Miljan Dašić**: Formal analysis (equal); Investigation (equal); Methodology (equal); Software (equal); Writing – review & editing (equal). **Paolo Nicolini**: Conceptualization (equal); Formal analysis (equal); Funding acquisition (equal); Investigation (equal); Methodology (equal); Software (lead); Supervision (equal); Writing – review & editing (equal).

DATA AVAILABILITY

The PINDOL code presented in this paper is publicly available under open-source license at https://github.com/acammarat/pindol. The data that support the findings of this study are available from the corresponding authors upon reasonable request.

REFERENCES

[1] D. Frenkel and B. Smit, *Understanding Molecular Simulation: From Algorithms to Applications* (Academic Press, San Diego, CA, 1996).

[2] W. D. Cornell, P. Cieplak, C. I. Bayly, I. R. Gould, K. M. Merz, D. M. Ferguson, D. C. Spellmeyer, T. Fox, J. W. Caldwell, and P. A. Kollman, "A second generation force field for the simulation of proteins, nucleic acids, and organic molecules," J. Am. Chem. Soc. **117**, 5179–5197 (1995).

[3] W. L. Jorgensen and J. Tirado-Rives, "The OPLS [optimized potentials for liquid simulations] potential functions for proteins, energy minimizations for crystals of cyclic peptides and crambin," J. Am. Chem. Soc. **110**, 1657–1666 (1988).

[4] B. R. Brooks, R. E. Bruccoleri, B. D. Olafson, D. J. States, S. Swaminathan, and M. Karplus, "CHARMM: A program for macromolecular energy, minimization, and dynamics calculations," J. Comput. Chem. **4**, 187–217 (1983).

[5] W. R. P. Scott, P. H. Hünenberger, I. G. Tironi, A. E. Mark, S. R. Billeter, J. Fennen, A. E. Torda, T. Huber, P. Krüger, and W. F. van Gunsteren, "The GROMOS biomolecular simulation program package," J. Phys. Chem. A **103**, 3596–3607 (1999).

[6] A. K. Rappe, C. J. Casewit, K. S. Colwell, W. A. Goddard, and W. M. Skiff, "UFF, a full periodic table force field for molecular mechanics and molecular dynamics simulations," J. Am. Chem. Soc. **114**, 10024–10035 (1992).

[7] K. Chenoweth, A. C. T. van Duin, and W. A. Goddard, "ReaxFF reactive force field for molecular dynamics simulations of hydrocarbon oxidation," J. Phys. Chem. A **112**, 1040–1053 (2008).

[8] J. Wildman, P. Repiščák, M. J. Paterson, and I. Galbraith, "General force-field parametrization scheme for molecular dynamics simulations of conjugated materials in solution," J. Chem. Theory Comput. **12**, 3813–3824 (2016).

[9] D. Dubbeldam, K. S. Walton, T. J. H. Vlugt, and S. Calero, "Design, parameterization, and implementation of atomic force fields for adsorption in nanoporous materials," Adv. Theory Simul. **2**, 1900135 (2019).

[10] J. A. Harrison, J. D. Schall, S. Maskey, P. T. Mikulski, M. T. Knippenberg, and B. H. Morrow, "Review of force fields and intermolecular potentials used in atomistic computational materials research," Appl. Phys. Rev. **5**, 031104 (2018).

[11] D. Dubbeldam, S. Calero, T. J. H. Vlugt, R. Krishna, T. L. M. Maesen, E. Beerdsen, and B. Smit, "Force field parametrization through fitting on inflection points in isotherms," Phys. Rev. Lett. **93**, 088302 (2004).

[12] R. M. Betz and R. C. Walker, "Paramfit: Automated optimization of force field parameters for molecular dynamics simulations," J. Comput. Chem. **36**, 79–87 (2015).

[13] L.-P. Wang and T. Van Voorhis, "Communication: Hybrid ensembles for improved force matching," J. Chem. Phys. **133**, 231101 (2010).

[14] W. Ouyang, O. Hod, and R. Guerra, "Registry-dependent potential for interfaces of gold with graphitic systems," J. Chem. Theory Comput. **17**, 7215–7223 (2021).

[15] H. Heinz and U. W. Suter, "Atomic charges for classical simulations of polar systems," J. Phys. Chem. B **108**, 18341–18352 (2004).

[16] C. Kramer, A. Spinn, and K. Liedl, "Charge anisotropy: Where atomic multipoles matter most," J. Chem. Theory Comput. **10**, 4488–4496 (2014).

[17] A. L. Lomize, M. Y. Reibarkh, and I. D. Pogozheva, "Interatomic potentials and solvation parameters from protein engineering data for buried residues," Protein Sci. **11**, 1984–2000 (2002).

[18] A. Warshel, P. K. Sharma, M. Kato, and W. W. Parson, "Modeling electrostatic effects in proteins," Biochim. Biophys. Acta, Proteins Proteomics **1764**, 1647–1676 (2006).

[19] J. N. Israelachvili, *Intermolecular and Surface Forces* (Elsevier, San Diego, CA, 2011).

[20] R. Car and M. Parrinello, "Unified approach for molecular dynamics and density-functional theory," Phys. Rev. Lett. **55**, 2471–2474 (1985).

[21] A. Warshel and M. Levitt, "Theoretical studies of enzymic reactions: Dielectric, electrostatic and steric stabilization of the carbonium ion in the reaction of lysozyme," J. Mol. Biol. **103**, 227–249 (1976).

[22] R. Elber, "Perspective: Computer simulations of long time dynamics," J. Chem. Phys. **144**, 060901 (2016).

[23] F. Grasselli, "Investigating finite-size effects in molecular dynamics simulations of ion diffusion, heat transport, and thermal motion in superionic materials," J. Chem. Phys. **156**, 134705 (2022).

[24] Y. Hu, J. Chen, and B. Wang, "On the intrinsic ripples and negative thermal expansion of graphene," Carbon **95**, 239–249 (2015).

[25] U. Monteverde, J. Pal, M. A. Migliorato, M. Missous, U. Bangert, R. Zan, R. Kashtiban, and D. Powell, "Under pressure: Control of strain, phonons and bandgap opening in rippled graphene," Carbon **91**, 266–274 (2015).

[26] B. Smith, L. Lindsay, J. Kim, E. Ou, R. Huang, and L. Shi, "Phonon interaction with ripples and defects in thin layered molybdenum disulfide," Appl. Phys. Lett. **114**, 221902 (2019).

[27] X. Gu, Y. Wei, X. Yin, B. Li, and R. Yang, "Colloquium: Phononic thermal properties of two-dimensional materials," Rev. Mod. Phys. **90**, 041002 (2018).

[28] A. Mahata and M. Asle Zaeem, "Size effect in molecular dynamics simulation of nucleation process during solidification of pure metals: Investigating modified embedded atom method interatomic potentials," Modell. Simul. Mater. Sci. Eng. **27**, 085015 (2019).

[29] S. H. Jamali, L. Wolff, T. M. Becker, A. Bardow, T. J. H. Vlugt, and O. A. Moultos, "Finite-size effects of binary mutual diffusion coefficients from molecular dynamics," J. Chem. Theory Comput. **14**, 2667–2677 (2018).

[30] S.-F. Tsay and C. F. Liu, "System-size effects in the molecular-dynamics simulation of metallic crystallization," Phys. Lett. A **192**, 374–378 (1994).

[31] F. Bottin, J. Bieder, and J. Bouchet, "a-TDEP: Temperature dependent effective potential for abinit—Lattice dynamic properties including anharmonicity," Comput. Phys. Commun. **254**, 107301 (2020).

[32] D. M. Wallace, *Thermodynamics of Crystals* (John Wiley & Sons, Inc, 1972).

[33] S. Baroni, S. de Gironcoli, A. Dal Corso, and P. Giannozzi, "Phonons and related crystal properties from density-functional perturbation theory," Rev. Mod. Phys. **73**, 515–562 (2001).

[34] F. Eriksson, E. Fransson, and P. Erhart, "The hiphive package for the extraction of high-order force constants by machine learning," Adv. Theory Simul. **2**, 1800184 (2019).

[35] L. Chaput, A. Togo, I. Tanaka, and G. Hug, "Phonon-phonon interactions in transition metals," Phys. Rev. B **84**, 094302 (2011).

[36] K. Parlinski, Z. Q. Li, and Y. Kawazoe, "First-principles determination of the soft mode in cubic ZrO_2," Phys. Rev. Lett. **78**, 4063–4066 (1997).

[37] L. Paulatto, F. Mauri, and M. Lazzeri, "Anharmonic properties from a generalized third-order *ab initio* approach: Theory and applications to graphite and graphene," Phys. Rev. B **87**, 214303 (2013).

[38] X. Gonze and J.-P. Vigneron, "Density-functional approach to nonlinear-response coefficients of solids," Phys. Rev. B **39**, 13120–13128 (1989).

[39] In principle, existing classical force fields can also be used for a fast calculation of the $\boldsymbol{\Theta}_p$ tensors, as the definition of the latter is not specific of the energy functional employed.

[40] K. Esfarjani and H. T. Stokes, "Method to extract anharmonic force constants from first principles calculations," Phys. Rev. B **77**, 144112 (2008).

[41] D. A. Case, "Normal mode analysis of protein dynamics," Curr. Opin. Struct. Biol. **4**, 285–290 (1994).

[42] L. Monacelli, R. Bianco, M. Cherubini, M. Calandra, I. Errea, and F. Mauri, "The stochastic self-consistent harmonic approximation: Calculating vibrational properties of materials with full quantum and anharmonic effects," J. Phys.: Condens. Matter **33**, 363001 (2021).

[43] J. M. Ziman, *Electrons and Phonons: The Theory of Transport Phenomena in Solids* (Oxford University Press, United Kingdom, 2001).

[44] S. Nosé, "A molecular dynamics method for simulations in the canonical ensemble," Mol. Phys. **52**, 255–268 (1984).

[45] S. Nosé, "A unified formulation of the constant temperature molecular dynamics methods," J. Chem. Phys. **81**, 511–519 (1984).

[46] W. G. Hoover, "Canonical dynamics: Equilibrium phase-space distributions," Phys. Rev. A **31**, 1695–1697 (1985).

[47] Although the term *normal equations* is commonly used in the theory for solving least squares problems with a different meaning [C. L. Lawson and J. Richard, *Solving Least Squares Problems* (Society for Industrial and Applied Mathematics, 1974)], we can use it in this context without ambiguities.

[48] A. Cammarata, P. Nicolini, K. Simonovic, E. Ukraintsev, and T. Polcar, "Atomic-scale design of friction and energy dissipation," Phys. Rev. B **99**, 094309 (2019).

[49] A. Cammarata, "Phonon-phonon scattering selection rules and control: An application to nanofriction and thermal transport," RSC Adv. **9**, 37491–37496 (2019).

[50] A. Cammarata and T. Polcar, "Control of energy dissipation in sliding low-dimensional materials," Phys. Rev. B **102**, 085409 (2020).

[51] N. K. Ravichandran and D. Broido, "Phonon-phonon interactions in strongly bonded solids: Selection rules and higher-order processes," Phys. Rev. X **10**, 021063 (2020).

[52] Y. Xia, V. I. Hegde, K. Pal, X. Hua, D. Gaines, S. Patel, J. He, M. Aykol, and C. Wolverton, "High-throughput study of lattice thermal conductivity in binary rocksalt and zinc blende compounds including higher-order anharmonicity," Phys. Rev. X **10**, 041029 (2020).

[53] Y. Chen, J. Ma, S. Wen, and W. Li, "Body-centered-cubic structure and weak anharmonic phonon scattering in tungsten," Npj Comput. Mater. **5**, 98 (2019).

[54] "pindol," The software is available free of charge, 2024, https://github.com/acammarat/pindol, last accessed 07 March 2024.

[55] K. Esfarjani, G. Chen, and H. T. Stokes, "Heat transport in silicon from first-principles calculations," Phys. Rev. B **84**, 085204 (2011).

[56] J. Shiomi, K. Esfarjani, and G. Chen, "Thermal conductivity of half-Heusler compounds from first-principles calculations," Phys. Rev. B **84**, 104302 (2011).

[57] O. Hellman, I. A. Abrikosov, and S. I. Simak, "Lattice dynamics of anharmonic solids from first principles," Phys. Rev. B **84**, 180301 (2011).

[58] O. Hellman, P. Steneteg, I. A. Abrikosov, and S. I. Simak, "Temperature dependent effective potential method for accurate free energy calculations of solids," Phys. Rev. B **87**, 104111 (2013).

[59] O. Hellman and I. A. Abrikosov, "Temperature-dependent effective third-order interatomic force constants from first principles," Phys. Rev. B **88**, 144301 (2013).

[60] N. Shulumba, O. Hellman, and A. J. Minnich, "Lattice thermal conductivity of polyethylene molecular crystals from first-principles including nuclear quantum effects," Phys. Rev. Lett. **119**, 185901 (2017).

[61] A. Togo and I. Tanaka, "First principles phonon calculations in materials science," Scr. Mater. **108**, 1–5 (2015).

[62] A. Togo, L. Chaput, and I. Tanaka, "Distributions of phonon lifetimes in Brillouin zones," Phys. Rev. B **91**, 094306 (2015).

[63] F. Zhou, W. Nielson, Y. Xia, and V. Ozoliņš, "Lattice anharmonicity and thermal conductivity from compressive sensing of first-principles calculations," Phys. Rev. Lett. **113**, 185501 (2014).

[64] J. Brorsson, A. Hashemi, Z. Fan, E. Fransson, F. Eriksson, T. Ala-Nissila, A. V. Krasheninnikov, H.-P. Komsa, and P. Erhart, "Efficient calculation of the lattice thermal conductivity by atomistic simulations with ab initio accuracy," Adv. Theory Simul. **5**, 2100217 (2022).

[65] A. Togo and I. Tanaka, Spglib: A software library for crystal symmetry sea.

[66] X. Gonze, B. Amadon, P.-M. Anglade, J.-M. Beuken, F. Bottin, P. Boulanger, F. Bruneval, D. Caliste, R. Caracas, M. Côté, T. Deutsch, L. Genovese, P. Ghosez, M. Giantomassi, S. Goedecker, D. Hamann, P. Hermet, F. Jollet, G. Jomard, S. Leroux, M. Mancini, S. Mazevet, M. Oliveira, G. Onida, Y. Pouillon, T. Rangel, G.-M. Rignanese, D. Sangalli, R. Shaltaf, M. Torrent, M. Verstraete, G. Zerah, and J. Zwanziger, "ABINIT: First-principles approach to material and nanosystem properties," Comput. Phys. Commun. **180**, 2582–2615 (2009).

[67] X. Gonze, F. Jollet, F. Abreu Araujo, D. Adams, B. Amadon, T. Applencourt, C. Audouze, J.-M. Beuken, J. Bieder, A. Bokhanchuk, E. Bousquet, F. Bruneval, D. Caliste, M. Côté, F. Dahm, F. Da Pieve, M. Delaveau, M. Di Gennaro, B. Dorado, C. Espejo, G. Geneste, L. Genovese, A. Gerossier, M. Giantomassi, Y. Gillet, D. Hamann, L. He, G. Jomard, J. Laflamme Janssen, S. Le Roux, A. Levitt, A. Lherbier, F. Liu, I. Lukačević, A. Martin, C. Martins, M. Oliveira, S. Poncé, Y. Pouillon, T. Rangel, G.-M. Rignanese, A. Romero, B. Rousseau, O. Rubel, A. Shukri, M. Stankovski, M. Torrent, M. Van Setten, B. Van Troeye, M. Verstraete, D. Waroquiers, J. Wiktor, B. Xu, A. Zhou, and J. Zwanziger, "Recent developments in the ABINIT software package," Comput. Phys. Commun. **205**, 106–131 (2016).

[68] X. Gonze, "A brief introduction to the ABINIT software package," Z. Kristallogr.—Cryst. Mater. **220**, 558–562 (2005).

[69] N. Troullier and J. L. Martins, "Efficient pseudopotentials for plane-wave calculations," Phys. Rev. B **43**, 1993–2006 (1991).

[70] L. Kleinman and D. M. Bylander, "Efficacious form for model pseudopotentials," Phys. Rev. Lett. **48**, 1425–1428 (1982).

[71] S. Goedecker, M. Teter, and J. Hutter, "Separable dual-space Gaussian pseudopotentials," Phys. Rev. B **54**, 1703–1710 (1996).

[72] H. J. Monkhorst and J. D. Pack, "Special points for Brillouin-zone integrations," Phys. Rev. B **13**, 5188–5192 (1976).

[73] Regardless the number of associated symmetry operations, any $\boldsymbol{q}$-point can be excluded from the anharmonic processes by the selection rules; in that case, it would contribute to the dynamics only with the corresponding kinetic and harmonic term of the potential energy.

[74] G. H. Lander, E. S. Fisher, and S. Bader, "The solid-state properties of uranium A historical perspective and review," Adv. Phys. **43**, 1–111 (1994).

[75] W. P. Crummett, H. G. Smith, R. M. Nicklow, and N. Wakabayashi, "Lattice dynamics of α-uranium," Phys. Rev. B **19**, 6028–6037 (1979).

[76] H. G. Smith, N. Wakabayashi, W. P. Crummett, R. M. Nicklow, G. H. Lander, and E. S. Fisher, "Observation of a charge-density wave in α-U at low temperature," Phys. Rev. Lett. **44**, 1612–1615 (1980).

[77] J. Bouchet, "Lattice dynamics of α uranium," Phys. Rev. B **77**, 024113 (2008).

[78] L. T. Lloyd, "Thermal expansion of alpha-uranium single crystals," J. Nucl. Mater. **3**, 67–71 (1961).

[79] L. T. Lloyd and C. Barrett, "Thermal expansion of alpha uranium," J. Nucl. Mater. **18**, 55–59 (1966).

[80] C. S. Barrett, M. H. Mueller, and R. L. Hitterman, "Crystal structure variations in alpha uranium at low temperatures," Phys. Rev. **129**, 625–629 (1963).

[81] T. Le Bihan, S. Heathman, M. Idiri, G. H. Lander, J. M. Wills, A. C. Lawson, and A. Lindbaum, "Structural behavior of α-uranium with pressures to 100 GPa," Phys. Rev. B **67**, 134102 (2003).

[82] J. Bouchet and F. Bottin, "Thermal evolution of vibrational properties of α-U," Phys. Rev. B **92**, 174108 (2015).

[83] G. Kresse and J. Hafner, "*Ab initio* molecular dynamics for liquid metals," Phys. Rev. B **47**, 558–561 (1993).

[84] G. Kresse and J. Hafner, "*Ab initio* molecular-dynamics simulation of the liquid-metal–amorphous-semiconductor transition in germanium," Phys. Rev. B **49**, 14251–14269 (1994).

[85] G. Kresse and J. Furthmüller, "Efficiency of ab-initio total energy calculations for metals and semiconductors using a plane-wave basis set," Comput. Mater. Sci. **6**, 15–50 (1996).

[86] G. Kresse and J. Furthmüller, "Efficient iterative schemes for *ab initio* total-energy calculations using a plane-wave basis set," Phys. Rev. B **54**, 11169–11186 (1996).

[87] G. Kresse and D. Joubert, "From ultrasoft pseudopotentials to the projector augmented-wave method," Phys. Rev. B **59**, 1758–1775 (1999).

[88] M. I. Aroyo, D. Orobengoa, G. de la Flor, E. S. Tasci, J. M. Perez-Mato, and H. Wondratschek, "Brillouin-zone database on the *Bilbao Crystallographic Server*," Acta Crystallogr., Sect. A: Found. Adv. **70**, 126–137 (2014).

[89] E. S. Tasci, G. de la Flor, D. Orobengoa, C. Capillas, J. M. Perez-Mato, and M. I. Aroyo, "An introduction to the tools hosted in the Bilbao Crystallographic Server," EPJ Web Conf. **22**, 00009 (2012).

[90] H. Tian, J. Tice, R. Fei, V. Tran, X. Yan, L. Yang, and H. Wang, "Low-symmetry two-dimensional materials for electronic and photonic applications," Nano Today **11**, 763 (2016).

[91] A. B. Kaul, "Two-dimensional layered materials: Structure, properties, and prospects for device applications," J. Mater. Res. **29**, 348 (2014).

[92] H. Li, J. Wu, Z. Yin, and H. Zhang, "Preparation and applications of mechanically exfoliated single-layer and multilayer MoS_2 and WSe_2 nanosheets," Acc. Chem. Res. **47**, 1067 (2014).

[93] M. Chhowalla, H. S. Shin, G. Eda, L.-J. Li, K. P. Loh, and H. Zhang, "The chemistry of two-dimensional layered transition metal dichalcogenide nanosheets," Nat. Chem. **5**, 263 (2013).

[94] A. K. Geim and I. V. Grigorieva, "Van der Waals heterostructures," Nature **499**, 419 (2013).

[95] A. Vanossi, N. Manini, M. Urbakh, S. Zapperi, and E. Tosatti, "*Colloquium*: Modeling friction: From nanoscale to mesoscale," Rev. Mod. Phys. **85**, 529 (2013).

[96] H. G. Füchtbauer, A. K. Tuxen, P. G. Moses, H. Topsøe, F. Besenbacher, and J. V. Lauritsen, "Morphology and atomic-scale structure of single-layer WS_2 nanoclusters," Phys. Chem. Chem. Phys. **15**, 15971 (2013).

[97] S. Helveg, J. V. Lauritsen, E. Lægsgaard, I. Stensgaard, J. K. Nørskov, B. S. Clausen, H. Topsøe, and F. Besenbacher, "Atomic-scale structure of single-layer MoS_2 nanoclusters," Phys. Rev. Lett. **84**, 951 (2000).

[98] R. Saito, Y. Tatsumi, S. Huang, X. Ling, and M. S. Dresselhaus, "Raman spectroscopy of transition metal dichalcogenides," J. Phys.: Condens. Matter **28**, 353002 (2016).

[99] D. C. Harris and M. D. Bertolucci, in *Symmetry and Spectroscopy*, *Dover Books on Chemistry* (Dover Publications, Mineola, NY, 1989).

[100] P. Atkins, J. De Paula, and R. S. Friedman, *Physical Chemistry*, 2nd ed. (Oxford University Press, London, England, 2013).

[101] S. Najmaei, Z. Liu, P. M. Ajayan, and J. Lou, "Thermal effects on the characteristic Raman spectrum of molybdenum disulfide (MoS_2) of varying thicknesses," Appl. Phys. Lett. **100**, 013106 (2012).

[102] N. A. Lanzillo, A. Glen Birdwell, M. Amani, F. J. Crowne, P. B. Shah, S. Najmaei, Z. Liu, P. M. Ajayan, J. Lou, M. Dubey, S. K. Nayak, and T. P. O'Regan, "Temperature-dependent phonon shifts in monolayer MoS_2," Appl. Phys. Lett. **103**, 093102 (2013).

[103] S. Mignuzzi, A. J. Pollard, N. Bonini, B. Brennan, I. S. Gilmore, M. A. Pimenta, D. Richards, and D. Roy, "Effect of disorder on Raman scattering of single-layer MoS_2," Phys. Rev. B **91**, 195411 (2015).

[104] H. Guo, Y. Sun, P. Zhai, H. Yao, J. Zeng, S. Zhang, J. Duan, M. Hou, M. Khan, and J. Liu, "Swift-heavy ion irradiation-induced latent tracks in few- and monolayer MoS_2," Appl. Phys. A **122**, 375 (2016).

[105] S. Sahoo, A. P. S. Gaur, M. Ahmadi, M. J.-F. Guinel, and R. S. Katiyar, "Temperature-dependent Raman studies and thermal conductivity of few-layer MoS_2," J. Phys. Chem. C **117**, 9042–9047 (2013).

[106] G. P. Srivastava and I. O. Thomas, "Temperature-dependent Raman linewidths in transition-metal dichalcogenides," Phys. Rev. B **98**, 035430 (2018).

[107] Z. Hu, Y. Bao, Z. Li, Y. Gong, R. Feng, Y. Xiao, X. Wu, Z. Zhang, X. Zhu, P. M. Ajayan, and Z. Fang, "Temperature dependent Raman and photoluminescence of vertical WS_2/MoS_2 monolayer heterostructures," Sci. Bull. **62**, 16–21 (2017).

[108] M. Öper, Y. Shehu, and N. K. Perkgöz, "Temperature-dependent Raman modes of $MoS_2/MoSe_2$ van der Waals heterostructures," Semicond. Sci. Technol. **35**, 115020 (2020).

[109] B. Schönfeld, J. J. Huang, and S. C. Moss, "Anisotropic mean-square displacements (MSD) in single-crystals of 2H- and 3R-MoS_2," Acta Crystallogr., Sect. B: Struct. Sci. **39**, 404–407 (1983).

[110] Z. Zhao, H. Zhang, H. Yuan, S. Wang, Y. Lin, Q. Zeng, G. Xu, Z. Liu, G. K. Solanki, K. D. Patel, Y. Cui, H. Y. Hwang, and W. L. Mao, "Pressure induced metallization with absence of structural transition in layered molybdenum diselenide," Nat. Commun. **6**, 7312 (2015).

[111] W. Schutte, J. De Boer, and F. Jellinek, "Crystal structures of tungsten disulfide and diselenide," J. Solid State Chem. **70**, 207–209 (1987).

[112] F. Belviso, A. Cammarata, J. Missaoui, and T. Polcar, "Effect of electric fields in low-dimensional materials: Nanofrictional response as a case study," Phys. Rev. B **102**, 155433 (2020).

[113] A. D. Becke and E. R. Johnson, "A simple effective potential for exchange," J. Chem. Phys. **124**, 221101 (2006).

[114] Phonopy-spectroscopy, https://github.com/JMSkelton/Phonopy-Spectroscopy, last accessed 05 March 2023.

[115] J. M. Skelton, L. A. Burton, A. J. Jackson, F. Oba, S. C. Parker, and A. Walsh, "Lattice dynamics of the tin sulphides SnS_2, SnS and Sn_2S_3: Vibrational spectra and thermal transport," Phys. Chem. Chem. Phys. **19**, 12452–12465 (2017).

[116] ascii-phonons, https://github.com/ajjackson/ascii-phonons, last accessed 05 March 2023.

[117] V_Sim, https://www.mem-lab.fr/en/Pages/L_SIM/Softwares/V_Sim.aspx, last accessed 05 March 2023.

[118] eigmap, 2023, https://github.com/acammarat/phtools/tree/main/eigmap, last accessed 17 March 2023.

[119] A. Cammarata and T. Polcar, "Fine control of lattice thermal conductivity in low-dimensional materials," Phys. Rev. B **103**, 035406 (2021).

[120] A. Del Monte, N. Manini, L. Guido Molinari, and G. Paolo Brivio, "Low-energy unphysical saddle in polynomial molecular potentials," Mol. Phys. **103**, 689–696 (2005).
[121] I. Mills and A. Robiette, "On the relationship of normal modes to local modes in molecular vibrations," Mol. Phys. **56**, 743–765 (1985).
[122] K. A. Dill, "Polymer principles and protein folding," Protein Sci. **8**, 1166–1180 (1999).
[123] M. Simoncelli, N. Marzari, and F. Mauri, "Wigner formulation of thermal transport in solids," Phys. Rev. X **12**, 041011 (2022).
[124] T. Luo and G. Chen, "Nanoscale heat transfer—From computation to experiment," Phys. Chem. Chem. Phys. **15**, 3389–3412 (2013).
[125] Y. Luo, X. Yang, T. Feng, J. Wang, and X. Ruan, "Vibrational hierarchy leads to dual-phonon transport in low thermal conductivity crystals," Nat. Commun. **11**, 2554 (2020).
[126] C. Yang, X. Wei, J. Sheng, and H. Wu, "Phonon heat transport in cavity-mediated optomechanical nanoresonators," Nat. Commun. **11**, 4656 (2020).
[127] S. Lee, D. Broido, K. Esfarjani, and G. Chen, "Hydrodynamic phonon transport in suspended graphene," Nat. Commun. **6**, 6290 (2015).
[128] H. S. Yoon, J. Oh, J. Y. Park, J. Kang, J. Kwon, T. Cusati, G. Fiori, G. Iannaccone, A. Fortunelli, V. O. Ozcelik, G.-H. Lee, T. Low, and S. C. Jun, "Phonon-assisted carrier transport through a lattice-mismatched interface," npg Asia Mater. **11**, 14 (2019).
[129] L. Lindsay, A. Katre, A. Cepellotti, and N. Mingo, "Perspective on *ab initio* phonon thermal transport," J. Appl. Phys. **126**, 050902 (2019).
[130] J.-M. Manceau, P. A. Loukakos, and S. Tzortzakis, "Direct acoustic phonon excitation by intense and ultrashort terahertz pulses," Appl. Phys. Lett. **97**, 251904 (2010).
[131] Y. Wang, L. Guo, X. Xu, J. Pierce, and R. Venkatasubramanian, "Origin of coherent phonons in Bi_2Te_3 excited by ultrafast laser pulses," Phys. Rev. B **88**, 064307 (2013).
[132] J. D. Schall, P. T. Mikulski, G. M. Chateauneuf, G. Gao, and J. A. Harrison, "5—Molecular dynamics simulations of tribology," in *Superlubricity*, edited by A. Erdemir and J.-M. Martin (Elsevier Science B.V., Amsterdam, 2007), pp. 79–102.
[133] A. I. Vakis, V. A. Yastrebov, J. Scheibert, L. Nicola, D. Dini, C. Minfray, A. Almqvist, M. Paggi, S. Lee, G. Limbert, J. F. Molinari, G. Anciaux, R. Aghababaei, S. Echeverri Restrepo, A. Papangelo, A. Cammarata, P. Nicolini, C. Putignano, G. Carbone, S. Stupkiewicz, J. Lengiewicz, G. Costagliola, F. Bosia, R. Guarino, N. M. Pugno, M. H. Müser, and M. Ciavarella, "Modeling and simulation in tribology across scales: An overview," Tribol. Int. **125**, 169–199 (2018).
[134] J. Lu and E. Vanden-Eijnden, "Infinite swapping replica exchange molecular dynamics leads to a simple simulation patch using mixture potentials," J. Chem. Phys. **138**, 084105 (2013).
[135] A. Jain, S. P. Ong, G. Hautier, W. Chen, W. D. Richards, S. Dacek, S. Cholia, D. Gunter, D. Skinner, G. Ceder, and K. a. Persson, "Commentary: The materials project: A materials genome approach to accelerating materials innovation," APL Mater. **1**, 011002 (2013).
[136] S. P. Huber, S. Zoupanos, M. Uhrin, L. Talirz, L. Kahle, R. Häuselmann, D. Gresch, T. Müller, A. V. Yakutovich, C. W. Andersen, F. F. Ramirez, C. S. Adorf, F. Gargiulo, S. Kumbhar, E. Passaro, C. Johnston, A. Merkys, A. Cepellotti, N. Mounet, N. Marzari, B. Kozinsky, and G. Pizzi, "AiiDA 1.0, a scalable computational infrastructure for automated reproducible workflows and data provenance," Sci. Data **7**, 300 (2020).
[137] F. Belviso, V. E. P. Claerbout, A. Comas-Vives, N. S. Dalal, F.-R. Fan, A. Filippetti, V. Fiorentini, L. Foppa, C. Franchini, B. Geisler, L. M. Ghiringhelli, A. Groß, S. Hu, J. Íñiguez, S. K. Kauwe, J. L. Musfeldt, P. Nicolini, R. Pentcheva, T. Polcar, W. Ren, F. Ricci, F. Ricci, H. S. Sen, J. M. Skelton, T. D. Sparks, A. Stroppa, A. Urru, M. Vandichel, P. Vavassori, H. Wu, K. Yang, H. J. Zhao, D. Puggioni, R. Cortese, and A. Cammarata, "Viewpoint: Atomic-Scale design protocols toward energy, electronic, catalysis, and sensing applications," Inorg. Chem. **58**, 14939–14980 (2019).

Integrating Newton's equations of motion in the reciprocal space — Supporting Information

Antonio Cammarata,[1, a)] Miljan Dašić,[1, 2] and Paolo Nicolini[1, 3, b)]

[1)]*Department of Control Engineering, Faculty of Electrical Engineering,*
Czech Technical University in Prague, Technicka 2, 16627 Prague,
Czech Republic

[2)]*Scientific Computing Laboratory, Center for the Study of Complex Systems,*
Institute of Physics Belgrade, University of Belgrade, Pregrevica 118, 11080 Belgrade,
Serbia

[3)]*Institute of Physics (FZU), Czech Academy of Sciences, Na Slovance 2, 18200 Prague,*
Czech Republic

[a)] Electronic mail: cammaant@fel.cvut.cz

[b)] Electronic mail: nicolini@fzu.cz

I. NORMAL COORDINATES

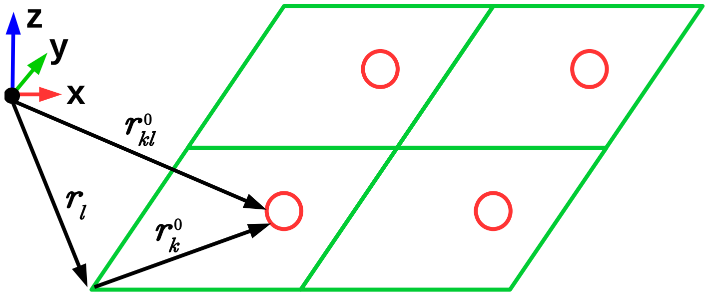

FIG. 1. Schematic representation of the position vectors used in the formalism of the normal coordinates. The position vector $\boldsymbol{r}^0_{kl}$ of the k-th atom (filled blue circle) in the l-th primitive cell (green parallelogram) can be written as the sum of the position $\boldsymbol{r}_l$ of the primitive cell and the position $\boldsymbol{r}^0_k$ of the atom with respect to the origin of the primitive cell.

Let us consider a periodic system made of N_0 primitive cells, each being identified by a cell index l and a vector $\boldsymbol{r}_l$ pointing to its origin. Let there be N atoms per primitive cell; the equilibrium positions of the atoms read

$$\boldsymbol{r}^0_{kl} = \boldsymbol{r}_l + \boldsymbol{r}^0_k \quad k = 1, 2, \dots, N \quad l = 1, 2, \dots, N_0 \tag{1}$$

where $\boldsymbol{r}^0_k$ represents the position of the k-th atom with respect to the origin of the primitive cell (Figure 1).

The set of vectors $\boldsymbol{r}^0_{kl}$ describes the structure of the perfect lattice. At a particular time t, the k-th atom within the l-th primitive cell, denoted by (kl), may be found at a position $\boldsymbol{r}_{kl}(t)$, which may differ from the equilibrium position. The time-dependent displacement is

$$\boldsymbol{u}_{kl}(t) = \boldsymbol{r}_{kl}(t) - \boldsymbol{r}^0_{kl} = \boldsymbol{r}_{kl}(t) - \boldsymbol{r}_l - \boldsymbol{r}^0_k. \tag{2}$$

The potential energy V of the whole crystal

$$V = V(\boldsymbol{r}_{11}, \boldsymbol{r}_{21}, \dots, \boldsymbol{r}_{kl}, \dots) \tag{3}$$

can be expanded about the equilibrium position in a Taylor series with respect to $\boldsymbol{u}_{kl}(t)$; by retaining only the second order of the expansion (harmonic approximation), the potential energy is written as

$$V = \frac{1}{2} \sum_{kl} \sum_{k'l'} \sum_{\alpha=1}^{3} \sum_{\beta=1}^{3} u^\alpha_{kl}(t) \Theta_{\alpha\beta}(kl, k'l') u^\beta_{k'l'}(t) \tag{4}$$

where $u^\alpha_{kl}(t)$ denotes the Cartesian component of $\boldsymbol{u}_{kl}(t)$ in the direction α. In order to simplify the formulae, we now drop the time dependence, keeping in mind that we are always dealing with dynamical displacements. The expansion coefficients $\Theta_{\alpha\beta}(kl, k'l')$ in Equation 4 are the partial derivatives of the potential energy with respect to the atomic displacements

$$\Theta_{\alpha\beta}(kl, k'l') = \left. \frac{\partial^2 V}{\partial u^\alpha_{kl} \partial u^\beta_{k'l'}} \right|_0, \tag{5}$$

where the calculation limit "0" as a subscript indicates that they are evaluated at the equilibrium position. Using the matrix notation

$$\mathbf{\Theta}(kl,k'l') = \begin{pmatrix} \Theta_{11}(kl,k'l') & \Theta_{12}(kl,k'l') & \Theta_{13}(kl,k'l') \\ \Theta_{21}(kl,k'l') & \Theta_{22}(kl,k'l') & \Theta_{23}(kl,k'l') \\ \Theta_{31}(kl,k'l') & \Theta_{32}(kl,k'l') & \Theta_{33}(kl,k'l') \end{pmatrix}, \tag{6}$$

Equation 4 reads

$$V = \frac{1}{2}\sum_{kl}\sum_{k'l'} \boldsymbol{u}_{kl}\mathbf{\Theta}(kl,k'l')\boldsymbol{u}_{k'l'}. \tag{7}$$

The matrix $\mathbf{\Theta}(kl,k'l')$ is the Cartesian force constant tensor and its elements $\Theta_{\alpha\beta}(kl,k'l')$ are the harmonic interatomic force constants. Within the harmonic approximation, the equation of motion for a particular atom (kl) with mass m_k is then given by

$$m_k\frac{d^2\boldsymbol{u}_{kl}}{dt^2} = -\sum_{k'l'}\mathbf{\Theta}(kl,k'l')\boldsymbol{u}_{k'l'}; \tag{8}$$

the dynamics of the system are described by $N \times N_0$ equations of the kind 8. The solution of this set of coupled differential equations is found by calculating the eigenvectors $\boldsymbol{e}$ of the dynamical matrix[1,2]; for each atom, it reads

$$\boldsymbol{u}_{kl} = \frac{1}{\sqrt{N_0 m_k}}\sum_{\boldsymbol{q}\geq 0}^{N_{\boldsymbol{q}}}\sum_{j=1}^{3N}\left(Q_{\boldsymbol{q},j}\boldsymbol{e}_k(\boldsymbol{q},j)\exp(i\boldsymbol{q}\cdot\boldsymbol{r}^0_{kl}) + c.c.\right) \tag{9}$$

where:

1. $\boldsymbol{u}_{kl}$ is the 3-dimensional cartesian vector representing the atomic displacement of the k-th atom in the l-th cell,
2. $\boldsymbol{q}$ is a 3-dimensional wave vector corresponding to a point of the reciprocal space,
3. $N_{\boldsymbol{q}}$ is the number of $\boldsymbol{q}$ points,
4. N_0 is the number of replicas of the primitive cell,
5. m_k is the mass of the k-th atom,
6. j is the label (*band* or *branch* index) of the normal mode at fixed $\boldsymbol{q}$,
7. the coefficients $Q_{\boldsymbol{q},j}$ are the *normal coordinates* of the mode $(\boldsymbol{q},j)$,
8. $\boldsymbol{e}_k(\boldsymbol{q},j)$ is the 3-dimensional cartesian vector formed by the components of the phonon eigenvector $\boldsymbol{e}(\boldsymbol{q},j)$ relative to the k-th atom,
9. $\exp(i\boldsymbol{q}\cdot\boldsymbol{r}^0_{kl})$ is the spatial modulation of the atomic displacement, depending on the equilibrium position $\boldsymbol{r}^0_{kl}$ of the k-th atom in the l-th primitive cell, and
10. "*c.c.*" indicates the complex conjugate of the first term in parenthesis.

In Equation 9, we exploited the fact that $Q_{-\boldsymbol{q},j} = Q^*_{\boldsymbol{q},\boldsymbol{j}}$; with $\boldsymbol{q} \geq 0$, we then indicate all the modes at $\boldsymbol{q} = \Gamma$ and at all the points in the set $\{\boldsymbol{q} : \boldsymbol{q}_i \neq -\boldsymbol{q}_j \forall i, j\}$, then excluding the existence of couple of vectors in which the components of the former are the opposite of the corresponding components of the latter. The phonon coordinate transformation (9) may be inverted to give

$$Q_{\boldsymbol{q},j} = \frac{1}{\sqrt{N_0}} \sum_{l=1}^{N_0} \sum_{k=1}^{N} \left(\sqrt{m_k} \exp(-i\boldsymbol{q} \cdot \boldsymbol{r}^0_{kl}) \boldsymbol{u}_{kl} \cdot \boldsymbol{e}_k(-\boldsymbol{q}, j) \right) \tag{10}$$

while the relation between the Cartesian and the normal accelerations is obtained by taking the second derivative of both sides of Equation 10 with respect to the time:

$$\ddot{Q}_{\boldsymbol{q},j} = \frac{1}{\sqrt{N_0}} \sum_{l=1}^{N_0} \sum_{i=1}^{N} \left(\sqrt{m_k} \exp(-i\boldsymbol{q} \cdot \boldsymbol{r}^0_{kl}) \ddot{\boldsymbol{u}}_{kl} \cdot \boldsymbol{e}_k(-\boldsymbol{q}, j) \right). \tag{11}$$

At each $\boldsymbol{q}$ point, the eigenvectors of the dynamical matrix are a complete basis for the Cartesian atomic positions; Equation 8 and Equation 11 are therefore two equivalent descriptions of the dynamics of the system.

II. DERIVATIVE OF THE ANHARMONIC TERMS OF THE POTENTIAL ENERGY

The general form of the Taylor series of the potential energy V written in terms of the atomic displacements $\boldsymbol{u}$ is

$$V(\boldsymbol{u}) = V_0 + \sum_{p\geq 1} \frac{1}{p!} \sum_{\substack{\alpha_1\ldots\alpha_p \\ i_1\ldots i_p}} \Theta^{\alpha_1\ldots\alpha_p}_{i_1\ldots i_p} \prod_{k=1}^{p} u^{\alpha_k}_{i_k} \tag{12}$$

where V_0 is the energy reference, p is the order of the terms in the sum, i_k and α_k identify the atom and the cartesian component of its displacement, respectively, and k enumerates the order of approximation; the cartesian tensors $\boldsymbol{\Theta}_p = \Theta^{\alpha_1\ldots\alpha_p}_{i_1\ldots i_p}$ are formed by the p-th order partial derivative of the potential with respect to the atomic positions calculated at the reference position. For $p \geq 3$, each tensor $\boldsymbol{\Theta}_p$ contains the information of the anharmonic interactions at the order $p-2$. By considering the transformation (9) and the Fourier transform of the tensors $\boldsymbol{\Theta}_p$ by means of the phonon eigenvectors, the anharmonic part of the potential energy can be written as[1,2]

$$V_{\text{anh}} = \sum_{p\geq 3} V_p = \sum_{p\geq 3} \frac{1}{p!} \sum_{\lambda_1\ldots\lambda_p} \Phi_{\lambda_1\ldots\lambda_p} \prod_{k=1}^{p} Q_{\lambda_k} \tag{13}$$

where λ_k is a short notation to indicate the phonon mode identified by the couple of indices $(\boldsymbol{q}_k, j_k)$; $\boldsymbol{q}_k$ runs over the set of the selected $\boldsymbol{q}$ points, while j_k runs over all the phonon modes at the $\boldsymbol{q}_k$ point.

In order to determine the general expression of the derivative of the anharmonic part of the potential energy, let us begin by considering the first anharmonic term in Equation 13, that is

$$V_3 = \frac{1}{3!} \sum_{\lambda_1\lambda_2\lambda_3} \Phi_{\lambda_1\lambda_2\lambda_3} Q_{\lambda_1} Q_{\lambda_2} Q_{\lambda_3} \tag{14}$$

and let us split the sum by isolating the terms containing a selected λ mode from those which do not contain it:

$$V_3 = \frac{1}{3!}\left[\sum_{\lambda_1\lambda_2\lambda_3\neq\lambda}\Phi_{\lambda_1\lambda_2\lambda_3}Q_{\lambda_1}Q_{\lambda_2}Q_{\lambda_3} + 3\sum_{\lambda_2\lambda_3\neq\lambda}\Phi_{\lambda\lambda_2\lambda_3}Q_{\lambda}Q_{\lambda_2}Q_{\lambda_3} + 3\sum_{\lambda_3\neq\lambda}\Phi_{\lambda\lambda\lambda_3}Q_{\lambda}^2Q_{\lambda_3} + \Phi_{\lambda\lambda\lambda}Q_{\lambda}^3\right] \tag{15}$$

in which we exploited the invariance of the tensor $\Phi_{\lambda_1\lambda_2\lambda_3}$ under permutation of its λ_k components in order to collect together equivalent summations; the subscript "$\lambda_1\lambda_2\lambda_3 \neq \lambda$" indicates that the indices cannot assume the value λ, and similarly for the other summation subscripts. The derivative of the first anharmonic term with respect to a selected Q_λ normal coordinate is then

$$\frac{\partial V_3}{\partial Q_\lambda} = \frac{1}{3!}\left[3\sum_{\lambda_2\lambda_3\neq\lambda}\Phi_{\lambda\lambda_2\lambda_3}Q_{\lambda_2}Q_{\lambda_3} + 6\sum_{\lambda_3\neq\lambda}\Phi_{\lambda\lambda\lambda_3}Q_{\lambda}Q_{\lambda_3} + 3\Phi_{\lambda\lambda\lambda}Q_{\lambda}^2\right] = \tag{16a}$$

$$= \frac{1}{3!}\left[3\sum_{\substack{\lambda_2\\ \lambda_3\neq\lambda}}\Phi_{\lambda\lambda_2\lambda_3}Q_{\lambda_2}Q_{\lambda_3} + 3\sum_{\lambda_3\neq\lambda}\Phi_{\lambda\lambda\lambda_3}Q_{\lambda}Q_{\lambda_3} + 3\Phi_{\lambda\lambda\lambda}Q_{\lambda}^2\right] = \tag{16b}$$

$$= \frac{1}{3!}\left[3\sum_{\substack{\lambda_2\\ \lambda_3\neq\lambda}}\Phi_{\lambda\lambda_2\lambda_3}Q_{\lambda_2}Q_{\lambda_3} + 3\sum_{\lambda_3}\Phi_{\lambda\lambda\lambda_3}Q_{\lambda}Q_{\lambda_3}\right] = \tag{16c}$$

$$= \frac{1}{3!}\left[3\sum_{\lambda_2\lambda_3}\Phi_{\lambda\lambda_2\lambda_3}Q_{\lambda_2}Q_{\lambda_3}\right] = \tag{16d}$$

$$= \frac{1}{2!}\sum_{\lambda_2\lambda_3}\Phi_{\lambda\lambda_2\lambda_3}Q_{\lambda_2}Q_{\lambda_3} \tag{16e}$$

where: *i*) we lifted the condition $\lambda_2 \neq \lambda$ which is present in the first sum of Equation 16a to obtain the first summation of Equation 16b, thus including three out of the six summations appearing as the second term in Equation 16a; *ii*) we lifted the condition $\lambda_3 \neq \lambda$ appearing in the second summation of Equation 16b to obtain the second summation of Equation 16c, thus including the last term of Equation 16b; *iii*) in the summation in Equation 16d we lifted the condition $\lambda_3 \neq \lambda$ appearing in the first summation of Equation 16c, thus including the last term of Equation 16c.

Let us now consider the second anharmonic term in Equation 13:

$$V_4 = \frac{1}{4!}\sum_{\lambda_1\lambda_2\lambda_3\lambda_4}\Phi_{\lambda_1\lambda_2\lambda_3\lambda_4}Q_{\lambda_1}Q_{\lambda_2}Q_{\lambda_3}Q_{\lambda_4}; \tag{17}$$

by isolating the terms containing Q_λ in an analogous way as we did for Equation 15, V_4 can be written as

$$\begin{aligned} V_4 =& \frac{1}{4!}\left[\sum_{\lambda_1\lambda_2\lambda_3\lambda_4\neq\lambda}\Phi_{\lambda_1\lambda_2\lambda_3\lambda_4}Q_{\lambda_1}Q_{\lambda_2}Q_{\lambda_3}Q_{\lambda_4} + 4\sum_{\lambda_2\lambda_3\lambda_4\neq\lambda}\Phi_{\lambda\lambda_2\lambda_3\lambda_4}Q_{\lambda}Q_{\lambda_2}Q_{\lambda_3}Q_{\lambda_4}\right.\\ &\left. + 6\sum_{\lambda_3\lambda_4\neq\lambda}\Phi_{\lambda\lambda\lambda_3\lambda_4}Q_{\lambda}^2Q_{\lambda_3}Q_{\lambda_4} + 4\sum_{\lambda_4\neq\lambda}\Phi_{\lambda\lambda\lambda\lambda_4}Q_{\lambda}^3Q_{\lambda_4} + \Phi_{\lambda\lambda\lambda\lambda}Q_{\lambda}^4\right] \end{aligned} \tag{18}$$

By following the same procedure that we used to write Equations 16, we can write down the expression of the derivative of V_4:

$$\frac{\partial V_4}{\partial Q_\lambda} = \frac{1}{4!}\left[4\sum_{\lambda_2\lambda_3\lambda_4\neq\lambda}\Phi_{\lambda\lambda_2\lambda_3\lambda_4}Q_{\lambda_2}Q_{\lambda_3}Q_{\lambda_4} + 12\sum_{\lambda_3\lambda_4\neq\lambda}\Phi_{\lambda\lambda\lambda_3\lambda_4}Q_\lambda Q_{\lambda_3}Q_{\lambda_4} + 12\sum_{\lambda_4\neq\lambda}\Phi_{\lambda\lambda\lambda\lambda_4}Q_\lambda^2 Q_{\lambda_4} + 4\Phi_{\lambda\lambda\lambda\lambda}Q_\lambda^3\right] = \tag{19a}$$

$$= \frac{1}{4!}\left[4\sum_{\substack{\lambda_2\\ \lambda_3\lambda_4\neq\lambda}}\Phi_{\lambda\lambda_2\lambda_3\lambda_4}Q_{\lambda_2}Q_{\lambda_3}Q_{\lambda_4} + 8\sum_{\lambda_3\lambda_4\neq\lambda}\Phi_{\lambda\lambda\lambda_3\lambda_4}Q_\lambda Q_{\lambda_3}Q_{\lambda_4} + 12\sum_{\lambda_4\neq\lambda}\Phi_{\lambda\lambda\lambda\lambda_4}Q_\lambda^2 Q_{\lambda_4} + 4\Phi_{\lambda\lambda\lambda\lambda}Q_\lambda^3\right] = \tag{19b}$$

$$= \frac{1}{4!}\left[4\sum_{\substack{\lambda_2\\ \lambda_3\lambda_4\neq\lambda}}\Phi_{\lambda\lambda_2\lambda_3\lambda_4}Q_{\lambda_2}Q_{\lambda_3}Q_{\lambda_4} + 8\sum_{\substack{\lambda_3\\ \lambda_4\neq\lambda}}\Phi_{\lambda\lambda\lambda_3\lambda_4}Q_\lambda Q_{\lambda_3}Q_{\lambda_4} + 4\sum_{\lambda_4\neq\lambda}\Phi_{\lambda\lambda\lambda\lambda_4}Q_\lambda^2 Q_{\lambda_4} + 4\Phi_{\lambda\lambda\lambda\lambda}Q_\lambda^3\right] = \tag{19c}$$

$$= \frac{1}{4!}\left[4\sum_{\substack{\lambda_2\\ \lambda_3\lambda_4\neq\lambda}}\Phi_{\lambda\lambda_2\lambda_3\lambda_4}Q_{\lambda_2}Q_{\lambda_3}Q_{\lambda_4} + 8\sum_{\substack{\lambda_3\\ \lambda_4\neq\lambda}}\Phi_{\lambda\lambda\lambda_3\lambda_4}Q_\lambda Q_{\lambda_3}Q_{\lambda_4} + 4\sum_{\lambda_4}\Phi_{\lambda\lambda\lambda\lambda_4}Q_\lambda^2 Q_{\lambda_4}\right] = \tag{19d}$$

$$= \frac{1}{4!}\left[4\sum_{\substack{\lambda_2\lambda_3\\ \lambda_4\neq\lambda}}\Phi_{\lambda\lambda_2\lambda_3\lambda_4}Q_{\lambda_2}Q_{\lambda_3}Q_{\lambda_4} + 4\sum_{\substack{\lambda_3\\ \lambda_4\neq\lambda}}\Phi_{\lambda\lambda\lambda_3\lambda_4}Q_\lambda Q_{\lambda_3}Q_{\lambda_4} + 4\sum_{\lambda_4}\Phi_{\lambda\lambda\lambda\lambda_4}Q_\lambda^2 Q_{\lambda_4}\right] = \tag{19e}$$

$$= \frac{1}{4!}\left[4\sum_{\substack{\lambda_2\lambda_3\\ \lambda_4\neq\lambda}}\Phi_{\lambda\lambda_2\lambda_3\lambda_4}Q_{\lambda_2}Q_{\lambda_3}Q_{\lambda_4} + 4\sum_{\lambda_3\lambda_4}\Phi_{\lambda\lambda\lambda_3\lambda_4}Q_\lambda Q_{\lambda_3}Q_{\lambda_4}\right] = \tag{19f}$$

$$= \frac{1}{4!}\left[4\sum_{\lambda_2\lambda_3\lambda_4}\Phi_{\lambda\lambda_2\lambda_3\lambda_4}Q_{\lambda_2}Q_{\lambda_3}Q_{\lambda_4}\right] = \frac{1}{3!}\sum_{\lambda_2\lambda_3\lambda_4}\Phi_{\lambda\lambda_2\lambda_3\lambda_4}Q_{\lambda_2}Q_{\lambda_3}Q_{\lambda_4}. \tag{19g}$$

Analogous derivations follow for the anharmonic terms of higher order. The general formula to calculate the derivative of the generic anharmonic term V_p ($p \geq 3$) with respect to a selected normal coordinate Q_λ is then

$$\frac{\partial V_p}{\partial Q_\lambda} = \frac{1}{(p-1)!}\sum_{\lambda_1\ldots\lambda_{p-1}}\Phi_{\lambda\lambda_1\ldots\lambda_{p-1}}\prod_{k=1}^{p-1}Q_{\lambda_k}. \tag{20}$$

This result will be useful in the next section where we derive the normal equations at any order of anharmonicity.

III. DERIVATION OF THE NORMAL EQUATIONS

In terms of the normal coordinates, the kinetic energy T of the system has the following diagonal form

$$T = \frac{1}{2}\sum_\lambda \dot{Q}_\lambda \dot{Q}_\lambda^*, \tag{21}$$

with "*" indicating the complex conjugation, while the potential energy reads

$$V = \frac{1}{2}\sum_{\lambda}\omega_{\lambda}^{2}Q_{\lambda}Q_{\lambda}^{*} + \sum_{p\geq 3}\frac{1}{p!}\sum_{\lambda_1\ldots\lambda_p}\Phi_{\lambda_1\ldots\lambda_p}\prod_{k=1}^{p}Q_{\lambda_k} \tag{22}$$

where the first term and the second summations are the harmonic and anharmonic part of the potential, respectively. By using Equation 21 and Equation 22, the Lagrangian $\mathscr{L}$ of the system is then

$$\mathscr{L} = T - V = \frac{1}{2}\sum_{\lambda}\dot{Q}_{\lambda}\dot{Q}_{\lambda}^{*} - \frac{1}{2}\sum_{\lambda}\omega_{\lambda}^{2}Q_{\lambda}Q_{\lambda}^{*} + \sum_{p\geq 3}\frac{1}{p!}\sum_{\lambda_1\ldots\lambda_p}\Phi_{\lambda_1\ldots\lambda_p}\prod_{k=1}^{p}Q_{\lambda_k} \tag{23}$$

from which we can derive the Euler-Lagrange equation for each mode λ:

$$\frac{d}{dt}\frac{\partial\mathscr{L}}{\partial\dot{Q}_{\lambda}} - \frac{\partial\mathscr{L}}{\partial Q_{\lambda}} = 0. \tag{24}$$

To perform the derivatives in Equation 24, let us first recall that the sum over λ in Equation 21 involves the normal coordinates at $\boldsymbol{q} = \Gamma$ and all the complex conjugated couples $\{(Q_{\boldsymbol{q},j}, Q_{-\boldsymbol{q},j}); Q_{-\boldsymbol{q},j} = Q_{\boldsymbol{q},\boldsymbol{j}}^{*})\}$ for $\boldsymbol{q} \neq \Gamma$. If we indicate with $\lambda > 0$ the generic mode $(\boldsymbol{q} \neq \Gamma, j)$ and with $\lambda < 0$ the corresponding mode $(-\boldsymbol{q} \neq \Gamma, j)$, the sum expressing the kinetic energy can be split into three terms:

$$T = \frac{1}{2}\sum_{j}\dot{Q}_{\Gamma j}^{2} + \frac{1}{2}\sum_{\lambda>0}\dot{Q}_{\lambda}\dot{Q}_{\lambda}^{*} + \frac{1}{2}\sum_{\lambda<0}\dot{Q}_{\lambda}\dot{Q}_{\lambda}^{*}, \tag{25}$$

which reduces to

$$T = \frac{1}{2}\sum_{j}\dot{Q}_{\Gamma j}^{2} + \sum_{\lambda>0}\dot{Q}_{\lambda}\dot{Q}_{\lambda}^{*} \tag{26}$$

because $Q_{-\boldsymbol{q},j} = Q_{\boldsymbol{q},\boldsymbol{j}}^{*}$, then the last two sums in Equation 25 are identical. Analogous observation applies on the sum appearing in the expression of the potential energy in Equation 22. Then, we recall that the normal coordinates $Q_{\Gamma j}$ and their time derivatives $\dot{Q}_{\Gamma j}$ are real quantities. Let us now evaluate the single terms of Equation 24:

$$\frac{\partial\mathscr{L}}{\partial\dot{Q}_{\lambda}} = \dot{Q}_{\lambda}^{*}, \quad \frac{d}{dt}\frac{\partial\mathscr{L}}{\partial\dot{Q}_{\lambda}} = \ddot{Q}_{\lambda}^{*}, \tag{27}$$

$$\begin{aligned}\frac{\partial\mathscr{L}}{\partial Q_{\lambda}} =& \frac{\partial}{\partial Q_{\lambda}}\left(-\frac{1}{2}\sum_{\lambda}\omega_{\lambda}^{2}Q_{\lambda}Q_{\lambda}^{*} - \sum_{p\geq 3}\frac{1}{p!}\sum_{\lambda_1\ldots\lambda_p}\Phi_{\lambda_1\ldots\lambda_p}\prod_{k=1}^{p}Q_{\lambda_k}\right)\\ =& -\omega_{\lambda}^{2}Q_{\lambda}^{*} - \sum_{p\geq 3}\frac{1}{(p-1)!}\sum_{\lambda_1\ldots\lambda_{p-1}}\Phi_{\lambda\lambda_1\ldots\lambda_{p-1}}\prod_{k=1}^{p-1}Q_{\lambda_k}\end{aligned} \tag{28}$$

where in the last equation we exploited the result expressed by Equation 20. Equation 24 then reads

$$\ddot{Q}_{\lambda}^{*} + \omega_{\lambda}^{2}Q_{\lambda}^{*} + \sum_{p\geq 3}\frac{1}{(p-1)!}\sum_{\lambda_1\ldots\lambda_{p-1}}\Phi_{\lambda\lambda_1\ldots\lambda_{p-1}}\prod_{k=1}^{p-1}Q_{\lambda_k} = 0 \tag{29}$$

or, in explicit form

$$\ddot{Q}_\lambda = -\omega_\lambda^2 Q_\lambda - \left(\sum_{p\geq 3} \frac{1}{(p-1)!} \sum_{\lambda_1\dots\lambda_{p-1}} \Phi_{\lambda\lambda_1\dots\lambda_{p-1}} \prod_{k=1}^{p-1} Q_{\lambda_k}\right)^* \tag{30}$$

which is the equation of motion of the single normal mode λ and, for this reason, we refer to it as *normal equation* of the mode λ. It is worthy to note here that Equation 30 reduces to the equation of the harmonic oscillator if all the $\Phi_{\lambda\lambda_1\dots\lambda_{p-1}}$ tensors are null, that is, in the absence of anharmonic interactions.

IV. DERIVATION OF THE NORMAL EQUATIONS INCLUDING THE NOSÉ-HOOVER THERMOSTAT

We here derive the normal equations including the Nosé-Hoover thermostat[3–5]; the notation is the same as in the previous section and in particular, we denote with $\dot{X}$ the time-derivative dX/dt. The starting point of the approach, followed by Nosé, is to scale the time by a new degree of freedom s, which acts as an external system[3]. This leads to the definition of new *virtual* variables, which we denote with a tilde under the symbol:

$$d\underset{\sim}{t} = s\,dt \tag{31}$$

$$\underset{\sim}{Q_\lambda} = Q_\lambda \tag{32}$$

$$\underset{\sim}{\dot{Q}_\lambda} = \frac{d\underset{\sim}{Q_\lambda}}{d\underset{\sim}{t}} = \frac{1}{s}\frac{d\underset{\sim}{Q_\lambda}}{dt} = \frac{1}{s}\dot{Q}_\lambda. \tag{33}$$

The Nosé Lagrangian[3] reads then as

$$\mathscr{L}_{\text{Nosé}} = s^2\frac{1}{2}\sum_\lambda \underset{\sim}{\dot{Q}_\lambda}\,\underset{\sim}{\dot{Q}_\lambda}^* - \frac{1}{2}\sum_\lambda \omega_\lambda^2 \underset{\sim}{Q_\lambda}\,\underset{\sim}{Q_\lambda}^* - \sum_{p\geq 3}\frac{1}{p!}\sum_{\lambda_1\dots\lambda_p}\Phi_{\lambda_1\dots\lambda_p}\prod_{k=1}^{p}\underset{\sim}{Q_{\lambda_k}} + \frac{1}{2}Q_{th}\left(\frac{ds}{d\underset{\sim}{t}}\right)^2 - gk_BT\ln s \tag{34}$$

where Q_{th} is the mass of the thermostat, k_B the Boltzmann constant, g an integer constant associated to the number of degrees of freedom of the system, and T the target temperature. The single terms of the Euler-Lagrange equations are:

$$\frac{\partial \mathscr{L}_{\text{Nosé}}}{\partial \underset{\sim}{\dot{Q}_\lambda}} = s^2\underset{\sim}{\dot{Q}^*_\lambda}, \qquad \frac{d}{d\underset{\sim}{t}}\frac{\partial \mathscr{L}_{\text{Nosé}}}{\partial \underset{\sim}{\dot{Q}_\lambda}} = 2s\frac{ds}{d\underset{\sim}{t}}\underset{\sim}{\dot{Q}^*_\lambda} + s^2\underset{\sim}{\ddot{Q}^*_\lambda} \tag{35}$$

$$\frac{\partial \mathscr{L}_{\text{Nosé}}}{\partial \underset{\sim}{Q_\lambda}} = \frac{\partial}{\partial \underset{\sim}{Q_\lambda}}\left(-\frac{1}{2}\sum_\lambda \omega_\lambda^2 \underset{\sim}{Q_\lambda}\,\underset{\sim}{Q_\lambda}^* - \sum_{p\geq 3}\frac{1}{p!}\sum_{\lambda_1\dots\lambda_p}\Phi_{\lambda_1\dots\lambda_p}\prod_{k=1}^{p}\underset{\sim}{Q_{\lambda_k}}\right) \tag{36a}$$

$$= -\omega_\lambda^2\underset{\sim}{Q_\lambda}^* - \sum_{p\geq 3}\frac{1}{(p-1)!}\sum_{\lambda_1\dots\lambda_{p-1}}\Phi_{\lambda\lambda_1\dots\lambda_{p-1}}\prod_{k=1}^{p-1}\underset{\sim}{Q_{\lambda_k}} \tag{36b}$$

$$\frac{\partial \mathscr{L}_{\text{Nosé}}}{\partial\left(\frac{ds}{d\underset{\sim}{t}}\right)} = Q_{th}\frac{ds}{d\underset{\sim}{t}}, \quad \frac{d}{d\underset{\sim}{t}}\frac{\partial \mathscr{L}_{\text{Nosé}}}{\partial\left(\frac{ds}{d\underset{\sim}{t}}\right)} = Q_{th}\frac{d^2s}{d\underset{\sim}{t}^2} \tag{37}$$

$$\frac{\partial \mathscr{L}_{\text{Nosé}}}{\partial s} = s\sum_{\lambda}\underset{\sim}{\dot{Q}_\lambda}\underset{\sim}{\dot{Q}^*_\lambda} - gk_BT\frac{1}{s}. \tag{38}$$

By putting everything together, the Euler-Lagrange equations read as

$$2s\frac{ds}{d\underset{\sim}{t}}\underset{\sim}{\dot{Q}^*_\lambda} + s^2\underset{\sim}{\ddot{Q}^*_\lambda} + \omega_\lambda^2\underset{\sim}{Q_\lambda}^* + \sum_{p\geq 3}\frac{1}{(p-1)!}\sum_{\lambda_1\ldots\lambda_{p-1}}\Phi_{\lambda\lambda_1\ldots\lambda_{p-1}}\prod_{k=1}^{p-1}\underset{\sim}{Q_{\lambda_k}} = 0 \tag{39}$$

$$Q_{th}\frac{d^2s}{d\underset{\sim}{t}^2} - s\sum_{\lambda}\underset{\sim}{\dot{Q}_\lambda}\underset{\sim}{\dot{Q}^*_\lambda} + gk_BT\frac{1}{s} = 0. \tag{40}$$

Let us come back to the *real* variables. First, let us remind that

$$\underset{\sim}{\ddot{Q}_\lambda} = \frac{d\underset{\sim}{\dot{Q}_\lambda}}{d\underset{\sim}{t}} = \frac{1}{s}\frac{d\underset{\sim}{\dot{Q}_\lambda}}{dt} = \frac{1}{s}\frac{d}{dt}\left(\frac{1}{s}\dot{Q}_\lambda\right) = \frac{1}{s}\left(-\frac{1}{s^2}\dot{s}\dot{Q}_\lambda + \frac{1}{s}\ddot{Q}_\lambda\right) = \frac{1}{s^2}\left(\ddot{Q}_\lambda - \frac{\dot{s}}{s}\dot{Q}_\lambda\right) \tag{41}$$

$$\frac{ds}{d\underset{\sim}{t}} = \frac{1}{s}\frac{ds}{dt} = \frac{\dot{s}}{s} \tag{42}$$

$$\frac{d^2s}{d\underset{\sim}{t}^2} = \frac{d}{d\underset{\sim}{t}}\left(\frac{ds}{d\underset{\sim}{t}}\right) = \frac{1}{s}\frac{d}{dt}\left(\frac{ds}{d\underset{\sim}{t}}\right) = \frac{1}{s}\frac{d}{dt}\left(\frac{\dot{s}}{s}\right) = \frac{1}{s}\frac{\ddot{s}s - \dot{s}\dot{s}}{s^2} = \frac{1}{s}\left[\frac{\ddot{s}}{s} - \left(\frac{\dot{s}}{s}\right)^2\right] \tag{43}$$

and then plug these into Equation 39 and Equation 40:

$$2s\frac{\dot{s}}{s}\frac{1}{s}\dot{Q}^*_\lambda + s^2\frac{1}{s^2}\left(\ddot{Q}^*_\lambda - \frac{\dot{s}}{s}\dot{Q}^*_\lambda\right) + \omega_\lambda^2 Q^*_\lambda + \sum_{p\geq 3}\frac{1}{(p-1)!}\sum_{\lambda_1\ldots\lambda_{p-1}}\Phi_{\lambda\lambda_1\ldots\lambda_{p-1}}\prod_{k=1}^{p-1}Q_{\lambda_k} = \tag{44a}$$

$$= 2\frac{\dot{s}}{s}\dot{Q}^*_\lambda + \ddot{Q}^*_\lambda - \frac{\dot{s}}{s}\dot{Q}^*_\lambda + \omega_\lambda^2 Q^*_\lambda + \sum_{p\geq 3}\frac{1}{(p-1)!}\sum_{\lambda_1\ldots\lambda_{p-1}}\Phi_{\lambda\lambda_1\ldots\lambda_{p-1}}\prod_{k=1}^{p-1}Q_{\lambda_k} = \tag{44b}$$

$$= \frac{\dot{s}}{s}\dot{Q}^*_\lambda + \ddot{Q}^*_\lambda + \omega_\lambda^2 Q^*_\lambda + \sum_{p\geq 3}\frac{1}{(p-1)!}\sum_{\lambda_1\ldots\lambda_{p-1}}\Phi_{\lambda\lambda_1\ldots\lambda_{p-1}}\prod_{k=1}^{p-1}Q_{\lambda_k} = 0 \tag{44c}$$

$$Q_{th}\frac{1}{s}\left[\frac{\ddot{s}}{s} - \left(\frac{\dot{s}}{s}\right)^2\right] - s\sum_{\lambda}\frac{1}{s}\dot{Q}_\lambda\frac{1}{s}\dot{Q}^*_\lambda + gk_BT\frac{1}{s} = \tag{45a}$$

$$= \frac{1}{s^2}Q_{th}\ddot{s} - \frac{1}{s}Q_{th}\left(\frac{\dot{s}}{s}\right)^2 - \frac{1}{s}\sum_{\lambda}\dot{Q}_\lambda\dot{Q}^*_\lambda + \frac{1}{s}gk_BT = 0 \Rightarrow \tag{45b}$$

$$\Rightarrow \frac{1}{s}Q_{th}\ddot{s} - Q_{th}\left(\frac{\dot{s}}{s}\right)^2 - \sum_{\lambda}\dot{Q}_\lambda\dot{Q}^*_\lambda + gk_BT = 0 \tag{45c}$$

where in the last step we exploited the fact that $s > 0$ by construction (see Equation 31). Moreover, the equations of motion can be furtherly simplified if one uses the approach described in Ref. 5, where the constant g is set equal to $3N$. Let us define an auxiliary variable ξ such that

$$\xi = \ln s; \tag{46}$$

it then follows that

$$\dot{\xi} = \frac{d\xi}{dt} = \frac{d}{dt}(\ln s) = \frac{1}{s}\frac{ds}{dt} = \frac{\dot{s}}{s} \tag{47}$$

and

$$\ddot{s} = \frac{d\dot{s}}{dt} = \frac{d}{dt}\left(s\dot{\xi}\right) = \frac{ds}{dt}\dot{\xi} + s\frac{d\dot{\xi}}{dt} = \dot{s}\dot{\xi} + s\ddot{\xi}. \tag{48}$$

By plugging these relations into Equation 44 and Equation 45, one gets

$$\dot{\xi}\dot{Q}^*_\lambda + \ddot{Q}^*_\lambda + \omega^2_\lambda Q^*_\lambda + \sum_{p\geq 3} \frac{1}{(p-1)!} \sum_{\lambda_1 \dots \lambda_{p-1}} \Phi_{\lambda\lambda_1\dots\lambda_{p-1}} \prod_{k=1}^{p-1} Q_{\lambda_k} = 0 \tag{49}$$

$$\frac{1}{s}Q_{th}\ddot{s} - Q_{th}\left(\frac{\dot{s}}{s}\right)^2 - \sum_\lambda \dot{Q}_\lambda \dot{Q}_\lambda{}^* + 3Nk_BT = \tag{50a}$$

$$= \frac{1}{s}Q_{th}\left(\dot{s}\dot{\xi} + s\ddot{\xi}\right) - Q_{th}\dot{\xi}^2 - \sum_\lambda \dot{Q}_\lambda \dot{Q}_\lambda{}^* + 3Nk_BT = \tag{50b}$$

$$= Q_{th}\frac{\dot{s}}{s}\dot{\xi} + Q_{th}\ddot{\xi} - Q_{th}\dot{\xi}^2 - \sum_\lambda \dot{Q}_\lambda \dot{Q}_\lambda{}^* + 3Nk_BT = \tag{50c}$$

$$= Q_{th}\ddot{\xi} - \sum_\lambda \dot{Q}_\lambda \dot{Q}_\lambda{}^* + 3Nk_BT = 0 \tag{50d}$$

or, finally in explicit form

$$\ddot{Q}_\lambda = -\omega^2_\lambda Q_\lambda - \left(\sum_{p\geq 3} \frac{1}{(p-1)!} \sum_{\lambda_1 \dots \lambda_{p-1}} \Phi_{\lambda\lambda_1\dots\lambda_{p-1}} \prod_{k=1}^{p-1} Q_{\lambda_k}\right)^* - \dot{\xi}\dot{Q}_\lambda \tag{51}$$

$$\ddot{\xi} = \frac{1}{Q_{th}}\left(\sum_\lambda \dot{Q}_\lambda \dot{Q}_\lambda{}^* - 3Nk_BT\right) \tag{52}$$

which are the NVT normal equations sampling the canonical ensemble. If $\dot{\xi}(t) = 0\ \forall t$, then Equation 51 reduces to the NVE normal equations as in Equation 30.

V. PARTITIONING THE $\boldsymbol{q}$-POINT SET

Following the example reported in the main text, the complete set[1] of wave vectors commensurate with the $3 \times 3 \times 3$ supercell is $\boldsymbol{q}_{333} = \{(m/3, n/3, p/3); m, n, p = 0, 1, 2\}$, corresponding to $81N$ Q_λ normal coordinates. Equivalently, thanks to the periodicity of the reciprocal space, the complete set can be chosen as $\boldsymbol{q}_{333} = \{(m/3, n/3, p/3); m, n, p = 0, \pm 1\}$. It is worthy to note here that the set can be partitioned in three subsets: *i*) the set G containing only the Γ point, *ii*) the set S containing the points $\{(m/3, n/3, p/3); m = n = 0; p = 1 \cup m = 0; n = 1; p = 0, \pm 1 \cup m = 1; n = 0, \pm 1; p = 0, \pm 1\}$ and *iii*) the set S^* containing the remaining points. It is easy to show that any vector in the set S^* can be obtained by changing the sign to all the components of some vectors in S. In other words, if we denote as $\boldsymbol{q}^S$ a generic vector in S, then the corresponding vector in S^* is built as $-\boldsymbol{q}^S$. However, the normal coordinates are tied by the relation $Q_{-\boldsymbol{q},j} = Q^*_{\boldsymbol{q},j}$;[1] therefore, it is enough to explicitly evolve only the normal coordinates corresponding to the $\boldsymbol{q}$ vectors in the G and S sets, as the normal coordinates for all vectors in the S^* set can be obtained by complex conjugation. The number of *non-redundant* $\boldsymbol{q}$-points in the complete $\boldsymbol{q}_{333}$ set is then $(3 \times 3 \times 3 - 1)/2 + 1 = 14$; the corresponding number of normal coordinates is $3N \times 14 = 42N$, which amounts to $(1 + 13 \times 2) \times 3N = 81N$ real variables, as for the Cartesian case, since the $Q_{\boldsymbol{q},j}$ are all complex quantities except for $\boldsymbol{q} = \Gamma$.

Let us now briefly consider another system, namely a $2 \times 2 \times 1$ supercell. In this case, the complete set is formed by the points Γ, $(1/2, 0, 0)$, $(0, 1/2, 0)$ and $(1/2, 1/2, 0)$. Notice that the point $(-1/2, 0, 0)$ is not included, as it corresponds to the border of the Brillouin zone, and it is then equivalent to $(1/2, 0, 0)$ thanks to the periodicity of the reciprocal lattice (analogous considerations apply for the remaining points with $-1/2$ as a component). In this case, it is therefore not possible to partition the complete set into S and S^* subsets: no $\boldsymbol{q} \neq \Gamma$ vector can be obtained *via* complex conjugation of any other vector in the set.

In the general case, a complete $\{\boldsymbol{q}\}$ set can be partitioned into three non-redundant subsets, namely G, H and S, where H contains all the points at the border of the Brillouin zone. We then call N_Γ, N_H and N_S the number of $\boldsymbol{q}$-points in the subset indicated by the subscript; by construction, $N_\Gamma = 1$ or 0 depending whether Γ is included or not in $\{\boldsymbol{q}\}$. The complete sampling of an $m \times n \times p$ supercell can then be obtained by considering the wave vectors forming the corresponding $G \cup H \cup S$ set and evolving explicitly the related normal coordinates during the dynamics.

VI. PREPARATION, RUN AND ANALYSIS OF NORMAL DYNAMICS SIMULATIONS

We here summarize the main steps necessary to run a Normal Dynamics (ND) simulation and process the output. We wrote some pre- and postprocessing codes in Fortran 90 which interface with `pindol` in order to prepare the input files for an ND run and convert the ND trajectory in standard formats which can be read by other softwares. The codes are available as part of the PINDOL package freely downloadable from the GITHUB repository[6]; the details on their usage are reported in the following subsections as well as in the relative README.md files present in the repository.

a. Preparation of the input files The necessary input to run an ND simulation are: *i*) the unit cell of the reference structure, *ii*) the corresponding eigenvectors and eigenfrequencies, and *iii*) the Fourier transformed tensor $\boldsymbol{\Phi}_3$.

The unit cell is specified in POSCAR format as in the VASP[7–11] software. The interatomic forces needed to obtain the phonon modes and the Cartesian $\boldsymbol{\Theta}_3$ tensor can be calculated by means of classical (i.e. force fields) or quantum descriptions. In the present work, we use the Density Functional Theory framework; the computational details of each case study are reported in the respective subsections of the main text. Once the interatomic forces are obtained, we use the PHONOPY software[12] to diagonalize the dynamical matrix and to calculate the $\boldsymbol{\Theta}_3$ tensor. Then, we use the home-made code named `qpoints` to extract the phonon eigenvectors and frequencies from the PHONOPY output, producing the `qmatrix.nd` and `freq.nd` files. The `qpoints` code can be easily extended to interface with other force constant calculators. The $\Phi_{\lambda\lambda_1\lambda_2}$ elements are then obtained by performing a Fourier transform of $\boldsymbol{\Theta}_3$ with the calculated phonon eigenvectors as a basis set.[1] To this aim, we use the home-made preprocessing code named `phind`, which produces the file `phi.nd`. The code exploits the symmetry of $\boldsymbol{\Phi}$ by index permutation, the complex conjugation relation between the elements, and considers only the $\{\lambda, \lambda_1, \lambda_2\}$ triplets which satisfy the selection rule $\Delta(\boldsymbol{q}+\boldsymbol{q}_1+\boldsymbol{q}_2) = 1$.[1,2] This reduces to the minimum the number of elements to be calculated in order to reconstruct the full $\boldsymbol{\Phi}_3$ tensor, as well as the amount of data to be stored in the volatile memory during the ND simulations or on the disk when writing the corresponding file. The number of $\Phi_{\lambda\lambda_1\lambda_2}$ elements can be further reduced by taking into account the phonon-phonon scattering selection rules involving the mode eigenvectors;[13] however, we did not implement this feature in `phind` yet. Since we want to be able to observe possible phase transformations during the dynamics, `phind` does not take into account the crystal symmetries: they would introduce constraints on the phonon interactions and reduce the number of degrees of freedom necessary for the phase transition to occur. `phind` takes advantage of the OpenMP[14] parallelization whenever available.

b. ND run The simulation settings such as the kind of ensemble and the integration interval are set in the `pindol.inp` input file. The ND simulation is then performed by the `pindol` executable, which reads the setting file, `qmatrix.nd`, `freq.nd` and `phi.nd`. The standard output contains information about the input setup and the evolving physical quantities, e.g., time of the simulation, harmonic, anharmonic and total energy, conserved quantity, temperature of the system. On user's request, `pindol` produces also three output files, which we may name as `normcoord.dat`, `normvel.dat` and `normacc.dat`, respectively; they contain the Q_λ normal coordinates, the $\dot{Q}_\lambda$ normal velocities and the $\ddot{Q}_\lambda$ normal accelerations at each time step: they are the trajectory of the normal dynamics simulation. The simulation is terminated when the number of time steps set in the input file is reached. The equations that are solved are of the form

$$\ddot{Q}_\lambda = -\omega_\lambda^2 Q_\lambda - \left(\sum_{\lambda_1\lambda_2} \Phi_{\lambda\lambda_1\lambda_2} Q_{\lambda_1} Q_{\lambda_2}\right)^* \tag{53}$$

reproducing the microcanonical (NVE) enseble, or

$$\ddot{Q}_\lambda = -\omega_\lambda^2 Q_\lambda - \left(\sum_{\lambda_1\lambda_2} \Phi_{\lambda\lambda_1\lambda_2} Q_{\lambda_1} Q_{\lambda_2}\right)^* - \dot{\xi}\dot{Q}_\lambda \tag{54}$$

$$\ddot{\xi} = \frac{1}{Q_{th}} \left(\sum_{\lambda} \dot{Q}_\lambda \dot{Q}_\lambda^* - 3Nk_B T\right) \tag{55}$$

reproducing the canonical (NVT) ensemble with the Nosé-Hoover thermostat[3–5]. The sum

$$\sum_{\lambda_1\lambda_2} \Phi_{\lambda\lambda_1\lambda_2} Q_{\lambda_1} Q_{\lambda_2} \tag{56}$$

appearing in Equation 53 and Equation 54 is evaluated over all the $\Phi_{\lambda\lambda_1\lambda_2}$ elements; a complete $\boldsymbol{\Phi}_3$ tensor is then in principle required to be stored in the memory. However, since the elements are of complex type and are represented with double precision, the available memory would strongly limit the maximum number of points in the $\{\boldsymbol{q}_i\}$ set and the maximum number of atoms in the system. To avoid such limitations, only a minimum number of $\Phi_{\lambda\lambda_1\lambda_2}$ elements are written in the `phi.nd` file (see previous paragraph) and stored in memory; the complete tensor is recovered and included in the sum on-the-fly during the simulation by the `calc_double_sum` routine. The number of operations required to reconstruct the tensor depends on the kind of $\{\lambda, \lambda_1, \lambda_2\}$ triplet; the technical details are reported as comments in the corresponding source code file provided as Supplemental Material or in the PINDOL repository.[6]

c. Postprocessing The files containing the ND trajectory can be used to monitor the amplitude evolution of specific phonon modes in order to identify phase transitions or relevant phonon scattering processes. Moreover, the ND trajectory can be converted into Cartesian format by means of the code `nd2xyz` included in the PINDOL package, which produces the files `ndtraj.xyz`, `ndvel.xyz` and `ndacc.xyz`, containing the Cartesian positions, velocities and accelerations, respectively. Such files can then be used for postprocessing to extract any physical quantity as in usual Cartesian simulations. In the presented case studies, we are interested into the calculation of the effective interatomic force constants[15–22], in order to show that the ND simulations are capable to take into account the effect of temperature as the standard Cartesian simulations. To this aim, we make use of the HIPHIVE software[23]; the relevant input files for HIPHIVE can be obtained by the `nd2hiphive` code included in the PINDOL package.

A. Preprocessing: qpoints

The `qpoints` code creates the qmatrix.nd and freq.nd files to be used by `phind` and `pindol`. The mandatory files for the `qpoints` code are the following:

1. FORCE_CONSTANTS generated by the PHONOPY[12] software;
2. geometry file in POSCAR format;
3. optional geometry file to be supplied to PHONOPY.

The input file must contain the following lines in the order; with *string* or *int* we indicate the fortran format of the value:

- *string* phonopy executable and related options if the geometry file used to create the FORCE_CONSTANTS is other than POSCAR
- *string* geometry file in POSCAR format
- *int int int* mesh used to generate the FORCE_CONSTANTS file
- *int* number of modes to skip (e.g. acoustic, rotational)
- *int int* ... *int int* $\boldsymbol{q}$ j labels of the modes to skip
- *int* number of $\boldsymbol{q}$-points in the $\{\boldsymbol{q}\}$ set
- *double double double* reduced components of the first $\boldsymbol{q}$-point
- ⋯
- *double double double* reduced components of the last $\boldsymbol{q}$-point

The code is executed with the command

```
qpoints qpt.inp
```

where `qpt.inp` is a generic name for the settings file. The $\{\boldsymbol{q}\}$ set must be specified in the order G, H, S, whereas each subset must not be necessarily present. For any use of `qpoints` other than ND simulations, the order of the points in the set can be arbitrary. The `q4phind` code present in the PINDOL repository[6] can be used to prepare the list of the points in the right order. Once executed, `qpoints` calls PHONOPY to create the `qpoints.yaml` containing the eigendisplacements and eigenfrequencies; these are then extracted into `qmatrix.nd` and `freq.nd` with the same units as in `qpoints.yaml`, which will be used by `phind` and `pindol`.

B. Preprocessing: phind

The `phind` code calculates the Fourier transform $\mathbf{\Phi}_3$ of the third-order force constants contained in the `fc3.dat`; the latter must be present in the folder where the code is executed together with the `qmatrix.nd` and `freq.nd` files. The `fc3.dat` can be created from the `fc3.hdf5` by using the `fc3_extract.py` python script as provided in the PINDOL package.

The settings file contains the following lines in the order:

1. *string* geometry file in POSCAR format
2. *int int int* mesh used to generate the `fc3.hdf5` (`fc3.dat`) file
3. *int* number of atomic types
4. *string double* atomic symbol and mass (amu) of the first atom type
5. $\cdots$
6. *string double* atomic symbol and mass (amu) of the last atom type
7. *int* flag to write the $(\boldsymbol{q}, j) \to \lambda$ map; 0 = no, 1 = yes
8. *int* flag to calculate the $\Phi_{\lambda\lambda'\lambda''}$ elements; 0 = no, 1 = yes

The code is executed with the command

```
phind phind.inp
```

where `phind.inp` is a generic name for the settings file. At the and of the execution, the `phi.nd` file is created to be used by `pindol`.

C. ND run: the PINDOL code

The `pindol` executable performs the ND simulation in the NVE or NVT ensembles, the latter generated by using the Nosé-Hoover thermostat[3–5]. The files that must be present in the folder where the code is executed are:

1. `qmatrix.nd` and `freq.nd` generated by `qpoints`, and `phi.nd` generated by `phind`;
2. the geometry reference file in LAMMPS or VASP POSCAR format, the same used to generate the files in the previous steps.

An initial configuration (i.e., atomic positions and velocities) can be provided as a file in LAMMPS or POSCAR format; alternatively, the velocities can be initialized before starting the simulation through the INITVEL keyword (see below). The settings are specified in the `pindol.inp` file. The file must contain the **ATOMS block**, with information on the atomic types:

ATOMS
`types` *int* # how many atom types
`atom` *string double* # name of the atom, atomic mass (amu)
END_ATOMS

where the number of atomic types must preceed the list of the atoms. The **ND block** is optional, and specifies the ND run:
ND
`nve` # NVE ensemble
or
`nvt` *double double double* # NVT ensemble with initial and final temperature (K) followed by the step (K) used for a linear ramp change of the temperature; if initial and final temperatures are the same, the temperature is not changed during the simulation
`integrator` *double* 22 both 1.d-15 # integration time step followed by the options for the DVODE solver
`runsteps` *int* # number of integration steps
`printcoord` *int* normcoord.dat # writing frequency of the normal coordinats file (e.g., `normcoord.dat`)
`printvel` *int* normvel.dat # writing frequency of the normal velocities file (e.g., `normvel.dat`)
`printacc` *int* normacc.dat # writing frequency of the normal accelerations file (e.g., `normacc.dat`)
END_ND

Mandatory keywords are:

REFCONF `poscar/lammps` POSCAR # reference geometry file (e.g., POSCAR) in POSCAR or LAMMPS format.
UNITS `real/metal` # units for the output; `real` = time in fs, energy in joule

Moreover, optional keywords can be specified:

DISTORT *int double* `all` # seed for the random number generation, maximum amplitude of atomic displacements in Å, keyword "all"
or, to distort the structure along specific normal coordinates
DISTORT *int double int int* … # seed for the random number generation, maximum amplitude of atomic displacements in Å, number of normal modes along which the distortions will be applied, pair(s) specifying the $\boldsymbol{q}$-point and the mode
INITCONF `poscar/lammps` POSCAR.init # initial atom positions and velocities in POSCAR or LAMMPS format are taken from the, e.g., POSCAR.init; the geometry must be a supercell commensurate with the $\{q\}$ set

INITVEL *double int* # velocities are initialized from a Gaussian distribution at the specified temperature; the next argument is the seed for the random number generator. Initial positions and velocities are written in the file specified by FINALCONF and the execution is terminated if the ND block is not provided.

FINALCONF `poscar/lammps` final.vasp # atom geometry and velocities calculated at the last step of the ND run or with the INITVEL keyword; the geometry is a supercell commensurate with the $\{\boldsymbol{q}\}$ set

WRITERESTART `final.restart` # at the end of the simulation, the restart file (e.g., `final.restart`) containing the final atom geometry and velocities is written; if the NVT ensemble is specified, the thermostat status is also written.

READRESTART `init.restart` # file (e.g., `init.restart`) used to continue the simulation

The last line of the setting file must contain the keywork END; any keyword after that is ignored. The code is executed with the command

```
pindol
```

The standard output contains information on the energy, the conserved quantity and the temperature at each time step. If the environmental variable OMP_NUM_THREADS is specified, `pindol` exploits the OpenMP parallelization.

D. Postprocessing: nd2xyz

The `nd2xyz` executable processes the trajectory contained in the file created by `pindol` specified with the `printcoord, printvel` and `printacc` keywords. The files `freq.nd` and `qmatrix.nd` must be present in the folder where the code is executed.

The setting file contains the following lines in the order:

1. POSCAR # reference geometry file in POSCAR format (e.g., POSCAR)
2. `normcoord.dat` # ND normal coordinate file (e.g., `normcoord.dat`); 0 = no file to convert
3. `normvel.dat` # ND normal velocities file (e.g., `normvel.dat`); 0 = no file to convert
4. `normacc.dat` # ND normal acceleration file (e.g., `normacc.dat`); 0 = no file to convert
5. *int* # number of atomic types
6. *string double* # atom symbol and mass (amu) of the first atom type
7. $\cdots$
8. *string double* # atom symbol and mass (amu) of the last atom type
9. *double double* # time window: initial and final time
10. *int* # 1 = use the last step of the input files regardless the time window specified above and write a POSCAR_last.vasp file containing atom positions and velocities in POSCAR format

The code is executed with the command

```
nd2xyz nd2xyz.inp
```

where `nd2xyz.inp` is a possible name for the settings file.

E. Postprocessing: nd2hiphive

The `nd2hiphive` code processes the normal coordinate and acceleration files to produce the necessary input for the HIPHIVE code[23]. The `qmatrix.nd` and `freq.nd` files must be present in the folder where the code is executed. The settings file contains the following lines in the order:

1. POSCAR # reference geometry file (e.g., POSCAR)
2. `normcoord.dat` # normal coordinate file (e.g., `normcoord.dat`)
3. `normacc.dat` # normal acceleration file (e.g., `normacc.dat`)

4. *int* # number of atomic types

5. *string double* # atom symbol and mass (amu) of the first atom type

6. ⋯

7. *string double* # atom symbol and mass (amu) of the last atom type

8. *double double double* # initial time, final time, time skip

The code is executed with the command:

```
nd2hiphive nd2hiphive.inp
```

where `nd2hiphive.inp` is a generic name for the settings file.

At the end of the execution, `nd2hiphive` produces the following files:

1. `ndhiPhive_prim.xyz`, the reference unit cell in XYZ format

2. `ndhiPhive_prim_dir.vasp`, the reference unit cell in POSCAR format and direct coordinates

3. `ndhiPhive_phonopy.py`, the python code to be used in the input file for the HIPHIVE software

4. `ndhiPhive_superc.xyz`, the supercell commensurate with the $\{\boldsymbol{q}\}$ set

5. `ndhiPhive_dispfor.xyz`, the position (Å) and forces (eVÅ^{-1}) in the time window specified in the settings file.

The HIPHIVE code is then called with a suitable python script to generate the effective second- and third-order force constant files. An example of such script can be found in the repository of the PINDOL software.

VII. EIGENVECTOR MAP BASED ON ATOMIC DISPLACEMENTS

Let's consider a phonon mode $(\boldsymbol{q}, j)$ with eigenvector $\boldsymbol{e}_{\boldsymbol{q},j}$ defined as

$$\boldsymbol{e}_{\boldsymbol{q},j} = (e_{x1}, e_{y1}, e_{z1}, \ldots, e_{xi}, e_{yi}, e_{zi}, \ldots, e_{xN}, e_{yN}, e_{zN})_j \tag{57}$$

where N is the number of atoms in the system, $\boldsymbol{q}$ is a vector of the reciprocal lattice, j is one of the $3N$ eigenvectors at the corresponding $\boldsymbol{q}$, and each $e_{\alpha i}$ element corresponds to the α-th cartesian component of the i-th atom. In the last case study, we focus on the contribution of each phonon mode to the total $\boldsymbol{u}_{kl}$ displacement; this corresponds to consider only one term at a time in the sum in Equation 9, that is

$$Q_{\boldsymbol{q},j}\boldsymbol{e}_k(\boldsymbol{q}, j)\exp(i\boldsymbol{q}\cdot\boldsymbol{r}^0_{kl}) + c.c. \tag{58}$$

Since we are analysing all the phonons that possibly contribute to the Raman signal, we select $\boldsymbol{q} = \Gamma = (0, 0, 0)$; therefore, the quantity $\exp(i\boldsymbol{q}\cdot\boldsymbol{r}^0_{kl})$ in Equation 9 and Equation 58 is equal to 1. The contribution of the mode (Γ, j) to the displacement $\boldsymbol{u}_{kl}$ then reduces to

$$Q_{\Gamma,j}\boldsymbol{e}_k(\Gamma, j). \tag{59}$$

The definition of a normal coordinate $Q_{\mathbf{\Gamma},j}$ at $\boldsymbol{q} = \Gamma$ is

$$Q_{\Gamma,j} = \frac{1}{\sqrt{N_0}} \sum_{l=1}^{N_0} \sum_{k=1}^{N} (\sqrt{m_k} \boldsymbol{u}_{kl} \cdot \boldsymbol{e}_k(\Gamma, j)) \tag{60}$$

where the number of unit cell $N_0 = 1$ as we are considering only the Γ point. By definition of the dynamical matrix at Γ[1], the eigenvector $\boldsymbol{e}_k(\Gamma, j)$ is real; therefore, also $Q_{\Gamma,j}$ is a real quantity, as no complex quantities appear in Equation 60. Since the amplitude $Q_{\Gamma,j}$ depends on the temperature, we can set $Q_{\Gamma,j} = 1$ for simplicity. So, the contribution of the mode (Γ, j) to the displacement $\boldsymbol{u}_{kl}$ is just the real part of the eigenvector $\boldsymbol{e}_k(\Gamma, j)$. For this reason, we consider only the real part when comparing two different eigenvectors $\boldsymbol{e}_k(\Gamma, j)$ and $\boldsymbol{e}'_k(\Gamma, j)$.

Since we are here interested only in comparing the direction of the displacements at the Γ point, it is convenient to define a corresponding vector $\boldsymbol{v}_{\Gamma,j}$ with $3N$ real components

$$\boldsymbol{v}_{\Gamma,j} = (x_1, y_1, z_1, \ldots, x_i, y_i, z_i, \ldots, x_N, y_N, z_N)_j \tag{61}$$

where x_i, y_i and z_i are the real part of the e_{xi}, e_{yi}, e_{zi} elements of the $\boldsymbol{e}_{\Gamma,j}$ vector, respectively. Let's now consider two structures which we label as "0" and "1"; we indicate with (Γ^0, j^0) and (Γ^1, j^1) two specific phonon modes of the structures 0 and 1, respectively. We name as $\boldsymbol{v}^0$ the atom displacement vector generated by the phonon (Γ^0, j^0) in the structure 0; we define $\boldsymbol{v}^1$ for the structure 1 in an analogous way. Since the phonon eigenvectors generate atom displacements which are periodic with the time, it is enough for us to compare only the direction of the eigendisplacements and neglect the verse; in other words, parallel and antiparallel displacements can be considered as equivalent for the present analysis. Therefore, we measure the angle α between the two displacements as

$$\alpha(\boldsymbol{v}^0, \boldsymbol{v}^1) = \arccos\left(\frac{|\boldsymbol{v}^0 \cdot \boldsymbol{v}^1|}{|\boldsymbol{v}^0||\boldsymbol{v}^1|}\right) \tag{62}$$

where the absolute value of the scalar product $\boldsymbol{v}^0 \cdot \boldsymbol{v}^1$ serves us to neglect the verse of the displacement. With this definition, the smaller the α value, the more similar the direction of the two sets of displacements. Therefore, in order to establish a map between two sets of vectors based on the atomic displacements, it is enough to calculate all the possible α values at varying (Γ^0, j^0) and (Γ^1, j^1) modes, and select the vector couples with the lowest α. Equation 62 is general and does not depend on the chemical composition nor depends on the physical phenomenon under consideration; the only requirement is that the $\boldsymbol{v}^0$ and $\boldsymbol{v}^1$ vectors belong to vectorial spaces of the same size, that is, they must have the same number of components.

As an example, let's consider the MoS/MoSe and MoS/WS systems. The E^1 Raman peak is generated by the (Γ, 12-13) phonons in the MoS/MoSe system, the two modes being degenerate; let's focus on the mode (Γ, 12). In order to find which is the phonon with the same displacement pattern in the MoS/WS system, we

1. build $\boldsymbol{v}^0$ from the (Γ, 12) phonon eigenvector of MoS/MoSe;
2. build $\boldsymbol{v}^1$ from a (Γ, $j \geq 4$) phonon eigenvector of MoS/WS; we neglect $j = 1, 2, 3$, as the acoustic modes at Gamma are surely not relevant for the Raman analysis;
3. calculate $\alpha(\boldsymbol{v}^0, \boldsymbol{v}^1)$;
4. repeat steps 2.-3. by varying j over all the modes of MoS/WS at Γ;

5. finally select the vector $\tilde{\boldsymbol{v}}^1$ which gives the minimum α value: $\tilde{\boldsymbol{v}}^1$ is the vector corresponding to $\boldsymbol{v}^0$.

In our case, the mode (Γ, 12) of the MoS/MoSe system corresponds to the mode (Γ, 11) of the MoS/WS system. By repeating the whole procedure for all the $\boldsymbol{v}^0$ vectors, we can establish a one-to-one map between all the eigenvectors of the two systems. Analogously, we use the same procedure to compare the eigenvectors of a selected system generated by simulations at different temperature; in this way, we can track the evolution of the corresponding eigenfrequencies without any ambiguities.

We implement the mapping procedure in the `eigmap` code,[24] which can be redistributed under the GNU General Public License[25] conditions.

REFERENCES

[1] D. M. Wallace, *Thermodynamics of Crystals* (John Wiley & Sons Inc, United States of America, 1972).

[2] J. M. Ziman, *Electrons and Phonons: The Theory of Transport Phenomena in Solids* (Oxford University Press, United Kingdom, 2001).

[3] S. Nosé, "A molecular dynamics method for simulations in the canonical ensemble," Mol. Phys. **52**, 255–268 (1984).

[4] S. Nosé, "A unified formulation of the constant temperature molecular dynamics methods," J. Chem. Phys. **81**, 511–519 (1984).

[5] W. G. Hoover, "Canonical dynamics: Equilibrium phase-space distributions," Phys. Rev. A **31**, 1695–1697 (1985).

[6] "PINDOL," The software is available free of charge at `https://github.com/acammarat/pindol` (2024), last retrieved 2024-03-07.

[7] G. Kresse and J. Hafner, "Ab initio molecular dynamics for liquid metals," Phys. Rev. B **47**, 558–561 (1993).

[8] G. Kresse and J. Hafner, "Ab initio molecular-dynamics simulation of the liquid-metal–amorphous-semiconductor transition in germanium," Phys. Rev. B **49**, 14251–14269 (1994).

[9] G. Kresse and J. Furthmüller, "Efficiency of ab-initio total energy calculations for metals and semiconductors using a plane-wave basis set," Comput. Mater. Sci. **6**, 15–50 (1996).

[10] G. Kresse and J. Furthmüller, "Efficient iterative schemes for ab initio total-energy calculations using a plane-wave basis set," Phys. Rev. B **54**, 11169–11186 (1996).

[11] G. Kresse and D. Joubert, "From ultrasoft pseudopotentials to the projector augmented-wave method," Phys. Rev. B **59**, 1758–1775 (1999).

[12] A. Togo and I. Tanaka, "First principles phonon calculations in materials science," Scr. Mater. **108**, 1–5 (2015).

[13] A. Cammarata, "Phonon-phonon scattering selection rules and control: an application to nanofriction and thermal transport," RSC Adv. **9**, 37491–37496 (2019).

[14] A. Silberschatz, P. B. Galvin, and G. Gagne, *Operating System Concepts* (John Wiley & Sons, Nashville, TN, 2012).

[15] K. Esfarjani and H. T. Stokes, "Method to extract anharmonic force constants from first principles calculations," Phys. Rev. B **77**, 144112 (2008).

[16] K. Esfarjani, G. Chen, and H. T. Stokes, "Heat transport in silicon from first-principles calculations," Phys. Rev. B **84**, 085204 (2011).

[17] J. Shiomi, K. Esfarjani, and G. Chen, "Thermal conductivity of half-Heusler compounds from first-principles calculations," Phys. Rev. B **84**, 104302 (2011).

[18] O. Hellman, I. A. Abrikosov, and S. I. Simak, "Lattice dynamics of anharmonic solids from first principles," Phys. Rev. B **84**, 180301 (2011).

[19] O. Hellman, P. Steneteg, I. A. Abrikosov, and S. I. Simak, "Temperature dependent effective potential method for accurate free energy calculations of solids," Phys. Rev. B **87**, 104111 (2013).

[20] O. Hellman and I. A. Abrikosov, "Temperature-dependent effective third-order interatomic force constants from first principles," Phys. Rev. B **88**, 144301 (2013).

[21] N. Shulumba, O. Hellman, and A. J. Minnich, "Lattice Thermal Conductivity of Polyethylene Molecular Crystals from First-Principles Including Nuclear Quantum Effects," Phys. Rev. Lett. **119**, 185901 (2017).

[22] F. Bottin, J. Bieder, and J. Bouchet, "a-TDEP: Temperature Dependent Effective Potential for Abinit – Lattice dynamic properties including anharmonicity," Comput. Phys. Commun. **254**, 107301 (2020).

[23] F. Eriksson, E. Fransson, and P. Erhart, "The Hiphive Package for the Extraction of High-Order Force Constants by Machine Learning," Adv. Theory Simul. **2**, 1800184 (2019).

[24] "`eigmap`," `https://github.com/acammarat/phtools/tree/main/eigmap` (2023), last retrieved 2023-03-17.

[25] "GNU General Public License, version 3," `http://www.gnu.org/licenses/gpl.html` (2007), last retrieved 2022-09-06.

LANGMUIR

pubs.acs.org/Langmuir Article

Effects of Water Content on the Transport and Thermodynamic Properties of Phosphonium Ionic Liquids

Igor Stanković,* Miljan Dašić, Mateja Jovanović, and Ashlie Martini

Cite This: *Langmuir* 2024, 40, 9049−9058

Read Online

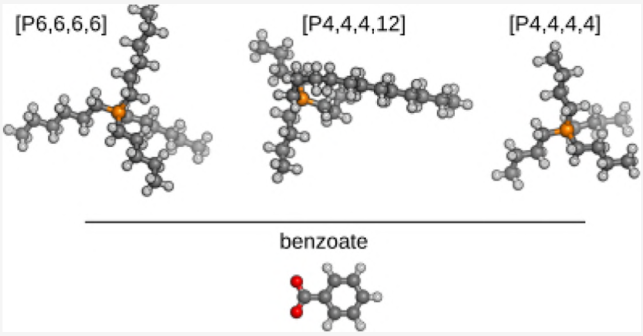

ABSTRACT: We present a numerical investigation of the influence of water content on the dynamic properties of a family of phosphonium-based room-temperature ionic liquids. The study presents a compelling correlation between structural changes in water−ionic liquid solutions and thermodynamic and transport properties across diverse systems. The results for phosphonium ionic liquids are compared with 1-butyl-3-methylimidazolium hexaphosphate ([bmim]PF_6) as a reference. Through this approach, phosphonium cation structure-related characteristics can be identified and placed within the broader context of ionic liquids. These insights are underpinned by observed changes in interaction energy, boiling point, diffusion rate, and viscosity, highlighting the crucial role of water molecules in weakening the strength of interactions between ions within the ionic liquid. The investigation also explains temperature-dependent trends in phosphonium cations, showing that alkyl group length and molecular symmetry are important tuning parameters for the strength of Coulomb interactions. These results contribute to a refined understanding of phosphonium ionic liquid behavior in the presence of water, offering valuable insights for optimizing their use in diverse fields.

■ INTRODUCTION

Ionic liquids (ILs) include a class of salts characterized by their ability to remain in a liquid state at room temperature, with a melting point below room temperature (300 K). Through the high versatility of large asymmetric and irregularly shaped organic or inorganic cations and anions, ILs possess unique physicochemical properties that make them relevant for wide-ranging modern applications. These properties include negligible vapor pressure, exceptional thermal stability, high viscosity, significant ion conductivity, a wide electrochemical window, and adjustable polarity.[1,2] Such attributes have led to the exploration of ILs in a diverse range of fields, including lubrication.[3−5] Hence, it would be advantageous if we could deduce relations between the molecular structure, transport, and lubrication properties of ILs.

ILs utilized for lubrication purposes incorporate different types of anions, both organic and inorganic, as well as various cations. Among the commonly employed cations are those based on ammonium, phosphonium,[6] imidazolium,[1] or pyridinium.[7] Notably, recent studies have highlighted the potential of phosphonium ILs for lubrication due to several advantageous characteristics.[3,8−10] Phosphonium ILs have been found to exhibit reduced wear and friction compared to commonly used oils, and even ammonium and imidazolium ILs.[8,11,12] Phosphonium ILs have also been reported to possess excellent resistance to corrosion and tribo-corrosion.[13] Their low volatility[9] enables recycling and reusability without volume loss, highlighting phosphonium ILs as leading candidates for lubricant applications. The length of the alkyl chain in cations has been found to influence the viscosity, melting point, and pressure-viscosity coefficients of ILs.[3,10] The influence of cationic alkyl chain length on the tribological properties of ILs in lubrication has been investigated.[1,6,12,14−16] Interestingly, Minami[12] observed a decrease in the coefficient of friction (COF) from 0.25 to 0.15 with increasing alkyl chain length (nC = 2 to 12), while Dold et al.[1] observed an increase in COF from 0.025 to 0.1. Studies have also considered ILs with the same cations but different anions. ILs change wetting behavior depending on the anion size,[6,14−16] from the absence of wetting to partial or complete wetting.

Water is commonly employed during the synthesis of ILs, and many ILs have a strong affinity for water. Consequently, the residual water in ILs significantly influences various properties such as density, viscosity, polarity, conductivity,

Received: January 29, 2024
Revised: March 28, 2024
Accepted: April 1, 2024
Published: April 19, 2024

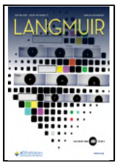

https://doi.org/10.1021/acs.langmuir.4c00372
Langmuir 2024, 40, 9049−9058

and solubility.[17,18] The solubility of ILs in water is particularly important for reducing emulsification in water-based lubricants. Both theoretical and experimental studies comparing different ILs based on the symmetric phosphonium [P4,4,4,4] cation revealed that solubility depends on the choice of anion.[19,20] Molecular dynamics (MD) simulations investigating the mixing behavior between phosphonium ILs with chloride and acetate anions and water showed that, while the anions were well solvated due to their small size, only the smallest cation [P2,2,2,2] was fully miscible with water, forming a homogeneous binary solution.[21] The analysis emphasized electrostatic nature of cation−anion and anion−water interactions, with van der Waals interactions playing a dominant role in cation−water interactions.[20]

Understanding the properties of water−ionic liquid systems is challenging due to different mechanisms and structural units that can contribute to the interaction, such as ion solvation, ion association, and numerous dynamic properties in the system. Molecular dynamics is a powerful technique to examine electrolyte properties because a direct correlation between the atomistic level information and macroscopic properties can be obtained.[6] Molecular dynamics simulations were carried out on four ILs based on the combinations of four different cations ([P6,6,6,6], [P4,4,4,12], [P4,4,4,4], and 1-butyl-3-methylimidazolium [bmim]) with two anions benzoate [benz] and hexafluorophosphate PF_6.[6,9,22] Both anions and [bmim] cations have similar molar masses. They are also roughly 50% lighter than the [P4,4,4,4] cation. Previous research has focused on the physical properties of imidazolium hydrophilic ionic liquid (IL) and water mixtures.[23−25] The cation side chain modification in imidazolium-based ILs was reported to significantly influence its aggregation in the presence of water.[26,27] Also, water-induced cluster formation could disrupt ion interactions[28] and, for mixtures with 70 mol % or more of water, the imidazolium-based IL systems behave as aqueous solutions.[28,29] Therefore, comparing anions and cations with systematically varied shapes and sizes is useful for studies aimed at understanding the effect of molecular shape and mobility on tribological and mixing properties of ILs in the presence of water.

Here, we present a comprehensive computational study of the influence of water concentration on the structure of IL as well as on the evolution of water−IL interactions. In particular, we perform molecular dynamics simulations for dilute water/IL systems for different anion types and phosphonium-based cations with a range of alkyl-chain lengths. The role of the symmetry and size of the phosphonium cation is examined. The results for three phosphonium-based ionic liquids are also compared with an imidazolium ionic liquid with a comparable molecular weight. The set of considered ionic liquid cation−anion pairs is depicted in Figure 1.

■ MATERIALS AND METHODS

Since the cation alkyl chain length affects the water affinity of ILs, the simulations include three different phosphonium cations, [P6,6,6,6], [P4,4,4,12], and [P4,4,4,4], in combination with benzoate [Benz] anion. The results for the phosphonium family are compared with the behavior of 1-butyl-3-methylimidazolium hexafluorophosphate ([bmim]PF_6) ionic liquid. Each simulation consisted of one ionic liquid homogeneously mixed with water. The initial configurations were obtained by random placement of ions $N_c = N_A = 80$ for [bmim]PF_6, 160 for [P6,6,6,6][benz] and [P4,4,4,12][benz], and 205 for [P4,4,4,4][benz] ILs into a cubic simulation box. The number of water molecules was adjusted accordingly to obtain the following mass volume fractions: $N_{H_2O} = 2590$ corresponding to the concentration of $45\%_{w,IL}$, $N_{H_2O} = 1520$ $60\%_{w,IL}$, and $N_{H_2O} = 304$ for $87\%_{w,IL}$.

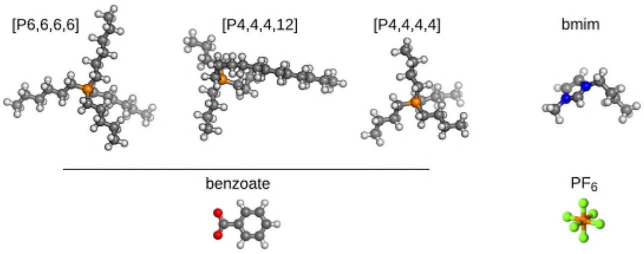

Figure 1. Snapshots of the molecular models of the three phosphonium ([P6,6,6,6], [P4,4,4,12], and [P4,4,4,4]) and 1-butyl-3-methylimidazolium [bmim] cations, as well as benzoate [benz] and PF_6 anions used in the simulations of ILs. Sphere colors correspond to atom type: white, H; gray, C; orange, P; red, O; green F; blue N. The images are generated with LigParGen.[30,31]

The interatomic interactions within ILs were characterized using the OPLS-AA force field derived from LigParGen.[30,31] The intramolecular forces inside the water were calculated with the SPC/*E* potential.[32,33] The interactions between ILs and water were calculated using the common Lorentz−Berthelot mixing rules.[34,35] In principle, the electronic polarizability of water and ionic liquid molecules should be considered to have an accurate depiction of their interactions and dynamics. However, previous simulations utilizing nonpolarizable water and IL models[6,36,37] have effectively captured crucial characteristics of the water−IL mixture, hence justifying the adequacy of the force fields adopted in this study. The value of the surface tension, as well as viscosity[38] and self-diffusion,[39] for the SPC/E models is found to be in reasonably good agreement with experiment.[32]

MD simulations were conducted using the open-source LAMMPS package[40] with a time step of 1 fs, and a typical length of simulation before property data were collected was 0.5 ns, which was sufficient for the energy to reach a steady state. To maintain the desired temperature, a Nosé−Hoover thermostat was utilized, while the velocity-Verlet algorithm was applied to solve the equations of motion.[41,42] The constant pressure (1 bar) simulations were performed with a barostat coupled to the overall box volume. The external pressure was specified as a scalar (isobaric ensemble). The damping parameters for the thermostat and barostat were 10 fs and 1 ps, respectively.

■ RESULTS

Impact of Water on the Ionic Liquid Structure.

Figure 2 illustrates the time-averaged interaction energies (u) between water and ions in four different ILs after a steady state was reached. These energies represent the combined effects of Coulombic and van der Waals forces between water and the surrounding ions. The corresponding potential energy values were derived from MD simulations of the ILs, as explained in the Materials and Methods section. We compare simulation results in equilibrium for water/IL systems for a concentrated $99.5\%_w$ and diluted $60\%_{w,IL}$ with water. The differences between the interaction energies of anions and cations with water are also outlined in Figure 3. These results reveal that the interaction energies between water and anions are 2−4 times higher than those between water and cations. This finding is consistent with previous molecular dynamics observations for imidazolium ILs.[27]

In the case of phosphonium ILs, the strength of the water−cation interaction decreased with the molecular weight of the cation from 7 kcal/mol for [P4,4,4,4][benz] to 2.8 kcal/mol for [P6,6,6,6][benz], considering a highly concentrated $99.5\%_w$

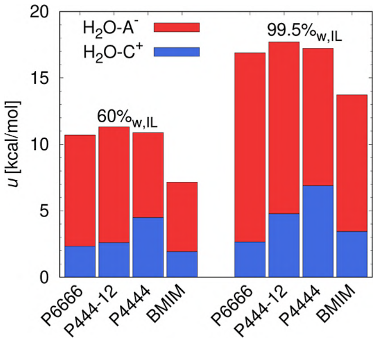

Figure 2. Interaction energies of water with cations, $u_{H_2O-C^+}$, and anions, $u_{H_2O-A^-}$, in four different simulated ILs. The results are shown for phosphonium benzoate [P6,6,6,6][benz], [P4,4,4,12][benz], [P4,4,4,4][benz], and 1-butyl-3-methylimidazolium hexafluorophosphate [bmim]PF_6 ionic liquids. The results are compared for IL weight fractions of 60%$_w$ and 99.5%$_w$.

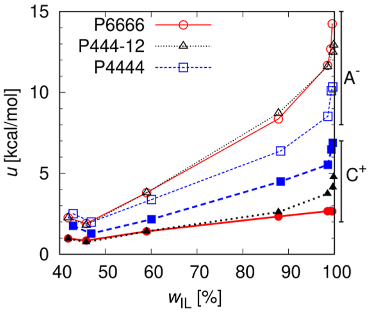

Figure 3. Comparison of the interaction energy of water with ions, $u_{H_2O-A^-}$ and $u_{H_2O-C^+}$, in three different ILs, with the ionic liquid weight fraction w_{IL} (A^- indicates anion and C^+ indicates cation). Generally, the interaction energy increases with the lower amount of absorbed water. The results are shown for the phosphonium benzoate [P6,6,6,6][benz], [P4,4,4,12][benz], and [P4,4,4,4][benz] ionic liquids.

ionic liquid. Conversely, the water and the benzoate ([benz]) anion followed an inverse trend, with their interaction energy increasing from 7 kcal/mol for [P4,4,4,4][benz] to 14 kcal/mol for [P6,6,6,6][benz], also in the 99.5%$_w$ system.

Both water−cation and water−anion interaction energy decreased in all cases with an increase of water content, e.g., a decrease in ionic liquid weight fraction w_{IL}, as shown in Figure 3. However, even at an ionic liquid weight fraction of 60%$_{w,IL}$, the interaction between water and the [P4,4,4,4] cation remained the strongest at 4.5 kcal/mol, while it was the weakest for the [P6,6,6,6] cation at 2.3 kcal/mol, cf. Figure 2. This relationship indicates that the energy of the water−cation interaction decreased with an increase in the alkyl chain length of the cation, which has been confirmed by measurements[43,44] and other modeling studies.[27] Consequently, due to the opposing trends in water interaction energies with the components of ionic liquids, all three phosphonium ionic liquids exhibited similar interaction energies with water across all investigated systems, approximately 17 kcal/mol for 99.5%$_{w,IL}$ and 11 kcal/mol for 60%$_{w,IL}$, as shown in Figure 2.

Our findings for the phosphonium ionic liquids suggest that, although the interaction energy between cations and water depends on the cation's molecular weight or molecular volume, the stronger interaction between anions and water compensates for this difference. This observation holds for a wide range of ionic liquid concentrations. The interaction energy between water and the ionic liquid is directly related (i.e., positively correlated) to ionic liquid weight fraction, decreasing to 30% of the calculated concentrated phosphonium ionic liquid values at 40%$_w$ ionic liquid content. In the case of the [bmim]PF_6 ionic liquid, the water−anion interaction energy was 10 kcal/mol, while the water−cation interaction energy was 3.5 kcal/mol for 99.5%$_{w,IL}$, making it roughly 20% weaker than the investigated phosphonium ionic liquids. This was expected since [bmim]PF_6 is immiscible with water.

A radial distribution function (RDF) analysis is conducted for phosphonium ILs using the central phosphorus (P^+) atom of the cation and the oxygen atoms of a benzoate carboxyl group and water, labeled as O^- and O_{H_2O}, respectively. This

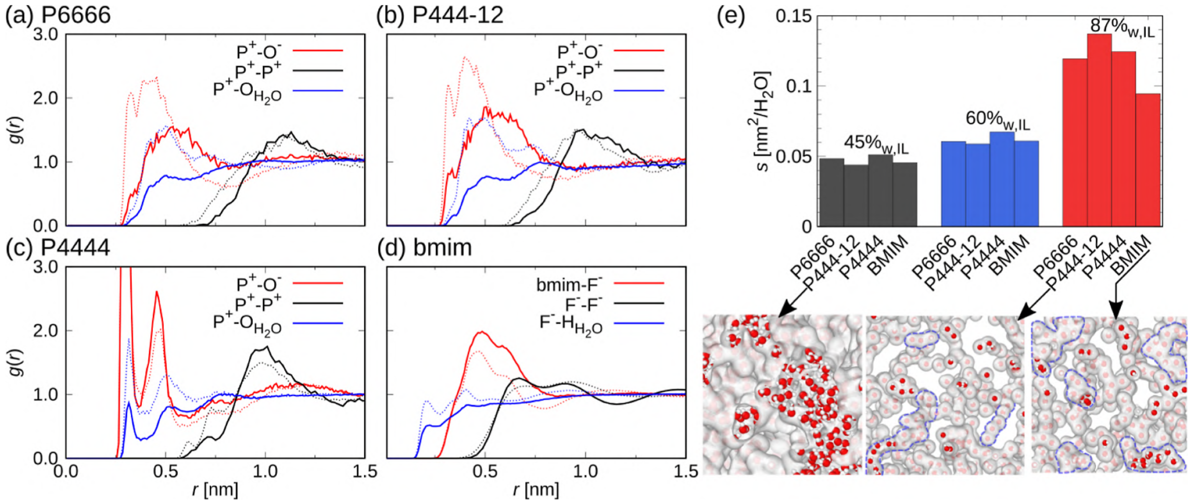

Figure 4. Radial distribution functions indicate interionic distances and ion−ion or ion−water coordination. RDFs show data for phosphonium (a) [P6,6,6,6][benz], (b) [P4,4,4,12][benz], (c) [P4,4,4,4][benz], and (d) [bmim]PF_6 ionic liquids for 87%$_{w,IL}$ and 60%$_{w,IL}$, indicated by the solid and dashed lines, respectively. (e) The specific surface of the water−ionic liquid interface is calculated as the total surface of all water pockets normalized with the number of water molecules in the system. Three lower panels show snapshots of the water clusters for [P4,4,4,12][benz] at 45%$_{w,IL}$ and 87%$_{w,IL}$ and [bmim]PF_6 at 87%$_{w,IL}$, from left to right, respectively.

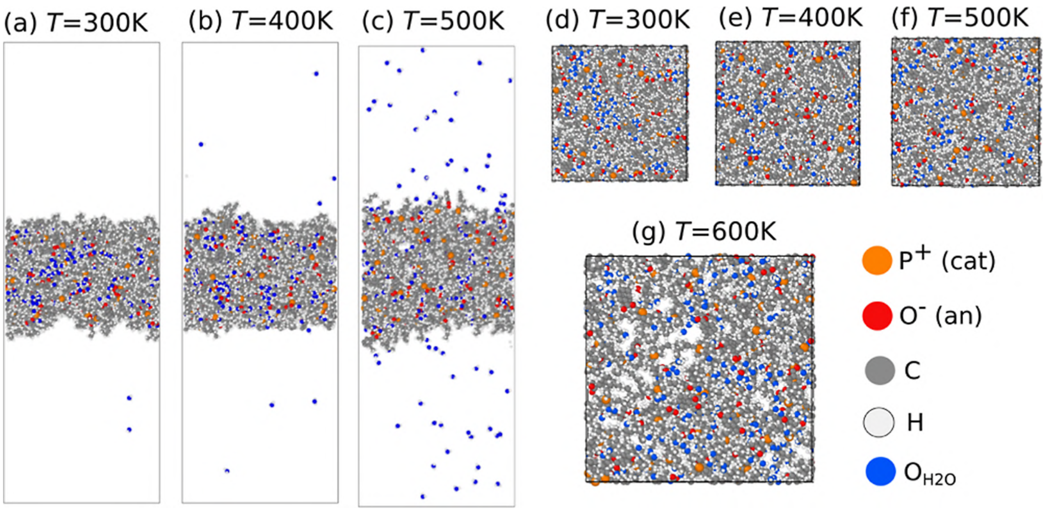

Figure 5. Snapshots of the phosphonium benzoate [P6,6,6,6][benz] 87$\%_{w,IL}$ system. Evolution with the temperature of a film consisting of ionic liquid and water at the center of the simulation box, with a 5 nm vacuum added to form an interface. The snapshots of the film are shown at temperatures (a) 300, (b) 400, and (c) 500 K. The critical water behavior in bulk is shown at temperatures (d) 300, (e) 400, (f) 500, and (g) 600 K. The simulations had periodic boundary conditions in all three Cartesian coordinate directions. The temperature increased while keeping the pressure constant at 1 bar. A cation's phosphorus atom is represented as orange, an anion's oxygen is red, water's oxygen is blue, carbon atoms are gray, and hydrogens are white.

analysis provides insights into the liquid structure of ILs by examining the distribution of ions and water molecules in their environment. Figure 4a–c displays the RDFs of phosphonium cation–anion (P^+–O^-), cation–cation (P^+–P^+), and cation–water (P^+–O_{H_2O}) interactions for 87$\%_{w,IL}$ and 60$\%_{w,IL}$, indicated by the solid and dashed lines, respectively. As shown in Figure 4, a solvation shell is evident in the cation–anion interaction, with a prominent peak observed at 0.5 nm in the P^+–O^- RDF. Furthermore, it can be observed from Figure 4 that the P^+–O^- interaction is inherently stronger than the P^+–P^+ interaction. The results suggest that an increase in the water fraction leads to significant differences in the local order of anions and cations.

One notable effect of introducing more water into the system is that the peak of the P^+–O^- RDF becomes more pronounced and shifts closer to the contact distance of the van der Waals volumes, as seen in Figure 4a–c. Specifically, the pronounced peaks of the P^+–O^- RDF for [P4,4,4,4][benz] in Figure 4c originate from the oxygens of the carboxyl group (refer to Figure 1). Compared to [P6,6,6,6] molecules, the shorter chains of [P4,4,4,4] are less likely to interfere with the benzene ring to which the carboxyl group is attached in benzoate.

The radial density of water molecules near the P^+ core of the phosphonium cation increases with higher water concentration and for shorter alkyl chain lengths, cf. Figure 4a,c. This indicates that water acts as a good solvent for phosphonium alkyl chains. In this scenario, interactions between the alkyl segments and solvent molecules are energetically favorable, and additional water causes the alkyl chains to expand into a linear configuration. As the alkyl chains expand, the anions and water molecules can approach the polar core of the phosphonium cation. The RDFs of P^+–P^+ for cation–cation interactions exhibit the first peak at 1 nm, twice the length of the P^+–O^- distance. The position and height of the P^+–P^+ RDFs remain unchanged with varying amounts of water in the system, indicating that the phosphonium benzoate ionic liquid possesses a fairly stable network structure of ions spanning the system.

Figure 4d shows RDFs for [bmim]PF_6, also for two ionic liquid concentrations 87$\%_{w,IL}$ and 60$\%_{w,IL}$, indicated by the solid and dashed lines, respectively. The cation–anion (bmim–F^-) peak was observed at 0.48 nm, comparable to peaks in [P6,6,6,6][benz] and [P4,4,4,12][benz] ionic liquids. Interestingly, opposite to the trend observed for phosphonium, [bmim]PF_6 RDFs do not show any significant changes with water concentration in Figure 4d. The radial density at the cation–anion peak decreases only slightly with increasing water concentration. For the anion–water–water interaction, RDFs show a steady increase from 0.23 nm at 87$\%_{w,IL}$, which evolves into a peak at 60$\%_{w,IL}$. This peak is followed by a second water shell at 0.46 nm for 60$\%_{w,IL}$ (reminiscent of [P4,4,4,4][benz] RDFs).

Analyzing the [bmim]PF_6 RDF for anion–anion (F^-–F^-) interactions shows the first broadest peak at 0.53 nm, whereas the second is at 0.89 nm, approaching much closer than anions in phosphonium ionic liquids. The weak influence of water on the structure of [bmim]PF_6, visible in Figure 4d F^-–O_{H_2O}, is expected since interaction energy between water and the [bmim]PF_6 system is weaker compared to phosphonium ionic liquids. For example, the interaction energy in the case of [bmim]PF_6 reaches 30% of the calculated phosphonium ionic liquids values at 60$\%_{w,IL}$, cf. Figure 2.

In the following, we investigate the self-organization of a water–ionic liquid system at a larger scale. Already at 87$\%_{w,IL}$, there are enough water molecules to create a connected network of water pockets throughout the system. This network of clusters adds a higher (microscopic) level to the water structure inside the ionic liquid. We employ the specific surface of the water–ionic liquid interface as a quantitative property of the water molecule pockets within the IL.

The specific surface is the total surface enveloping water clusters normalized by the number of water molecules in the system. To generate the surface enveloping water molecule clusters, we used a method that utilizes the superposition of 3D

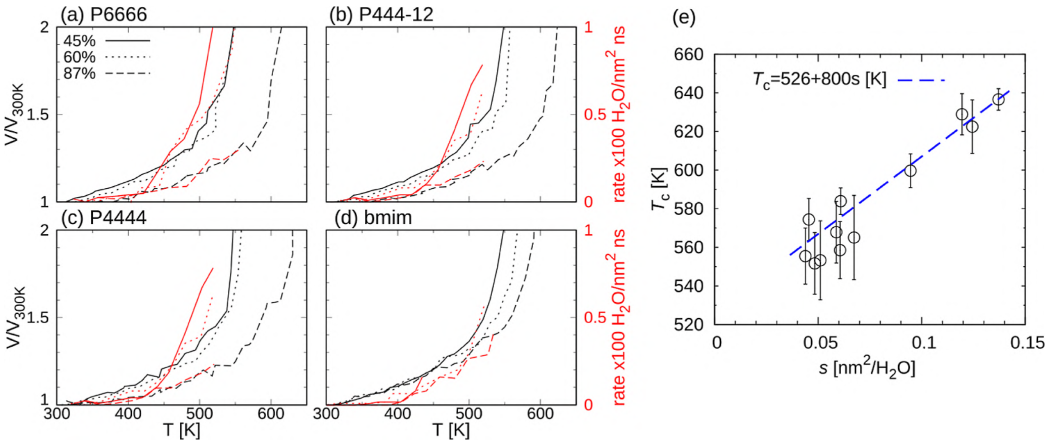

Figure 6. Evolution of volume (black) and rate of evaporation (red) with increasing temperature for ionic liquid $45\%_{\mathrm{w,IL}}$, $60\%_{\mathrm{w,IL}}$, and $87\%_{\mathrm{w,IL}}$ content, indicated by the solid, dotted, and dashed lines, respectively. The panels show data for phosphonium benzoate (a) [P6,6,6,6][benz], (b) [P4,4,4,12][benz], (c) [P4,4,4,4][benz], and (d) [bmim]PF_6 ionic liquids. (e) Dependence of critical temperature T_c associated with volume expansion in panels (a–d), i.e., $V \propto e^{-T_c/T}$ on the specific surface s of the water–ionic liquid interface. The curve is obtained by a linear fit of the points.

Gaussian functions at each particle site.[45] The algorithm generates a density map by aggregating Gaussian densities on a 3D lattice within a bounding box, guaranteeing the inclusion of all particles. Two pivotal parameters shaping the isosurface morphology are the radius scaling, which adjusts the Gaussian function width based on the visible particle radius multiplied by a scaling factor (in this case, set to 1.25), and the Gaussian isosurface value, a threshold determining the distance of the contour surface from particle centers (here, set to 0.1). The chosen parameter values lead to a reduced threshold and broader particle-assigned volumes, effectively preventing the gaps within water clusters which could unphysically increase the surface.

Figure 4e shows the evolution of the normalized specific surface (s) of the water–ionic liquid interface with water concentration. The higher content of water results in a smaller contact surface to the ionic liquid, as water molecules cluster together. Conversely, the specific surface of the contact increases as the water quantity decreases.

Snapshots showing only water molecules visualize the evolution of the water network shape with ionic liquid content in Figure 4e. The increase of specific surface in case of a higher ionic liquid content is more than two times, cf. Figure 4e for $87\%_{\mathrm{w,IL}}$. Inspection of configurations for [P4,4,4,12][benz] and [bmim]PF_6 indicates that water clusters are becoming linear, i.e., water orders into a network of elongated pockets and stays interconnected into a network. Additionally, at low water content (i.e., $87\%_{\mathrm{w,IL}}$), there is a difference of 30% in the specific surface between phosphonium ionic liquids and the [bmim]PF_6 system. This difference can be traced to the existence of the larger water clusters in [bmim]PF_6 as opposed to phosphonium ionic liquids, denoted on snapshots in Figure 4e with dashed lines. This observation is fully in line with a weak influence of water content on the RDFs of [bmim]PF_6 and in turn its weaker interaction energy compared to the investigated phosphonium ionic liquids.

Boiling Point of Water–Ionic Liquid Systems. In this section, we examine the simulation results of water evaporation and analyze the boiling point of the water–IL system. Snapshots of the two simulation setups are shown in Figure 5.

The first set of simulations comprises a film consisting of ionic liquid and water at the center of the simulation box, with a 5 nm vacuum added to form a liquid–vapor interface. The snapshots of such an interface with [P6,6,6,6] [benz] $87\%_{\mathrm{w,IL}}$ are shown in Figure 5a–c. MD simulations of four liquid–vapor interfaces for different ionic liquid–water solutions were carried out, and the temperature was increased in 20 K steps every 0.2 ns in the range 300–560 K. The well-defined liquid–vapor interface was observed for all ionic liquid–water systems at temperatures below 450 K. In simulations, the water molecules in the solution detached from the surface and evaporated into the vacuum, as well as, reabsorbed back into the interface, see Figure 5a–c. At 400 K, with a kinetic energy of 0.8 kcal/mol for water molecules, the surface released adsorbed water due to the molecules having sufficient kinetic energy to leave the droplet. We follow the evolution of the evaporation rate, i.e., the number of water molecules released into vacuum through the unit of surface area (28 nm^2) in a given time frame (0.2 ns).

The evaporation rate is modeled by the Arrhenius equation $k \propto e^{E_A/k_BT}$. The Arrhenius equation postulates a threshold energy governing individual collisions between molecules. These collisions result in the molecule acquiring sufficient kinetic energy to overcome adhesion to the surface and undergo evaporation. Here, based on the simulated evaporation rate, cf. Figure 6, we estimated the activation energy (E_A) for the evaporation process to be between 5 and 10 kcal/mol, which is comparable to the intermolecular binding energy. The simulated intermolecular binding energy of water and cations is approximately 2 kcal/mol, while for anions, it is around 8 kcal/mol (cf. Figure 2). Notably, the water evaporation rates increased above 400 K, ranging to quite substantial 10–50 molecules/nm^2ns (see Figure 6). Similar observations were made by Chaban and Prezhdo[46] for 1-butyl-3-methylimidazolium tetrafluoroborate [C_4C_1IM][BF4]-water solution, who saw a temperature increase of up to 25 K in water boiling point from vapor–liquid equilibrium. Our findings show a rapid increase in the evaporation rate at temperatures above 400 K. Furthermore, the rate of evaporation in phosphonium ionic liquids depends on the quantity of water in the system, while the film's interior

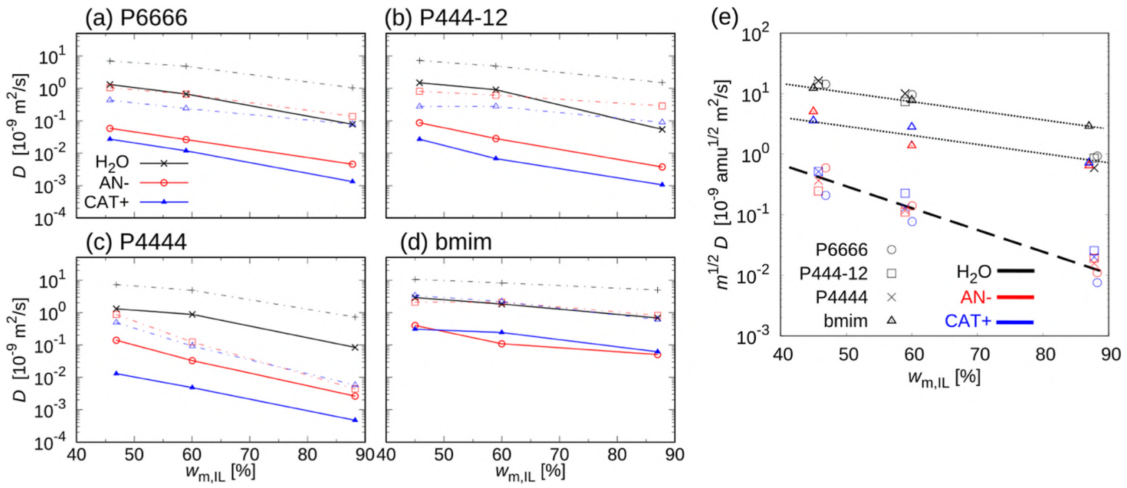

Figure 7. Dependence of the coefficient of diffusion of anions, cations, and water (H_2O) on ionic liquid content $w_{\mathrm{m,IL}}$. The full lines are simulated at 300 K and dotted lines at 400 K. The panels show data for phosphonium (a) [P6,6,6,6], (b) [P4,4,4,12], (c) [P4,4,4,4], and (d) [bmim]PF_6 ionic liquids. (e) Evolution of the diffusion coefficient scaled with the square root of the mass of the molecule ($D \propto 1/\sqrt{m}$) for different concentrations.

remains fairly stable due to the water molecule's binding energy being 10 times higher than the kinetic energy of water molecules. One should note that Gibbs ensemble Monte Carlo simulations are necessary to fully characterize the vapor−liquid equilibria of IL−H_2O systems and mitigate the size effects.[47,48] These simulations rely on vapor−liquid phase exchange to equilibrate the chemical potential.

To investigate critical water behavior in bulk, we conduct simulations shown in the right side panels of Figure 5d−g. The simulations have periodic boundary conditions in all three Cartesian coordinate directions.

Figure 6a−d shows the evolution of the volume ($V/V_{300\mathrm{K}}$) of the bulk systems with temperature. As the temperature increases in 20 K steps every 0.2 ns while keeping the pressure constant at 1 bar, the overall volume gradually expands 10−20% depending on the water/IL fraction up to temperature 500 K, keeping absorbed superheated water. The coefficient of expansion, representing the fractional change in volume per unit change in temperature, decreases from 1.4×10^{-3} K^{-1} to 0.7×10^{-3} K^{-1} for $60\%_{\mathrm{w,IL}}$ and $87\%_{\mathrm{w,IL}}$, respectively.

At the boiling point of the water−IL system, the liquid structure is disrupted, leading to the formation of water bubbles in the gas phase within the ionic liquid. Even in a pure water system, the surface tension of water plays a crucial role in preventing the formation and growth of bubbles until the temperature exceeds the boiling point.[49] It is therefore not surprising that the high boiling points and surface tension of ionic liquid will increase the boiling point of the mixed system compared to pure water (i.e., 273 K).

The boiling point of bulk ionic liquids is influenced by the amount of ionic liquid, which prevents rapid water expansion. Consequently, for all three phosphonium systems at low water content, i.e., $87\%_{\mathrm{w,IL}}$, the onset of the volume expansion is delayed by about 60 K compared to the other two concentrations ($45\%_{\mathrm{w,IL}}$ and $60\%_{\mathrm{w,IL}}$), cf. Figure 6a-c. Surprisingly, the [bmim]PF_6 system exhibits only a 20 K increase of boiling point when increasing the concentration of ionic liquid from $60\%_{\mathrm{w,IL}}$ to $87\%_{\mathrm{w,IL}}$, cf. Figure 6d. We observe a similar trend in water evaporation rates for [bmim]PF_6.

A possible relationship between the molecular structure of the water−ionic liquid system (analyzed in the previous section) and the critical temperature associated with an exponential volume expansion, i.e., $V \propto e^{-T_c/T}$, due to water bubble creation is outlined in Figure 6e. In particular, the specific surface of the water−ionic liquid interface could be instrumental in this, cf. Figure 4e. One can observe that a higher specific contact area of water to ionic liquid s leads to more pronounced retardation of vapor pocket formation, i.e., higher T_c. In all investigated systems, water is mixed with ionic liquid. Still, the geometry of the water pockets evolves with concentration and depends also on the molecular structure of the ionic liquid, as demonstrated in Figure 6d. To some extent, we can rely on macroscopic considerations: for the vapor pocket to expand and form a bubble, the temperature must be sufficient to generate enough vapor pressure to overcome the surface tension. This excess pressure is inversely proportional to the diameter of the bubble formed. The existence of larger water clusters, which can overcome intramolecular forces created by the strong Coulomb cohesion forces in the ionic liquid, reduces critical temperature.

One of the appealing attributes of ILs for various applications is their remarkably low volatility, e.g., high boiling point. This is important since it is sometimes erroneously claimed that ILs are nonvolatile. Rebelo et al.[50] demonstrated that ILs could undergo thermal vaporization, allowing for the estimation of boiling points and critical temperatures. Later, indirect and direct methods were employed to measure vapor pressure.[51,52] Simulations indicate that imidazolium ionic liquids have critical temperatures around 1200 K, with a decrease in critical temperature as the alkyl chain length on the cation increases, but still far above the temperatures studied here.[47,48]

In practical systems, we may encounter scenarios where water molecules are removed from the vicinity of the ionic−liquid surface. The resulting interface would experience a local rapid depletion and evaporation would be limited by the rate at which water diffuses through and between water pockets (seen in Figure 4) to the surface, an aspect we will explore in the following section.

Simulations of Diffusion in the Water−Ionic Liquid System. The diffusivity of cations, anions, and water, D_s, was investigated using the Einstein relation for molecular move-

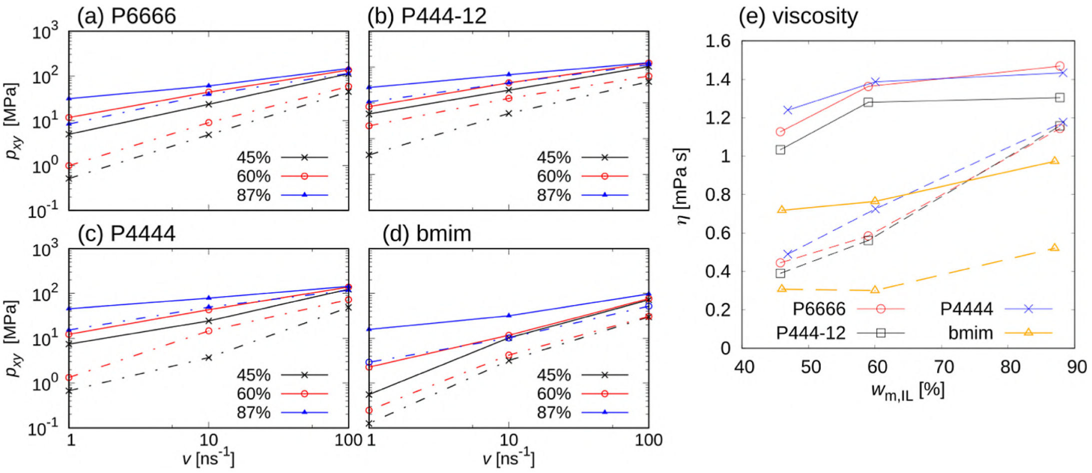

Figure 8. Dependence of shear stress p_{xy} on shear rate v for different ionic liquid contents $w_{m,IL}$. The water is denoted black, anion red, and cation blue. The panels show data for phosphonium (a) [P6,6,6,6], (b) [P4,4,4,12], (c) [P4,4,4,4], and (d) [bmim]PF_6 ionic liquids. The lines serve as a guide to the eye. (e) Dependence of viscosity $\eta = p_{xy}/v$ across all systems at $v = 100$ ns^{-1} on ionic liquid weight fraction $w_{m,IL}$. The solid lines in all panels are simulated at 300 K and dashed—dotted lines at 400 K.

ment in liquid, $6D_s t = \sum_{i=1}^{N} \langle (\vec{r}_i - \vec{r}_i^{\,0})^2 \rangle$, linking diffusion coefficient to the evolution with time of the mean-square of the displacement (msd) of the center of mass position $\vec{r}_i$ for each molecule (ion or water) i. The msd over time is represented by the brackets $\langle\rangle$, N denotes the number of ions, and the factor 6 accommodates the three-dimensional nature of the system. The ionic liquid simulations at 300 K are found to be mostly subdiffusive based on the observation that a linear fit to the msd as a function of time on a log—log scale has a slope <1. To compare the diffusivity of different systems, we focus on the portion of the msd curve after 1.5 ns where all systems exhibit a linear dependence of the msd on time, cf. refs 53 and 54. Using the method of least-squares on msd values, we calculate the diffusion coefficient for all systems and their different components (i.e., cations, anions, and water molecules).

From Figure 7, it can be observed that, as the mass fraction of ionic liquid increases, the diffusion coefficient D of all IL—water system components decreases. The absolute values of the ion diffusion constants, approximately 10^{-11} m^2/s, are an order of magnitude smaller than those of water at ambient temperatures and this difference increases with concentration, cf. refs 55 and 56. A most significant difference in water transport between the three phosphonium ionic liquids and [bmim]PF_6 is visible at a high ionic liquid volume fraction (87%$_{w,IL}$). The diffusion coefficient values for water decrease by an order of magnitude with increasing concentration of phosphonium ionic liquids, from 2×10^{-8} m^2/s at a fraction of 45%$_{w,IL}$ to below 10^{-9} m^2/s at a fraction of 87%$_{w,IL}$. On the other hand, the water diffusion coefficient in [bmim]PF_6 decreases to a third of its value at 45%$_{w,IL}$, i.e., from 3×10^{-8} m^2/s to 1×10^{-8} m^2/s in the range 45%$_{w,IL}$ to 87%$_{w,IL}$, respectively. This is due to a weaker interaction energy between the ionic liquid and water, as outlined in Figure 2 and the corresponding section.

At 400 K, we observe that, for all investigated ionic liquids, the diffusion coefficient decreases with increasing ionic liquid concentration $w_{w,IL}$ to a third of its value at 45%$_{w,IL}$. The self-diffusion coefficients at 400 K are an order of magnitude higher than at 300 K. Such an increase in mobility cannot be explained solely by an increase in thermal velocity ($v_{\text{therm}} \propto \sqrt{T}$) but also indicates a change in dynamics of water association with ionic liquid and other water molecules due to temperature.

One can observe that the slope of the diffusion rate D with IL content $w_{w,IL}$ at 300 K is similar for all phosphonium anions and cations independent of their cationic alkyl chain lengths. On the other hand, cation's structure changes the evolution of diffusion rate with the concentration of ionic liquid at 400 K. The two phosphonium liquids with higher alkyl group content [P6,6,6,6] and [P4,4,4,12] exhibit higher diffusional mobility compared to [P4,4,4,4], cf. Figure 7a—c, especially at high ionic liquid concentrations. This indicates that alkyl group content is a tuning parameter for strong Coulomb interactions between the central phosphorus atom in the cation and oxygen of the anion molecule. Figure 7e shows the scaling of the diffusion coefficient with the square root of the mass of the molecule ($D \propto 1/\sqrt{m}$). The water behaves similarly in all four systems and the three phosphonium benzoate pairs also follow a similar trend. In contrast, [bmim]PF_6 is more mobile than the phosphonium ionic liquids, with the diffusion being an order of magnitude larger when corrected for its mass.

Water—IL System under Shear. We calculated the shear stress evolution with shear rate through nonequilibrium molecular dynamics simulations in a box with periodic boundary conditions. In bulk simulations, the entire simulation box undergoes shear, causing changes in its shape. The simulation box's deformation and the subtraction of a velocity bias due to deformation, i.e., the shear-induced velocity of flow, are accomplished with the SLLOD thermostat.[57,58]

The results reveal that shear stress decreases with rising temperature across all systems, as shown in Figure 8a—d. The change in shear stress with temperature is particularly pronounced in the case of the [bmim]PF_6 ionic liquid and low ionic liquid content (45%$_{w,IL}$). Weak interaction of water with [bmim]PF_6 results in almost 50% lower shear stress than that of the phosphonium ionic liquids. Further, viscosity is lower for the asymmetric phosphonium cation molecule [P4,4,4,12] compared to the symmetric one [P6,6,6,6]. Higher symmetry facilitates close packing, promoting increased ionic interaction, compared to interactions with water, as observed in the energies in Figure 2 and contact surface in Figure 4e, cf. also ref 59.

The viscosity $\eta = p_{xy}/v$ is calculated across all systems at the highest shear rate $v = 100\ \text{ns}^{-1}$ and depicted in Figure 8e. The results demonstrate that an increase in water content leads to a decrease in viscosity across all systems. This observation suggests two considerations: first, since water is less viscous than ionic liquids, the addition of water is expected to lower the overall viscosity. Second, in alignment with the results for interaction energy, diffusion rate, and boiling point, the presence of water molecules decreases the strength of interactions between ions. These weaker interactions result in higher mobility of cations and anions and yield less viscous solutions at higher water content.

Closer inspection of Figure 8a−d indicates the presence of shear thinning in all ionic liquids at 300 K, described by a power law function with an exponent smaller than one, $p_{xy} \propto v^n$ and $n < 1$. For our systems, the exponent at $87\%_{\text{w,IL}}$ and 300 K is $n = 0.25$ for [P4444], $n = 0.35$ for [P444−12] and [P6666], and $n = 0.4$ for [bmim]. The addition of water reduces the effect of shear thinning, increasing the exponents. The most striking change occurs for [bmim]PF_6, which, according to our simulations, recovers its viscous behavior at elevated water amounts ($45\%_{\text{w,IL}}$, cf. Figure 8d). At 400 K and for ionic liquid content $w_{\text{IL}} \leq 60\%_{\text{w,IL}}$, the symmetric cation phosphonium [P4,4,4,4][benz] and [P6,6,6,6][benz] ionic liquids as well as imidazolium [bmim]PF_6 ionic liquid recover viscous shear stress dependence on the shear rate ($n = 1$).

When considering how water alters the lubricating properties of the ionic liquid, it is crucial to acknowledge the significant role played by the interaction of water with solid interfaces (see ref 36). In small quantities, water resists slip and increases friction; however, intriguingly, this tendency slightly reverses with higher water content.[60,61] Additionally, water can accumulate on surfaces, via diffusion as it strongly adheres to charged surfaces. We find that the diffusion rate of a specific ionic liquid is independent of its molecular structure and solely dependent on the water content. Consequently, the presence of water can pose a significant practical concern, particularly in systems where controlling the friction or electrochemical reactions is important.

CONCLUSIONS

We have investigated the behavior of phosphonium ionic liquids, trying to link their molecular structure to their thermodynamic and kinetic behavior. The distinctive structural features of phosphonium ionic liquids, particularly the cationic alkyl chain length, molecular symmetry, and the consequential tuning of Coulomb interactions, have emerged as key determinants influencing their dynamic behavior. Our findings underscore the intricate relationship between water content and the rate of evaporation in phosphonium ionic liquids. In addition to the remarkable stability of bulk ionic liquid-water solutions attributed to the substantial binding energy of water molecules to the ionic liquid and high surface tension, evaporation is affected by the amount of water within the system. The interplay between molecular interactions that suppress evaporation and retard the transition from liquid to gas is highlighted. With respect to diffusion, our investigation has delineated temperature-dependent trends in three phosphonium benzoate ionic liquids. The scaling of the diffusion coefficient with the square root of molecule mass further elucidates the influence of molecular weight on the diffusion dynamics of these systems. The comparison with a reference [bmim]PF_6 ionic liquid highlights the latter's exceptional mobility, surpassing phosphonium ionic liquids by an order of magnitude when corrected for mass. Concerning the connection between molecular interactions, water content, and viscosity, the increase in water content correlates consistently with a decrease in viscosity across all systems. This phenomenon underscores the significant role of water molecules in weakening interactions between ions.

This study supports the continued development of phosphonium-based room-temperature ionic liquids that are emerging as promising environmentally friendly lubricants, distinguished by their simple synthesis process. With high viscosity, high thermal stability, and low vapor pressure, ionic liquids exhibit a versatile nature that promotes them as lubricants of choice for challenging and inaccessible operational environments. The variability of their properties, influenced by factors like cation alkyl chain length and the choice of anion, introduces customization possibilities. The potential for establishing a circular economy is underscored by their biodegradability, paving the way for recovery and reusability, not only in lubrication, but also across diverse domains, spanning from battery electrolyte development to CO_2 reduction. Continuing research focused on linking their molecular, microscale, and thermodynamic properties will potentially enable tuning of properties to meet specific application requirements.

AUTHOR INFORMATION

Corresponding Author

Igor Stanković − *Scientific Computing Laboratory, Center for the Study of Complex Systems, Institute of Physics Belgrade, University of Belgrade, Belgrade 11080, Serbia*; orcid.org/0000-0001-5756-7196; Email: igor.stankovic@ipb.ac.rs

Authors

Miljan Dašić − *Scientific Computing Laboratory, Center for the Study of Complex Systems, Institute of Physics Belgrade, University of Belgrade, Belgrade 11080, Serbia*; orcid.org/0000-0002-1739-0784

Mateja Jovanović − *Scientific Computing Laboratory, Center for the Study of Complex Systems, Institute of Physics Belgrade, University of Belgrade, Belgrade 11080, Serbia*

Ashlie Martini − *Department of Mechanical Engineering, University of California, Merced, California 95343, United States*; orcid.org/0000-0003-2017-6081

Complete contact information is available at:
https://pubs.acs.org/10.1021/acs.langmuir.4c00372

Notes

The authors declare no competing financial interest.

ACKNOWLEDGMENTS

I.S., M.D., and M.J. acknowledge the support of the Ministry of Science, Technological Development, and Innovation of the Republic of Serbia, through the Institute of Physics Belgrade. I.S. gratefully acknowledges financial support from the Fulbright Visiting Scholar Program for his visit to the University of California Merced. Numerical calculations were run on the PARADOX supercomputing facility at the Scientific Computing Laboratory of the Institute of Physics Belgrade. I.S. is grateful to Ting Liu for the fruitful discussions and advice.

■ REFERENCES

(1) Dold, C.; Amann, T.; Kailer, A. Influence of structural variations on imidazolium-based ionic liquids. *Lubric. Sci.* **2013**, *25*, 251−268.

(2) Dašić, M.; Stanković, I.; Gkagkas, K. Molecular dynamics investigation of the influence of the shape of the cation on the structure and lubrication properties of ionic liquids. *Phys. Chem. Chem. Phys.* **2019**, *21*, 4375−4386.

(3) Zhou, F.; Liang, Y.; Liu, W. Ionic liquid lubricants: designed chemistry for engineering applications. *Chem. Soc. Rev.* **2009**, *38*, 2590−2599.

(4) Hayes, R.; Warr, G. G.; Atkin, R. At the interface: solvation and designing ionic liquids. *Phys. Chem. Chem. Phys.* **2010**, *12*, 1709−1723.

(5) Gkagkas, K.; Ponnuchamy, V.; Dašić, M.; Stanković, I. Molecular dynamics investigation of a model ionic liquid lubricant for automotive applications. *Tribol. Int.* **2017**, *113*, 83−91.

(6) Liu, T.; Panwar, P.; Khajeh, A.; Rahman, M. H.; Menezes, P. L.; Martini, A. Review of Molecular Dynamics Simulations of Phosphonium Ionic Liquid Lubricants. *Tribol. Lett.* **2022**, *70*, 44.

(7) Aparicio, S.; Atilhan, M. Mixed Ionic Liquids: The Case of Pyridinium-Based Fluids. *J. Phys. Chem. B* **2012**, *116*, 2526−2537.

(8) Scarbath-Evers, L. K.; Hunt, P. A.; Kirchner, B.; MacFarlane, D. R.; Zahn, S. Molecular features contributing to the lower viscosity of phosphonium ionic liquids compared to their ammonium analogues. *Phys. Chem. Chem. Phys.* **2015**, *17*, 20205−20216.

(9) Rahman, M. H.; Khajeh, A.; Panwar, P.; Patel, M.; Martini, A.; Menezes, P. L. Recent progress on phosphonium-based room temperature ionic liquids: Synthesis, properties, tribological performances and applications. *Tribol. Int.* **2022**, *167*, 107331.

(10) Pensado, A.; Comunas, M.; Fernández, J. The pressure−viscosity coefficient of several ionic liquids. *Tribol. Lett.* **2008**, *31*, 107−118.

(11) Minami, I.; Kita, M.; Kubo, T.; Nanao, H.; Mori, S. The Tribological Properties of Ionic Liquids Composed of Trifluorotris-(pentafluoroethyl) Phosphate as a Hydrophobic Anion. *Tribol. Lett.* **2008**, *30*, 215−223.

(12) Minami, I. Ionic liquids in tribology. *Molecules* **2009**, *14*, 2286−2305.

(13) Cai, M.; Yu, Q.; Liu, W.; Zhou, F. Ionic liquid lubricants: when chemistry meets tribology. *Chem. Soc. Rev.* **2020**, *49*, 7753−7818.

(14) Bou-Malham, I.; Bureau, L. Nanoconfined ionic liquids: effect of surface charges on flow and molecular layering. *Soft Matter* **2010**, *6*, 4062−4065.

(15) Beattie, D. A.; Espinosa-Marzal, R. M.; Ho, T. T.; Popescu, M. N.; Ralston, J.; Richard, C. J.; Sellapperumage, P. M.; Krasowska, M. Molecularly-thin precursor films of imidazolium-based ionic liquids on mica. *J. Phys. Chem. C* **2013**, *117*, 23676−23684.

(16) Wang, Z.; Priest, C. Impact of nanoscale surface heterogeneity on precursor film growth and macroscopic spreading of [Rmim][NTf2] ionic liquids on mica. *Langmuir* **2013**, *29*, 11344−11353.

(17) Oster, K.; Goodrich, P.; Jacquemin, J.; Hardacre, C.; Ribeiro, A.; Elsinawi, A. A new insight into pure and water-saturated quaternary phosphonium-based carboxylate ionic liquids: Density, heat capacity, ionic conductivity, thermogravimetric analysis, thermal conductivity and viscosity. *J. Chem. Thermodyn.* **2018**, *121*, 97−111.

(18) Sheridan, Q. R.; Schneider, W. F.; Maginn, E. J. Anion Dependent Dynamics and Water Solubility Explained by Hydrogen Bonding Interactions in Mixtures of Water and Aprotic Heterocyclic Anion Ionic Liquids. *J. Phys. Chem. B* **2016**, *120*, 12679−12686.

(19) Wu, H.; Maginn, E. J. Water solubility and dynamics of CO2 capture ionic liquids having aprotic heterocyclic anions. *Fluid Phase Equilib.* **2014**, *368*, 72−79.

(20) Zhao, Y.; Tian, L.; Pei, Y.; Wang, H.; Wang, J. Effect of Anionic Structure on the LCST Phase Behavior of Phosphonium Ionic Liquids in Water. *Ind. Eng. Chem. Res.* **2018**, *57*, 12935−12941.

(21) Venkatesan, S. S.; Huda, M. M.; Rai, N. Molecular insights into ionic liquid/aqueous interface of phosphonium based phase-separable ionic liquids. *AIP Adv.* **2019**, *9*, 045115.

(22) Pivnic, K.; Bresme, F.; Kornyshev, A. A.; Urbakh, M. Structural Forces in Mixtures of Ionic Liquids with Organic Solvents. *Langmuir* **2019**, *35*, 15410−15420.

(23) McDaniel, J. G.; Verma, A. On the Miscibility and Immiscibility of Ionic Liquids and Water. *J. Phys. Chem. B* **2019**, *123*, 5343−5356.

(24) Liu, W.; Zhao, T.; Zhang, Y.; Wang, H.; Yu, M. The Physical Properties of Aqueous Solutions of the Ionic Liquid [BMIM] [BF4]. *J. Solution Chem.* **2006**, *35*, 1337−1346.

(25) Sturlaugson, A. L.; Fruchey, K. S.; Fayer, M. D. Orientational Dynamics of Room Temperature Ionic Liquid/Water Mixtures: Water-Induced Structure. *J. Phys. Chem. B* **2012**, *116*, 1777−1787.

(26) Feng, S.; Voth, G. A. Molecular Dynamics Simulations of Imidazolium-Based Ionic Liquid/Water Mixtures: Alkyl Side Chain Length and Anion Effects. *Fluid Phase Equilib.* **2010**, *294*, 148−156.

(27) Klähn, M.; Stüber, C.; Seduraman, A.; Wu, P. What Determines the Miscibility of Ionic Liquids with Water? Identification of the Underlying Factors to Enable a Straightforward Prediction. *J. Phys. Chem. B* **2010**, *114*, 2856−2868.

(28) Niazi, A. A.; Rabideau, B. D.; Ismail, A. E. Effects of water concentration on the structural and diffusion properties of imidazolium-based ionic liquid-water mixtures. *J. Phys. Chem. B* **2013**, *117*, 1378−1388.

(29) Blahušiak, M.; Schlosser, S. ˇ. Physical properties of phosphonium ionic liquid and its mixtures with dodecane and water. *J. Chem. Thermodyn.* **2014**, *72*, 54−64.

(30) Jorgensen, W. L.; Maxwell, D. S.; Tirado-Rives, J. Development and testing of the OPLS all-atom force field on conformational energetics and properties of organic liquids. *J. Am. Chem. Soc.* **1996**, *118*, 11225−11236.

(31) Dodda, L. S.; Cabeza de Vaca, I.; Tirado-Rives, J.; Jorgensen, W. L. LigParGen web server: an automatic OPLS-AA parameter generator for organic ligands. *Nucleic Acids Res.* **2017**, *45*, W331−W336.

(32) Vega, C.; de Miguel, E. Surface tension of the most popular models of water by using the test-area simulation method. *J. Chem. Phys.* **2007**, *126*, 154707.

(33) Chatterjee, S.; Debenedetti, P. G.; Stillinger, F. H.; Lynden-Bell, R. M. A computational investigation of thermodynamics, structure, dynamics and solvation behavior in modified water models. *J. Chem. Phys.* **2008**, *128*, 124511.

(34) Lorentz, H. A. Ueber die Anwendung des Satzes vom Virial in der kinetischen Theorie der Gase. *Ann. Phys.* **1881**, *248*, 127−136.

(35) Allen, M. P.; Tildesley, D. J. *Computer Simulation of Liquids*; Oxford University Press, 2017.

(36) Feng, G.; Jiang, X.; Qiao, R.; Kornyshev, A. A. Water in Ionic Liquids at Electrified Interfaces: The Anatomy of Electrosorption. *ACS Nano* **2014**, *8*, 11685−11694.

(37) Martins, V. L.; Nicolau, B. G.; Urahata, S. M.; Ribeiro, M. C. C.; Torresi, R. M. Influence of the Water Content on the Structure and Physicochemical Properties of an Ionic Liquid and Its Li+ Mixture. *J. Phys. Chem. B* **2013**, *117*, 8782−8792.

(38) Mao, Y.; Zhang, Y. Thermal conductivity, shear viscosity and specific heat of rigid water models. *Chem. Phys. Lett.* **2012**, *542*, 37−41.

(39) Mahoney, M. W.; Jorgensen, W. L. Diffusion constant of the TIP5P model of liquid water. *J. Chem. Phys.* **2001**, *114*, 363−366.

(40) Plimpton, S. Fast parallel algorithms for short-range molecular dynamics. *J. Comput. Phys.* **1995**, *117*, 1−19.

(41) Evans, D. J.; Holian, B. L. The Nose−Hoover thermostat. *J. Comput. Phys.* **1985**, *83*, 4069−4074.

(42) Spreiter, Q.; Walter, M. Classical molecular dynamics simulation with the Velocity Verlet algorithm at strong external magnetic fields. *J. Comput. Phys.* **1999**, *152*, 102−119.

(43) Huddleston, J. G.; Visser, A. E.; Reichert, W. M.; Willauer, H. D.; Broker, G. A.; Rogers, R. D. Characterization and comparison of hydrophilic and hydrophobic room temperature ionic liquids incorporating the imidazolium cation. *Green Chem.* **2001**, *3*, 156−164.

(44) Cammarata, L.; Kazarian, S. G.; Salter, P. A.; Welton, T. Molecular states of water in room temperature ionic liquids. *Phys. Chem. Chem. Phys.* **2001**, *3*, 5192−5200.

(45) Krone, M.; Stone, J.; Ertl, T.; Schulten, K. Fast Visualization of Gaussian Density Surfaces for Molecular Dynamics and Particle System Trajectories. *EuroVis-Short Papers*, 2012.

(46) Chaban, V. V.; Prezhdo, O. V. Water Phase Diagram Is Significantly Altered by Imidazolium Ionic Liquid. *J. Phys. Chem. Lett.* **2014**, *5*, 1623−1627.

(47) Rai, N.; Maginn, E. J. Vapor−Liquid Coexistence and Critical Behavior of Ionic Liquids via Molecular Simulations. *J. Phys. Chem. Lett.* **2011**, *2*, 1439−1443.

(48) Rai, N.; Maginn, E. J. Critical behaviour and vapour-liquid coexistence of 1-alkyl-3-methylimidazolium bis-(trifluoromethylsulfonyl)amide ionic liquids via Monte Carlo simulations. *Faraday Discuss.* **2012**, *154*, 53−69.

(49) Dergarabedian, P. The Rate of Growth of Vapor Bubbles in Superheated Water. *J. Appl. Mech.* **1953**, *20*, 537−545.

(50) Rebelo, L. P. N.; Canongia Lopes, J. N.; Esperança, J. M. S. S.; Filipe, E. On the Critical Temperature, Normal Boiling Point, and Vapor Pressure of Ionic Liquids. *J. Phys. Chem. B* **2005**, *109*, 6040−6043.

(51) Paulechka, Y.; Zaitsau, D. H.; Kabo, G.; Strechan, A. Vapor pressure and thermal stability of ionic liquid 1-butyl-3-methylimidazolium Bis(trifluoromethylsulfonyl)amide. *Thermochim. Acta* **2005**, *439*, 158−160.

(52) Earle, M. J.; Esperança, J. M.; Gilea, M. A.; Canongia Lopes, J. N.; Rebelo, L. P.; Magee, J. W.; Seddon, K. R.; Widegren, J. A. The distillation and volatility of ionic liquids. *Nature* **2006**, *439*, 831−834.

(53) Doherty, B.; Zhong, X.; Gathiaka, S.; Li, B.; Acevedo, O. Revisiting OPLS Force Field Parameters for Ionic Liquid Simulations. *J. Chem. Theory Comput.* **2017**, *13*, 6131−6145.

(54) Kowsari, M. H.; Alavi, S.; Ashrafizaadeh, M.; Najafi, B. Molecular dynamics simulation of imidazolium-based ionic liquids. I. Dynamics and diffusion coefficient. *J. Chem. Phys.* **2008**, *129*, 224508.

(55) Shaikh, A. R.; Ashraf, M.; AlMayef, T.; Chawla, M.; Poater, A.; Cavallo, L. Amino acid ionic liquids as potential candidates for CO2 capture: Combined density functional theory and molecular dynamics simulations. *Chem. Phys. Lett.* **2020**, *745*, 137239.

(56) Devanathan, R.; Venkatnathan, A.; Rousseau, R.; Dupuis, M.; Frigato, T.; Gu, W.; Helms, V. Atomistic Simulation of Water Percolation and Proton Hopping in Nafion Fuel Cell Membrane. *J. Phys. Chem. B* **2010**, *114*, 13681−13690.

(57) Evans, D. J.; Morriss, G. Nonlinear-response theory for steady planar Couette flow. *Phys. Rev. A: At., Mol., Opt. Phys.* **1984**, *30*, 1528−1530.

(58) Daivis, P. J.; Todd, B. A simple, direct derivation and proof of the validity of the SLLOD equations of motion for generalized homogeneous flows. *J. Chem. Phys.* **2006**, *124*, 194103.

(59) Barnhill, W. C.; Qu, J.; Luo, H.; Meyer, H. M. I.; Ma, C.; Chi, M.; Papke, B. L. Phosphonium-Organophosphate Ionic Liquids as Lubricant Additives: Effects of Cation Structure on Physicochemical and Tribological Characteristics. *ACS Appl. Mater. Interfaces* **2014**, *6*, 22585−22593.

(60) Fajardo, O. Y.; Bresme, F.; Kornyshev, A. A.; Urbakh, M. Water in Ionic Liquid Lubricants: Friend and Foe. *ACS Nano* **2017**, *11*, 6825−6831.

(61) Noël, O.; Mazeran, P.-E.; Stanković, I. Nature of Dynamic Friction in a Humid Hydrophobic Nanocontact. *ACS Nano* **2022**, *16*, 10768−10774.